Infrared Spectroscopy of HII Regions And Starburst Galaxies

Ruth Mary Doherty

Presented for the Degree of Doctor of Philosophy
at the University of Edinburgh
1994

This thesis is solely my own composition, except where specifically indicated in the text.

Ruth Doherty,
June 1994.

Abstract

This thesis is concerned with testing models of the infrared HeI 2.058μm/Brγ ratio as a function of effective temperature in HII regions. This ratio is known to be sensitive to effective temperatures in the range T_{eff}=32–38,000K. Near-infrared observational data from ultracompact (UC) HII regions, compact HII regions and giant HII regions or the nuclei of starburst galaxies is presented and analysed for this purpose.

Observations of UCHII regions show that HII region models with an electron densities of $n_e=10^4 cm^{-3}$, electron temperatures in the range T_e=5,000–10,000K and a Galactic helium abundance can reproduce the observed HeI 2.058μm/Brγ ratios in these objects, subject to one condition. As the electron temperature is increased from T_e=5,000K, microturbulence is incorporated into the model which counteracts the increase in the HeI 2.058μm/Brγ ratio with electron temperature. Microturbulent velocities of the order $\sim$20kms^{-1} are required at T_e=10,000K, in agreement with observed radio recombination line and high resolution HeI and HI measurements.

Lower HeI 2.058μm/Brγ ratios are generally found in larger objects classed as compact HII regions, consistent with lower electron densities or lower stellar effective temperatures, or a combination of both effects in such objects. Alternative electron densities have been calculated from radio continuum measurements and provide evidence to suggest that electron densities are slightly lower in most of the compact HII regions than in the UCHII regions.

Detailed density gradient modelling of the HeI 2.058μm/Brγ ratio has been performed, which reveals the need for realistic density distributions and explicit integration over the volume of the source when attempting to model specific HII regions. Accurate integrated electron densities or density gradients act as an alternative to microturbulence to bring theoretical HeI 2.058μm/Brγ ratios into agreement with observations for electron temperature models higher than T_e=5,000K.

Finally, a large sample of starburst galaxies are analysed. The HeI 2.058μm/Brγ ratios are much lower than found in compact or UCHII regions consistent with the

proposal that the integrated HeI 2.058 μm/Brγ emission is generally dominated by low density giant HII regions present in these galaxies. Effective temperatures derived from the HeI 2.058 μm/Brγ ratio are consistent with those estimated from FIR fine structure lines. From consideration of new models of the HeI 2.058 μm/Brγ ratio, the combination of optical HeI/Hβ data with HeI 2.058 μm/Brγ observations extends the sensitivity of these model ratios to a wider range of effective temperatures.

Acknowledgements

I acknowledge the SERC for funding three years of my studies and my observing trips.

I would like to express my sincere gratitude to my supervisor, Phil Puxley, for his commitment and continuous guidance and instruction throughout my Ph.D. To Stuart Lumsden, my adopted other supervisor, I wish to express my everlasting thanks for all his patience, confidence and endless time spent imparting some of his vast knowledge of physics to me. I am indebted to Phil James for his valuable aid, advice and support. I would also like to thank Phil, Stuart and Phil for numerous readings of this manuscript and who between them have taught me everything I know. Many thanks to Peter Brand, my university supervisor for advice and discussions. Thanks to Suzie for teaching me about CGS4 and to Karen for help with Unix.

To my dear friends Isabelle and Phil for their friendship and much more besides. To Stuart, so much thanks for everything really, especially the e-mails. For knowing the right things to say and picking up the pieces I'd like to thank Suzie. Thanks to Andy, for laughing at me and waiting for me in the pub. I would like to thank my office mates and agony columnists Dave and Hugh. I was extremely fortunate to be in the same year as Isabelle, Kathy and Bob. To Richard for having footsteps to follow in, and to Pippa, Lance, Richard, Karen and Karen for being there. Thanks to Malcolm and Reni for making my observing trips to Hawaii so memorable.

Back home, thanks to my good friends and flatmates Eirian, Emma, Jenny and Peter for putting up with me and for a real home to come back to. I would also like to thank Glenn, Anna, Kate and Ailsa for being there especially when I needed them.

Up north, to my dear friends and fellow conservationists, Andy (and for the mutual phone calls too), Judith, Kath, Kate, Tonya and Jack for their inspiration, encouragement and all the fun times. Hopefully, there'll be many more.

I would to thank my parents for their support and encouragement in my career direction especially recently. Finally, thanks to Nicola, Hazel and Michael for more than words can say.

Contents

Chapter 1

Introduction

1.1 HII regions–A basic description

By solving numerically the equation of transport for hydrogen-ionizing photons, together with the condition for ionization/recombination balance, Strömgren (1939) showed that spheres of almost fully ionized gas should exist around hot O stars with a rather sharp transition to the outlying, almost fully neutral gas. Thus, the concept of an HII region arose. His work was motivated in an effort to explain the discovery by Struve and Elvey (1938) of ionized emission lines of hydrogen in the Milky Way, as opposed to Eddington's (1934) prediction that hydrogen is not ionized in normal regions of the interstellar medium.

Writing this equation for ionization and recombination equilibrium in standard notation:

$$n_{H^\circ} \int_{\nu_0}^{\infty} \frac{4\pi J_\nu}{h\nu} a_\nu(H^0) d\nu = n_e n_p \alpha(H^0, T_e) \tag{1.1}$$

J_ν is the mean intensity of radiation, and $4\pi J_\nu/h\nu$ is the number of incident photons per unit area per unit time per unit frequency interval, $a_\nu(H^0)$ is the ionization cross-section for a photon with energy $h\nu$ above the threshold $h\nu_0$ and n_{H^0} is the neutral atom density per unit volume. The LHS of eqn 1.1 represents the number of photoionizations per unit

time per unit volume. n_e and n_p are the electron and proton or ion densities per unit volume and $\alpha(H^0,T_e)$ is the recombination coefficient, and the RHS of eqn 1.1 represents the number of recombinations per unit volume per unit time. By integrating over the volume, the distance from the nebula at which the transition to n_p=0 occurs can be found.

The sharp transition is defined by the so-called Strömgren radius R_s given by:

$$Q(H^o) = \int_{\nu_o}^{\infty} \frac{L_\nu}{h\nu} d\nu = \frac{4\pi}{3} R_s^3 \alpha_B n_e n_p \tag{1.2}$$

where $Q(H^0)$ is the number of ionizing photons per unit time emitted from the star, L_ν is the luminosity of the star and α_B is the case B recombination coefficient (discussed in section 1.2.2). Strömgren further pointed out that these photons have energies greater than that required to merely ionize hydrogen, thus they could be important for heating the gas.

The development of HII region theory coupled with observations, in the radio in particular, led to the establishment of an evolutionary sequence for HII regions. This was followed by a classification scheme by Israel (1967), based on electron density and diameter values for these objects.

In the initial stage, following the onset of nuclear burning in one or more O or B stars, an ionization front (IF) is set up in the molecular cloud and an ultracompact (UC)HII region (class I, Israel 1967, see table 1.1) evolves. These regions are small (diameter d<0.15pc), extremely dense ($n_e > 3\times10^3 cm^{-3}$) and obscured in the optical as well as being optically thick at radio frequencies $\leq$ a few GHz. These objects were first discovered in the late 1960's when resolutions comparable with UCHII region diameters were achieved with radio interferometers . These radio observations showed that HII regions sometimes contained very compact (d<1 pc) components of high emission measure ($EM>10^6 cm^{-6} pc$). The first completely convincing case became the isolated compact HII region DR 21 (Ryle and Downes 1967).

UV photons cause rapid ionization and the energy excess heats up the gas to $\sim$ $T_e=10^4$K, about a factor of 100 higher than the temperature of the surrounding gas in

the neutral molecular cloud (Spitzer and Savedoff 1950). This creates a large pressure differential, producing a rapid expansion. Cooling of the gas is discussed in section 1.2.3.

The density of the region decreases with time and a compact HII region (class II, table 1.1) forms. The size of a compact HII region lies in the range 0.1-1.0 pc and they have typical densities greater than $10^3 cm^{-3}$ (table 1.1).

Observationally, there seems to be some overlap amongst authors, between objects classed as UCHII regions and compact HII regions, due to different source sizes measured for the same object. In this thesis, a sample of UCHII regions are studied in chapters 2 and 3. This sample is a subset of the UCHII regions observed by Wood and Churchwell (1989) at 5 and 15 GHz. These objects fall into class I of Israel (1967) with the exception of the two core-halo sources in the sample which fall in class II (compact sources) according to their diameters and electron densities, derived in chapter 5. In chapter 4, a sample of compact HII regions selected from their measured source sizes at 1.4GHz by Zoonermatkermani *et al.* (1990) are studied; all these objects fall into class II.

As HII regions evolve, they disperse the surrounding gas and dust and are no longer fully embedded in their natal molecular cloud. Consequently, these objects are visible in the optical which leads them to be termed as classical HII regions (class IV, table 1.1) *e.g.* the Orion Nebula, Sharpless objects (1959), *e.g.* S104, S162, because they were the first category of HII regions to be observed. See Fich (1993) for a recent review of properties of these regions.

Assuming that the expansion velocity of the compact HII region is comparable to the thermal sound speed of 10 kms^{-1}, the nebular size increases, the gas density drops and the nebula becomes a diffuse, extended or giant HII region (class V, table 1.1) after $\sim 10^4$ years. Diffuse, extended or giant HII regions are recognized by their larger diameters $\geq$a few pc, and densities $n_e \leq$ a few$\times 10^2 cm^{-3}$. The geometries of these objects are rather more complicated. Observations and a discussion of giant HII regions in external galaxies are presented in chapter 6. Such evolved HII regions appear to fit into one of four structural types: rings, core-halos, smooth structures and irregular or filamentary structures. For further discussion of these objects see Churchwell (1975, and references therein).

Definition				Properties						
Class	$n_e(cm^{-3})$	d(pc)	E.M. (pc cm^6)	Nature	Examples	Optical appearance	Group properties	OH/H_2O masers	$S(20\mu m)/S(6cm)$	Ionized mass ($M_\odot$)
(1)	(2)	(3)	(4)	(5)	(6)	(7)	(8)	(9)	(10)	(11)
I	> 3000	<0.15	$> 10^6$	Ultra-compact	W3OH, S157B	Obscured	Never isolated	+	$< 10^4$	$\simeq 10^{-2}$
II	> 1000	0.1–1.0	$> 10^5$	Compact	W3A, K3-50	Strongly reddened	Never isolated	–	$< 10^3$	$\simeq 1$
III	100–3000	0.15–10	1×10^4–3×10^6	Dense	S158, S90	Partially obscured	Sometimes isolated	–	$< 5 \times 10^2$	$\simeq 10$
IV	100–100	1–30	5×10^2–1×10^5	Classical	S104, S162	Globules, bright rims	Sometimes in groups	–	$< 10^2$	$\simeq 10$–5×10^2
V	3–50	10–300	$< 5 \times 10^5$	Giant	Core, NGC5461	Complex or diffuse	—	–	–	$\simeq 500$–5×10^6
VI	10	> 100	$< 1 \times 10^5$	Super-giant	Envelope, NGC5461	Structure-less	—	–	–	$\simeq 10^6$–10^8

* From Israel (1976b).

Table 1.1: HII region classification scheme based on source diameters and electron densities taken from Israel (1967).

The rest of this introduction deals mainly with UC and compact HII regions (the subject of chapters 1–5), first predicted by Davidson and Harwit (1967). These objects are deeply embedded in their parental molecular cloud, and thus are powerful far-infrared sources, since dust re-emits the UV radiation from the exciting stars at this wavelength. Thus, the main observable radiation from these objects will be at infrared and radio wavelengths. In this chapter the fundamental physics of compact HII regions is described, and the main observational results and modelling work are summarised. This framework is used throughout this thesis to determine the physical properties of UC and compact HII regions. The basic physical processes are described in section 1.2 and a discussion of modifications necessary due to dust is given in section 1.3. In section 1.4, previous results from radio and infrared observations are discussed and techniques for determining physical properties are sketched out. The modelling of compact HII regions is the subject of section 1.5 and models that are used in the context of this thesis are introduced. Finally, in section 1.6, the aims of this thesis, their relationship to previous work and the chapter contents of this thesis are outlined.

1.2 The physics of ionized gaseous nebulae

The physics of compact HII regions, dealt with in this thesis, concerns the nature of the hot OB powering stars, primarily the effective temperature, T_{eff}, and the physical properties *e.g.* electron densities, of the envelope of ionized gaseous material formed around these stars. The physical radiation processes discussed are restricted to those mechanisms which produce observable radiation from UC and compact HII regions *i.e.* radiation emitted at radio and infrared frequencies. The emission from the ionized gas in HII regions is produced from continuum and discrete processes principally: bound-bound transitions, free-bound transitions and free-free (Bremsstrahlung) transitions. Bound-bound transitions can only occur between discrete atomic levels, whilst in the other two processes one or both levels are in the continuum.

1.2.1 Continuum processes

Recombination of electrons in the ionized plasma is followed by emission of discrete photons in bound-bound transitions and also by emission of continuum radiation in free-bound transitions. Since hydrogen is the most abundant element (90% by number), the HI continuum will be the strongest. Free-bound transitions, are strongest in the optical, but at infrared and radio frequencies the free-free continuum is dominant (Ferland 1980). Free-free or Bremsstrahlung radiation arises from emission of a photon by an electron which is accelerated in the vicinity of an ion.

With the emphasis on dust enshrouded UC and compact HII regions, only infrared and radio continuum processes are discussed further. The infrared continuum in HII regions is produced by a combination of mechanisms in addition to free-free transitions, *e.g.* thermal emission by hot small dust grains, which makes interpretation of physical parameters difficult. Fortunately, the radio continuum is only produced by free-free transitions in HII regions. Thermal electrons have a characteristic black body spectrum, whose shape is given by the Planck function $B_\nu(T)$. At radio frequencies $B_\nu(T) \sim 2\nu^2 kT/c^2$. The intensity of the free-free radiation is found from solution of the equation for transport of radiation through matter *i.e.* the ionized plasma. The equation of radiative transfer is:

$$\frac{dI_\nu}{ds} = -k_\nu I_\nu + j_\nu \tag{1.3}$$

I_ν is the intensity of the radiation emitted from the source, $k_\nu = n a_\nu$ is the absorption coefficient, n is the number density of absorbing particles and a_ν is the absorption cross-section; j_ν is the emission coefficient. $B_\nu(T)$ can be defined as j_ν/k_ν. Further, the optical depth in a material (here an ionized plasma), τ_ν, is :

$$\tau_\nu = \int_{s_1}^{s_2} k_\nu ds \tag{1.4}$$

If the gas is optically thin $\tau < 1$, a photon of frequency ν will travel a distance $\Delta s = s_2 - s_1$, unhindered by the absorbing material. Conversely if the gas is optically thick $\tau_\nu > 1$, a photon of energy ν would be absorbed and re-emitted many times before travelling a

distance Δs. The optical depth for free-free radiation given by Mezger and Henderson (1967) is:

$$\tau_\nu = 8.24 \times 10^{-2} T_e^{-1.35} \nu^{-2.1} EM \tag{1.5}$$

where T_e is the electron temperature, and EM (pc cm^{-6}) the emission measure. The free-free emission, S_ν, is given by the solution of eqn 1.3 for no incident radiation:

$$S_\nu \propto B_\nu (1 - e^{-\tau_\nu}) \tag{1.6}$$

Therefore for $\tau_\nu \gtrsim 1$, the radio spectrum has a profile $S_\nu \propto \nu^{+2}$, whilst for $\tau_\nu \lesssim 1$, $S_\nu \propto \nu^{0.1}$.

Combining these last two equations it is seen that S_ν is a function of electron temperature, T_e, and emission measure, EM, which is in turn a function of electron density, n_e and source volume. For an assumed T_e, the integrated electron density can be estimated from an observed radio flux density, S_ν, if the optical depth in the free-free continuum and the source diameter is known. The equations of Panagia and Walmsley (1978), which use idealized density distribution models: (spherical, cylindrical, Gaussian or homogeneous density distributions), are used extensively to calculate mean or integrated electron densities in chapter 5, where effects of density clumping and gradients are also discussed.

Rubin (1968b) formulated a relation between the free-free flux density for an optically thin plasma, S_ν, and the number of ionizing photons produced from the star, *i.e.* N_{Lyc} the Lyman continuum photon flux. Thus, from an observed radio flux density, the number of ionizing photons can be deduced if the electron temperature and distance to the source is known. Using stellar atmosphere models, *e.g.* Kurucz (1979), the effective temperature of the exciting star(s) can then be estimated. N_{Lyc} can also be inferred from HI recombination lines, discussed shortly. Further, N_{Lyc} can be translated into a theoretical intensity for a given recombination line. This technique is described in section 2.4 and used in subsequent chapters to estimate the extinction to an HII region.

1.2.2 Recombination lines

Following recombinations or captures of electrons into excited levels of HI, bound-bound or discrete radiation is emitted by atoms undergoing radiative transitions in cascading down to the ground state. A recombination line spectrum of HI, HeI and other elements is observed in HII regions. The strongest recombination lines result from optical and infrared transitions. Recombination lines from high n-levels are seen in the radio, where n is the principal quantum number, which defines the system of discrete energy levels within an atom. The formation of recombination lines in hydrogen atoms is now discussed.

The important processes involved are captures leading to downward-radiative transitions and collisional transitions. Any collisional interaction must conserve both energy and angular momentum. Collisions of excited atoms in high n-levels with protons, can cause a change in energy levels predominantly from n$\rightarrow$n$\pm$1. Meanwhile, collisions with electrons redistribute angular momentum between L$\rightarrow$L$\pm$1 states within the same n-level. L is the orbital quantum number physically related to angular momentum. Collisional ionization becomes important in high n-levels (n>15) *i.e.* in radio recombination lines, above electron temperatures of T_e ~15,000K (Clegg, 1987), which is higher than generally assumed for HII regions.

The population in any level is given by a balance between arrivals: direct recombinations, collisional transitions and downward spontaneous transitions versus departures; collisional transitions either upwards or downwards, and downward spontaneous transitions. The atom returns to its lowest energy state, emitting photons with discrete energies *i.e.* recombination line photons. For any recombination line, the emission coefficient, j_ν, which represents the intensity, or total energy of photons emitted in that transition, can be calculated. Effective recombination coefficients, α_{eff}, for a transition are also often used where:

$$n_p n_e \alpha_{eff} = \frac{4\pi j_\nu}{h\nu} \tag{1.7}$$

Both these parameters are dependent on electron temperature, T_e.

The population of any nL level can be defined entirely in terms of local plasma

properties: proton and electron densities and electron temperature. To account for deviations from thermal equilibrium, departure coefficients, b_{nL}, are introduced. In thermal equilibrium all b_{nL} factors are equal to unity. To solve the emission line spectrum for HI, b_{nL} factors are calculated for each level. The most recent and most comprehensive work, which calculates a complete solution for the line intensities for an HI atom for several electron densities and temperatures, is that of Hummer and Storey (1987).

The recombination process described so far, assumes that all line photons emitted in a nebula escape without absorption, and therefore without causing further upward transitions–case A (Baker and Menzel, 1938). Case A is a good approximation for gaseous nebulae that are optically thin in all HI Lyman lines, however, generally HII regions are optically thick to Lyman photons and case B of Baker and Menzel (1938) applies. For case B, direct recombinations into, or cascades down to, the 1^1S electronic state produce a Lyman continuum or line photon, which ionizes or excites another hydrogen atom close to the source of emission. Thus, apart from Lyman emission by atoms at the edge of the nebula, only photons produced by transitions between higher n-levels can escape. Case B is used in the derivation of the Strömgren radius (eqn 1.2) and is a result of the on-the-spot (OTS) approximation used (Zanastra 1951). In this approximation any ionizing photon emitted in the nebula is absorbed elsewhere in the nebula.

Calculation of a complete series of line intensities can be extended to the two-electron HeI atom which consists of singlet and triplet levels. These two sets of non-degenerate levels, meaning the energies of different L states are different (unlike hydrogen), can be solved separately since all transition probabilities between them are small. The triplet levels always follow case B, because downward radiative transitions to 1^1S only occur by low-probability forbidden-line transitions. Forbidden lines are discussed in section 1.2.3. Effectively, the 2^3S level is the lowest term in the HeI triplet series since depopulation only occurs by forbidden transitions to 1^1S, or collisional transitions which are discussed above. Thus the lifetime of excited atoms in the 2^3S level is long compared with other excited levels, and this level is termed metastable. Hence, the 2^3S population is large and optical depth or self absorption effects in allowed transitions (2^3S–n^3P), arising from the 2^3S level, may be important as densities increase. Robbins (1968) calculates self absorption effects in the HeI triplet series and the resulting decrease or enhancement

of recombination line in the HeI triplet series.

In HII regions, generally case B is a better approximation for the HeI singlets, however any Lyman photon emitted from the 1^1S–2^1P transition can instead be absorbed by hydrogen. Smits (1991a,b) produces the most sophisticated model of intensities in the HeI recombination spectrum to date.

In HII regions, collisional transitions in low n-levels of HI, are insignificant in comparison with recombination and spontaneous transitions, in populating excited levels. As discussed above, in HeI the 2^3S level is highly metastable, and an atom in this excited state will collide with many electrons before it undergoes a forbidden transition to 1^1S. Therefore, as the electron density increases there is a greater probability that an atom in the 2^3S level will be collisionally de-excited or excited to other n=2 or higher levels. These collisional processes couple the n=2 singlet and triplet series. Clegg (1987) describes a complete level population equation for the 2^3S level and Smits (1991a,b) solves the HeI recombination line spectrum for these populations, including these effects. Accurate collision strengths from n=2 to other n=2 and higher levels have been calculated by Berrington and Kingston (1987).

Once HI and HeI line intensities have been calculated, the ratio of HeI/HI lines can be used to predict effective temperatures of the ionizing stars, since this ratio is a measure of the number of photons output by the exciting star(s) with energies capable of ionizing helium, to those capable of ionizing hydrogen.

Recombination line profiles are now discussed and then the section is concluded with a description of emission line radiation which results from collisionally excited forbidden transitions.

Line shape

The natural line width $\Delta E \propto (1/\Delta t) \sim A$, arises from the uncertainty principle, where A is the spontaneous transition probability. The line shape has a characteristic Lorentzian or damping profile. Recombination lines are further broadened as a result of thermal motions of atoms in the ionized gas, whereby a photon emitted from an atom with

frequency ν will have a Doppler-shifted frequency $\nu'=\nu(1 + V/c)$ when absorbed by a neighbouring atom for a relative velocity V between the two atoms. The velocities of the moving atoms have a Maxwellian distribution and the thermal Doppler width is:

$$\Delta v_D = \sqrt{\frac{2kT_e}{m}} \tag{1.8}$$

A line width is commonly quoted as a full width half maximum value, FWHM, which is equal to $1.66\times\Delta v_D$. The resulting line profile has a Gaussian distribution. The thermal Doppler width of hydrogen atoms is 12.9 kms^{-1}, whilst that of helium is 6.4 kms^{-1} at T_e=10,000K. In contrast the natural line width is $\ll$1 kms^{-1}, therefore Doppler line broadening dominates the natural line width.

Further sources of line broadening may come from microturbulent motions *i.e.* turbulent motions on scales comparable to the mean free path that a photon travels before it is absorbed by a neighbouring atom. Microturbulence is discussed in detail in chapter 2. Garay and Rodríguez (1983) postulate microturbulent motions of order 30 kms^{-1} in UCHII regions, 20 kms^{-1} in compact HII regions and 15 kms^{-1} in extended HII regions. The absorption cross-section a_0 is given by:

$$a_0 = \frac{3\lambda^3}{8\pi}\left(\frac{m_{He}}{2\pi kT_e}\right)A = \frac{3\lambda^3 A}{8\pi^{3/2}\Delta V_D} \tag{1.9}$$

λ is the wavelength of the transition, A is the spontaneous emission coefficient, and ΔV_D is the Doppler width. Any microturbulent broadening decreases the absorption cross-section in a line and thus the optical depth in the line (section 1.2.1). In section 1.2.2, optical depth effects in the HeI singlet series were discussed. Microturbulent motions in an HII region cause the emergent HeI recombination spectrum to shift towards case A, since the smaller optical depth in the HeI 1^1S–2^1P Lyman transition results in a larger fraction of photons which photoionize hydrogen.

One further line broadening process is impact or pressure broadening due to interatomic collisions, this line profile is a lorentzian. Generally, pressure broadening is not important in HII regions unless electron densities are high, $n_e > 10^5 cm^{-3}$.

1.2.3 Collisionally excited lines

The process of photoionization continuously feeds energy into the gas. If there were no means of losing this energy, the temperature would increase indefinitely. Therefore, this process must be balanced by cooling processes. In the infrared, for compact HII regions in molecular clouds, the most important cooling process is collisional excitation followed by radiative emission.

Collisional excitation is important in less abundant species such as O, N and S since the excitation energies from the ground state to higher levels, ΔE, are smaller than those of H and He. Every collisional excitation, expends the kinetic energy of that electron by converting that energy into radiant energy, *i.e.* emission of a optically thin photon, which cools the electron gas. Hence, these species are important coolants in a nebula. Other cooling processes are recombination and free-free emission in which radiation escapes the nebula.

Balancing populations for a simple 2-level atom, from Osterbrock (1989), the intensity of the emitted line radiation is given by:

$$I = n_2 A_{21} h\nu_{21} = n_e n_1 q_{12} h\nu_{21} \left[\frac{1}{1 + \frac{n_e q_{21}}{A_{21}}} \right] \tag{1.10}$$

The populations in the upper and lower levels are denoted by n_2 and n_1 respectively. A_{21} is the spontaneous transition coefficient for the transition, q_{12} the collisional excitation strength per unit volume from the lower to the upper level, and q_{21} the collisional de-excitation line strength. The collisional excitation and de-excitation strengths are related by:

$$q_{12} = \frac{w_2}{w_1} q_{21} e^{-h\nu_{21}/kT_e} \tag{1.11}$$

The statistical weights for the two levels are w_1 and w_2. In the low density limit $n_e \rightarrow 0$ and the bracketed term in eqn 1.10 tends to unity. The intensity in the line will then be a function of the density terms and collision strength. Every upward collisional transition is followed by a spontaneous transition and emission of a line photon. The collision strength is a function of electron temperature, $q_{21} \propto 1/T_e^{1/2}$.

As the electron density increases such that $n_e \rightarrow \infty$ the line intensity becomes dependent on the ratio of the collisional excitation and de-excitation strengths, the spontaneous transition coefficient and the density in the lower level. A Boltzmann population ratio is set up; the two populations are in the ratio of their statistical weights, eqn 1.11. Thus any collisional excitation leads to either a spontaneous transition and emission of a line photon or collisional de-excitation. As the density increases the probability of collisional de-excitation increases. For any given line there is a critical density, above which collisional transitions dominate spontaneous transitions, defined as:

$$n_c = \frac{A_{21}}{n_e q_{21}} \tag{1.12}$$

This analysis can be extended to many level systems within an atom; the ratios of two collisionally excited or forbidden lines are widely used as electron temperature and density indicators. If there is a sizeable energy difference between two collisionally excited lines these lines will be strongly dependent on T_e. Two collisionally excited lines which have a small energy difference between them are dependent mainly on electron density. This technique is further explained in chapter 5 in connection with electron density determination. The advantage is that the ratio of a pair of collisionally excited lines is independent of the ionizing spectrum of the stars in the HII region.

Now that the basic physical processes in a compact HII region have been discussed this next section explains how dust can modify the emitted radiation inside and exterior to HII regions.

1.3 Dust

As the stellar UV and optical radiation propagates outward from hot, young O or B stars, it is converted to increasingly longer IR wavelengths by repeated absorption and emission by circumstellar dust. The dust grains radiate like black bodies, characterized by the temperatures of the grains, but modified by an emissivity law. Grain emissivity is a function of wavelength with an index β between -1 and -2. The grain temperatures decrease with increasing distance from the star. For hot small grains surrounding the

stars, T_g ~400K and further out or beyond the nebula, T_g ~20K. This is due to the increasing dilution of the radiation field and decreasing ability of the dust to absorb the increasingly longer wavelength radiation. At large enough distances from the star, the radiation is shifted to far-infrared (FIR) wavelengths where dust is an ineffective absorber and the radiation escapes mostly as FIR emission.

In embedded dusty regions, the luminosity in the range 5–300 μm is a good approximation to the total luminosity (Thronson and Harper 1979). If the distance to the source is known, continuum observations from IRAS (at 12, 25, 60 and 100 μm) enable the total luminosity of the source to be estimated. Luminosity measures can then be inverted to obtain estimates of the effective temperatures of the powering star(s) by use of stellar atmosphere models *e.g.* those of Kurucz (1979); see section 2.6.

Assuming that the dust is exterior to the HII region, the main effect of dust is extinction of radiation. Extinction is wavelength dependent and longer wavelength radiation suffers less extinction; at millimetre and radio wavelengths radiation is unattentuated by dust. The standard or Whitford (1958) interstellar extinction curve describes extinction as a function as wavelength. Draine (1989) has produced an extinction curve for wavelengths in the range 0.7–5 μm which is described by a power law with index -1.75, which is in good agreement with the standard interstellar extinction curve at these wavelengths. The equation of radiative transfer (1.3) enables correction for extinction effects. For a pure absorber (ignoring scattering processes) the solution of eqn 1.3 is:

$$I_\nu = I_{\nu 0} e^{-\tau_\nu} \tag{1.13}$$

where $I_{\nu 0}$ is the intrinsic intensity emitted from the edge of the HII region and I_ν is the intensity of radiation as seen by the observer. Two methods for calculating extinction are commonly used. Radio measurements, either continuum or line, are used to calculate the intrinsic intensity for a given line (see section 1.2.1). Alternatively, if two lines are considered, the differential extinction can be calculated by comparison of theoretical and observed line ratios; application of the interstellar extinction curve allows for correction of lines of other wavelengths. These calculations and further properties of the named extinction curves are discussed in chapters 2 and 6.

In reality, it is unlikely that HII regions are dust-free; dusty HII region models were first calculated by Mathis (1971) and Petrosian, Silk and Field (1972). A recent review on the subject is by Mathis (1986). Dust absorption peaks at energies or wavelengths near those required for the ionization of hydrogen (Draine 1985). Thus dust absorbs hydrogen ionizing photons in preference to helium ionizing photons. As a result, the size of the Strömgren sphere is reduced in comparison to that of a dust–free HII region excited by the same stars. In this case, extinction estimates calculated from eqn 1.13, which assumes purely foreground extinction will be inappropriate (see section 6.4).

1.4 Recent UC and compact HII region observations

1.4.1 Radio observations–continuum + line

Since the first compact HII regions such as DR21 (Ryle and Downes 1967) and W49A (Mezger, Schrami and Terzian 1967) were discovered, many more have been discovered with the increasing sensitivity and resolution of radio telescopes. However, the properties of only a few large well-known star formation regions such as Orion, M17, W3, W49 and DR 21 had been extensively studied until recently. The continuum surveys of Wood and Churchwell (1989), Garay (1989) and Kurtz, Wood and Churchwell (1994) have identified a large number of UC and compact HII regions and investigated their physical properties. There have also been a number of radio continuum Galactic plane surveys of compact radio sources *e.g.* Downes *et al.* (1980), Wink, Mezger and Altenhoff (1982), Lockman (1989), Zoonermatkermani *et al.* (1990) and Becker *et al.* (1994). In addition to the UC and compact HII regions already identified, a large number of these surveyed radio sources are potential UC or compact HII regions.

Important results concerning the geometry of these HII regions were first discovered in the radio. HII regions had been assumed to be Strömgren spheres, due to their unresolved appearance with low resolution single dish radio telescopes. Well-resolved imaging revealed geometrical structures in a number of UC or compact HII regions which were clearly not spherically symmetric.

The first of these came to light with observations by Zuckerman (1973) who concluded that the Orion nebula lies on the edge of a molecular cloud described as a bright, ridgelike core surrounded by a less bright envelope. The structure resembles a bubble, or blister of ionized gas on the edge of a molecular cloud (see fig 1.1). Since then, more blister HII regions have been identified *e.g.* M17, 30 Dor (Icke, Gatley and Israel 1980). All these HII regions fall into class III and IV (see table 1.1) termed dense and classical HII regions; a number of these objects are optically visible.

The first blister models were produced by Tenorio-Tagle (1979) and Bodenheimer, Tenorio-Tagle and Yorke (1979). When a star forms near the edge of a molecular cloud, its IF moves outwards radially until it reaches the edge of the molecular cloud. There it encounters the much lower density intercloud medium. The expansion proceeds preferentially towards directions of decreasing density *i.e* into the intercloud medium causing a partially bound ionized nebula out of the cloud. This density gradient sets up a pressure differential, driving material from the ionization bounded denser sides within the molecular cloud, into a conical volume streaming towards the density bounded directions. This is called the champagne flow phase. The resultant "blister" structure is produced. The geometry of such a HII region would be better represented by an axially symmetric object (Rubin 1986). For a full description of the dynamics of this model see Yorke (1986, and references therein). Yorke, Tenorio-Tagle and Bodenheimer (1983, 1984) have extended these calculations to construct radio maps and line profiles from their models. Theoretical radio continuum (Icke *et al.* 1980) and line emission models (Rubin 1984) from such HII regions show qualitative agreement with observations. Recently, Baldwin *et al.* (1991) modelled the observed line emission, for a large number of optical and near-infrared transitions, in Orion with a blister model and found satisfactory agreement with observations.

The surveys of Garay (1989), Wood and Churchwell (1989) and Kurtz, Wood and Churchwell (1994) detected a large number of UCHII regions, amongst which shell-like and cometary structures were common. To observe such number counts in the Galactic plane suggests that the lifetimes of UCHII regions must be greater than 10^4 yrs (Churchwell 1990). However, assuming the expansion velocity of an HII region is $\sim$10 kms^{-1} the lifetime of these UC and compact HII regions (Class I and II, table 1.1) is

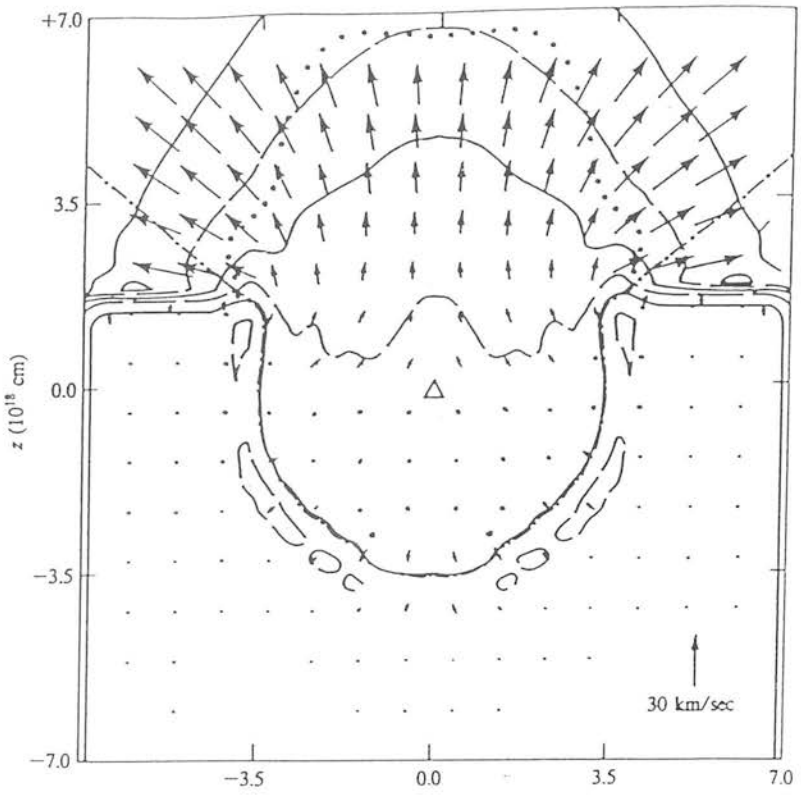

Figure 1.1: Blister HII region model by Bodenheimer, Tenorio-Tagle and Yorke, (1979).

expected to be only $\sim 10^3$yr. Therefore some process(es) must be hindering the expansion of UC and compact HII regions.

One of the earliest known and best studied UCHII regions, W3(OH) shown in fig 1.2, has a shell-like morphology (Scott 1981, Dreher and Welch 1981). Three mechanisms to generate a central cavity and surrounding shell structure are outlined below:

a) The champagne effect which is described above. Such a model would result in an evacuated cavity and a bright rim of ionized gas surrounding the ionization bounded sides of the HII region. However, a gap in the rim or shell would occur where the HII region has expanded into the intercloud medium. This gap is inconsistent with observations of shell structures (*e.g.* Turner and Matthews, 1984).

b) The effect of radiation pressure on the dust which is coupled to the gas, driving material outwards to produce a shell. However, it is predicted that this shell should inevitably break up (Turner and Matthews, 1984).

c) The effect of stellar wind which is the favoured explanation of shell-like morphologies in UCHII regions. Strong stellar winds are produced in O and early B stars (Abbot and

Hummer 1985). If a wind is produced during the UCHII region phase, it will sweep up material and create a central cavity in the ionized gas.

The latter two mechanisms could explain the prolonged lifetime of UCHII regions with shell morphologies. Because HII regions evolve rapidly they may not be in equilibrium. An outer shell of gas and dust (a remnant of star formation) which may still be collapsing inwards is stopped by the radiation pressure of the star or ram pressure of its stellar wind, thus maintaining the shell cavity in the centre. This infalling gas would slow the expansion of the ionized gas, extending the life of a UCHII region. Evidence for infall from observed OH maser radial velocities, is given by Reid *et al.* (1980) and Garay, Reid and Moran (1985). Wood and Churchwell (1989) observe many HII regions with shells and cometaries which seem to have central cavities or holes in the ionized gas. It is unlikely so many objects would be seen if they were not supported by a stellar wind or radiation pressure on dust within the HII region.

An alternative model, has recently been proposed to explain both the extended lifetime and the cometary appearance of a substantial fraction of these UCHII regions. This cometary structure of G34.26 is shown in fig 1.3. As for the shell-like morphologies, a stellar wind is required to maintain a central cavity. The longer lifetimes of cometary UCHII regions is inconsistent with blister models. Bow shock models (see fig 1.4) which explain the cometary morphology are favoured by Wood and Churchwell (1989).

In this model, the embedded O stars are in motion relative to the ambient molecular cloud and have formed a neutral molecular bow shock supported by a stellar wind from the ionizing star. A bow shock would provide a dense medium which would halt the IF in the forward and perpendicular directions of motion, causing the HII region to be confined in these directions, producing the cometary structure observed (see fig 1.4). In the vicinity of the bow shock, the ram pressure produced by the ambient molecular gas flowing around the bow shock, due to the star's motion through the molecular cloud, is balanced by the stellar wind pressure on the ionized gas; thus the nebula is static. This model could plausibly increase the lifetime of an HII region in its ultracompact phase to be consistent with the numbers observed in the Galaxy (Wood and Churchwell 1989). Furthermore, Mac-Low *et al.* (1991) have produced bow shock models that can explain

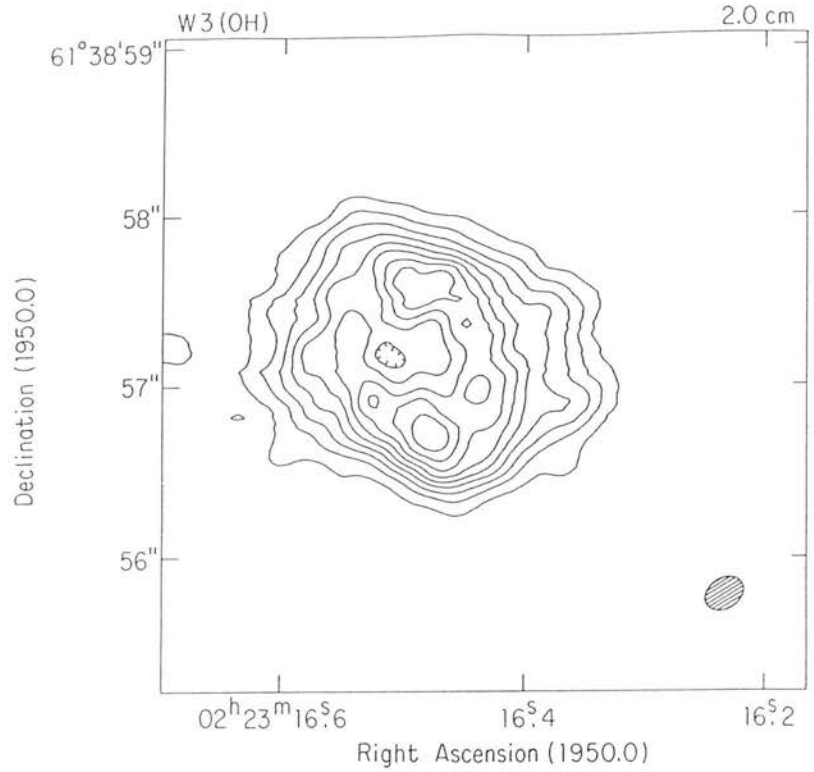

Figure 1.2: A radio continuum map of W3(OH) from Dreher and Welch (1981), showing the shell-like appearance of this object.

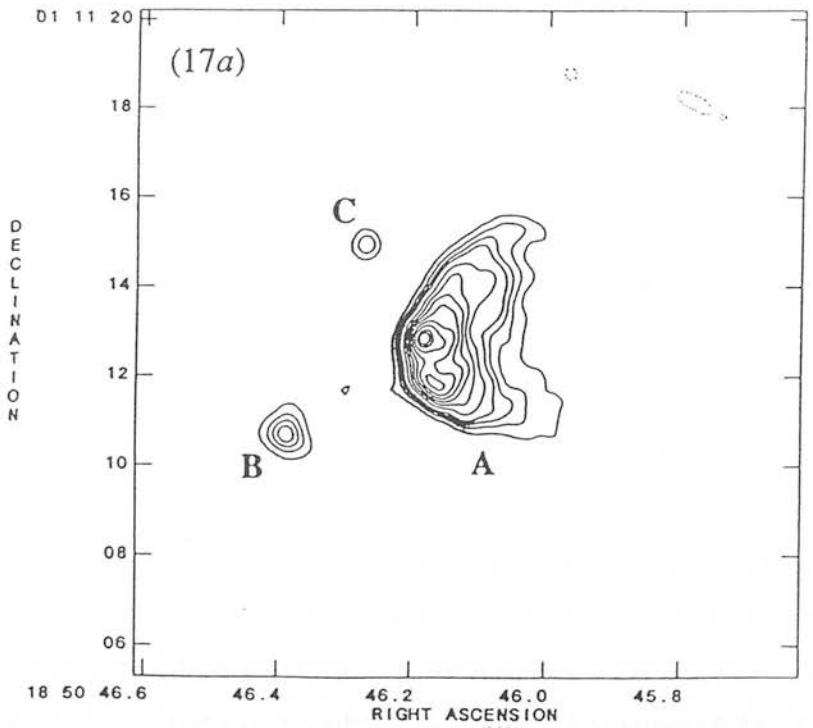

Figure 1.3: A 15GHz radio continuum map of the cometary UCHII region G34.26 by Wood and Churchwell (1989).

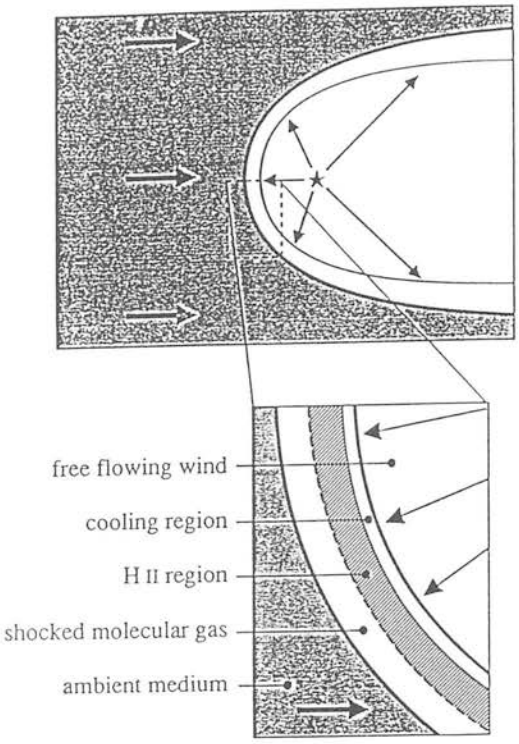

Figure 1.4: Bow shock HII region model from Churchwell (1990).

not just the cometary, but all the other observed morphologies, except for shell-like structures, seen in UCHII regions.

One further explanation of the longer UCHII region lifetimes is that by Hollenbach, Johnstone and Shu (1992) which predicts that UCHII regions are the result of flows from photoionization of accreting disks around O stars. The UCHII regions are long-lived because they are constantly being replenished by material from the accretion disk. A stellar wind may or may not be present.

Radio recombination lines

Over the past decade very sensitive observations of radio recombination lines (RRL's) using high angular resolution synthesis telescopes have been available. RRL's result from transitions between high n levels; their physics is complicated by stimulated emission, collisional ionization and pressure broadening processes. The advantage of studying radio recombination lines is that they are unaffected by extinction. In the radio, the continuum

is not weak in comparison with the line radiation and must be included when predicting line intensities. Radio measurements are described in terms of brightness temperatures, $T_{b\nu}$, where

$$T_{b\nu} = T_e(1 - e^{-\tau_\nu}) \tag{1.14}$$

The line to continuum brightness temperature ratio yields the electron temperature in a nebula. Typical electron temperatures of T_e=5–12,000K are found in HII regions (Wink *et al.* 1982). Radio measurements of electron temperatures in HII regions first showed an abundance gradient from the center of our Galaxy (Churchwell and Walmsley 1975, Viner, Clarke and Hughes 1976). Such an abundance gradient had been found from optical studies in other galaxies (*e.g.* Aller 1942) but extinction towards the center of our Galaxy had hindered such observations. By combining observations of two or more RRL's electron densities can be estimated. Very high n-transitions cannot not be used because pressure broadening will be important.

The central velocity of a line can be used to determine the distance to the nebula (see section 4.5.3) and maps of large systematic motions of the gas throughout the nebula can be constructed. The width describes broadening processes on microscopic scales in the gas *e.g.* microturbulence. From the maps of velocity structure of RRL's, Garay, Rodríguez and van Gorkum (1986), showed evidence for expansion in several UCHII regions. Garay and Rodriguez (1983) found the line widths of compact HII regions to be considerably broader than those of diffuse HII regions and concluded that the larger widths in UC and compact HII regions are due to turbulent motions.

Millimetre recombination lines arising in lower n levels have been measured by a number of authors, *e.g.* Sorochenko *et al.* (1969), Waltman *et al.* (1973) in Orion. Recently, Gordon and Walmsley (1990) and Forster *et al.* (1990) have extended observations of millimetre lines to a number of HII regions. Millimetre observations are also unaffected by extinction and not generally complicated by stimulated emission processes or pressure broadening. Like other recombination measurements of radio and millimetre HeI/HI line strengths can be used to predict helium abundances.

1.4.2 Infrared Observations

In 1970, Low and Aumann (1970) reported the detection of large far-infrared continuum fluxes from M17. A short time later, Harper and Low (1971) showed that intense far-infrared emission was a common characteristic of compact HII regions. Many HII regions could radiate much of their energy at wavelengths around 100 μm, this energy being that of the central star re-radiated from cool dust in and around the HII region. Further, a very strong approximately linear correlation was found between the integrated radio and FIR flux densities from Galactic HII regions (Harper and low 1971). This correlation suggests that it is the O stars that are the main source of energy input into the grains. This correlation between the total luminosity and the radio continuum has been used as a diagnostic of spectral type for a single main sequence star or cluster of stars (*e.g.* Jennings 1975); both quantities measure effective temperatures of single stars and the combination of the two quantities reveals cluster temperatures (see section 2.6).

The IRAS mission provided FIR continuum spectra for a large number of HII regions identified from radio measurements. From near–infrared, IRAS and millimetre observations (see Chini, Krügel and Wargau 1987), and sub-millimetre observations (Hoare, Roche and Glencross 1991), it has been shown that the energy distributions of compact HII regions are all similar. This is because when the dust cloud is optically thick in the near and mid-infrared then the emergent spectrum is insensitive to effective temperatures of the exciting star(s). The observed energy distribution depends mostly on the column density of dust, its optical properties and density distribution (Hoare *et al.* 1991). Approximately, for an HII region of constant density n_e=10^4cm^{-3}, the emission above 100 μm comes from cool dust around the ionized nebula, $\sim$20 μm from the warm dust in the HII region, at $\sim$5 μm only from very hot grains near the star, and below $\sim$3 μm free–free and bound–free transitions from the gas are the main emission mechanisms. An increase in density shifts the maximum of the IR emission towards shorter wavelengths, because the radius of the HII region shrinks and the grains are closer to the star and therefore hotter. Mid-infrared imaging of the warm dust in several UCHII regions carried out by Ball *et al.* (1992) and Keto *et al.* (1992) is in agreement with this picture. Krügel and Mezger (1975) developed models of IR emission from warm dust

surrounding O stars. In these models a single grain size was used. These models have been superceded by models that use a distribution of grain sizes. Recently, Chini *et al.* (1986), Hoare *et al.* (1991) and Churchwell, Wolfire and Wood (1990) have produced models of the IR dust emission associated with UCHII regions.

Whilst continuum far–infrared measurements are diagnostics of the dust in and surrounding HII regions, infrared line radiation emanates from forbidden and permitted transitions in the ionized plasma. One infrared line feature due to dust is the broad 9.7 μm absorption feature, attributed to silicate grains, and is often seen in HII regions (Jourdain de Muizon, Cox and Lequeux 1990, Simpson and Rubin, 1990). The optical depth in this feature has been related to the extinction in a nebula (*e.g.* Roche and Aitken 1984). A number of polycyclic aromatic hydrocarbon (PAH) features have also been detected (Jourdain *et al.* 1990).

Permitted HI bright transitions of the Paschen, Brackett and Pfund series are seen in the near infrared. The HeI 2.058 μm, 2^1P–2^1S, transition is observed if there is considerable optical depth in the singlet Lyman series (*e.g.* Thompson and Tokunaga 1980), the case B assumption for HeI (section 1.2.2). The equivalent triplet HeI 1.083 μm, 2^3P–2^3S transition is bright since the 2^3S level is the effective ground state for the triplet series (section 1.2.2). Forbidden transitions of heavier elements are rife in the infrared. Lacy 1981, summarizes the infrared observations up to then, of near to far-infrared emission lines in HII regions.

More far-infrared forbidden lines have been detected since airborne observations have been made, *e.g.* by the Kuiper airborne observatory, as the atmosphere is mostly opaque for wavelengths between 30–300 μm from the ground. The far-infrared fine structure lines [OIII] at 52 and 88 μm and of [SIII] at 19 and 33 μm have been used as density diagnostics in HII regions (see *e.g.* Megeath *et al.*, 1990 and references therein). These lines are sensitive in the ranges n_e=10^3–10^4cm^{-3}. This procedure is outlined in section 1.2.3. and discussed in section 5.2. Any two line pairs are sensitive only within a range of electron density, therefore measurements from different line pairs may represent electron densities in different ionized zones. Rubin *et al.* (1994) give maximum sensitivities for different lines.

The excitation, or level of ionization, of a region is best determined by comparison of lines of several ionization states of an element. The mid-infrared lines of [NeII] (12.8 μm), [Ar III] (9.0 μm) and [SIV] (10.5 μm) are observable from the ground and their ratios have been used by Lacy *et al.* (1979), Rank *et al.* (1978), and Lacasse *et al.* (1980) to estimate effective temperatures in the HII regions Sgr A, G333.6 and G298.2 and W3 respectively. Recently, Simpson and Rubin (1984), Hoare *et al.* (1991) and Colgan *et al.* 1991 have used these techniques on some or all of the UCHII regions G29.96, G45.12, G75.84 and W3A. Such lines can also be used to set limits on elemental abundances of these ions; this technique is described and used by Herter *et al.* (1981) and Simpson and Rubin (1990).

1.5 HII region line strength models

Any HII region model must incorporate the physical processes described in section 1.2 and must reproduce the ionization structure and line strengths. In the following sequence these models must :

a) solve the equations of ionization and thermal balance for a range of stellar temperatures incorporating the physical processes described in section 1.2, *e.g.* Rubin (1968a).

b) for a range of effective temperatures, T_{eff}, calculate the emergent spectrum of the ionizing flux and hence a total number of ionizing photons, N_{Lyc}. Widely used stellar atmosphere models are those by Kurucz (1979).

c) then solve the equation of radiative transfer, for tabulated frequencies in stellar atmosphere models, radially outwards to the edge of the nebula. Gaseous properties of the nebula, *i.e.* electron temperatures, densities and abundances are input into this calculation and hence emergent line fluxes calculated.

Resultant fluxes can be compared to observations. The following model parameters are then adjusted to obtain the best match the observations: elemental abundances (initially assumed Solar), the geometry, the density distributions and/or clumping factor, and the spectral distribution of the stellar ionizing flux *i.e.* the effective temperature.

Uncertainties occur because of difficulties in calculating atomic data for the complex

heavier elements. A general conclusion from models of HII regions is that they do not show the high degree of ionization in the forbidden lines that is predicted for the hot O stars whose presence is deduced from radio observations (Herter, Helfer and Pipher 1983; Rubin, Hollenbach and Erickson, 1983; Simpson and Rubin, 1984). Either the stellar atmosphere models are not accurate or dust internal to the HII region is affecting the emergent spectrum. Abbot and Hummer (1985) find that mass loss through strong stellar winds, a property of all O and late B stars, affects the emergent spectrum and should be considered in stellar atmosphere models. Observational uncertainties arise mainly from extinction corrections.

Much work on HII region modelling stems from early papers by Hjellming (1966) and Rubin (1968a) who developed the technique for detailed numerical modelling of HII regions. The equations of ionization and thermal equilibrium were solved iteratively and Rubin (1968a) allowed for an arbitrary radial density distribution. For a full description of this spherically symmetric model see Rubin (1968a) who calculates the emission coefficient for a number of optical and far-infrared lines as a function of radius. Dust was incorporated later by Balick (1975) and Sarazin (1977). Recent models including detailed modelling of heavy elements have been made by Stańiska (1982) and Rubin (1985) who list predicted line fluxes for a number of different models.

After blister HII regions were discovered observationally (Zuckerman 1973), and continuum modelling commenced (*e.g.* Icke *et al.* 1980), modelling of line fluxes from such HII regions was initiated by Rubin (1984). In Rubins' (1984) model the geometry/density distribution simulating an HII region blister model, near the edge of a molecular cloud, was represented by an exciting source embedded within an exponential density gradient perpendicular to the plane parallel configuration. As in his spherical models (Rubin 1968a), line fluxes for the brightest transitions of ionized species of H, C, N, O, Ne, S and Ar in the optical and infrared were calculated.

Other papers have focused on deciphering physical properties of specific nebulae, particularly effective temperatures and element abundances as discussed in section 1.4.2.

Other theoretical models to be mentioned are those by Evans and Dopita (1985). They have computed an extensive grid of photoionization models with conditions ap-

popriate to observed HII regions. Their models are spherically symmetric with uniform density, uniform filling factor, and an empty zone surrounding the source *i.e.* a shell-like structure. They have applied these models to produce diagnostic diagrams of effective temperatures of HII regions from the prominent optical emission lines observed. Rubin *et al.* (1994) have similarly produced diagnostic T_{eff} diagrams for the [S III] (19 μm)/[O III] (52 μm) and [NIII] (57 μm)/[NII] (122 or 205 μm) line pairs, using the Rubin (1985) models discussed above.

Recently, a sophisticated photoionization code CLOUDY (see Ferland 1993) has become available for general use. Although this code was initially designed for modelling active galactic nuclei, it is adaptable to HII regions. It has the capacity to predict the line intensities of roughly 500 lines; parameters to be specified, as above, are the shape and intensity of the incident continuum, and the chemical composition and geometry of the gas, including its radial extent and density distribution as a function of radius. Baldwin *et al.* (1991) used this code to model Orion as a blister HII region and calculate its physical properties.

1.5.1 HeI 2.058 μm/Brγ models

Doyon, Puxley and Joseph (1992, hereafter DPJ) have attempted to simply model the HeI 2.058 μm/Brγ ratio in order to make effective temperature predictions. The atomic data for helium and hydrogen are well established, which is not the case for heavier elements. Thus, interpretation of any HeI/HI ratio will be subject to smaller uncertainities in atomic data. The ratio of HeI/HI measures the relative volumes of the two ionized zones; the HeI/HI ratio increases strongly with effective temperature until the two zones become coincident at an effective temperature of T_{eff} ~38,000K (see section 2.5.1). This ratio is also a function of electron temperature and density and helium abundance. Any dust interior to the HII region will preferentially absorb hydogen ionizing photons, therefore the effective temperature at which the two ionized volumes become coincident is lower.

The HeI 2.058 μm line appears as a bright transition in HII region spectra that are optically thick to HeI Lyman photons (Treffers *et al.* 1976, Wynn–Williams *et al.*, 1978,

Thompson and Tokunaga, 1980); this is the case B assumption for singlets.

DPJ have calculated these line strengths simply for a spherical HII region; specifically, the solution of the equation of radiative transfer has been acheived using the OTS approximation (section 1.2.2). However, their resulting ionization structure is in good agreement with that predicted from Rubin (1985) who solves the equation of radiative transfer fully.

Geballe *et al.* (1984) first pointed out the importance of the neutral He/H fraction and the resultant HeI 2.058 μm line strength as effective temperatures increase. Shields (1993, hereafter Shields) models the HeI 2.058 μm/Brγ ratio taking account of this effect. He uses the elaborate CLOUDY (see Ferland 1993) code and solves for radiative transfer at each point in the nebula for spherical symmetry and plane parallel assumptions. Kurucz model atmospheres were used by both authors.

Further details and modifications of the DPJ models are given in chapter 2; Shields models are described fully in chapter 4. Both models are used extensively throughout this thesis.

1.6 Thesis aims and outline

The aim in this thesis is to test these models with observations of HII regions. To this end, near–infrared spectra of the HeI 2.058 μm and Brγ recombination lines have been taken in samples of UC and compact HII regions. As discussed above, the emphasis is towards analysis of samples of UC and compact HII regions, where geometries are not so complex in these younger unevolved objects and simple spherically symmetric models may be more respresentative. Near-infrared measurements are advantageous for such embedded objects since extinction estimates are less important than for shorter wavelength observations (see section 1.3), and sensitive infrared instruments have recently become available. Using these observations it is hoped to fully calibrate the models of the HeI 2.058 μm/Brγ ratio *vs.* T_{eff}. Other processes not examined in the models *e.g* collisional excitation (DPJ models), microturbulence and varying density distributions are investigated in order to constrain these models fully. Effective temperatures can be

translated into masses of stars in HII regions. Once this is acheived, predictions as to the upper mass limit of the IMF can be made both in our own and other galaxies.

Chapter 2 compares UCHII region observations of the HeI 2.058μm/Brγ ratio with models, and makes predictions about gas properties and motions. In chapter 3, these predictions are tested further by using observations of the HeI 2.113μm blend for the same UCHII region sample. Compact HII regions are studied to examine the accuracy of the models used at lower electron densities in chapter 4. Alternative electron density calculations from radio continuum measurements are the subject of chapter 5, together with a discussion of the effect of different density distributions on the modelled HeI 2.05μm/Brγ ratio. Starburst Galaxies are the subject of the penultimate chapter in this work. Observations of the HeI 2.058μm/Brγ ratio are compared to HeI/HI observations in the optical and a new method of estimating effective temperatures is outlined. The final chapter is dedicated to summarising the conclusions drawn from each chapter and making suggestions for future work.

Chapter 2

The HeI 2.058μm/Brγ ratio – Ultracompact regions

2.1 Introduction

In this chapter, UCHII regions which are the least evolved, and therefore geometrically less complex than compact or diffuse HII regions, are studied. The aim in this and the following chapter is to examine the dependence of the HeI (2^1P–2^1S) 2.058μm[1] to HI Brγ 2.165μm[1] ratio on effective stellar temperature for less complex, unevolved HII regions in our own Galaxy, and to quantify modifications to the ratio due to density, and line and continuum radiative transfer effects. This ratio in HII regions has been modelled by DPJ and is a measure of the relative number of helium to hydrogen ionizing photons, which is strongly dependent on the effective temperature of the exciting source and hence on its mass. This strong mass dependence means that the HeI 2.058μm/Brγ ratio integrated over the stellar population should be a strong function of the upper mass limit, M_u, of the initial mass function (IMF) whilst remaining fairly insensitive to the lower mass limit, M_l (DPJ).

Other transitions, such as the mid–infrared fine structure lines [SIV] λ10.5μm, [ArIII] λ9.0μm and [NeII] λ12.8μm (Aitken *et al.* 1982), and the optical fine structure lines

[1]The wavelengths are quoted in air.

[OIII] $\lambda\lambda$ 4959, 5007 and Hβ (Campbell, Terlevich and Melnick 1986), have been used as similar diagnostics to constrain stellar effective temperatures. Advantages of the HeI 2.058μm/Brγ line ratio are as follows: (i) both lines are close in wavelength and lie in the K window where dust extinction is an order of magnitude smaller than at visual wavelengths, (ii) the lines are intrinsically bright, the HeI 2^1P level being boosted by the 1^1S– 2^1P 0.0584μm resonance line transition, and (iii) the variation in the helium abundance throughout the interstellar medium is less dramatic than that of the heavier elements *e.g.* Rayo, Peimbert and Torres-Peimbert (1982).

In this chapter, observations of the HeI 2.058μm/Brγ ratio in a sample of UCHII regions are presented in order to examine radiative transfer and density effects on the theoretical models. Section 2.2 describes the observational details; sections 2.3 and 2.4 examine the corrections for the effects of telluric absorption on the HeI line flux and dust extinction towards each source, respectively. In section 2.5 the theoretical models are described and the effects of collisional excitation and internal dust on the HeI 2.058μm/Brγ ratio are discussed. In section 2.6 the results of the observations of UCHII regions are compared with these models.

2.2 Observations and Data Reduction

The UCHII regions observed and their equatorial coordinates are given in table 2.1. They were selected from an extensive VLA survey at 5 and 15GHz by Wood and Churchwell (1989) so as to sample the range of spectral types of the ionizing stars for UCHII regions, namely O4 to B1. Infrared spectra of the UCHII regions were obtained on the 3.8m United Kingdom Infrared Telescope (UKIRT) on the nights of 1990, Sept 2 and 3. Observations were made with the cooled grating spectrometer CGS2 using a circular aperture of $5\widehat{''}$. CGS2 is a linear array of 7 detector elements. The 633 lines/mm grating provided an instrumental resolution at 2.2μm of $\sim$ 730, or 400 kms^{-1}, where the resolution is set by the size of the detector element. Wavelength coverage is obtained by changing the grating position; the on–chip exposure time was 1.5 seconds for each of the 21 grating positions which covered the range 2.0 to 2.2μm. At each grating position, three sub-spectra were taken, each obtained by stepping the grating slightly. These

sub-spectra were then combined to produce the properly sampled final spectrum. The observations were sky subtracted by nodding the telescope 30–40 arcsec off the source, to a position determined from previous infrared imaging by P. Puxley using IRCAM (see section 4.2.2) so as to be free of emission from surrounding sources. Bright Ar and Kr lines of known wavelength were used to calibrate the wavelength scale.

Subsequent observations were obtained on the night of 1991 June 23 with the newly commissioned cooled grating spectrometer CGS4 (Mountain *et al.* 1990), the first spectrometer with a two dimensional array on UKIRT, and the most sensitive near infrared spectrometer on any telescope to date. The dimensions of the array are 58×62 3.1$\widehat{''}$×3.1 $\widehat{''}$ pixels. Therefore CGS4 has the capacity for much greater wavelength coverage than CGS2, with the one grating position. CGS4 is also a long slit spectrometer, 30 spatial detector rows are normally illuminated providing a long slit of 92$\widehat{''}$, and this instrument operates in the wavelength range 1–5 μm.

CGS4 uses an internal calibration unit containing a number of arc lamps that were used for wavelength calibration and a black body continuum source for flat–fielding. At 2.2 μm the resolving power of CGS4 with the 75 lines/mm grating and 150mm focal length camera is $\sim$ 340, or 900 kms^{-1}. With this configuration it is possible to observe the whole K band (2.0–2.4 μm) window simultaneously without changing grating position. Other gratings are available, in particular high resolution spectroscopy is possible with the echelle which has a resolution of $\sim$40 kms^{-1} at 2.2 μm and coverage of 0.015 μm at this wavelength. The latter configuration was used to obtain the high resolution spectrum of G29.96 in fig 2.4. To ensure that the spectra were fully sampled, the detector was stepped 4 times over 2 pixels for the wavelength range 2.0–2.4 μm. This over-sampling also enables rejection of bad pixel data. By sliding along the slit, offset positions of 30 arcsec W were used for sky subtraction. The spectra were flat–fielded by observation of a black–body at 1073 K, taken with the same instrumental configuration as the astronomical targets. Wavelength calibration accurate to 0.002 μm was carried out using observations of atmospheric OH emission lines here since no arc spectra had been taken. After ratioing with standards, as described below, the final spectra were obtained by summing spatially the central 5 detector rows along the slit to give a 3.1 × 15.5 arcsec^2 synthesised aperture.

Object	Equatorial Coordinates $\alpha(1950)$	$\delta(1950)$	Distance kpc
G5.48	17 55 58.65	-24 20 43.24	14.3
G5.97	18 00 36.44	-24 22 53.74	1.9
G15.04	18 17 31.68	-16 12 57.94	2.1
G29.96	18 43 27.07	-02 42 36.46	9.0
G35.20	18 59 14.05	01 09 03.12	3.2
G43.89	19 12 02.82	09 17 19.10	10.3
G45.07	19 11 00.42	10 45 42.87	9.7
G45.12	19 11 06.24	10 48 25.82	9.5

Table 2.1: UCHII region sources with equatorial co-ordinates.

Name	Equatorial Coordinates $\alpha(1950)$	$\delta(1950)$	K mag	Spectral Type
BS 6746	18 02 34.5	-30 25 46.5	0.66	KOIII
BS 6798	18 08 16.8	-19 51 16.3		A4V
BS 7314	19 14 38.2	38 02 41.6	1.66	KOIII
SAO 104272	18 53 53.7	18 02 29.0		K2I
SAO 104728	19 17 32.0	11 26 28.6		A2

Table 2.2: Standard stars observed for calibration.

2.2.1 CGS4 and Data Reduction

General infrared spectroscopic techniques and those specific to CGS4 are now described. Dark, flat and arc spectra are generally taken at the beginning and end of the nights with the same configuration as the object spectrum for calibration purposes.

Dark frames are taken with the array blanked off, using the same exposure time as the source, to enable subtraction of the correct amount of dark current which builds up in the detector during that length of exposure.

Flat frames measure the relative responses, referred to as the gain, of each pixel in the detector array. Division by this "flat-field" then removes these intrinsic pixel-to-pixel variations which are a function of wavelength. For infrared imaging, blank sky frames are used to produce a flatfield (*c.f.* IRCAM section 4.2.2). For spectral observations, sky lines render the use of blank sky observations unfeasible for flatfielding. For linear array spectrometers, this underlying pixel-to-pixel variation is removed by ratioing the object with a standard star. However, for CGS4, each of the $3.1'' \times 30$ spatial rows would have to be treated in this fashion and therefore for practical purposes, a black body source, which uniformly fills the slit, as described above, was used.

At infrared wavelengths, sky spectra (or frames) must be taken at regular intervals for removal of temporal variations of OH lines (scale of ~10 minutes, Ramsay, Mountain and Geballe 1992), from each object spectrum.

Bright spectral line sources, commonly arc lamps, are used in the near-infrared for wavelength calibration. Standard stars are used for flux calibration and correction for atmospheric absorption and instrumental response. Before these techniques are descibed in detail, a discussion of the reduction procedure involved with CGS4 is carried out.

CGS4 has an automatic data reduction system which combines the four "integrations", as defined by the sampling procedure (section 2.2), at each half pixel position to produce an "observation". The dark observation is then subtracted from the flat, the spectral shape of the black body and filter profiles are removed by a polynomial fit, and a normalised flat spectrum produced. A bad pixel mask is also applied to flag any bad pixels; henceforth these pixels are ignored by the data reduction system. All arc,

sky, standard star and source observations are then ratioed by this flatfield to produce "reduced observations".

To calculate errors correctly, manual data reduction was continued hereafter to produce fully calibrated data using Figaro software routines (Shortridge 1991). With one dimensional spectrometers, the data would then be coadded, but with CGS4 this procedure is more complex because of the spatial extent of the array and a few more stages are required before co-addition of the data. Briefly this involves sky subtraction, object row extraction and de-rippling.

For the galaxies and HII regions observed, the emission was not extended outside three rows either side of the central spatial row in the array. Therefore, sky observations were made by sliding ~10 rows or 31″ along the slit. This doubles the on-source exposure time and also reduces observation overheads by avoiding the need for imaging the sky to find offset positions (see section 4.2.2). Equal consecutive integrations on the object and the sky are carried out, and the sky subtracted from each object row integration. Any residual sky lines are removed by polynomial fitting. Each object-sky observation is extracted and stacked together in a separate image to obtain one image of a series of object-sky spectra at the same spatial position. Ripples are removed if necessary at this stage. Rippling effects are a product of the object moving in and out of the slit between integrations, caused by seeing effects or windshake of the telescope. Thus, when the four integrations are combined a periodic ripple pattern appears on the spectrum due to different absolute flux levels with each integration. This is corrected for by producing a template of the ripple spectrum from an area of the continuum which exhibits a clear ripple pattern; this pattern is extended to cover the spectrum and the resulting template formed. Division by the template spectrum should leave a ripple free spectrum. The spectra are then coadded so all the information is contained in a single spectrum.

Lastly, wavelength calibration and ratioing by standard stars is performed. As discussed above, commonly arc spectra are taken to calibrate the wavelength scale. The conventional method for correction of the instrumental response and atmospheric absorption is to divide the object spectrum by that of a standard star, and then to multiply by a black body with effective temperature appropriate to that of the spectral standard so

as to remove the coarse spectral shape of the star. Spectroscopic standards (those pertaining to the UCHII regions observed are listed in table 2.2) are generally observed at regular intervals between source observations so that airmass variations are minimal. For all K band observations presented in this thesis A-type stars were chosen where possible, because, apart from their Brγ absorption lines at 2.165μm, they have featureless spectra in the K window. Such Brγ absorption lines can be removed from the stellar spectrum by interpolation. If not already known, the magnitude of the spectroscopic standard can be determined by comparison of its spectrum with that of a flux standard, observed on the same night and close in airmass. Flux calibration techniques are described further in section 4.2.1.

However, the HeI line lies amidst strong CO_2 telluric absorption around 2.06μm. Division by the spectroscopic standard will correct the continuum around the HeI 2.058μm line but not the line itself which is intrinsically extremely narrow, (1/10–1/45 of the resolution of the instrument for CGS2 and CGS4 respectively). The correction applied to the UCHII regions for this effect is discussed in more detail in section 2.3.

Returning, to the UCHII region data, the final fully calibrated spectra are shown in figs 2.1a–j. The HeI and Brγ recombination lines were fitted with gaussian profiles in the case of the CGS2 data, and triangular profiles for the CGS4 data (the convolution of the slit on square pixels), which are good approximations to the instrumental profiles. Both lines were fitted simultaneously with the same best fitting FWHM equivalent to the instrumental profile since the change in dispersion will be negligible ($\leq$ 0.001 μm) between the two lines.

2.3 Correction for Atmospheric absorption

The molecules CO_2, H_2O and O_2 in the earth's atmosphere are responsible for the presence of several strong absorption bands at infrared wavelengths. In the K window there is a CO_2 absorption feature at 2.06μm. At high resolution this absorption feature consists of a host of sharp individual lines, corresponding to rotational transitions within the CO_2 molecule. From radio recombination line (RRL) measurements of the UCHII

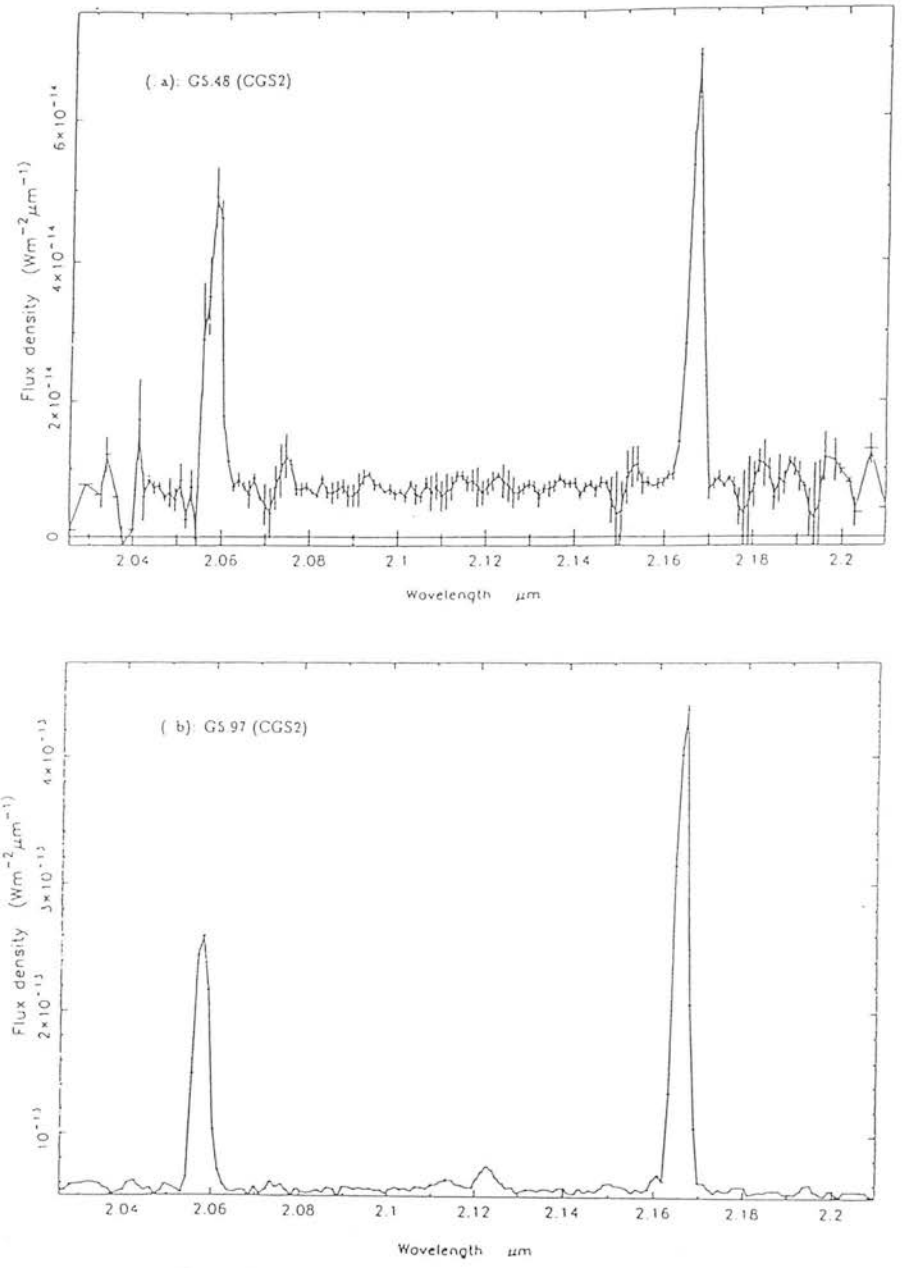

Figure 2.1: K-band spectra of UCHII regions, showing the bright HeI 2.058 μm and Brγ lines as well as the weaker HeI 2.113 μm blend. Observations a–f were taken with CGS2 and g–J are subsequent observations taken with CGS4.

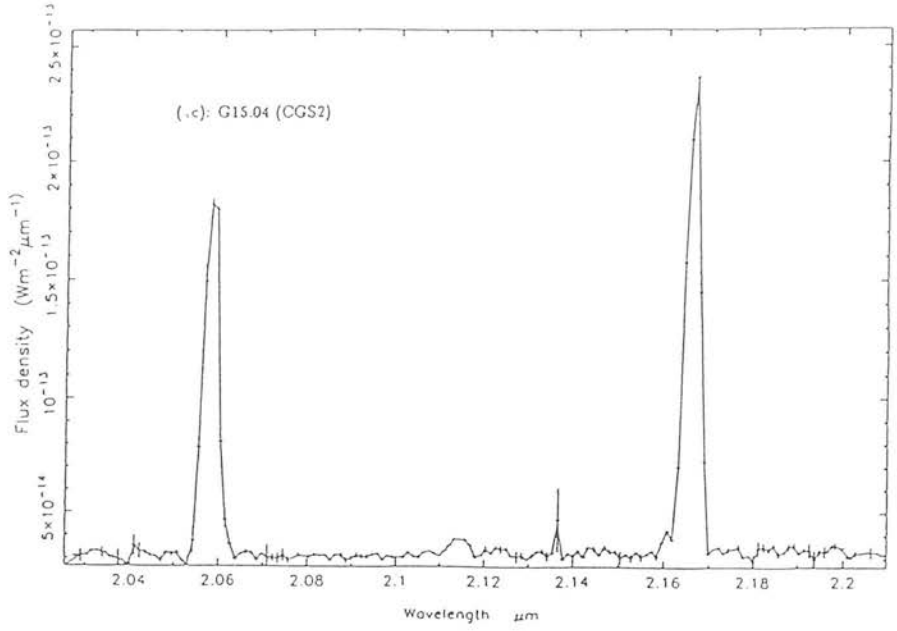
(c): G15.04 (CGS2)
Flux density (Wm^{-2}μm^{-1})
Wavelength μm

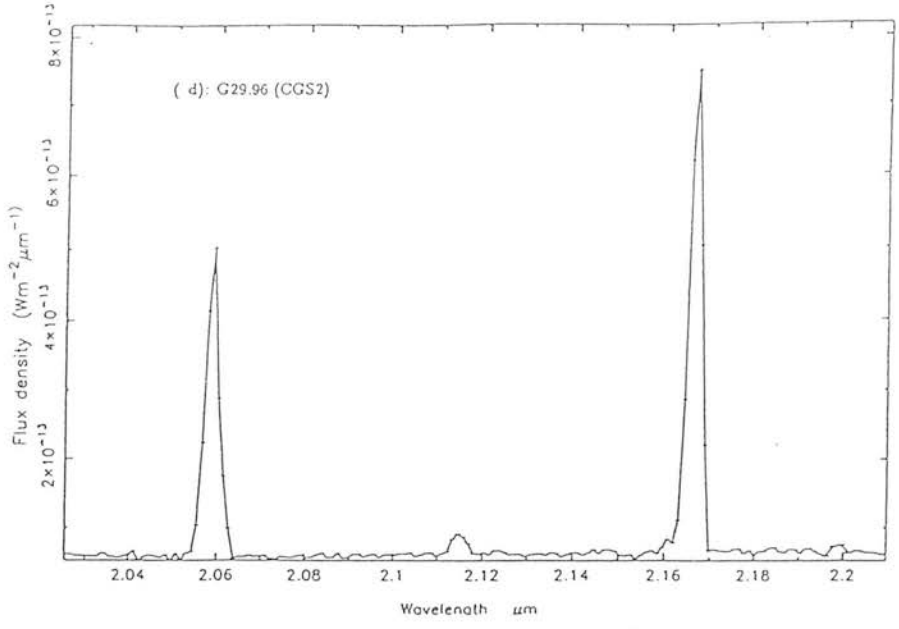
(d): G29.96 (CGS2)
Flux density (Wm^{-2}μm^{-1})
Wavelength μm

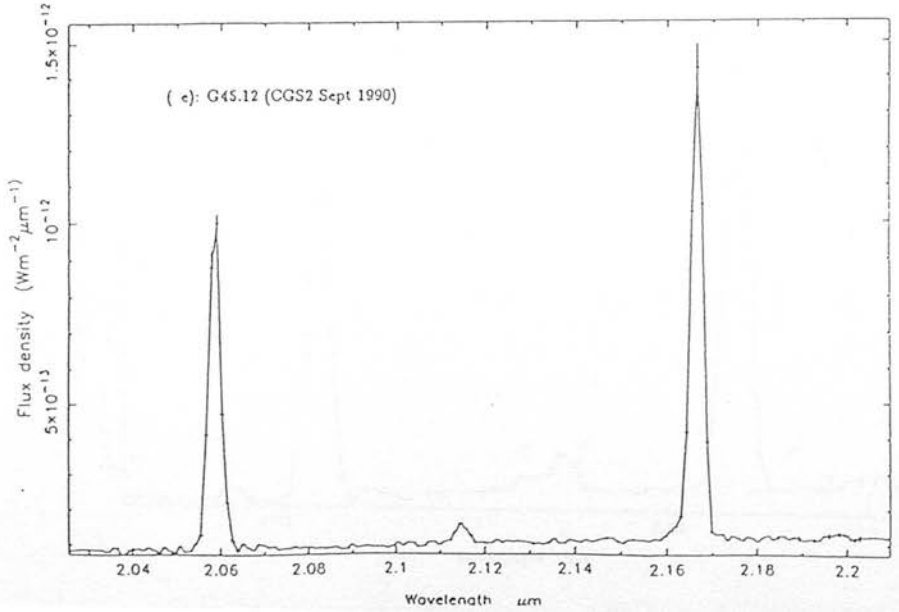
(e): G45.12 (CGS2 Sept 1990)
Flux density (Wm^{-2}μm^{-1})
Wavelength μm

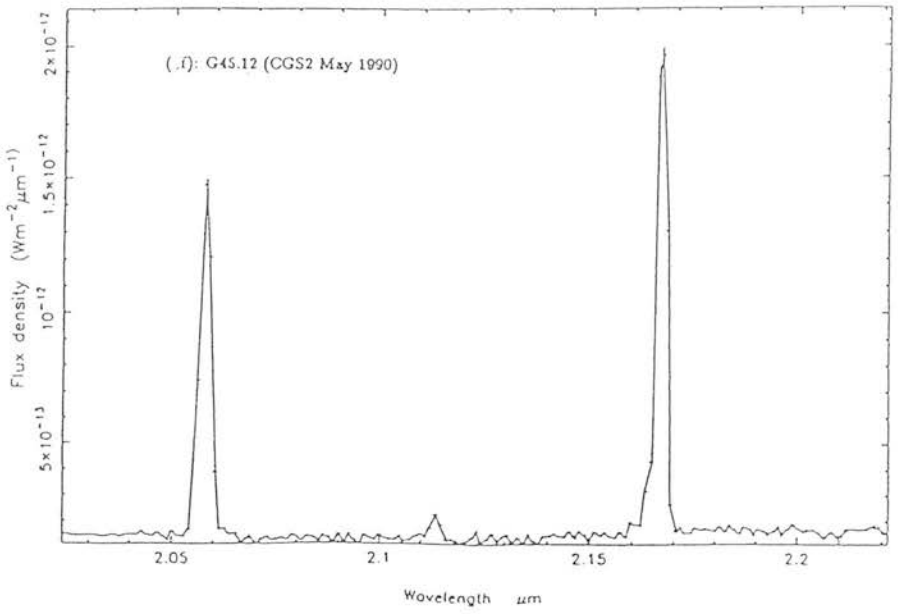
(f): G45.12 (CGS2 May 1990)
Flux density (Wm^{-2}μm^{-1})
2×10^{-12}
1.5×10^{-12}
10^{-12}
5×10^{-13}
2.05
2.1
2.15
2.2
Wavelength μm

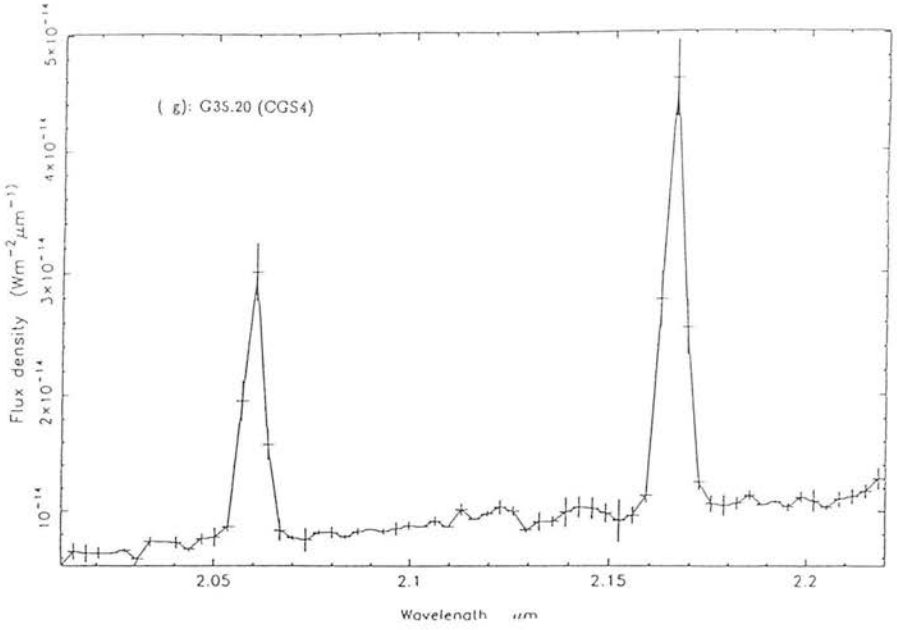
(g): G35.20 (CGS4)
Flux density (Wm^{-2}μm^{-1})
5×10^{-14}
4×10^{-14}
3×10^{-14}
2×10^{-14}
10^{-14}
2.05
2.1
2.15
2.2
Wavelength μm

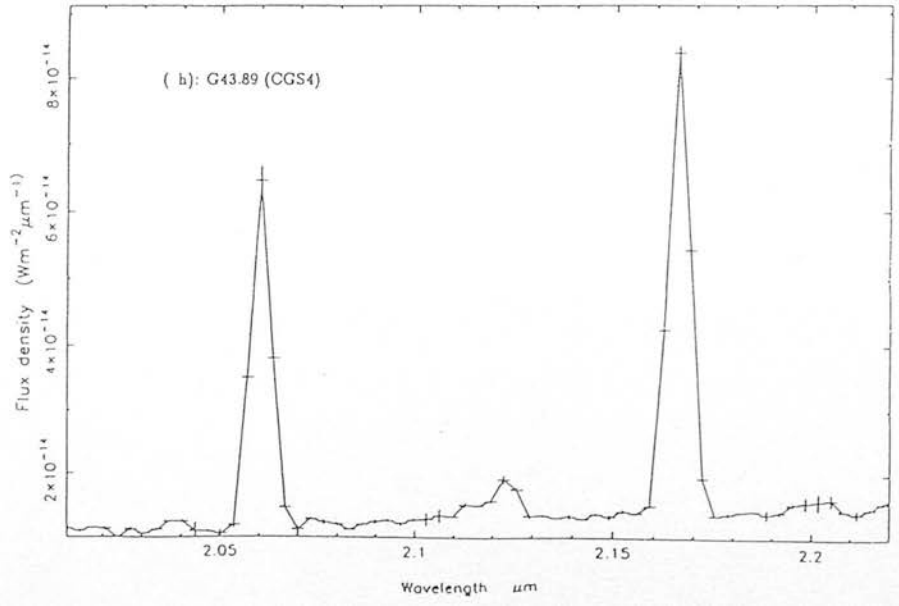
(h): G43.89 (CGS4)
Flux density (Wm^{-2}μm^{-1})
8×10^{-14}
6×10^{-14}
4×10^{-14}
2×10^{-14}
2.05
2.1
2.15
2.2
Wavelength μm

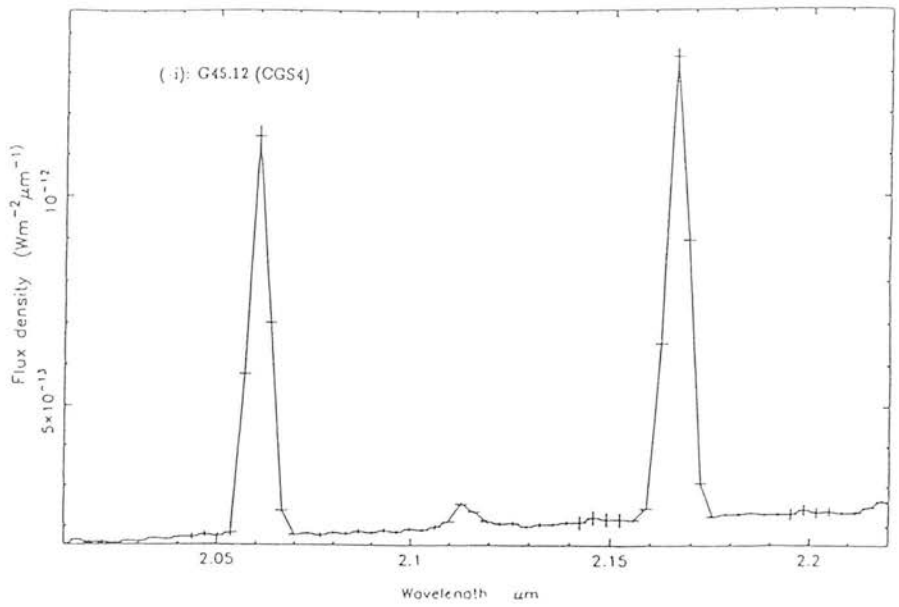
(i): G45.12 (CGS4)
Flux density (Wm^{-2}μm^{-1})
10^{-12}
5×10^{-13}
2.05
2.1
2.15
2.2
Wavelength μm

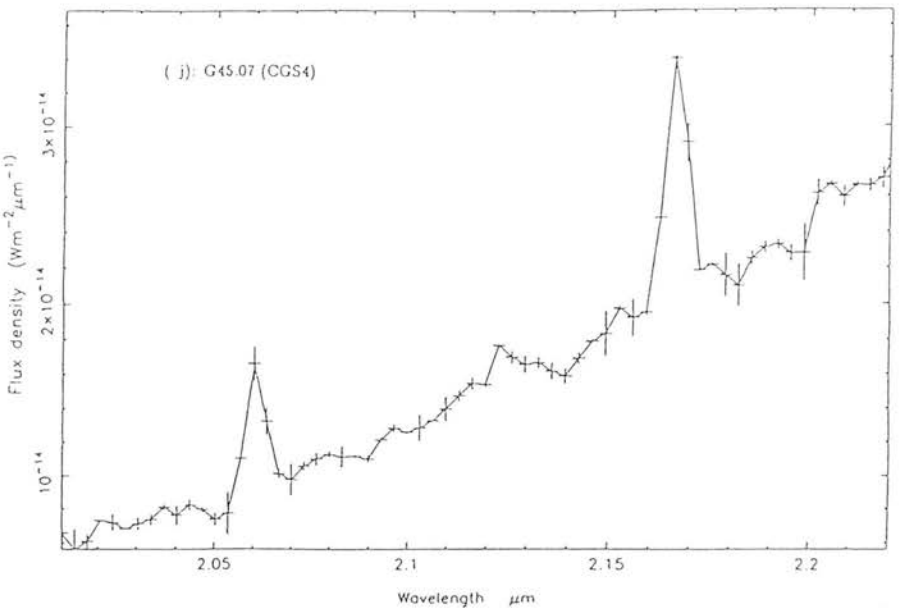
(j): G45.07 (CGS4)
Flux density (Wm^{-2}μm^{-1})
3×10^{-14}
2×10^{-14}
10^{-14}
2.05
2.1
2.15
2.2
Wavelength μm

regions at H76α, H90α and H110α (Wood and Churchwell 1989, Wink *et al.* 1982, Downes *et al.* 1980), assuming RRL broadening is dominated by processes other than thermal motions (see section 2.6), the intrinsic width of the HeI 2.058 μm emission line is inferred to be $\sim$ 20–40 kms^{-1} which is only 2–4 times greater than the width, and only 3.5–4.5 times less than the separation, of the individual telluric lines which comprise the CO_2 absorption feature at 2.06 μm. The instrumental resolution, 400 kms^{-1} for CGS2 and 900 kms^{-1} for CGS4, is such that the individual CO_2 lines are heavily smoothed when convolved with the instrumental profile. However, since the atmospheric transmission affecting the line is a rapidly varying function of wavelength, the amount of HeI line absorption will depend critically on the relative radial velocity of the earth and HII region, *c.f.* analysis of the HeI 1.083 μm line by Kingdon and Ferland (1991). For example, if the HeI emission line coincides with that of a telluric line then a substantial amount of the HeI line flux will be absorbed before reaching the telescope, whereas, if the HeI line falls between absorption lines (spacing interval 90 kms^{-1}) an insignificant amount of the line flux will be absorbed before reaching the telescope. At the resolution employed the smoothed transmission would have the same value in both cases, thus making it impossible to differentiate between these two extreme cases; in the first instance the flux replaced on division by the standard will be underestimated and in the latter overestimated. Therefore to calculate accurately the amount of flux lost on transmission through the atmosphere, it is necessary to know the HeI line width and the radial velocity of the source. The date of the observation must also be known, because a given HeI emission line will shift by up to 30 kms^{-1}, with respect to the telluric lines, as a result of the earth's orbital motion.

The method employed to estimate the percentage of HeI flux absorbed for each UCHII region was as follows :

(i) A synthetic HeI emission line was generated with a FWHM derived from radio recombination line (RRL) observations for each UCHII region; H110α (Downes *et al.* 1980), H76α (Wood and Churchwell 1989) and H76α and H90α (Wink *et al.* 1982). Comparison of RRL line widths of H40α, H50β and He40α by Gordon and Walmsley (1990) for a sample of HII regions show the HeI recombination line widths to be similar to the HI line widths.

(ii) The radio recombination line local standard of rest (LSR) velocities were transformed into geocentric velocities for the date of the observations so as to discern the Doppler shifted position of the HeI line (see table 2.3). This transformation involved the resolution of two separate velocity components in the direction of the object, that of the sun with respect to the LSR (with standard solar motion), and that of the earth around the sun.

(iii) The atmospheric transmission spectrum around the wavelength of the HeI line was generated from a radiative transfer model using the programme HITRAN, originally developed by the U.S. Air Force Geophysical Laboratory, giving the transmission profile appropriate for Mauna Kea. The telluric line shape, characterized by a Voigt profile, is a convolution of collisional broadening by air molecules and thermal broadening and is a function of column density. The latter varies with the airmass which was recorded for each UCHII observation.

(iv) The synthetic HeI line was multiplied by the transmission spectrum over the same wavelength range and, from integration under the incident and transmitted profiles, the percentage of HeI flux lost by telluric absorption was calculated for each UCHII region.

For the UCHII regions on the dates observed, the percentage HeI line flux lost ranged from 5–36 % (table 2.3). The errors on the RRL values for the LSR velocity, hence on the wavelength of the line centre, and the FWHM, were incorporated into the modelling to calculate the errors on the percentage flux lost (table 2.3).

If F_λ is the helium line profile and T_λ the atmospheric transmission, then the atmospheric correction factor applied to each UCHII region is :

$$\bar{T} \times \frac{\int F_\lambda d\lambda}{\int F_\lambda T_\lambda d\lambda}$$

where the integration is performed over a wavelength range corresponding to about six times the RRL width. The factor $\bar{T}$ arises because the object spectrum has been divided by the spectral standard which corrects for the continuum flux lost due to telluric absorption, and for the instrumental response. Consequently, the HeI line in the HII region spectrum has already been divided by the smoothed atmospheric transmission in

Object	Velocities (kms^{-1}) LSR	Geocentric	HeI flux absorbed %
G5.48	22.9	39.3	5±1
G5.97	3.5	19.8	23±2
G15.04	11.5	24.7	13±3
G29.96	95.3	102.6	26±4
G35.20[1]	47.9	23.8	13±6
G43.89[1]	52.5	26.1	10±7
G45.07[1]	47.7	21.3	18±3
G45.12	58.7	59.6	10±2
G45.12[2]	58.7	22.6	17±2
G45.12[1]	58.7	32.3	11±3

[1] Taken with CGS4 June 1991.

[2] Repeat observation, taken with CGS2 May 1990.

Table 2.3: Atmospheric Corrections.

the standard around 2.058 μm. Therefore a further correction factor, $\bar{T}$ (found to be in the range 0.82–0.86), representing this average percentage atmospheric transmission in the standard at 2.058 μm, must be applied.

2.4 Correction for Dust Extinction

The dust extinction to an HII region can be calculated by comparing the observed Brγ line flux with the value inferred from the free–free radio flux density using hydrogen recombination theory. Wood and Churchwell (1989) measured the free–free flux densities integrated over the source, for their large sample of UCHII regions at both 5 and 15 GHz. Relating the number of Lyman continuum photons to the free–free integrated flux density S_ν, for an electron temperature and density of T_e=10^4 K and n_e=10^4 cm^{-3} respectively, and a ratio of recombinations to Brγ photons $N_{Lyc}/N_{Br\gamma} \sim 70$ (Hummer and Storey 1987), gives a theoretical Brγ flux (Rubin 1968b) of :

$$I_{Br\gamma}^{\rm theo} = 8.25 \times 10^{-15} \left(\frac{\nu}{\rm GHz}\right)^{0.1} \left(\frac{S_\nu}{\rm Jy}\right) \tag{2.1}$$

if the free–free continuum is optically thin. This is not the case for UCHII regions which are optically thick at 5GHz and marginally so at 15GHz (see table 2.4). In the case of finite optical depth equation (1) becomes :

$$I_{Br\gamma}^{\rm theo} = 1.08 \times 10^{-14} \left(\frac{S_{\rm 15GHz}}{\rm Jy}\right) \left(\frac{\tau_{\rm 15GHz}}{1 - e^{-\tau_{\rm 15GHZ}}}\right) \tag{2.2}$$

The free–free optical depth was calculated, from the 5GHz and 15GHz flux densities given by Wood and Churchwell (1989), for each UCHII region by iteration of eqn 4.3. At high spatial resolution, these VLA observations may resolve out extended emission resulting in an underestimate of the total flux density and an optical depth weighted towards the compact regions of the source. Such extended emission might be detected in these lower resolution infrared observations, resulting in an underestimate of the extinction. However, this effect is not expected to be a significant problem for most of this sample, which are dominated by a central source, with the possible exceptions of G5.48 and G5.97

Object	τ_{15GHz}	C_k	Brγ flux $\times 10^{-16}$Wm^{-2}	HeIλ2.058/Brγ ratio Observed	Corrected
G5.48	0.13	1.21	2.15±0.09	0.761	0.823±0.072
G5.97	0.30	1.17	14.9±0.1	0.564	0.688±0.032
G15.04	0.77	1.11	8.19±0.08	0.790	0.858±0.044
G29.96	0.20	1.26	24.9±0.1	0.681	0.997±0.048
G35.20[1]	0.10	1.55	2.30±0.19	0.610	0.891±0.122
G43.89[1]	0.10	1.25	4.79±0.06	0.697	0.788±0.052
G45.07[1]	0.63	1.52	0.84±0.05	0.545	0.820±0.108
G45.12	0.40	1.24	44.6±0.10	0.698	0.799±0.041
G45.12[2]	0.40	1.20	65.1±0.5	0.695	0.838±0.029
G45.12[1]	0.40	1.19	75.0±1.4	0.857	0.929±0.038

[1]Taken with CGS4 June 1991.

[2]Repeat observation, taken with CGS2 May 1990.

Table 2.4: The HeI 2.058 μm/Brγ ratio in UCHII regions.

which have a core–halo morphology. Assuming purely foreground extinction, the dust optical depth may thus be calculated from the observed and predicted Brγ emission:

$$I_{Br\gamma}^{obs} = I_{Br\gamma}^{theo} e^{-\tau_{Br\gamma}} \tag{2.3}$$

The dust optical depths at Brγ of the UCHII regions ranged from $\tau_{Br\gamma}$=1.1–4.9. From the Brγ extinction values, by application of the interstellar extinction curve of Draine (1989) which assumes a power law with spectral index –1.75 in the range 0.7–5 μm, C_k, the differential interstellar extinction correction factor between HeI (2.058 μm) and Brγ (2.165 μm) was calculated, where:

$$C_k = e^{(\tau_{HeI} - \tau_{Br\gamma})} = e^{\tau_{Br\gamma}((2.058/2.165)^{-1.75} - 1)} = e^{0.0909 \times \tau_{Br\gamma}}. \tag{2.4}$$

For T_e= 10,000 K, C_k proved to be in the range 1.11–1.55 (table 2.4); for an electron temperature of 5,000K, C_k would be reduced by a factor of 0.96. More detailed calculations

of τ_{15GHz} are discussed in section 4.3.

The resultant HeI 2.058 μm/Brγ ratios and their errors, corrected for extinction and atmospheric absorption, are given in table 2.4.

2.5 Model HeI/Brγ Line Flux Ratios

2.5.1 The Basic Models

Basic models of the HeI 2.058 μm/Brγ ratio *vs.* effective temperature T_{eff} are presented here. These models and adaptations of these models are used in later chapters, including further extensions from comparison with recent models discussed in chapter 4. The theoretical HeI 2.058 μm/Brγ ratio for stellar effective temperatures ranging from 25,000 – 50,000 K, equivalent to spectral types of B1–O4, has been modelled by DPJ. For stars with these spectral types, they determined fluxes for the helium and hydrogen ionizing photons using the Kurucz (1979) stellar atmosphere models. The Lyman continuum flux is roughly described by a steep power law function of the mass ($N_{Lyc} \propto m^{\alpha}$). For stars with masses in the range 10–40 $M_{\odot}$, corresponding to effective temperatures in the range 22,500–41,000K, the index α is ~ 7 and ~ 11 for H and He respectively (Puxley 1988). Therefore the relative helium to hydrogen ionizing fluxes, and hence the HeI 2.058 μm/Brγ ratio, are a strong function of the stellar mass. The equations derived by DPJ for the line flux as a function of ionizing photon flux are :

$$\frac{I_{HeI\lambda 2.058}}{I_{Br\gamma}} = \frac{N^{He}_{Lyc}}{N^{H}_{Lyc}} \frac{\alpha_{\rm B}(H^+)}{\alpha_{\rm B}(He^+)} \frac{\alpha_{HeI\lambda 2.058}}{\alpha_{Br\gamma}} \frac{\lambda_{Br\gamma}}{\lambda_{HeI2.058}}, \qquad R_{He^+} < R_{H^+} \tag{2.5}$$

$$\frac{I_{HeI\lambda 2.058}}{I_{Br\gamma}} = \frac{N_{He}}{N_{H}} \frac{\alpha_{HeI\lambda 2.058}}{\alpha_{Br\gamma}} \frac{\lambda_{Br\gamma}}{\lambda_{HeI2.058}}, \qquad R_{He^+} = R_{H^+}. \tag{2.6}$$

where R_{He^+} and R_{H^+} are the radii of the helium and hydrogen ionized zones respectively. N^{He}_{Lyc}/N^{H}_{Lyc} is the relative number of helium and hydrogen ionizing photons and N_{He}/N_{H} is the helium abundance. $\alpha_{\rm B}(H^+)$ and $\alpha_{\rm B}(He^+)$ are the total recombination coefficients for hydrogen and helium (case B) respectively. $\alpha_{HeI\lambda 2.058}$ and $\alpha_{Br\gamma}$ are the effective recombination coefficients of the HeI 2.058 μm and Brγ transitions.

The radii of the two ionized zones R_{He^+} and R_{H^+} coincide at a critical stellar effective temperature when the photons emitted from the recombination of helium dominate the ionization of hydrogen and hence the HeI 2.058 μm/Brγ ratio saturates. As can be seen from equation (2.6), above this saturation temperature the ratio is solely dependent on the helium abundance.

Values for the hydrogen and helium recombination coefficients are given in table 2.5 for electron temperatures of T_e= 10,000K and 5,000K and densities of n_e=10^2, 10^4 and 10^6cm^{-3}. Inferred values of T_e for the sample UCHII regions are given by Wood and Churchwell (1989) and Downes *et al.* (1980) and lie in the range 6–11,000K, with uncertainties of up to 2,500K. Similarly, electron densities inferred by Wood and Churchwell (1989) from peak radio flux density measurements lie in the range n_e=10^4–10^5cm^{-3}. Integrated electron densities as calculated in chapter 5 are found to be in the range n_e=10^3–10^5cm^{-3} for these objects, thus the n_e=10^4cm^{-3} model is most representative.

Values for the $\alpha_{HeI\lambda 2.058}$ effective recombination coefficient are derived from recent HeI recombination line spectrum models by Smits (1991a) who tabulates the line strength of HeI 2.058 μm relative to HeI 4472Å. The $\alpha_{HeI\lambda 2.058}$ effective recombination coefficient is the recombination coefficient from all levels to the 2^1P singlet level, multiplied by the fraction of those atoms which radiatively decay to the 2^1S level, emitting a 2.058 μm photon.

Smits (1991a,b) has published comprehensive HeI recombination line strengths for case B using the most up to date atomic data. He has followed the work of Brocklehurst (1972) with corrections as discussed by Hummer and Storey (1987). He also calculates line strengths for the HI recombination spectrum and obtains the same results as Hummer and Storey (1987) from which the Brγ line strength was obtained. Details of the physical processes involved are given in section 1.2.2, namely, spontaneous transitions, radiative recombinations and collisional transitions. The n=2 levels are treated separately because of substantial coupling between the singlet and triplet levels due to the metastability of the 2^3S and, to a lesser extent, the 2^1S levels.

Smits (1991a) also calculates the HeI singlet line strengths for case A. In this scenario, all atoms in the 2^1P level decay to the 1^1S ground state and hence escape the nebula.

Recomb. coeff	$T_e=10^4$K			$T_e=5\times10^3$K		
$cm^{-3}s^{-1}$	$n_e=10^2cm^{-3}$	$n_e=10^4cm^{-3}$	$n_e=10^6cm^{-3}$	$n_e=10^2cm^{-3}$	$n_e=10^4cm^{-3}$	$n_e=10^6cm^{-3}$
$\alpha_B(H^+)$[1]	2.59×10^{-13}	2.59×10^{-13}	2.59×10^{-13}	4.54×10^{-13}	4.54×10^{-13}	4.54×10^{-13}
$\alpha_B(He^+)$[1]	2.73×10^{-13}	2.73×10^{-13}	2.73×10^{-13}	4.34×10^{-13}	4.34×10^{-13}	4.34×10^{-13}
$\alpha_{Br\gamma}$[2]	3.74×10^{-15}	3.71×10^{-15}	3.63×10^{-15}	7.90×10^{-15}	7.85×10^{-15}	7.68×10^{-15}
$\alpha_{HeI\lambda2.058}$[3]	4.25×10^{-14}	6.78×10^{-14}	8.03×10^{-14}	7.68×10^{-14}	9.16×10^{-14}	1.05×10^{-13}

[1] Values from Osterbrock 1989.

[2] Values from Hummer and Storey 1987.

[3] Values from Smits'1991a.

Table 2.5: Recombination coefficients for HI and HeI.

Therefore, as case A is approached the HeI 2.058 μm line strength will decrease. As the HeI 2.058 μm line is observed to be strong in the UCHII regions the case A assumption is excluded from these present studies.

For electron densities applicable to UCHII regions given above, the 2^1P singlet level population is substantially enhanced by collisions from the metastable 2^3S triplet level. This mechanism has been included in the Smits' models and is discussed in detail in section 2.5.2. As a consequence, the effective HeI 2.058 μm recombination coefficient, unlike that of Brγ, is highly density dependent (table 2.5).

Atoms in the 2^1P state decay with a probability of 0.999 to the ground state (1^1S) with emission of a line photon at 0.0584 μm. The resonance line photon will either be promptly reabsorbed by a neighbouring helium atom and return to the 2^1P excited level or ionize a neutral hydrogen atom. In the absence of dust, approximately one third of the 0.0584 μm photons are absorbed by hydrogen whilst two thirds are scattered by helium atoms ultimately to populate the 2^1S level, via emission of a 2.058 μm photon. To account for this process the HeI 2.058 recombination coefficients derived from Smits and given in table 2.5, have been multiplied by a factor of 2/3 for T_e=10,000K, or 3/4 for T_e=5,000K. The different multiplicative factors are a result of the dependence of the HeI absorption cross-section on electron temperature (see eqn 1.9). Comparison with the hydrogen ionization rate derived from the Kurucz (1979) model atmospheres implies that the total number of hydrogen ionizing photons is increased by a negligible amount, and thus the Brγ flux is unaffected.

Figs 2.2 and 2.3 show the theoretical HeI 2.058 μm/Brγ ratio *vs* stellar effective temperature for two electron temperatures, T_e= 10,000 and 5,000K respectively, calculated from equations (2.5) and (2.6). The three solid model curves represent the low density case $n_e=10^2$ cm^{-3}, the high density case $n_e=10^6$ cm^{-3} and an intermediate density $n_e=10^4$ cm^{-3}. The latter value is most representative of the densities of the UCHII regions (Wood and Churchwell 1989). For an assumed Galactic abundance of N_{He}/N_H=0.1 the He and H ionizing zones coincide near an effective stellar temperature of 38,000 K (O7 star). In fig 2.2, for an electron temperature of T_e=10,000K the HeI 2.058 μm/Brγ ratio saturates at a ratio of 0.80 ($n_e=10^2$ cm^{-3}), 1.28 ($n_e=10^4$ cm^{-3}) and 1.55 ($n_e=10^6$

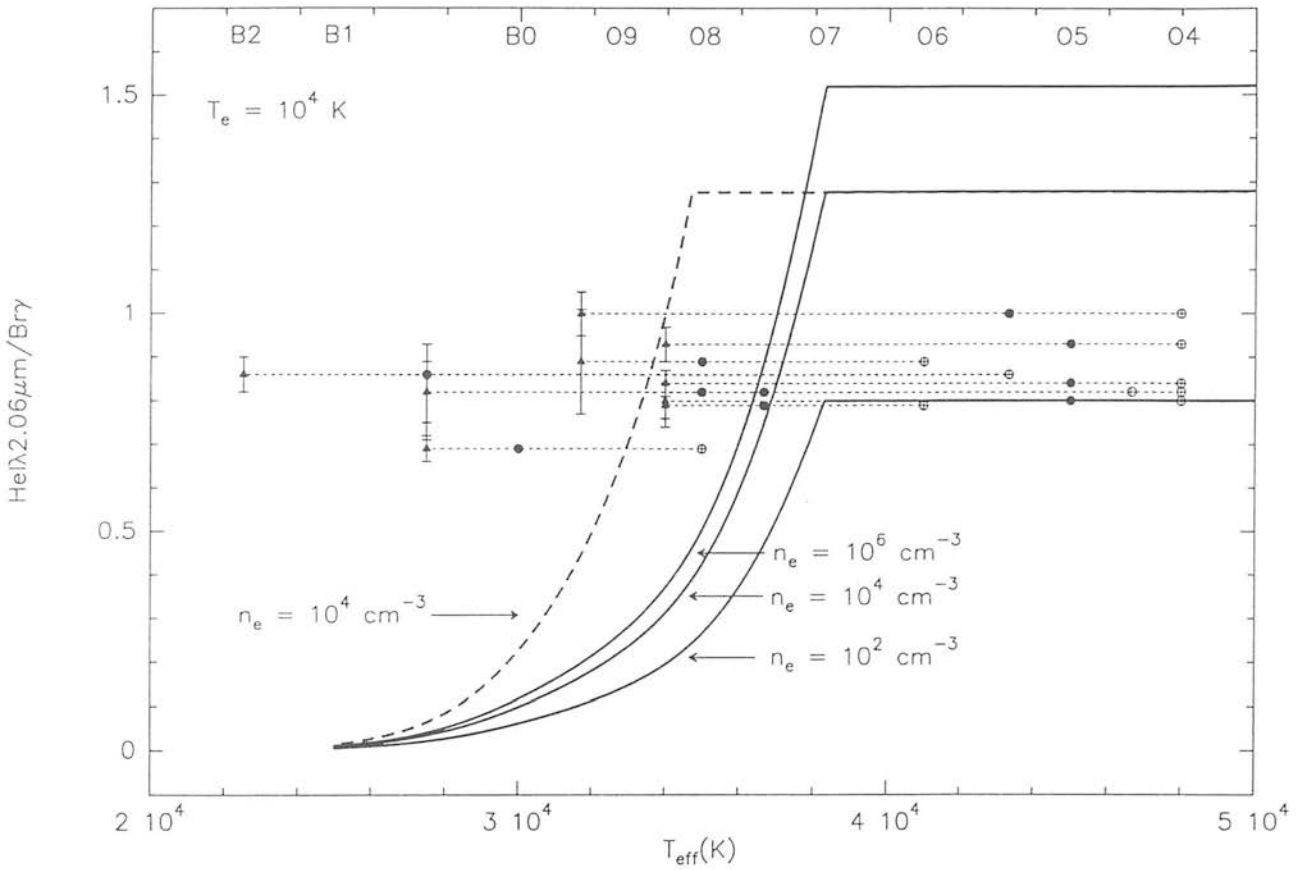

Figure 2.2: The HeI 2.058 μm/Brγ ratio *vs.* stellar effective temperature for an electron temperature of T_e=10,000K and electron densities of n_e=10^2, n_e=10^4 and n_e=10^6cm^{-3}. The dashed curve represents the line ratio for dusty HII regions for n_e=10^4cm^{-3}. All curves are calculated for a Galactic helium abundance of 0.1. T_{eff} is estimated from N_{Lyc} (filled circles) and L_{IR} (open circles) appropriate to single stars, and N_{Lyc}/L_{IR} (filled triangles), appropriate to a cluster of stars. Error bars (1σ) show the uncertainty in the HeI 2.058 μm/Brγ ratio after correction for extinction and telluric absorption.

cm^{-3}). Corresponding saturation ratios for T_e= 5,000K, (fig 2.3) are 0.75, 0.89 and 1.08 respectively.

If hydrogen were relatively more ionized than helium in the He^+ zone, then helium atoms would reprocess almost all of the 0.0584 μm photons and the fraction of atoms which are de-excited to the 2^1S state would be much closer to unity. In this case the curves labelled $n_e=10^2 cm^{-3}$ and $n_e=10^4 cm^{-3}$ would saturate at values of 1.2 and 1.92 (1.00 and 1.19) respectively for T_e= 10,000 K (T_e= 5,000 K).

2.5.2 Effects of Collisional Excitation

Above a critical density of 4-6 $\times$ 10^3 cm^{-3} the triplet 2^3S (metastable) HeI level is preferentially collisionally excited to the 2^1P and 2^1S levels (Osterbrock 1989) rather than undergoing single photon decay at 19.8eV to the ground state. This will enhance the population of the HeI 2^1P level, and thus increase the HeI 2.058 μm/Brγ ratio. To examine the importance of this mechanism, treated in detail by Smits, consider an HII region with an electron temperature and density of T_e= 10,000 K and $n_e=10^4 cm^{-3}$. Osterbrock estimates that of all 2^3S to singlet collisions, 72% of the 2^3S de-population, 17% lead to population of 2^1P. The fraction of all helium recombinations to singlet and triplet states are in the ratio 1:3, and approximately 2/3 of all singlet captures lead to 2^1P. Therefore the enhancement of the HeI 2.058 μm/Brγ ratio is given by :

$$\frac{\text{recombinations to } 2^1P + \text{collisions from } 2^3S}{\text{recombinations to } 2^1P} \simeq \frac{\frac{1}{4}\times\frac{2}{3} + \frac{3}{4}\times 0.17 \times 0.72}{\frac{1}{4}\times\frac{2}{3}} = 1.55 \qquad (2.7)$$

Smits models (1991a,b) include collisional transitions from all levels down to n=3. Due to substantial coupling between the n=2 singlet and triplet levels the n=2 metastable levels have been solved as a separate problem to the rest of the atom. Smits used a matrix inversion method to calculate the populations in these four n=2 levels simultaneously. For the n=2 levels the following processes have been included : (i) allowed spontaneous

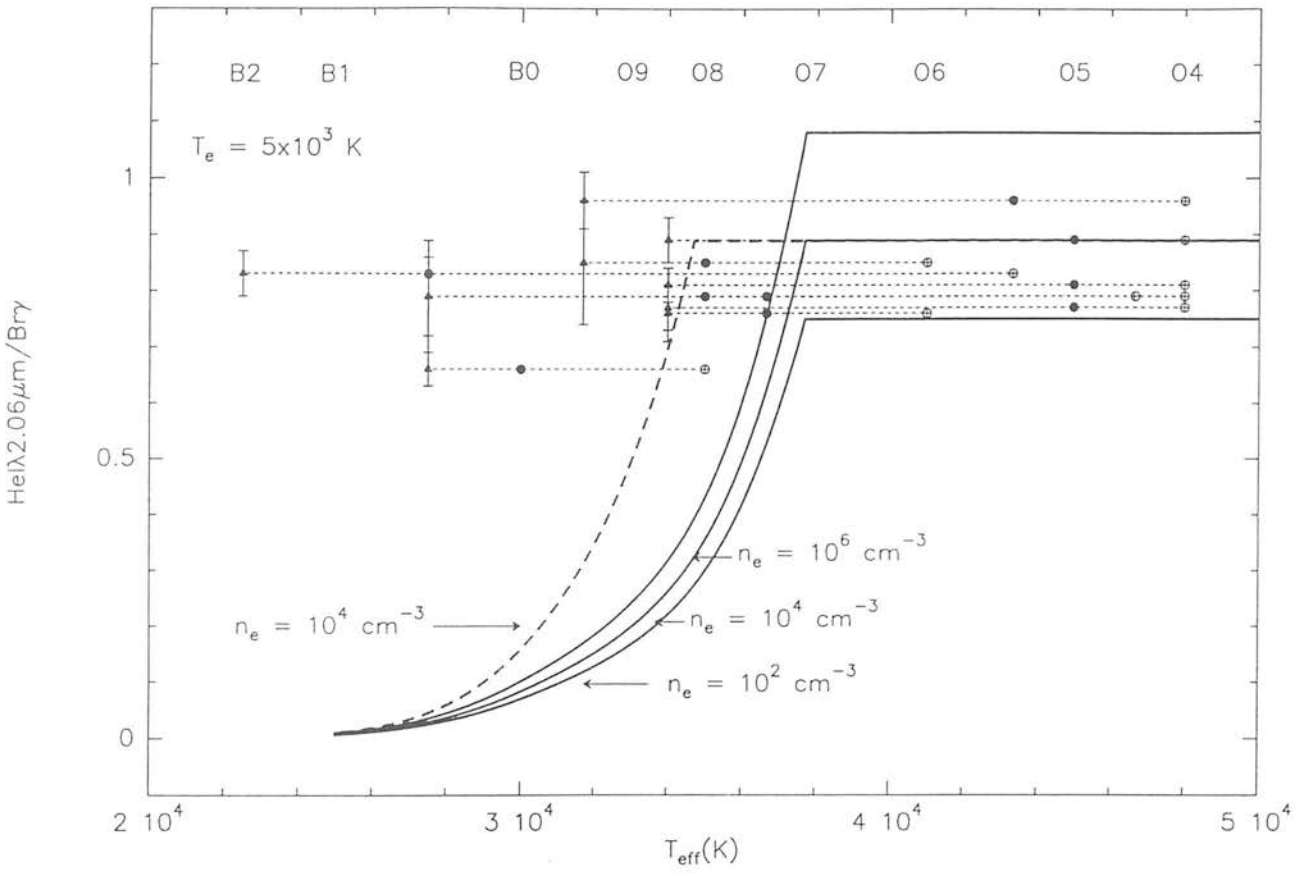

Figure 2.3: The HeI 2.058 μm/Brγ ratio *vs.* stellar effective temperature for an electron temperature of T_e=5,000K (symbols as fig 2.2).

transitions from levels n≥3 (ii) direct radiative recombination and (iii) collisional excitation and de-excitation within the n=2 level.

In his more detailed calculation, Smits (1991a), using recent collision cross-sections finds an enhancement of 1.58 for this temperature and density. For an electron temperature of T_e= 5,000K this factor decreases due to the dependence of the collision cross-sections on T_e.

The vertical displacement of the curves labelled $n_e=10^4 cm^{-3}$ and $n_e=10^6 cm^{-3}$ from the curve labelled $n_e=10^2 cm^{-3}$ in figs 2.2 and 2.3 represent the effect of collisional excitation on the HeI 2.058 μm/Brγ ratio.

Photo-ionization

Photo-ionization from the 2^3S level may be an important process since it can decrease the 2^3S population. Clegg and Harrington (1989) have investigated this mechanism in various planetary nebulae and show photo-ionization by Lyα to be the dominant photo-ionization process. Their equation (12) gives the ratio of 2^3S depopulation by photo-ionization by Lyα compared with collisions to singlets. The line intensity of Lyα is governed by the rate of destruction of these photons by dust. Using the dust parameters from DPJ, corresponding to a gas-to-dust mass ratio of 10^{-2}, a ratio for the depopulation of 2^3S of $\sim$ 0.13 was obtained. For a gas-to-dust mass ratio lower by a factor of 10, Clegg and Harrington (1989) obtain a ratio of 0.18. Since the fraction of collisions from 2^3S to 2^1P is only 17% of total collisions at T_e = 10,000K, photoionization from 2^3S reduces the 2^1P population by 0.17×0.13 $\sim$ 2% and thus, the effect on the HeI 2.058 μm/Brγ ratio is also negligible. The extra ionizations will increase the number of recombining atoms to the 2^1P level. However since the population $N(2^3S)/N(He^+) \sim 10^{-6}$ at $n_e= 10^4 cm^{-3}$ (Clegg 1987), this overall increase in the 2^1P population due to additional ionization from 2^3S is negligible.

2.5.3 Effects of Internal Dust

Wood and Churchwell (1989) discuss evidence for the presence of internal dust in UCHII regions. The effects of this dust are potentially twofold. Firstly, dust absorbs some fraction of the helium and hydrogen ionizing photons. The dust photo–absorption cross-section peaks around 800Å (15.5eV), much closer to the Lyman limit for hydrogen than for helium, and thus dust competes predominantly with hydrogen in absorbing ionizing photons. As a result, the radius of the Strömgren sphere for hydrogen will be smaller than if no dust were present whereas the corresponding radius for helium will be relatively unaffected. Consequently, these radii will coincide, and hence the HeI 2.058 μm/Brγ ratio will saturate, at lower stellar effective temperatures in a dusty HII region.

The dashed curves labelled $n_e=10^4 cm^{-3}$ in figs 2.2 and 2.3 represent the HeI 2.058 μm/Brγ ratios recalculated for dusty HII regions, based on the models of DPJ, for such an electron density. The effect of dust within an HII region is shown by the horizontal displacement of the dashed curves from the solid curves. At a density of $n_e= 10^4 cm^{-3}$ dust has a considerable effect on the line flux ratio, causing the HeI 2.058 μm/Brγ ratio to saturate at a temperature of about 35,000 K (O8 star). However, as pointed out by DPJ, the dusty model is highly sensitive to the dust-to-gas mass ratio. DPJ use a ratio of 10^{-2} which is the value for the diffuse interstellar medium; models of dusty HII regions by Chini *et al.* (1986) and Hoare *et al.* (1991) suggest that the dust-to-gas mass ratio is lower by about a factor of 10. In this case dust will have a considerably reduced effect on the HeI 2.058 μm/Brγ ratio (DPJ).

The second possible effect of internal dust, which was not incorporated into the simple dusty HII region models of DPJ, is to alter the value of the effective HeI 2.058 μm recombination coefficient from its value in a dust free environment. As discussed in section 2.5.1 in the absense of dust, at T_e=10,000K approximately one third of the 0.0584 μm photons are absorbed by hydrogen whilst two thirds are reprocessed by helium atoms. Using the dusty HII region models of DPJ, the absorption of 0.0584 μm photons by dust has been investigated further. These models assume the uniform grain size distribution of Mathis, Rumpl and Nordsieck (1977) including both silicate and graphite particles, for grains of radii 0.005 μm up to 0.25 μm, and a constant dust-to-gas mass

ratio of 10^{-2}. The mean free path of a 0.0584 μm photon before (a) absorption by a helium atom, at T_e=10,000 K, ultimately resulting in population of the 2^1S level, (b) photoionization of a hydrogen atom, and (c) absorption by dust were calculated. The mean free path lengths are approximately in the ratio 1:2:6000, hence dust absorbs a negligible fraction of 0.0584 μm photons and therefore has virtually no effect on the effective HeI 2.058 μm recombination coefficient.

Recent models by Shields use a complex photoionization code to predict the theoretical HeI 2.058 μm/Brγ ratio as a function of effective temperature T_{eff}. Shields models show good agreement with the above models until T_{eff} becomes greater than 38,000K, where Shields models turnover and decrease rapidly instead of reaching a saturation value as found in the DPJ models. These models and the reason for discrepancies at higher T_{eff} are discussed fully in chapter 4.

2.6 Comparison with Observations

To compare observed HeI 2.058 μm/Brγ recombination line ratios with the theoretical curves in figs 2.2 and 2.3, the spectral type of the exciting stars in the UCHII regions must be determined. Both the radio and IRAS fluxes from these UCHII regions can be used to estimate the spectral types by comparison with models from Puxley (1988), obtained by integrating Kurucz (1979) model atmospheres and using the conversion between effective temperature, mass, radius and spectral type from Landolt–Börnstein (1982). The radio flux density yields a lower limit to the number of Lyman continuum photons N_{Lyc} (Wood and Churchwell 1989) since dust inside the HII region can absorb a significant number of ionizing photons. Integration of the IRAS fluxes for each UCHII region gives the infrared luminosity L_{IR}. For computational simplicity the flux at 1mm is assumed to be the same as that at 12 μm in order to correct for the luminosity outside the IRAS bands. These values of L_{IR} are in excellent agreement with those given for several of the UCHII regions by Chini *et al.* (1987). The spectral type derived from the IRAS fluxes will be an upper limit as the size of the IRAS beam ($5\hat{\ }\times3\hat{\ }$ at 100 μm) is much greater than that of a typical UCHII region ($\sim5\hat{\ }$). The spectral types derived from N_{Lyc} and L_{IR} are given in table 2.6, assuming that a single star is responsible for

Object	IRAS (L_{IR}) (single star)	Radio (N_{Lyc}) (single star)	N_{Lyc}/L_{IR} (cluster)
G5.48	O4.5	O8	B0.5
G5.97	O8	B0	B0.5
G15.04	O5.5	B0.5	B2
G29.96	O4	O5.5	O9.5
G35.20	O6	O8	O9.5
G43.89	O6	O7.5	O8.5
G45.07	O4	O7.5	B0.5
G45.12	O4	O5	O8.5

Table 2.6: Spectral type estimates derived from observed properties.

the emission.

Studies of compact HII regions by Lacy, Beck and Geballe (1982) and Hoare *et al.* (1991) conclude that such regions may be excited by a cluster of stars. Therefore, a third estimate of the spectral type, *i.e.* the effective stellar temperature T_{eff}, was evaluated for an HII region excited by a stellar cluster. The ratio of N_{Lyc}/L_{IR}, dependent only on the effective temperature of the radiation from the cluster, yields a lower limit to the characteristic spectral type, because of dust and the IRAS beam size. This limit is in agreement to within 1 subclass with the cluster temperature derived by Lacy *et al.* (1982) for G29.96 and 0.5 of a subclass for T_{eff} derived by Hoare *et al.* (1991) for G45.12 from analysis of the mid–infrared fine structure lines. These values, which are lower limits for T_{eff}, are several subclasses lower those found by assuming the emission to be from a single source. The three estimates of the effective temperature for each UCHII region are shown in figs 2.2 and 2.3. The dotted lines joining the estimates of T_{eff} represent the uncertainty in the spectral types of the exciting stars in the UCHII regions.

The corrected observed HeI 2.058 μm/Brγ ratios from table 2.4, are plotted on figs

2.2 and 2.3 against the model curves (the data for figure 2.3 are scaled by the dust extinction factor appropriate to T_e=5,000K). For the UCHII region G45.12, data were obtained with both CGS2 and CGS4. The CGS2 data points are entirely consistent after atmospheric corrections are applied and also consistent with the CGS4 fluxes for HeI and Brγ (difference of 1.66σ).

For an electron temperature of T_e=5,000K (fig 2.3), the observed line ratios, are generally in good agreement with the predicted model for a density of $n_e = 10^4$ cm^{-3}, if the exciting star(s) are hotter than 35,000K, or O8, consistent with the range of estimated spectral types for these objects (table 2.6).

From fig 2.2, for a gas temperature of T_e=10,000K, as inferred for several UCHII regions by Wood and Churchwell (1989) and Downes *et al.* 1980, three conclusions might be drawn. First, the observed HeI 2.058 μm/Brγ ratios are consistent with these objects lying on the rising part of the n_e=10^4cm^{-3} curves. In this case T_{eff} must be in the range 32–37,000K depending on the dust content inferred in these UCHII regions. Further, if UCHII regions have similar dust contents then they all fall on either the dashed (dusty) curve, or the solid (less dusty or non-dusty) curves. Either curve, constrains a very narrow range of effective temperatures, within one spectral type, for the whole UCHII region sample, which seems unlikely. Additional, and more conclusive, evidence against this range of T_{eff} is also given in section 3.4.1. The one exception to this is G5.97, which is seen to have a lower HeI2.058 μm/Brγ ratio than the predicted model for n_e=10^2 cm^{-3}, and hence has a genuinely lower T_{eff}.

Secondly, the UCHII regions have $T_{eff} \geq$35,000K and have a dust-to-mass gas ratio similar to that in the interstellar medium or $T_{eff} \geq$38,000K and a much lower dust-to-mass gas ratio. In this case the observed line ratios lie closer to the saturated value of the curve labelled $n_e = 10^2$ cm^{-3} rather than the curve labelled $n_e = 10^4$ cm^{-3} (fig 2.2). This is clearly unlikely since the densities of these UCHII regions, as discussed in section 5.1, lie in the range 10^4–10^5 cm^{-3}.

Thirdly, the UCHII regions have the same range of T_{eff} as above, but at the much higher densities known to exist. In this event, the HeI 2.058 μm/Brγ ratio must be reduced by some other cause and plausible explanations are given below.

In order to reconcile these low observed ratios with the high inferred electron densities from Wood and Churchwell (1989), one suggestion is that there are large density variations throughout the UCHII regions. In this case, the integrated HeI 2.058 μm/Brγ ratio is much less than the HeI 2.058 μm/Brγ ratio in the denser areas of the UCHII regions (see also chapter 5). From the mean observed HeI 2.058 μm/Brγ ratios the predicted beam–averaged electron densities of these objects would have to be $\sim 10^2$–10^3cm^{-3} for T_e=10,000K (fig 5.3). Analysis of the long slit CGS4 data for G43.89 suggest that the HeI 2.058 μm/ Brγ ratio varies across the source, being greatest at the central position and decreasing outwards, consistent with a gradient in electron density. However, when these observations were made there was a small mis–alignment between the dispersion axis and the detector rows which results in the HeI and Brγ lines being sampled at slightly different spatial positions and thus this result, whilst suggestive, must be regarded as only preliminary.

Other mechanisms which may alter the HeI 2.058 μm/Brγ ratio and account for the discrepancy between the observed values and the model predictions for UCHII regions with T_e=10,000K (fig 2.2) are now considered.

Inspection of the HII region models as described by equations (2.5) and (2.6), reveals that the only parameters subject to significant uncertainty are N^{He}_{Lyc}/N^{H}_{Lyc}, N_{He}/N_H and $\alpha_{HeI\lambda 2.058}$; each parameter is considered in turn. N^{He}_{Lyc}/N^{H}_{Lyc}, the relative ionization rates of helium to hydrogen depends on the reliability of the stellar atmospheric models. Comparison of different stellar atmosphere models by Skillman (1989) shows that the Kurucz models are in fairly good agreement with observed ionization distributions. However, it must be noted that the presence of stellar winds may dramatically affect the emerging spectrum. Although the helium abundance N_{He}/N_H is less varied across the interstellar medium than that of the heavier metals, nevertheless there is an abundance gradient throughout the Galaxy. For the observations at T_e=10,000K to be consistent with the curve labelled $n_e = 10^4$ cm^{-3} the helium abundance would have to be $\sim$ 0.07, a value which is less than the primordial value and therefore this possibility may be discounted.

The HeI 2.058 μm effective recombination coefficient $\alpha_{HeI\lambda 2.058}$ was discussed in section 5.2, and the mean free path of a 0.0584 μm photon before absorption by helium and

ionization by hydrogen were compared. The mean free path is inversely proportional to the absorption cross-section for a given electron density. The absorption cross-section at the line centre for a helium resonance line, a_0, can be written;

$$a_o = \frac{3\lambda^3 A}{8\pi}\left(\frac{1}{\Delta V_D}\right) \tag{2.8}$$

A is the Einstein coefficient and ΔV_D is the thermal Doppler width which is ~ 6 kms^{-1} for helium atoms at T_e= 10,000K. Assuming this width and electron temperature, comparison of mean free path lengths implies that 2/3 of the photons from the HeI 2^1P level are reprocessed by helium atoms and 1/3 ionize hydrogen. However, the RRL width measurements of the UCHII regions, at about 20–45 kms^{-1} in a 2.6$\widehat{'}$ beam, are considerably broader than the thermal width, and thus further broadening process(es) are occurring. Possible mechanisms are : (i) pressure broadening due to electron impacts, (ii) bulk motions of the ionized gas, and (iii) turbulence. In their study of G29.96, Wood and Churchwell (1991) see no evidence of (i) and Garay (1989) concludes that pressure broadening of the RRL, H76α, is negligible in their observations of compact HII regions. To be rigorous, a full set of radiative transfer equations should be solved incorporating the effects of processes (ii) and (iii), however, the importance of these mechanisms in a simple model can be examined.

Consider the scenario whereby further broadening of the helium 1^1S–2^1P resonant line is solely due to turbulent motions and thus a Gaussian distribution remains appropriate. The effective Doppler width becomes :

$$V_D^2 = \frac{2kT}{m_{he}} + V_{turb}^2 \tag{2.9}$$

If this process increases the line width to ~ 17 kms^{-1}, then only ~ 0.44 of the resonance line photons from the HeI 2^1P level are reprocessed by helium. The value of the HeI 2.058 μm effective recombination coefficient would therefore decrease by a factor of ~ 1.52, and the theoretical HeI 2.058 μm/Brγ ratio, for T_e= 10,000K and a Galactic abundance of 0.1, would saturate at a value of 0.84. This saturation value is in good agreement with the observed HeI 2.058 μm/Brγ ratios (see table 2.4).

It is necessary to examine whether this prediction is compatible with RRL meaurements for the UCHII regions. The radio recombination line FWHM values are taken from observations of H76α (Wood and Churchwell 1989), H76α, H90α (Wink *et al.* 1982) and H110α (Downes *et al.* 1980) for each object and given in table 3.3. Where two measurements are available for a given object the mean value was used.

For purely thermal motions the expected FWHM for a hydrogen line is 21.4 kms^{-1}, whereas observed line FWHM values for HI are in the range 25–38 kms^{-1}. This difference can be attributed to turbulent or other small scale broadening FWHM velocities of 13–31 kms^{-1} assuming a Gaussian distribution. Increasing the effective HeI Doppler width to 17 kms^{-1} implies a turbulent FWHM velocity of 26 kms^{-1} and an overall HI FWHM velocity of 34 kms^{-1}, consistent with these RRL observations.

Note that any increase of the HeI absorption line width must be on scales less than or comparable to the mean free path length of a HeI and HI 0.0584 μm photon which is of order 10^{12}cm for $n_e=10^4 cm^{-3}$. Therefore a homogeneous HII region with an constant expansion velocity of $\sim$ 30 kms^{-1} will explain the RRL observations but will not broaden the HeI line since the scale length, *i.e.* the radius of the HII region (see table 3.3), is much larger than the mean free path length of $\sim 10^{12}$cm. Thus, the absolute probabilities for absorption by helium or hydrogen are unchanged and the HeI 2.058 μm line strength unaffected. Similarly, a velocity gradient over the HII region was considered. Garay *et al.* (1986) find a gradient of 16 kms^{-1} per arcsec for G45.07. The FWHM velocity for helium atoms is 10.7 kms^{-1}, therefore broadening velocities greater than 10.7 kms^{-1} occurs over a scale length of 10.7/16$\times$(radius in arcsec) which translates to $\sim 10^{16}$cm for G45.07 much greater than the mean free path length. Therefore, the same argument as above applies and the HeI 2.058 μm line strength is unchanged. A high resolution spectrum of HI and HeI lines in G29.96 is given in fig 2.4, providing some evidence for microturbulence. The line width observed in these lines ($\sim$35 kms^{-1}), is a combination of the instrumental FWHM profile of 20 kms^{-1} added in quadrature to the thermal line width plus any additional turbulent or large scale broadening motions. The measured velocity shifts across the face of this nebula are $\sim$ 10 kms^{-1} over 0.1pc (S. Lumsden, private communication). Assuming a similar velocity gradient exists along the line of sight, the additional broadening observed implies a turbulent velocity width of $\sim$25

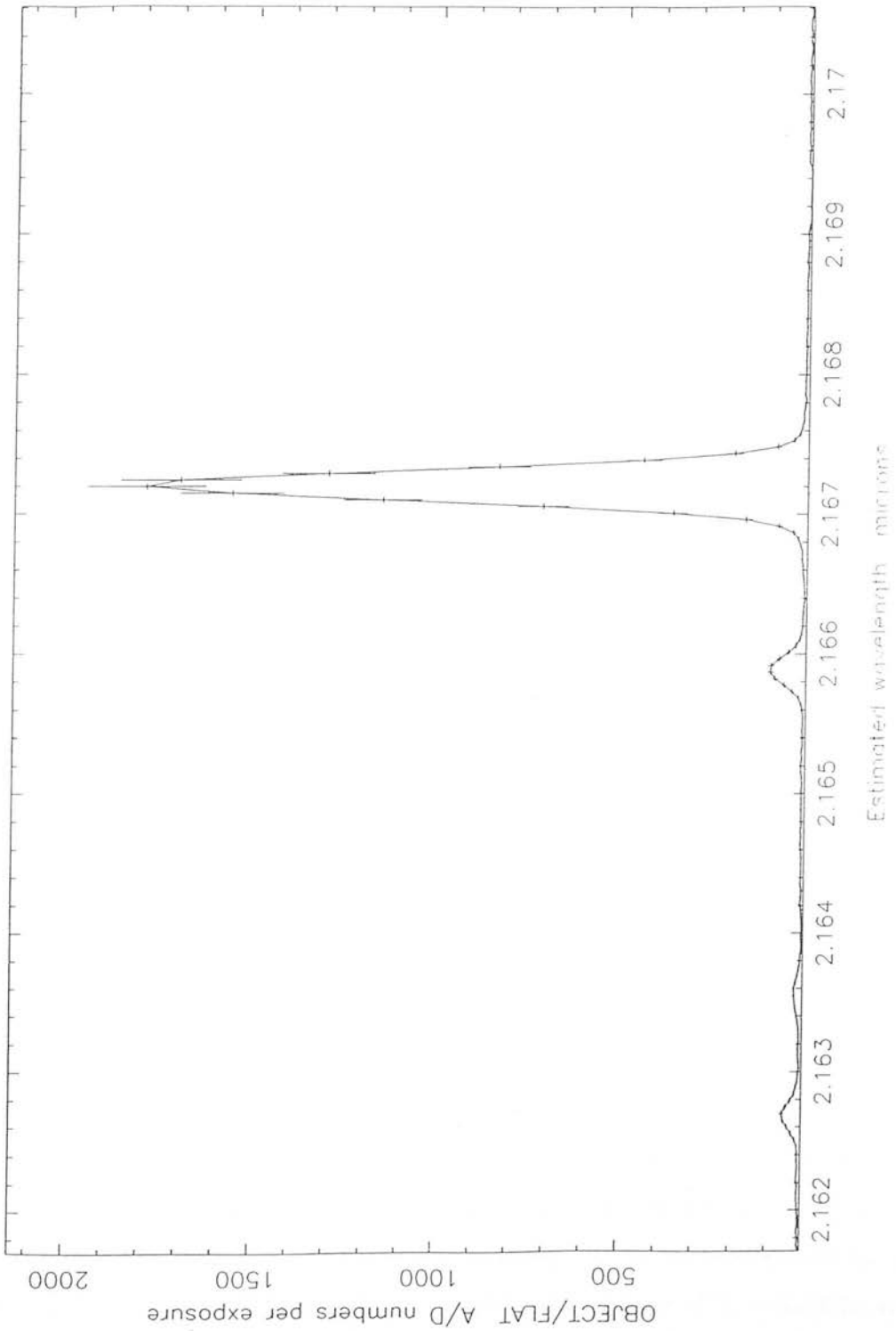

Figure 2.4: High resolution spectra of G29.96, showing the bright Brγ line, the weaker resolved HeI 7^3F–4^3D and HeI 7^1F–4^1D lines shown here at 2.1626 μm and 2.1635 μm, and the HeI $7^{1,3}$G–$4^{1,3}$F blend here at 2.1659 μm.

kms^{-1}, in agreement with predicted microturbulent motions from comparison of observed and theoretical HeI 2.058μm/Brγ ratios.

Shields models are in agreement with the above conclusions if T_{eff} is less than 38,000K in these objects. A fuller consideration of his models is deferred until compact HII region data is also considered in chapter 4.

A detailed discussion of each UCHII region is performed in chapter 3 after further observations of these objects have been analysed. In general, to summarize the results of this chapter, the observations of UCHII regions are consistent with two possible models: (a) an HII region model for an electron temperature of T_e=5,000K and an electron density of n_e= 10^4 cm^{-3} assuming purely Doppler broadening or (b) an electron temperature of T_e=10,000K and an electron density of n_e= 10^4 cm^{-3} where line broadening, *e.g.* due to turbulence, is important on scales comparable with the 0.0584μm HeI photon mean free path (10^{12}cm; *cf.* HII region radius of $\sim$ 10^{16}cm).

2.7 Conclusions

K band measurements of HeI 2.06 μm and Brγ recombination lines were carried out for a sample of UCHII regions with spectral types B1–O4 and the results compared to theoretical predictions. Modifications to the models due to collisional excitation and radiative transfer effects have been investigated. The following conclusions were drawn within the context of the models based on DPJ:

(i) The observed ratios are in good agreement with either the theoretical HII region model for an electron temperature of T_e=5,000K, an electron density of n_e= 10^4 cm^{-3} and a Galactic helium abundance assuming purely thermal broadening of the HeI line; alternatively, if the intrinsic HeI line width is broadened, *e.g.* by turbulent motions of the ionised gas, to $\sim$ 17 kms^{-1} then, for an electron temperature of T_e=10,000K, an electron density of n_e= 10^4 cm^{-3} and a Galactic helium abundance the effective HeI 2.058μm recombination coefficient and consequently the theoretical HeI 2.058μm/Brγ ratio would decrease sufficiently to be consistent with these UCHII region observations. The RRL measurements of the observed UCHII regions are broadly consistent with the

latter model but small beam measurements of the HeI 2.058 μm and Brγ line widths are needed as a definitive test. Without further observations it is not possible to distinguish between these models.

(ii) The HeI 2.058 μm/Brγ ratio is not a good indicator of effective temperature in UCHII regions as the presence of dust can limit the sensitivity to spectral types earlier than about O8. Observations of less dense HII regions, so that the complications due to collisional excitation may be neglected, and which are of later spectral type are required.

(iii) For observations of the narrow HeI line at 2.058 μm, the effect of telluric CO_2 absorption must be calculated. For these observations, this absorption removed 5–36 % of the HeI line flux for different UCHII regions. As the intrinsic width of the HeI line is comparable with that of the individual CO_2 atmospheric lines, these amounts will vary throughout the year.

Chapter 3

Further HeI observations of UCHII regions

3.1 Introduction

From analysis of observed values for the HeI 2.058μm/Brγ ratio in a sample of UCHII regions in chapter 2, it was possible to constrain models of the ionization structure of UCHII and HII regions. The aim in this chapter is to critically examine modifications to the models *e.g.* due to collisional and radiative transfer effects (sections 2.5.2 and 2.6 respectively), by use of further HeI recombination line measurements.

Several theoretical UCHII region models were proposed to fit the observations. The observed values of this ratio were generally in good agreement with two models:
a) an UCHII region with an electron temperature of T_e=5,000K, an electron density of n_e=10^4cm^{-3} and purely thermal HeI line broadening.
b) an UCHII region with an electron temperature of T_e=10,000K, an electron density of n_e=10^4cm^{-3} and with HeI line broadening due to turbulent motions within the nebula, of the order 10–20 kms^{-1}. The essence of these models is that line broadening of HeI is required for electron temperatures greater than 5,000K to be in agreement with the observations. The observed HeI 2.058μm/Brγ ratios require larger turbulent motions, *e.g.* HeI line broadening as much as $\sim$20 kms^{-1}, as the electron temperature is increased

up to T_e=10,000K. These two electron temperatures encompass the range of electron temperatures of the UCHII regions derived from RRL measurements by Downes *et al.* (1980) and Wink *et al.* (1982) which are given in table 3.1. Therefore models a) and b) can be considered as extremes and the observed UCHII regions might each be best represented as some intermediate model on the continuum between them.

In a number of the UCHII regions studied, the recombination lines of HeI 4^3S–3^3P, 2.1126 μm and HeI 4^1S–3^1P, 2.1137 μm have also been detected as a blend which will be referred to as the $4^{1,3}S$–$3^{1,3}P$ blend hereafter. By examining the line ratios of HeI 2.113/HeI 2.058 μm and HeI 2.113 μm/Brγ it is possible to extend these models to apply to specific UCHII regions and to study further the physical processes, including radiative transfer effects, in UCHII and HII regions. The HeI 2.113/HeI 2.058 μm ratio should be purely a function of the properties of the plasma *i.e.* electron temperature and density within the HII region. The HeI 2.113 μm/Brγ ratio translates into a measure of He^+/H^+ which for a given helium abundance describes the ionization structure of the HII region. This ratio, in contrast to HeI 2.058 μm/Brγ ratio, should be only weakly dependent on ionized gas properties since collisional excitation from the HeI 2^3S level has considerably less effect on the HeI 2.113 μm line. Radiative transfer effects retain some dependence of the HeI 2.113 μm line on nebular gas properties.

In section 3.2, the observations and correction factors applicable to the observed line ratios are described. In section 3.3, theoretical values for these ratios are established, using up to date recombination line strengths (Smits 1991a,b). Modifications to the HeI 2.113 μm line strength, are calculated, resulting from a large population in the HeI 2^3S level are calculated. With these modifications to the theoretical models in mind, observations and theory are compared in section 3.4 and the conclusions presented.

3.2 Observations

The UCHII regions observed are described in chapter 2. Of the eight objects observed the $4^{1,3}S$–$3^{1,3}P$ blend was detected in four of the objects. The reduction procedure is described in section 2.2 and the spectra shown in fig 2.1. The $4^{1,3}S$–$3^{1,3}P$ blend,

detected in objects g15.04 (fig 2.1c), g29.96 (fig 2.1d) and g45.12 (fig 2.1e), taken with CGS2 in Sept 1990, was fitted with a Gaussian of FWHM taken as the best fitting FWHM for the bright HeI 2.058 and Brγ 2.165 μm lines and equal to the instrumental profile. The resolving power of CGS2 is $\sim$ 400 kms^{-1} and that of CGS4 is $\sim$ 900 kms^{-1}, whilst the intrinsic HeI line width is $\sim$ 20–40 kms^{-1} and the separation between the 4S–3P singlet and triplet lines is $\sim$ 150 kms^{-1}. Thus the recombination lines will be unresolved and blended and the FWHM should reflect that of the instrumental profile. The $4^{1,3}$S–$3^{1,3}$P blend was also detected in objects g43.89 (fig 2.1h) and g45.12 (fig 2.1j) observed with CGS4 in June 1991 and triangular profiles, again basically instrumental profiles were fitted to determine the line flux. In g43.89 molecular hydrogen was also present at 2.1218 μm, so both lines were fitted simultaneously with the FWHM from HeI 2.058 μm and Brγ to minimize contamination of HeI $4^{1,3}$S–$3^{1,3}$P from molecular hydrogen in emission. The raw line fluxes and their 1σ errors, are given in table 3.1. For the remaining objects, with the exception of G45.07, the latter fitting procedure was employed to determine 2σ upper limits and these are also given in table 3.1. For g45.07 the unusual sloping continuum made it impossible to obtain any reasonable upper limit.

The line ratios of HeI $4^{1,3}$S–$3^{1,3}$P 2.113 μm/HeI 2^1P–2^1S 2.058 μm and HeI $4^{1,3}$S–$3^{1,3}$P 2.113 μm/Brγ were then calculated. An atmospheric correction factor was incorporated into the HeI $4^{1,3}$S–$3^{1,3}$P/HeI 2.058 μm ratio, since the HeI 2.058 μm line lies embedded in an atmospheric absorption band of CO_2 at 2.06 μm. The appropriate atmospheric correction factor for each UCHII region has been calculated in section 2.3. Both ratios were corrected for differential extinction, converting the values used in section 2.4 to values appropriate for the wavelengths of the two lines in question. The extinction correction was no more than 10% and has the effect of decreasing the HeI 2.113/HeI 2.058 μm ratio, and increasing the HeI 2.113 μm/Brγ ratio. The extinction correction was calculated for T_e=10,000K only, since the difference at T_e=5,000K (section 2.4) is well within observational errors. With the above corrections applied the resultant ratios are given in table 3.1. Values for HeI 2.113 μm/HeI 2.058 μm lie in the range 0.045–0.107 and values for HeI 2.113 μm/Brγ lie in the range 0.029–0.081.

Object	HeIλ2.113/HeIλ2.058 ratio		HeIλ2.113/Brγ ratio		$^{a}T_e$ (K)	$^{b}T_e$ (K)
	Observed	Corrected	Observed	Corrected		
G5.48[1]	<0.103	<0.095	<0.077	<0.081	6000±1100	10800±3000
G5.97[1]	<0.058	<0.045	<0.027	<0.029	6500±700	6500±3000
G15.04	0.048±0.003	0.045±0.003	0.036± 0.002	0.038±0.002	7000±1000	9100±1000
G29.96	0.077±0.002	0.060±0.002	0.052± 0.001	0.058±0.002		6100±3000
G35.20[1,2]	<0.115	<0.107	<0.070	<0.079		8500±3000
G43.89[2]	0.054±0.006	0.053±0.005	0.038±0.004	0.042±0.004	5900±1600	[c]7500±1100
G45.12	0.067±0.004	0.066±0.003	0.047±0.002	0.052±0.003	8200±1100	10100±3000
G45.12[2]	0.068±0.006	0.062±0.006	0.053±0.005	0.057±0.006	8200±1100	10100±3000

[1]Only upper limits were obtained for these objects.

[2]Taken with CGS4 June 1991.

[a]Electron temperatures from Wink *et al.* 1982.

[b]Electron temperatures from Downes *et al.* 1980.

[c]Measurement from Wink *et al.* 1982 also.

Table 3.1: Observed line ratios in UCHII regions.

3.3 Theoretical line ratios

The volumes of the He^+ and H^+ zones in an HII region are controlled by the number of helium and hydrogen ionizing photons and therefore any helium to hydrogen recombination line ratio measures the relative volumes of the two ionized zones. Above a certain stellar effective temperature the photons produced from helium recombinations monopolize the ionization of hydrogen and the two ionized volumes are coincident. DPJ calculate this temperature to be 38000K (O7 star). Following DPJ, the theoretical HeI 2.113 μm/Brγ line ratio is given by:

$$\frac{I_{HeI\lambda 2.113}}{I_{Br\gamma}} = \frac{N_{Lyc}^{He}}{N_{Lyc}^{H}} \frac{\alpha_{\rm B}(H^+)}{\alpha_{\rm B}(He^+)} \frac{\alpha_{HeI\lambda 2.113}}{\alpha_{Br\gamma}} \frac{\lambda_{Br\gamma}}{\lambda_{HeI2.113}}, {\rm V_{He+}} < {\rm V_{H+}} \tag{3.1}$$

$$\frac{I_{HeI\lambda 2.113}}{I_{Br\gamma}} = \frac{N_{He}}{N_{H}} \frac{\alpha_{HeI\lambda 2.113}}{\alpha_{Br\gamma}} \frac{\lambda_{Br\gamma}}{\lambda_{HeI2.113}}, {\rm V_{He+}} = {\rm V_{H+}}. \tag{3.2}$$

where V_{He+} and V_{H+} are the volumes of the helium and hydrogen ionized zones respectively and other parameters are as defined in 2.5.1.

As with the HeI2.058 μm/Brγ ratio, the HeI 2.113 μm/Brγ ratio (eqn 3.1) will be sensitive to the relative ionization rates, hence stellar effective temperatures, up to 38000K. Above this temperature the two ionized volumes V_{He+} and V_{H+} become coincident, and the HeI 2.113 μm/Brγ ratio (eqn 3.2) is dependent on the helium abundance. An helium abundance of 0.1 is assumed for all these calculations. Moreover, the HeI 2.113 μm line strength, and hence the HeI 2.113 μm/Brγ ratio, will be fairly insensitive to electron density. This is because collisional cross-sections from the 2^3S level to the n$\geq$4 levels, which affect the 2.113 μm blend, are much smaller than cross-section values to the other n=2 sublevels, which affect the 2.058 μm line (Berrington and Kingston 1987). However, the ratio of HeI 2.113/HeI 2.058 μm is thus highly sensitive to electron density.

Values for HeI recombination line strengths, from which the recombination coefficients in eqn 3.1 can be readily derived, are taken from Smits (1991a,b) and are given in table 3.2 along with values for hydrogen recombination coefficients (Hummer and Storey, 1987) for electron temperatures of T_e= 10,000K and 5,000K and gas densities

$\alpha_{H,He}$	$T_e=10^4K$			$T_e=5\times10^3K$		
$cm^{-3}s^{-1}$	$n_e=10^2cm^{-3}$	$n_e=10^4cm^{-3}$	$n_e=10^6cm^{-3}$	$n_e=10^2cm^{-3}$	$n_e=10^4cm^{-3}$	$n_e=10^6cm^{-3}$
$\alpha_B(H^+)$[1]	2.59×10^{-13}	2.59×10^{-13}	2.59×10^{-13}	4.54×10^{-13}	4.54×10^{-13}	4.54×10^{-13}
$\alpha_B(He^+)$[1]	2.73×10^{-13}	2.73×10^{-13}	2.73×10^{-13}	4.34×10^{-13}	4.34×10^{-13}	4.34×10^{-13}
$\alpha_{Br\gamma}$[2]	3.74×10^{-15}	3.71×10^{-15}	3.63×10^{-15}	7.90×10^{-15}	7.85×10^{-15}	7.68×10^{-15}
$\alpha_{HeI\lambda2.058}$[3]	4.25×10^{-14}	6.78×10^{-14}	8.03×10^{-14}	7.68×10^{-14}	9.16×10^{-14}	1.05×10^{-13}
$\alpha_{HeI\lambda2.1126}$[3]	1.01×10^{-15}	1.02×10^{-15}	1.02×10^{-15}	1.42×10^{-15}	1.43×10^{-15}	1.46×10^{-15}
$\alpha_{HeI\lambda2.1137}$[3]	4.38×10^{-16}	4.41×10^{-16}	4.43×10^{-16}	6.37×10^{-16}	6.44×10^{-16}	6.56×10^{-16}

[1] Values from Osterbrock 1989.

[2] Values from Hummer and Storey 1987.

[3] Values from Smits'1991a,b.

Table 3.2: Recombination coefficients for HI and HeI

of n_e=10^2, 10^4 and 10^6 cm^{-3}. As noted in section 2.5.1, these values are similar to the observed ranges (see also table 3.1). As discussed there, the HeI 2.058μm recombination coefficient has been scaled by a factor of 2/3 at T_e=10,000K (~3/4 at T_e=5,000K) to account for deviations from case B.

Fig 3.1 shows the predicted HeI 2.113μm/Brγ ratios *vs* stellar effective temperature for electron temperatures of T_e=10,000K and 5,000K. The theoretical HeI 2.113μm/Brγ ratio saturates at values of 0.040 (T_e=10,000K) and 0.027 (T_e=5,000K) for an O7 star corresponding to an effective temperature of 38,000K, assuming no dust to be present (solid curve). For a dusty HII region (section 2.5.3), the ratio saturates at a lower temperature since dust preferentially absorbs hydrogen ionizing photons emitted from the source. The percentage absorption depends on the n_e and the dust-to-gas mass ratio; for n_e=$10^4$$cm^{-3}$ and a dust-to-gas mass ratio of 10^{-2}, the helium and hydrogen ionized zones are coincident and therefore the HeI 2.113μm/Brγ ratio saturates at a temperature of 35,000K or O8 star (dashed curve). At T_e=10,000K, the theoretical HeI 2.113/2.058μm ratio has values 0.050 (n_e=$10^2$$cm^{-3}$), 0.032 ($n_e$=$10^4$$cm^{-3}$) and 0.027 ($n_e$=$10^6$$cm^{-3}$). Equivalent values at T_e=5,000K are 0.039, 0.033 and 0.029. Before a detailed comparison of the observed line ratios with the models is carried out, it is instructive to examine the physical processes which may affect these ratios.

Further physical processes, other than those calculated by Smits (1991a), which stem from a large population of atoms in the HeI 2^3S and 2^1S metastable levels (lifetimes t=7874 and 0.02s respectively) may significantly alter the theoretical ratios established above. A sufficiently large n=2 population potentially gives rise to a) collisional excitation from n=2 up to higher levels, b) photoionization from 2^3S and 2^1S and c) significant optical depths in line transitions emanating from the 2^3S and 2^1S levels. Additionally, line broadening of the HeI 1^1S–2^1P resonance line proposed in model b) section 2.6, will affect the theoretical results. All these mechanisms are investigated below.

3.3.1 Collisional excitation

Collisional excitation has been shown to cause a significant increase in the HeI 2.058μm line strength (Smits 1991a). Collisional excitation from the highly metastable 2^3S level

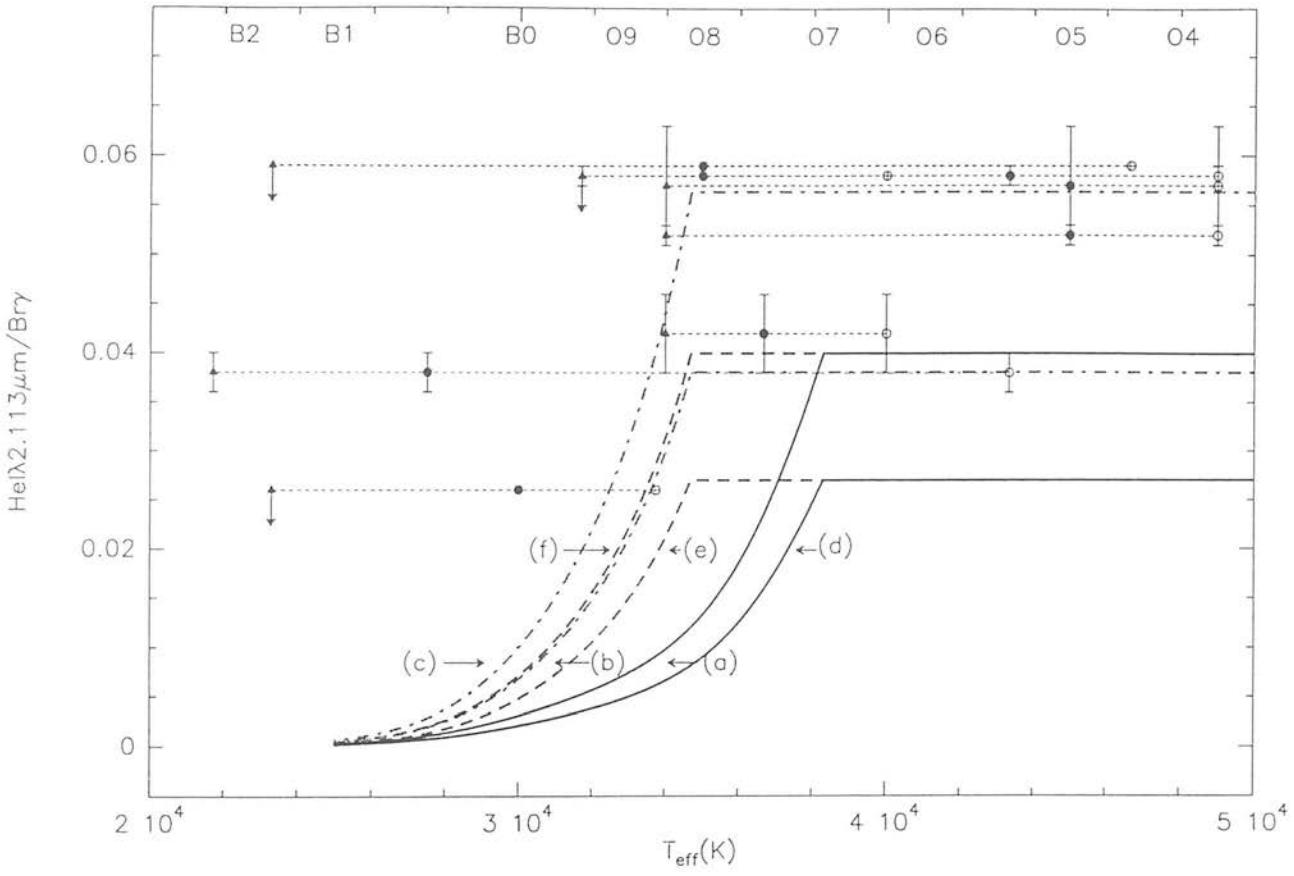

Figure 3.1: The HeI 2.113μm/Brγ ratio *vs.* stellar effective temperature for an electron density of $n_e=10^4 cm^{-3}$ (or higher) and electron temperatures of T_e=10,000K (curves a,b and c) and 5,000K (curves d,e and f.) Curves a) and d) (solid curves) are non-dusty curves whilst b) and e) (dashed curves) are dusty curves for this electron density and a dust-to-gas mass ratio of 10^{-2}. Curves c) and f) (dot-dash curves) are the dusty curves incorporating the maximum correction for optical depth effects found for these UCHII regions (see text). The symbols are the same as in fig 2.1.

to the 2^1P and 2^1S states is discussed in detail in section 2.5.2. To summarize, beyond a critical density of 3–7$\times10^3$cm^{-3}, collisional excitation to the singlets becomes the most important process for depopulation of the 2^3S state. Thus the HeI 2^1P–2^1S 2.058μm line strength is a strong function of density as can be seen from comparison of the HeI 2.058μm line strengths relative to the HeI 4472 line at different densities in table 2 by Smits (1991a). The 4472Å line is relatively unperturbed by collisions or other effects (Clegg, 1987). Collisional effects on the HeI 2.113μm line strength resulting from excitation from 2^3S to n$\geq$ 4 are now examined.

Calculations by Smits (1991b) reveal that the HeI 2.1137μm and 2.1126μm line strengths only vary slightly with electron density. Smits notes that at nebular densities, collisional de-excitation from n$\geq$ 3 to n=2 is negligible compared to spontaneous transition rates, but collisional excitation from the metastable levels into n$\geq$ 3 level, not included in table 2, is possibly an important depopulating process. This possibility is now examined. Table 4 of Smits (1991a) gives strengths for various HeI lines, relative to the 4472Å line, caused by collisions from the metastable levels to n=3 (see fig 3.2, an HeI energy level diagram for reference). For these calculations Smits uses electron collision cross-sections from Berrington and Kingston (1987). Comparison of tables 4 and 2 by Smits (1991a), give the ratio, C/R, of excitation by collisions from the 2^3S metastable level with those by recombinations. As an example, the 3^3S–2^3P, 7065Å line arises from the next lowest ^{3}S state from which the 4^3S–3^3P, 2.1126μm line originates, and has C/R=1.02 for n_e=10^4cm^{-3} and T_e=10,000K. This value for the 7065Å transition suggests that the effect of collisions on 4^3S–3^3P, 2.1126μm line, might also be significant.

Collision cross-sections from the metastable levels to n=4 have very recently been calculated by Berrington (private communication) enabling calculation of C/R for the 2.1126μm line; from Clegg (1987):

$$\mathrm{C/R} = \frac{N(2^3S)k_{eff}\lambda}{N(He^+)\alpha_{eff}} \tag{3.3}$$

where the ratio of the population of atoms in the 2^3S level to the total number of recombining atoms, given from the equation of balance for the 2^3S population (Clegg

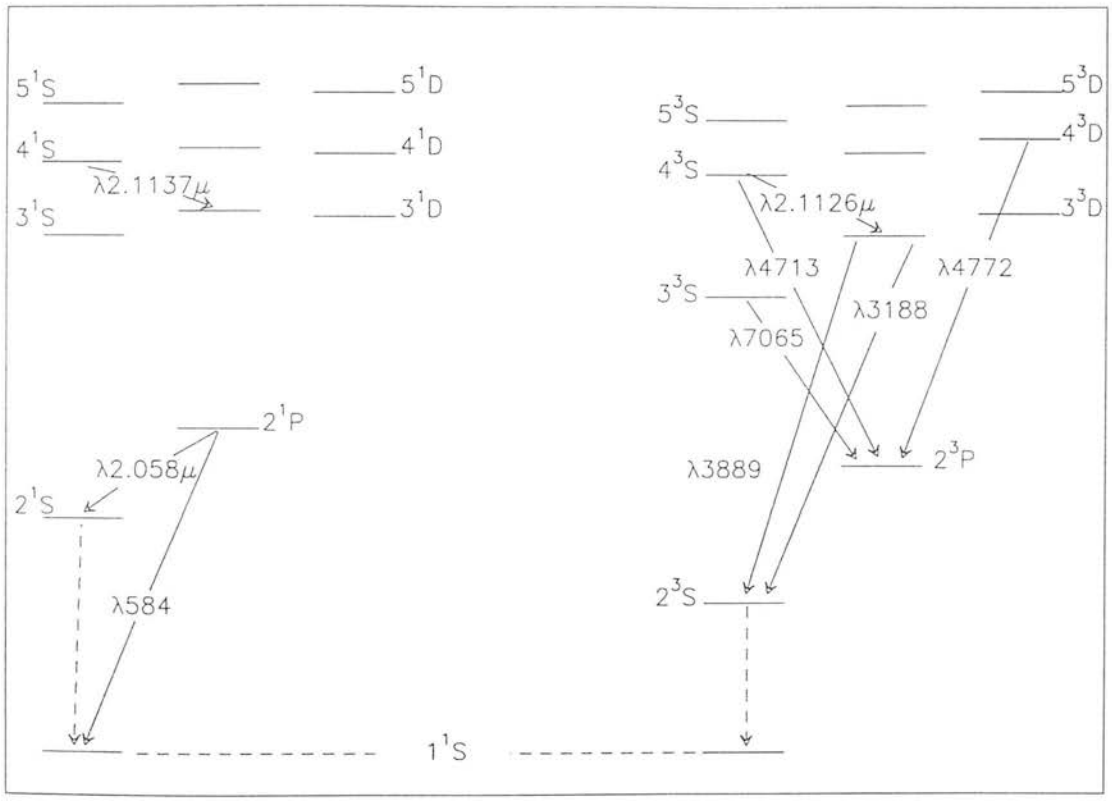

Figure 3.2: Partial energy-level diagram of HeI showing lines for which optical depth effects are investigated in this chapter, along with the reference 4472Å line.

1987) is:

$$N(2^3S)/N(He^+) = 5.79 \times 10^{-6} t_e^{-1.18}/(1 + 3110 t_e^{-0.51} n_e^{-1}) \quad (3.4)$$

Here t_e=$T_e/10^4$, α_{eff} is the effective recombination coefficient and k_{eff} is the effective collision rate inclusive of branching ratios. For the 4^3S–3^3P, 2.1126 μm line:

$$k_{eff} = (q_{2^3S,4^3P} \times br_{4^3P,4^3S} + q_{2^3S,4^3S}) \times br_{4^3S,3^3P} \quad (3.5)$$

where $br_{4^3P,4^3S}$, $br_{4^3S,3^3P}$ are the appropriate branching ratios. $q_{2^3S,4^3P}$,$q_{2^3S,4^3S}$ are the collisional excitation coefficients obtained from Berrington (private communication); the n=5 level was incorporated into the calculation of these rates. For n_e=10^4cm^{-3}, T_e=10,000K, $q_{2^3S,4^3P}$ = 2.175×10^{-12} and $q_{2^3S,4^3S}$ = 3.397×10^{-12} cm^{3}s^{-1}. Higher order terms could have been included but are likely to be several orders of magnitude smaller and therefore of negligible effect. The ratio of N(2^3S)/N(He^+) for n_e=10^4cm^{-3}, T_e=10,000K is 4.417×10^{-6}. Using branching ratios from Wiese, Smith & Glennon (1966), C/R= 6.16×10^{-3} and thus collisional effects from the 2^3S level are inconsequential for the 2.1126 μm line.

A similar calculation for the 4^1S–3^1P line at 2.1137 μm yields a even smaller value for C/R, of 2.05×10^{-3}. At T_e=5,000K these values are a factor of $\sim$ 50 smaller still. Therefore, collisional excitation from the 2^3S level is an unimportant excitation mechanism for the 2.113 μm blend under these physical conditions. For the 2^1P–2^1S, 2.058 μm transition, collisions from the 2^3S level to singlet levels n$\geq$3 can also enhance the 2.058 μm collision line strength. For the same density conditions, this further enhancement is marginal, $\sim$3% (T_e=10,000K) and 0.2% (T_e=5,000K).

The significance of collisions from the 2^1S level ~~are~~ is now examined. An equation of balance, analogous to eqn 3.4, for the 2^1S population, yields N(2^1S)/N(He^+)$\sim$ 10^{-11}, for n_e=10^4cm^{-3} and T_e=10,000K, a value much lower than for N(2^3S). Consequently the ratio of C/R for the three lines is of the order 10^{-7} and thus, collisional excitation from the 2^1S level to higher levels is negligible compared to radiative recombinations for these lines.

Since collisional excitation from the metastable 2^3S and 2^1S levels to levels $n \geq 3$ has a negligible effect on the $4^{1,3}S$–$3^{1,3}P$ 2.113 μm blend or the 2^1P–2^1S, 2.058 μm lines the values obtained from Smits (1991a,b) given in table 3.2 remain accurate.

3.3.2 Photo-ionization

Smits (1991a) does not include collisions from the metastable levels to $n \geq 3$ in his table 2 because the population in these levels may be affected by photoionization. At a density of $n_e = 10^4 cm^{-3}$, 72% of the depopulation of 2^3S atoms occurs by collisional excitation to singlets and 28% by the forbidden radiative transition 2^3S–1^1S. Photoionization of atoms in the 2^3S level may also be a significant depopulation process. The empirical formulae of Clegg and Harrington (1989) was used in section 2.5.2 to investigate this mechanism for the 2.058 μm line in the observed UCHII regions. Photo–ionization was expected to contribute to no more then 18% of the depopulation of 2^3S when compared to collisional transfer to singlets which reduces the 2.058 μm line strength by no more than ~4%. Similarly, the overall increase in recombining atoms due to additional ionizations was estimated to be negligible (section 2.5.2). Furthermore, these extra recombinations increase the populations of the HeI 4^3S, 4^1S and 2^1S levels by the same percentage, which cancels when the ratio of the HeI $4^{1,3}S$–$3^{1,3}P$ blend/HeI 2.058 μm line strengths are compared. Thus, photoionization effects do not significantly alter present theoretical line ratio calculations.

3.3.3 Radiative transfer effects in HeI

Optical depth effects in the Metastable levels

For a large population in 2^3S, absorption of line radiation by helium atoms in 2^3S must be considered (Pottasch 1962). A substantial 2^3S population will create a significant optical depth in many of the lines of the n^3P–2^3S series (Robbins 1968). For each absorption of an n^3P–2^3S photon there is an increased probability for decay by an alternative cascade route. The relative probabilities for each transition are given by the branching ratios.

Smits (1991a,b) has not included self absorption effects in his modelling, so by using the simple examination below the effect on the HeI triplet lines strengths is investigated. In particular, a large optical depth in the 2^3S–4^3P, 3188Å line, will result in enhancement of the 4^3S–3^3P line (see fig 3.2). The 4^3S–3^3P 2.1126μm line originates from the same upper level as the 4^3S–2^3P, 4713Å line for which self absorption effects have been evaluated by Robbins (1968) in table 3. Any self absorption in the 3188Å line will enhance the population in the 4^3P level and thus enhance the 4713Å and the 2.1126μm lines by the same percentage. Similarly, opacity in higher members of the series can also contribute, but this is included in Robbins (1968) calculations.

Fig 3.3 uses table 3 from Robbins (1968) and shows the increase in the line strength of the 4713Å line, relative to the 4472Å line, with optical depth in the 3889Å line which is the 2^3S–3^3P transition (solid lines). The optical depth in the line centre for zero expansion is given by:

$$\tau(\lambda 3889) = N(2^3S)\kappa(\lambda 3889)R \tag{3.6}$$

$\kappa(\lambda 3889)=5.8\times10^{-14}\mathrm{cm}^{-2}$ is the absorption cross-section for the λ3889 line and R is the radius for the He^+ region. The dotted curves depict the corresponding decrease in the 3188Å line. The 4472Å line arises from the 4^3D level and should only be slightly affected by self absorption affects (Osterbrock 1989). The different curves correspond to different expansion velocities for the nebula where $w=V_R/V_{TH}$. V_R is the maximum expansion velocity of the nebula and V_{TH} is the thermal velocity of the helium atoms. Higher expansion velocities decrease self absorption affects. This is discussed in detail below.

Robbins (1968) solves an integral equation of radiative transfer, to calculate modifications to various line strengths due to self absorption; namely the decrease in the 2^3S–n^3P series, where $n\geq3$, and the resultant increase in the n^3S and n^3D populations. Robbins assumes nebulae to be uniformly expanding spheres, of constant temperature, density and with a constant velocity gradient, V(r)=kr.

In his table 3, Robbins (1968) lists various line strengths at different optical depths for $\tau(\lambda 3889)$, for V_R/V_{TH}=0,3 & 5 and T_e=10,000K. Robbins (1968) uses a value of $n_e=10^4\mathrm{cm}^{-3}$ for the electron density in these calculations and claims variations with n_e

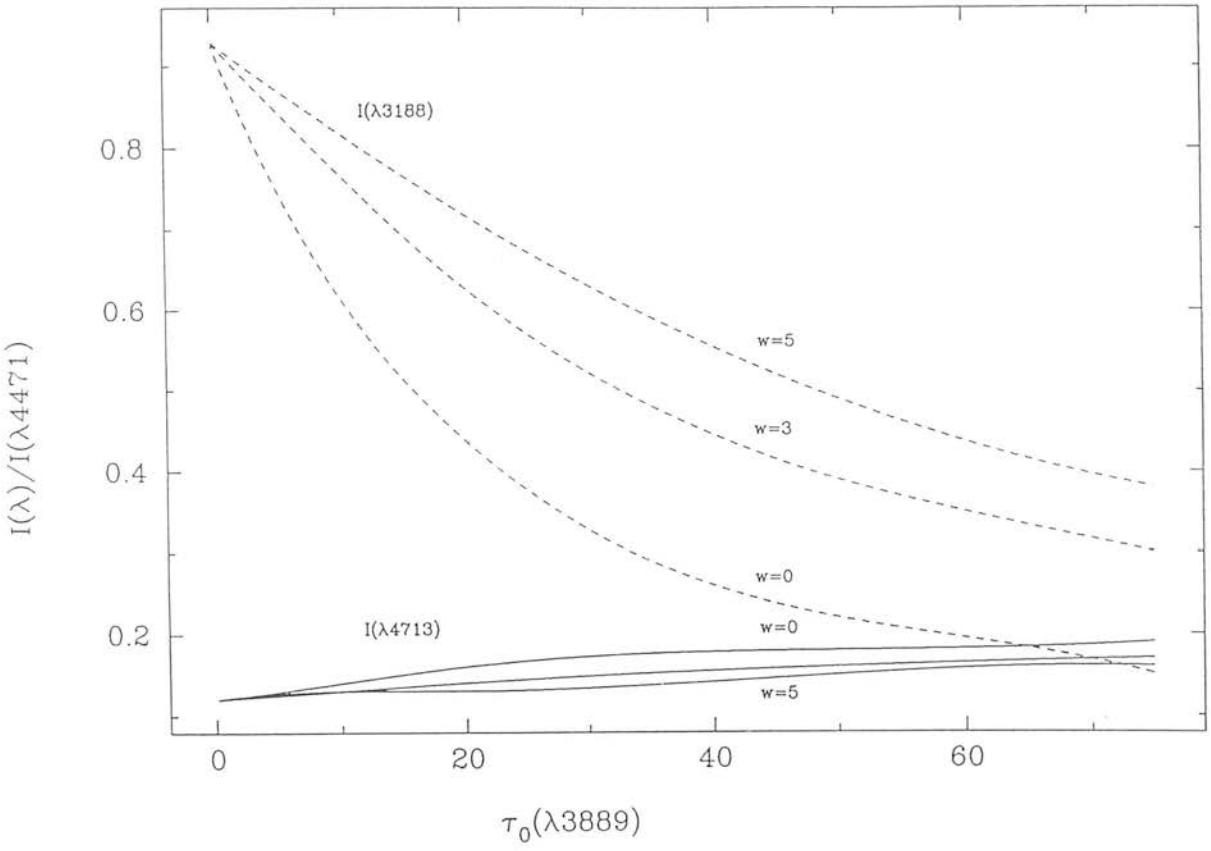

Figure 3.3: Radiative transfer effects due to finite optical depths in the 3889Å line. The decrease in the ratio of I(λ3188)/I(λ4472) and increase in the I (λ4713)/I(λ4472) ratio with $\tau_0(\lambda 3889)$ is shown with dotted and solid lines respectively. Static (w=0) and expanding (w$\neq$0) nebulae are depicted for T_e=10,000K.

are small. Comparison of table 4 (T_e=20,000K) and table 3 (T_e=10,000K), from Robbins (1968), show that the increase in the HeI line strength with $\tau(\lambda3889)$ is insensitive to T_e.

Three cases which represent different velocity motions of an HII region are examined:
case 1) A static nebula V_R/V_{TH}=0, with the helium atoms moving in thermal motion. The Doppler width for helium, $V_{TH}=(2kT/m)^{1/2}$=6.4kms^{-1} at T_e=10,000K.
case 2) An expanding nebula where V_R produces the observed RRL width, in which case

$$V_R \sim \sqrt{V_{RRL}^2 - V_{TH}^2}$$

For a given expansion velocity, photons emitted in a given line from the centre of the nebula will have a given rest frequency ν_L whilst further out in the nebula, assuming a constant velocity gradient, the motions of the atoms will redshift the absorption to $\nu_L^{'}$. Therefore, the optical depth in the He^+ zone will reflect the scale over which the velocity shifts the line sufficiently so as not to absorb itself. Robbins (1968) incorporates this process into his modelling. The greater the expansion velocity, the greater the wavelength shift between two photons emitted a given distance apart in the nebula and the less likelihood of a photon being reabsorbed further out in the nebula.
case 3) A nebula where turbulent motions are the dominant broadening mechanism for the $\lambda3889$ and $\lambda3188$ lines, and V_R=0. For this case, the lines are broadened from their thermal width, by turbulent motions to the observed radio recombination line (RRL) width for the UCHII regions, defined here as V_{Turb}. (Note that RRL widths are given as FWHM values; V used here is denotes Doppler widths where V=FWHM/1.665). Since the optical depth at the line centre τ is inversely proportional to the line width, $\tau(\lambda3889)$ must be scaled accordingly:

$$\tau(\lambda3889)_{Turb} = \tau(\lambda3889)_{TH} \times V_{TH}/V_{Turb}$$

Realistically, both expansion and turbulent motions are likely to co-exist and both will influence the line width.

For each case, using the appropriate value of V_R/V_{TH} and $\tau(\lambda3889)$ from eqn 3.6 allows the increase in the line strength for a given HeI line to be calculated from table

3 of Robbins (1968). For calculating $\tau(\lambda 3889)$ (eqn 3.6) the radius of the UCHII region can be derived from theory or observations. If a single star is responsible for the observed emission then a theoretical radius value R=R_s, the Strömgren radius of the H^+ zone, can be calculated (see section 1.1);

$$R_s = \left(\frac{3N_{Lyc}}{4\pi n_e n_h \alpha_B(H^0)} \right)^{1/3}$$

N_{Lyc} are the number of hydrogen ionizing photons and $\alpha_B(H^0)$ is the hydrogen (case B) recombination coefficient. For an assumed T_e, N_{Lyc} can be found from the integrated radio flux densities for the UCHII regions and the distance to the source, both of which are given by Wood and Churchwell (1989). Alternatively, N_{Lyc} can be found from the IRAS fluxes using the calibration of Puxley (1988), based on Kurucz model atmospheres (1979) and the mass, luminosity relations of Landolt–Börnstein (1982), to relate L_{IR} to N_{Lyc}. The relative size of the He^+ zone can be found from comparison of fig 2.2. However, studies by Lacy *et al.* (1982) and Hoare *et al.* (1991) surmise that a cluster of stars is responsible for the emission for their sample of compact HII regions. The observations, in chapter 2, are unable to discriminate whether a single star or a cluster serves to represent the nature of the emission.

This issue is circumvented by using the measured radii as calculated from the VLA radio maps of the UCHII regions by Wood and Churchwell (1989). Radii values at 15GHz are used; radii measured at 5GHz do not change $\tau(\lambda 3889)$ values significantly. For core-halo sources the radius is taken to be the mean of the minimum and maximium halo radii values. As the emission from UCHII regions is most probably dominated by compact regions at the centre of the source, it is expected that most of the flux as seen in the radio is contained within the $5''$ beam. Comparison of the VLA radio maps reveals that at least 90% of the radio flux will be encompassed in a $5''$ beam.

These radii and the calculated $\tau(\lambda 3889)$ values are given in table 3.3 for each UCHII region, for the three cases, a static nebula (V_{static}), an expanding nebula (V_{exp}) and a nebula with microturbulent motions (V_{turb}), outlined above. The resultant increase in the 4^3S–3^3P 2.1126μm line strength, and the enhancement factor $C_{\tau 2.113}$ in the HeI 2.113μm/Brγ ratio is given in cols 8–10 of table 3.3 for each object. This enhancement

ranged from 6–41%. The final theoretical ratios are given in cols 11–13 of table 3.3.

Collisions are not explicitly included in Robbins' (1968) models. The effects of this are twofold. First, collisions depopulate the 2^3S level, and hence $N(2^3S)$ and $\tau(\lambda 3889)$ must be calculated using eqn 3.4. Secondly, collisions also create a separate additional component to the HeI 2.113μm line flux, as was carried out in section 3.3.1.

The consequence of optical depth effects in the less metastable 2^1S level are now considered. As discussed in section 3.3.1, for the same electron temperature and density the population in the 2^1S level is a factor of 10^5 lower than that in $N(2^3S)$. For an HII region of radius R in pc, using the equivalent of eqn 3.6 yields an optical depth value of $\tau(\lambda 2.058\mu m)=0.14R$ for the 2^1S–2^1P transition. Measured radii for these UCHII regions, taken from Wood and Churchwell (1989), lie in the range R=0.003–0.2pc, thus $\tau(\lambda 2.058\mu m)$ the optical depth for photons from 2^1S–2^1P transitions, is less than 0.02 which is negligible here. The transition probability for 2^1S–3^1P (λ5016Å) transition is higher than for the 2^1S–2^1P transition but the absorption coefficient (see eqn 2.8) is lower. This gives a smaller line optical depth $\tau(\lambda 5016)\leq 0.014R$ for the same physical conditions. Transition probabilities and absorption coefficients, to even higher n^1P levels, become increasingly smaller with greater n. Optical depth effects in higher members of the 2^1S–n^1P series will therefore be insignificant and the 4^1S–3^1P, 2.1137μm transition and the corresponding line ratios will be unaffected by self absorption.

To reiterate, optical depth effects from the 2^3S to higher triplet levels are significant and must be included in calculation of the HeI 2.1126μm line strength. Other optical depth effects in the 2^1S level to higher singlet levels do not affect either the HeI 2.058 or 2.1137μm line strengths.

1^1S–2^1P HeI line broadening

In sections 2.5.1 and 2.6 optical depth effects in the 1^1S–2^1P line at 0.0584μm and the effect of HeI line broadening on the HeI 2.058μm coefficient at T_e=10,000K were examined. From eqn 2.8, the cross-section for a 0.0584μm photon to absorption by HeI is inversely proportional to the line width. From these studies a mean increase in the HeI

Object	diameter in "	radii in cm $\times 10^{17}$	RRL FWHM kms^{-1}	$\tau(\lambda 3889)$			$C_{\tau_{2.113}}$			HeIλ2.113 μm/Brγ			HeIλ2.113 μm/Brγ
				V_{static}	V_{exp}	V_{turb}	V_{static}	V_{exp}	V_{turb}	V_{static}	V_{exp}	V_{turb}	observed
G5.48	1.8	6.96	25±3	160	70	160	1.41	1.35	1.41	0.056	0.054	0.056	<0.081
G5.97	8.5	1.91	27±1	45	18	45	1.35	1.30	1.23	0.027	0.028	0.025	<0.029
G15.04	1.2	0.09	25±1	2	1	2	1.00	1.06	1.00	0.040	0.042	0.040	0.038±0.002
G29.96	7.0	4.51	30±1	106	38	106	1.41	1.35	1.35	0.056	0.054	0.054	0.058±0.002
G35.20	6.6	1.31	32±2	31	10	31	1.23	1.17	1.12	0.049	0.047	0.045	<0.079
G43.89	3.9	2.70	29±5	63	24	63	1.41	1.35	1.23	0.056	0.054	0.049	0.042±0.004
G45.12	5.9	2.78	38±4	65	18	65	1.41	1.30	1.23	0.056	0.054	0.049	0.057±0.006

Table 3.3: The HeI 2.113 μm/Brγ ratio in UCHII regions for T_e=10,000K.

line width from 6 kms^{-1} to $\sim$17 kms^{-1} due to *e.g.* turbulent motions was postulated to explain the observed mean HeI 2.058μm/Brγ ratio value of 0.84. Broadening of the HeI line width to 17 kms^{-1} (FWHM of 28 kms^{-1}), decreases the theoretical HeI 2.058μm line strength by a factor of 1.52, thus increases the HeI 2.113/HeI 2.058μm ratio by the same factor. Case 3) in section 3.3.3, assumes that microturbulent motions are responsible for the observed RRL line widths in the UCHII regions.

If these turbulent motions are assumed to be large over scales comparable with the mean free path length for a HeI 0.0584μm photon before reabsorption, then HeI line broadening must be incorporated into this calculation. In table 3.4, the correction factor, cols 2–4, and the corrected HeI 2.113/HeI 2.058μm line ratio, cols 5–7, are given for the three cases in section 3.3.3. Thus for case 3) turbulent motions affect the HeI 2.058μm line strength as well as the HeI 2.113μm line strength. Again, large scale motions and microturbulence may both contribute to the observed RRL line width.

To summarize the results in section 3.3.3, optical depth effects in the 2^3S level increase the HeI 2.113μm line strength and thus both the HeI 2.113/HeI 2.058μm and HeI 2.113μm/Brγ line ratios. Corrected theoretical ratios for each HII region are given in table 3.3 (cols 11–13) and 3.4 (cols 5–7). The correction factor $C_{\tau 2.113}$ (table 3.3) and $C_{\tau 2.113+2.058}$ (table 3.4) and the corresponding ratios for a static nebula (case 1) are greater than for an expanding nebula (case 2), since the absorption is redshifted further as the HII region expands, (see fig 3.3). For case 3) an HII region with microturbulent line broadening of HeI atoms decreases the optical depth in the line centre and the correction factor for the HeI 2.113μm line strength and the HeI 2.113μm/Brγ is less than for case 1). For the HeI 2.113/HeI 2.058μm line ratio this broadening also decreases the HeI 2.058μm line strength and therefore increases the HeI 2.113/HeI 2.058μm line ratio. Optical depth effects in the 2^1S level, collisional excitation from n=2 to n>3 and photoionization processes were found to be inconsequential for these calculations.

Object	$C_{\tau_{2.113+2.058}}$			HeIλ2.113/λ2.058 models			HeIλ2.113/λ2.058 observed
	V_{static}	V_{exp}	V_{turb}	V_{static}	V_{exp}	V_{turb}	
G5.48	1.41	1.35	2.14	0.045	0.043	0.068	<0.095
G5.97	1.35	1.30	1.87	0.043	0.042	0.060	<0.045
G15.04	1.00	1.06	1.52	0.032	0.034	0.049	0.045±0.003
G29.96	1.41	1.35	2.06	0.045	0.043	0.061	0.060±0.002
G35.20	1.23	1.17	1.70	0.039	0.037	0.054	<0.107
G43.89	1.41	1.35	1.87	0.045	0.043	0.060	0.053±0.005
G45.12	1.41	1.35	1.87	0.045	0.043	0.060	0.064±0.006

Table 3.4: The HeI 2.113/HeI 2.058 μm ratio in UCHII regions for T_e=10,000K.

3.4 Comparison with Observations

3.4.1 The HeI 2.113 μm/Brγ ratio

The observed HeI 2.113μm/Brγ ratios in each UCHII region are plotted against the predicted model ratios for T_e=10,000K and T_e=5,000K in fig 3.1. The spectral types inferred for the UCHII regions from radio flux densities (closed circles), IRAS fluxes (open circles) and the ratio of L_{IR}/ N_{Lyc} (triangles) are discussed in section 2.6 and given in table 2.6. The latter (lower limit) estimate is independent of the ionization structure of the source and thus may represent either a cluster or a single star, whilst the other two estimates assume a single star powers the HII region.

The solid curves labelled a) are the non-dusty models which are virtually the same for any of the electron densities specified in section 2.5.1. Addition of dust has marginal effect on the low density $n_e=10^2 cm^{-3}$ models; the dashed curves b) shows the effect of dust for a high density $n_e=10^4 cm^{-3}$ model. As discussed in section 3.3, and evident in fig 3.1 the maximum value of this ratio is reached for a cooler effective temperature T_{eff}=35,000K.

At low density $n_e=10^2 cm^{-3}$, the optical depth in the 3889 line, $\tau(\lambda 3889)$, is small and optical depth effects negligible. In fig 3.1 the dot-dash curves c) include optical depth effects in the HeI 4^3S–3^3P 2.1126μm line for a dusty $n_e=10^4 cm^{-3}$ model. For this electron density, these curves represent the maximum increase in the HeI 2.1126μm line strength given in table 3.3 of 1.58 which corresponds to an increase of 1.41 in the HeI 2.113μm blend, and consequently in the HeI 2.113μm/Brγ ratio.

The scatter amongst the observed HeI 2.113μm/Brγ ratios is large and generally in both plots the observed values are higher than the predicted values for the objects, if optical depth effects are not included in the modelling. Inclusion of optical depth effects brings the observed ratios and predicted ratios to a much better agreement. As the higher electron temperature is found to be more representative of the sample of UCHII regions the observations are compared to individual models for the one electron temperature in table 3.3 and the implications for lower electron temperatures are discussed more

generally.

For every UCHII region, the theoretical HeI 2.113μm/Brγ ratio corrected for optical depth effects at T_e=10,000K is given in table 3.3 for 1) a static nebula where the atoms are moving with thermal velocities, 2) an expanding nebula and 3) a nebula with turbulent motions. The observed HeI 2.113μm/Brγ ratios are given in the last column of table 3.3 for comparison.

For all objects except G5.97, the observed HeI 2.113μm/Brγ ratios are consistent with effective temperatures greater than 35,000K (for both electron temperatures except G43.89 which is discussed in detail below), predicted from n_e=10^4cm^{-3} dusty models. Effective temperatures greater than 35,000K or an O8 star are also in agreement with spectral type estimates listed in table 2.6. This corroborates the assumptions in chapter 2, that effective temperatures $T_{eff} \geq$35,000K are more likely. This data also rule out lower densities of n_e=10^2cm^{-3} for these models. Hence, the general picture that these UCHII regions have electron densities $\sim 10^4$cm^{-3}, electron temperatures in the range 5,000–10,000K and a dust-to-gas mass ratio of 10^{-2} as found in the ISM is correct here. For all UCHII regions, the dusty n_e=10^4cm^{-3} model was taken as most representative and except for G5.97, it was assumed these objects lay on the saturated part of the curve; here the value of the HeI 2.113μm/Brγ ratio is 0.04. The correction factor $C_{\tau 2.113}$ calculated in table 3.3 was applied to this inrinsic value expected for the UCHII regions (except for G5.97) to correct for optical depth effects.

For G5.97, comparison of spectral type estimates in table 2.6 reveal the maximum T_{eff} for this object to be 35,000K. In addition, the observed HeI 2.058μm/Brγ ratio (0.68) and HeI 2.113/Brγ ratio (0.29) are consistently lower than for other objects, which supports a lower T_{eff} in this object. The spectral type range for G5.97 also rules out the low density n_e=10^2cm^{-3} model (see fig 3.1). An initial ratio of 0.02 was assumed for G5.97, (mean value from dusty and non dusty model at T_e=10,000K, for an O8 star), *c.f.* table 2.6, before corrections for optical depth effects, $C_{\tau 2.113}$, were applied.

For the three cases outlined in section 3.3.3, the observed and corrected ratios are consistent to within 2σ except G43.89. G43.89 falls within the errors (1.8σ) for a turbulent HII region model (case 3) only. However, from fig 3.1, G43.89 fits a HII region

model for T_e=5,000K rather well. $\tau(\lambda 3889)$ at T_e=5,000K is approximately three times its value at T_e=10,000K and the HeI 2.113μm/Brγ line ratio becomes 0.038, 0.035 and 0.038 for HII region cases 1), 2) and 3) respectively discussed in section 3.3.3. All these three representations fit the observed ratio for G43.89 within 2σ errors. Wink *et al.* (1982) derive an electron temperature of 5900±1000 for H76α for G43.89 in good agreement with these theoretical predictions. Therefore, these observations are consistent with electron temperatures nearer T_e=10,000K, bar G43.89 which falls nearer the lower end of the temperature range for these objects (table 3.1).

From this analysis, the importance of the inclusion of optical depth effects in the models is illustrated. Consequently, one overall HII region model cannot explain all the observations since local effects need to be evaluated. Modelling each UCHII region separately, demonstrates that good agreement between the predicted and observed HeI 2.113μm/Brγ ratios can be found. However, from this ratio alone the velocity structure in each UCHII region cannot be deciphered or the validity of an assumed density of $n_e=10^4 cm^{-3}$ tested.

3.4.2 The HeI 2.113/HeI 2.058 μm ratio

Theoretical HeI 2.113/HeI 2.058μm ratio values are given in section 3.3. From this line ratio, density and velocity structure predictions of HII region models a) in which $n_e=10^4 cm^{-3}$, T_e=5,000K and velocity motions are purely thermal and model b) for $n_e=10^4 cm^{-3}$, T_e=10,000K and microturbulence in the nebula may be examined (see section 2.6). Only for the lower density $n_e=10^2 cm^{-3}$ is there a significant difference between the HeI 2.113/HeI 2.058μm values for the two electron temperatures T_e=10,000K and 5,000K. Since $n_e=10^4 cm^{-3}$ is most representative of the measured electron densities for these objects (section 3.3), this electron density is assumed appropriate for these present studies to avoid confusion. Thus, for this electron density both electron temperatures produce the same theoretical results and the one electron temperature T_e=10,000K is used hereafter, which more closely reproduces the observed HeI 2.113μm/Brγ ratio values.

Theoretical HeI 2.113/HeI 2.058μm ratios, corrected for optical depth effects in the

HeI 2.1126μm line, are given for individual UCHII regions in table 3.4 (cols 5–7) for n_e=10^4cm^{-3} and the same three sets of physical conditions outlined in section 3.3.3. The observed HeI 2.113/HeI 2.058μm ratios are also given in table 3.4 (col 8) for comparison.

For case 1) a static nebula at n_e=10^4cm^{-3} and case 2) an expanding nebula most theoretical ratios remain considerably less than observed values; G5.48, G5.97 (upper limits), and G43.89 fit either a static nebula model or an expansion model to within 2σ. Although the values for case 1) are larger than than for case 2) the difference is not greater than 0.003, a value $\leq 1\sigma$ errors on the observed ratios, and thus it is not possible to establish a preferred model. Hence, for a nebula expanding with a velocity V_R/V_{TH} $\leq$ 5, the models for a static nebula will remain accurate, since observational errors in the line ratio of 0.03 or $\sim$ 10% are to be expected. Since the observed FWHM RRL measurements are not greater than 50 kms^{-1} (Downes *et al.* 1980) this approximation is assumed to be valid for all HII regions.

For case 3), microturbulence within an HII region, broadening of the HeI 0.0584μm line width to the observed RRL width is also taken into account. A standard broadened maximum HeI line Doppler width of 17 kms^{-1} is assumed, and justified in section 2.6, and a corresponding correction factor of 1.52 incorporated into the correction factor $C_{\tau 2.113+2.058}$ for V_{Turb} given in table 3.4 (col 4). The corrected predicted HeI 2.113/HeI 2.058μm ratios are given in table 3.4 (col 7). For this case, all corrected theoretical UCHII regions at n_e=10^4cm^{-3} are consistent with observations to within 2σ except G5.97. Therefore, for an electron density of n_e=10^4cm^{-3} the models suggest some microturbulence for all UCHII regions excluding G5.97. The three most simplistic cases have been considered, however it is quite plausible that large scale systematic motions are occurring in an HII region with microturbulence. The difference between values for case 2) and 3)(table 3.3) are less than the 1σ error bars associated with the observed ratio for that object. Therefore, again as a first approximation a model incorporating microturbulent and large scale coherent motions can be represented by a model with purely microturbulent motions.

A synopsis of the comparison of observed and proposed theoretical models for each UCHII region in turn is given below.

G5.48 has an upper limit HeI 2.113μm/Brγ ratio consistent with either electron temperature within the errors, likewise the HeI 2.058μm/Brγ ratio. The HeI 2.113/HeI 2.058μm (upper limit) ratio is consistent with cases 1), 2) or 3) a static, expanding or microturbulent nebula.

G5.97 has a lower range of possible stellar effective temperatures, 28-34,000K and fits the $n_e=10^4 cm^{-3}$ dusty models of chapter 2 exclusive of HeI line broadening for both electron temperatures. The HeI 2.113/HeI 2.058μm ratio disagrees with a microturbulent model. Therefore, turbulent motions are not apparent in this UCHII region.

The HeI 2.113μm blend measurement is also an upper limit for G35.20. Consequently, the observations of the three lines can be matched by either electron temperature and all the velocity structures proposed in section 3.3.3.

The HeI 2.113μm/Brγ line ratio for G43.89 at T_e=10,000K is only consistent (1.8σ) with the turbulent model. Fig 3.1 shows the observed HeI 2.113μm/Brγ ratio value is in good agreement with all three cases at T_e=5,000K. The HeI 2.058μm/Brγ ratio for lower electron temperatures does not require substantial turbulent motions. The HeI 2.113/HeI 2.058μm line ratio for G43.89 is consistent with all three cases at T_e=10,000K.

For the remaining UCHII regions G15.04, G29.96 and G45.12 the HeI 2.113/HeI 2.058μm observed line ratios are only consistent with a microturbulent model, and the HeI 2.113μm/Brγ ratios only consistent with a high electron temperature model, T_e ~10,000K. For this temperature, the HeI 2.058μm/Brγ ratio requires microturbulence motions producing line broadening of order 15–20 kms^{-1}. From table 3.1, RRL measurements imply electron temperatures nearer T_e=10,000K for G15.04 and G45.12, in good agreement with these results. From table 3.1, G29.96 has a lower electron temperature T_e=6100±3000K, the upper limit to this T_e value is inferred for consistency with the above results.

For completeness, this analysis could be repeated for the lower density model $n_e=10^2 cm^{-3}$ although such a low density is considered to be inappropriate in UCHII regions. However, a density gradient is possibly representative and would result in a lower integrated

electron density, and consequently a smaller HeI 2.058μm/Brγ ratio. In section 2.6 an integrated electron density value of $\sim 10^3$ cm^{-3} was calculated to be consistent with the observations, without the inclusion of local motions. Both mechanisms are conceivably present in HII regions. Density gradients are discussed in chapter 5.

To summarize these findings, analysis of the HeI 2.113μm/Brγ ratio shows that optical depth effects in 2^3S–n^{3}P transition are important, affecting the observed line fluxes. This ratio is independent of n_e and therefore less complicated to model than either the HeI 2.058μm/Brγ or the HeI 2.113/HeI 2.058μm line ratios. The HeI 2.113/HeI 2.058μm ratio must be modified to account for optical depth effects and HeI line broadening if appropriate. Available RRL widths give the amount of HeI line broadening expected.

Therefore, for G5.48, G35.20 and G43.89 both models a) and b) (section 2.6) are plausible for these objects and thus any model with an electron temperature in the range T_e=5,000K–10,000K and the corresponding amount of HeI line broadening up to $\sim$20 kms^{-1} for n_e=10^{4}cm^{-3}, is also appropriate for these UCHII regions. Whereas for G15.04, G29.96 and G45.12 the observations are only consistent with model b) requiring a higher electron temperature and sizeable microturbulent motions, 15–20 kms^{-1}. Fig 3.1 shows that the observations of G5.97 are only consistent with dusty UCHII region models. If the stellar effective temperatures obtained from radio fluxes presupposing a single star or a cluster are deemed most realistic then all UCHII regions, bar G29.96 and G45.12, require a dusty UCHII region model. For G29.96 and G45.12 either a dusty or non-dusty model is consistent.

3.5 Conclusions

The HeI $4^{1,3}$S–$3^{1,3}$P blend at 2.113μm has been observed in several UCHII regions. For those objects in which the blend was not observed upper limits have been estimated. For the same objects studies of the HeI 2.058μm/Brγ ratios yield two possible models to be consistent with the observations. Basically, for a higher electron temperature, a greater HeI line width attributable to microturbulent motions of up to $\sim$15–20 kms^{-1} at

T_e=10,000K, is required to be consistent with the observations. The aim of this chapter was to test the physical mechanisms proposed in these models, specifically velocity motions, collisional excitation and radiative transfer processes.

The emphasis in this chapter is that the two models a) and b) described in chapter 2 should be considered extremes and that individual UCHII regions observed fall between the two models.

The theoretical HeI 2.113μm/Brγ and HeI 2.113/HeI 2.058μm ratios were constructed for the same physical conditions as for model a) and b). For calculating theoretical values for the HeI 2.113μm line strength values from Smits (1991a) were used. Further physical processes, the result of the metastability of the HeI n=2 levels, were investigated, namely, collisional excitation from the HeI 2^3S level to n$\geq$3, photoionization from 2^3S, and optical depth effects in the 2^1S–n^{1}P, and 2^3S–n^{3}P transitions for n$\geq$3. Only the latter process was found to affect the HeI 2.113μm line strength. Since optical depth is dependent on the source size, each UCHII region was modelled individually for n_e=10^4cm^{-3} and T_e=10,000K and a general model was formulated for n_e=10^4cm^{-3} and T_e=5,000K. Additionally, three velocity structure cases were examined, 1) a static nebula, 2) a nebula with large scale expansion and 3) a nebula with microturbulence. The differences between cases 1) and 2) were within observational errors for each UCHII region. For case 3) the HeI 2.058μm line strength also needs to be modified for line broadening as the result of turbulent motions.

Theoretical models in the temperature range T_e=5,000K–10,000K could be constructed for all UCHII regions which gave good agreement with the observations of the three line ratios. From comparison with observed line ratios it was found models within this temperature range with appropriate microturbulent velocities (of 15–20 kms^{-1}) are plausible for the UCHII regions G5.48, G35.20 and G43.89. Both electron temperatures T_e=10,000K and T_e=5,000K are consistent with the observations of G5.97, however microturbulence is inconsistent. The remaining UCHII regions G15.04, G29.96 and G45.12 were found only to be consistent with an higher electron temperature and microturbulent velocities, in the order of 15–20 kms^{-1}, which are generally in good agreement with the observed RRL measurements for these UCHII regions, (*c.f.* model b). Therefore, evi-

dence for microturbulent motions of $\sim$20 kms^{-1} in almost half of this sample of objects, which explains the observed RRL measurements for these UCHII regions is concluded. For the other UCHII regions, G5.48, G35.20 and G43.89 either microturbulent motions in the UCHII region or a large scale expansion velocity over the region, both in the order of 20 kms^{-1}, can account for the observed RRL line widths.

Additionally, an electron density of n_e $\sim 10^4 cm^{-3}$ is found to be in good agreement with all these observations. Dusty models are required for G5.97 and are preferred if radio or cluster stellar temperatures are assumed for the rest of the UCHII regions.

Chapter 4

The HeI 2.058 μm/Brγ ratio in Compact HII regions

4.1 Introduction

A picture of an UCHII region powered by hot O or B stars expanding to lower densities into a molecular cloud is described in section 1.1. In chapters 2 and 3, the HeI 2.058, HeI 2.113 and Brγ line ratios and physical properties in UCHII regions have been examined. The aim of this chapter is to focus on compact HII regions described in section 1.1, in which densities are lower so that the HeI 2.058 μm line will not be dominated by collisional excitation effects. Thus, the less complex low density HII region models of the HeI/HI line ratios *vs.* T_{eff} can be tested. The only setback is that the geometry in these slightly more evolved HII regions (class II, table 1.1) might be more complicated, thus any approximations relating to the geometry of these sources is less reliable.

The HII regions studied in this chapter were selected from a catalogue of small diameter radio sources in the Galactic plane, by Zoonermatkerani *et al.* (1990). This survey of the galactic plane was carried out at 1.4GHz using the VLA. The survey was able to detect radio sources brighter than 25mJy and less than $20\widehat{''}$ in diameter although some larger and fainter sources were observed. From this survey the candidates were selected to satisfy the following criteria :

1) The sources have integrated 1.4GHz flux densities greater than 150 mJy, so that they are easily detectable in the infrared.
2) The object size (Zoonermatkerani *et al.* 1990) was greater than $7^{\widehat{\prime\prime}}$ and preferably $10^{\widehat{\prime\prime}}$, in order that our sample subset comprised compact and diffuse HII regions with lower densities than in our previous studies.

In section 4.2, the observations and data reduction procedures are discussed in detail. In section 4.3, corrections to observations are dealt with, including a detailed method for calculating the extinction. In section 4.4, new and previous HII region models are compared and in section 4.5, the observed HeI 2.058μm/Brγ ratios are compared with theoretical values and a discussion of the spectral types in HII regions is presented.

4.2 Observations

The objects observed are given in table 4.1 with their coordinates which are the Zoonermatkerani *et al.* (1990) radio positions. Spectra were obtained with UKT9, a single channel photometer/spectrometer. All these objects were firstly imaged using IRCAM on UKIRT to obtain clear sky offset positions so as to avoid chopping onto a nearby emission line source which is highly probable within such crowded fields.

4.2.1 UKT9

Observations were made at UKIRT on May 31, 1991 and Oct 17, 1991, and subsequent service observations were obtained on Aug 19, 1992 with UKT9, using the CVF, circular variable filter, which operates in the wavelength range 1.3–2.6μm. The resolving power with the CVF is $\sim$120. Since the radio sizes of these sources, as determined from Zoonermatkerani *et al.* (1990), were in the range 8–$18^{\widehat{\prime\prime}}$, a $19.6^{\widehat{\prime\prime}}$ aperture, the largest with UKT9, was employed to ensure that all the flux from the object was contained within the beam. A number of scans were taken ($\sim$ 8 on object), in the wavelength range 2.00-2.22μm, with 1/2 sampling which gives a wavelength step size of 0.0077μm. The exposure time per scan on each object was 20s. Each CVF scan was completed in

the main beam before nodding to the offset sky position determined from imaging the nearby sky described below in section 4.2.2.

Wavelength Calibration

The wavelength scale was calibrated by comparison of the central wavelength of an observed Brγ line with the expected wavelength, given by the rest wavelength for Brγ plus the wavelength shift due to the radial velocity, for a given object. The planetary nebula IC 5117 was observed specifically for this purpose. For the service observations wavelength calibrators were not observed. To calibrate the spectra of the HII regions observed, radio recombination line velocities listed for several of those objects by Downes *et al.* (1980) were used. A mean correction, derived from these HII regions with known radial velocities, was applied. This wavelength shift was no more $\sim 10^{-3}\,\mu$m.

Flux Calibration

The standard techniques for flux calibration and correction for atomspheric absorption and instrumental response described in 2.2.1 were applied. A "flux" standard – a bright star of known K magnitude– was observed at the beginning and end of the night and "spectral" standards of similar airmasses to those of the target HII regions were observed between HII region observations. The flux standard provides a raw calibration from counts/sec to $\mathrm{Wm}^{-2}\,\mu\mathrm{m}^{-1}$ for both the spectral standards and the object spectra, whilst the spectral standard is observed in order to remove instrumental response and atmospheric absorption effects from the HII region spectra. All standards and their magnitudes are given in table 4.2.

Comparison of counts/sec at K between flux standard and spectral standard yields a calibrated spectrum according to the following equations:

$$m_{flux} - m_{std} = -2.5\log\frac{C_{flux}}{C_{std}} \tag{4.1}$$

where C_{flux} and C_{std} are the average values of the counts around 2.2μm in each spectrum. m_{flux} is the K magnitude of the flux standard and m_{std} the required spectral

Object	Equatorial Coordinates α(1950)	δ(1950)
G9.617+0.196	18 03 15.29	-20 32 04.9
G10.965+0.009	18 06 45.83	-19 27 04.8
G18.304-0.390	18 22 52.95	-13 12 02.6
G37.874-0.399	18 59 24.43	04 08 31.1
G45.454+0.060	19 11 59.88	11 03 57.8
G49.491-0.369	19 21 22.24	14 25 16.2
G57.548-0.272	19 37 29.78	21 30 33.9
G76.188+0.098	20 22 03.00	37 28 24.5
G77.965-0.007	20 27 46.23	38 51 14.0
G105.627+0.339	22 30 52.62	58 12 51.2

Table 4.1: Object list.

Standard	Equatorial Coordinates α(2000)	δ(2000)	K mag	Spectral Type
BS 6616	17 47 33.5	-27 49 51	2.57	F7II
BS 6715	18 01 23.0	-17 09 25		K3III
BS 7208	19 02 27.5	08 22 27		K2III
BS 7648	20 00 58.8	08 33 29		K5III
BS 7314	19 16 22.0	38 08 01	1.66	KOIII
BS 8633	22 40 18.3	53 50 46		KOIII
BS 8541	22 24 30.9	49 28 35	4.25	B9I
HD 203586[1]	21 21 37.1	39 48 12	6.86	A0
HD 161903[1]	17 45 43.3	-01 47 34	7.02	A2

[1] IRCAM standards (B1950 Coordinates).

Table 4.2: Standard Star list.

standard K magnitude for calibration purposes. Then flux calibration can be performed by use of the conversion derived for a 0th magnitude star by Mountain *et al.* (1985):

$$F_\lambda(Wm^{-2}\,\mu m^{-1}) = 4.13 \times 10^{-10} \times 10^{-0.4m_K} \qquad (4.2)$$

To ascertain the consistency of this calibration method, the K magnitude of each spectral standard derived from eqn 4.1 was compared with the K magnitude value inferred from the spectral type and V magnitude, of the spectral standard, as taken from the Bright Star Catalogue making use of the conversion tables of V-K colours from Koorneef (1983). Fig 4.1 shows a linear curve for calibration of log counts/sec at 2.2 μm *vs* broad band K magnitude (Puxley 1988) based on data taken with UKT9 in 1986 and 1987. The solid line is the best straight line fit to his observations; all his data points lie on this line within $\pm$ 10% uncertainties. Although these are broad band K magnitudes, provided there are no obvious absorption or emission features in the stellar spectra, the narrow band K measurements should be comparable. For all the standards observed with UKT9, the counts/sec with 10% uncertainty errors are plotted against their quoted K magnitude for the flux standards, and that obtained from the V magnitude and V-K colours for the spectral standards, in fig 4.1.

For the UKT9 service observations taken in Aug 1992, only a flux standard was observed for calibration of the compact HII region data and for the observations taken in Oct 1991, the derived K magnitudes from both methods described above agreed to within 5%, for the one spectral standard BS 8633 observed. However, the K magnitudes inferred from the V-K colours, of the spectral standards observed in May 1991 differed significantly from the K magnitudes derived from eqn 4.1. This can be explained only if either the observing conditions were not photometric on that night, or, if the V magnitudes or stellar temperatures for these standards, or the calibration tables by Koorneef (1983) are inaccurate. Observations of the same spectral standard taken two hours apart in the first half of the night yield the same counts/sec values after airmass correction, thus observing conditions appear to have been fairly stable on that night. Returning to fig 4.1, for the data taken in May 1991 the K magnitude of flux standard BS6616 (m_K=2.57) agreed with the predicted K magnitude from the counts/sec measured. Whilst the K magnitudes for two of the spectral standards also agreed with the expected K magni-

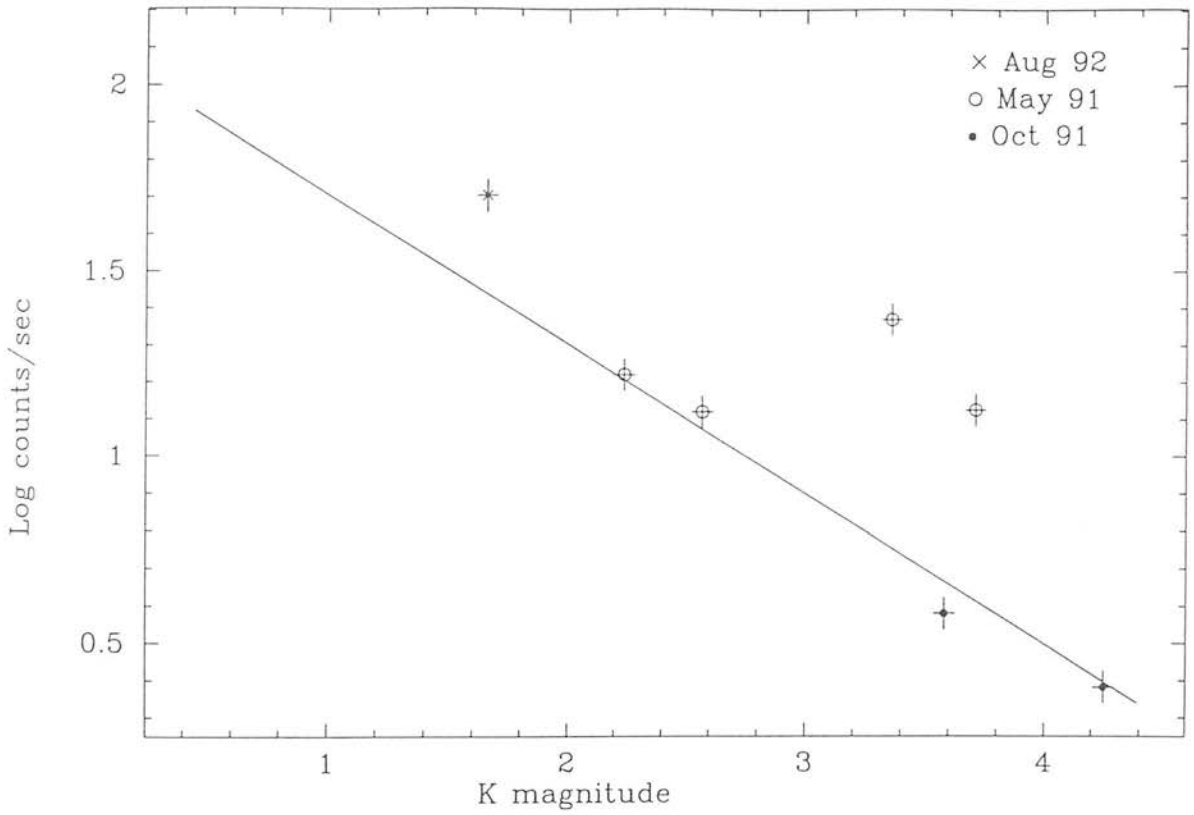

Figure 4.1: Counts/sec *vs.* broad-band K magnitude. The straight line is a best fit to observations taken with UKT9 by Puxley (1988). The data from this chapter is plotted with 1σ errors.

tude, two of the spectral standards have K magnitudes inferred from V-K colours, that suggest considerably more signal at 2.2 μm than was measured, suggesting errors on this calibration method. Therefore, the flux standard BS6616 was used to infer a K magnitude and thus calibrate the spectral standards and HII regions observed on that night. For consistency, this method of calibration was employed for the other two nights also.

In section 4.2.2 an independent data set of the same compact HII regions is flux calibrated, enabling a further check on the consistency of the flux calibration used here. Fortunately line ratios are the primary concern and flux calibration is not of paramount importance. However such discrepancies in calibration suggest these flux values cannot be considered greatly accurate. Brγ fluxes are used to obtain extinction estimates in section 4.3. Again, fortunately it is the differential extinction correction factor C_k that is important, and even if the extinction at $\tau_{Br\gamma}$ is only accurate to 50% the error on C_k is not greater than 10%.

Line fitting

The major advantage with UKT9 is the availability of the large aperture of $19.6\widehat{''}$. However the spectral resolution is low compared with other instruments, such as CGS4. Since the resolving power of UKT9 corresponds to a velocity of $\sim$ 2500 kms^{-1} at 2.2 μm, then the line profile will be purely a reflection of the instrumental profile since the observed HeI and HI line widths are no greater than 50 kms^{-1} (Downes *et al.* 1980, Wink *et al.* 1982). The instrumental line profile is accurately represented by a Gaussian with FWHM of 0.018 μm at 2.165 μm. Thus, the raw HeI 2.058 μm and Brγ line flux ratios and their 1σ error bars were obtained, by fitting the data with this profile, and are given in table 4.6. Table 4.3 gives the Brγ fluxes. The spectra are shown in figs 4.2a–j.

4.2.2 IRCAM

Since HII regions by their very nature occur in crowded fields, when moving the telescope to a sky position it is important to ensure that we are not chopping onto an emission source. Images had been obtained in a previous observing run and accurate sky positions

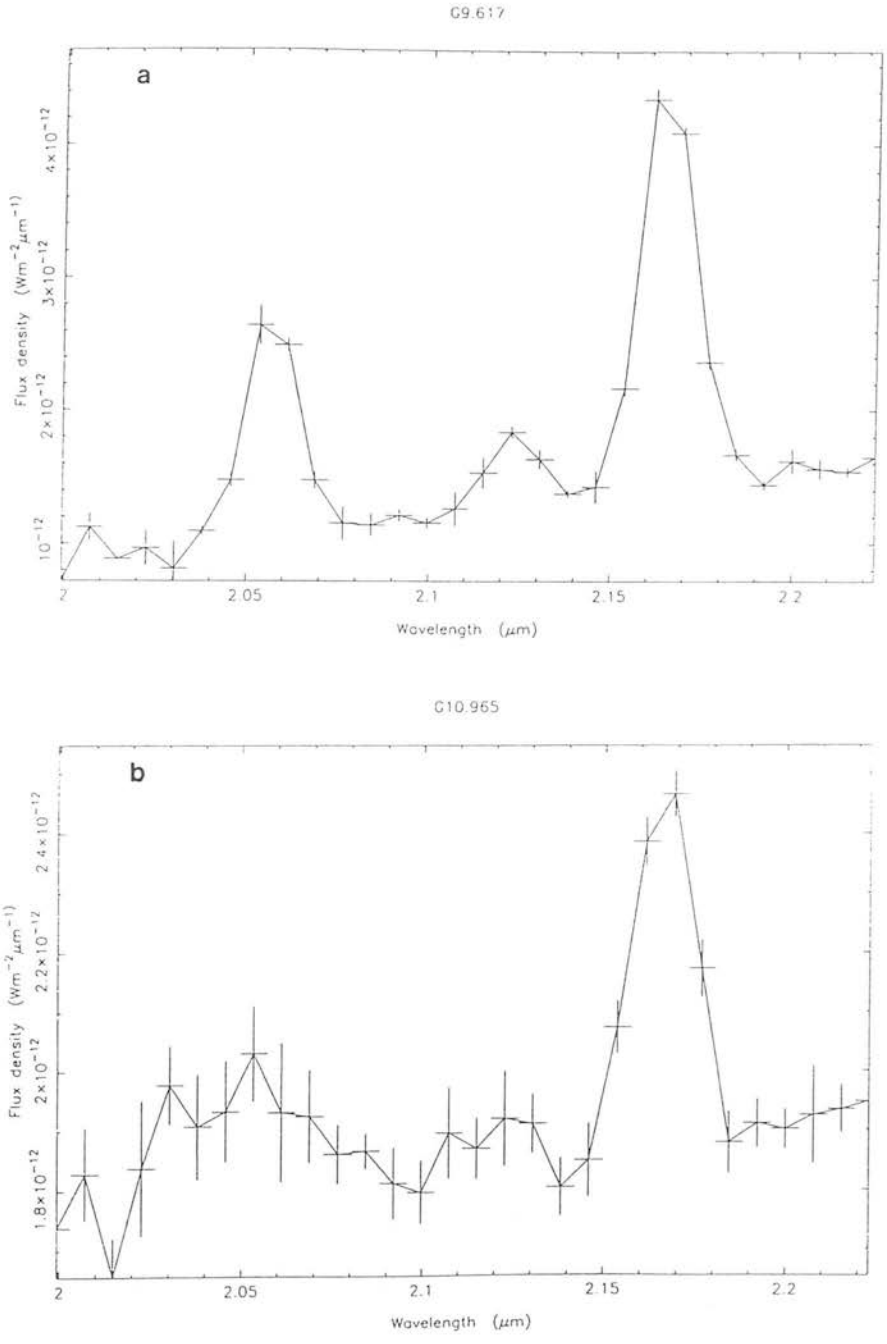

Figure 4.2: K-band spectra of 10 compact HII regions taken with UKT9.

G18.304

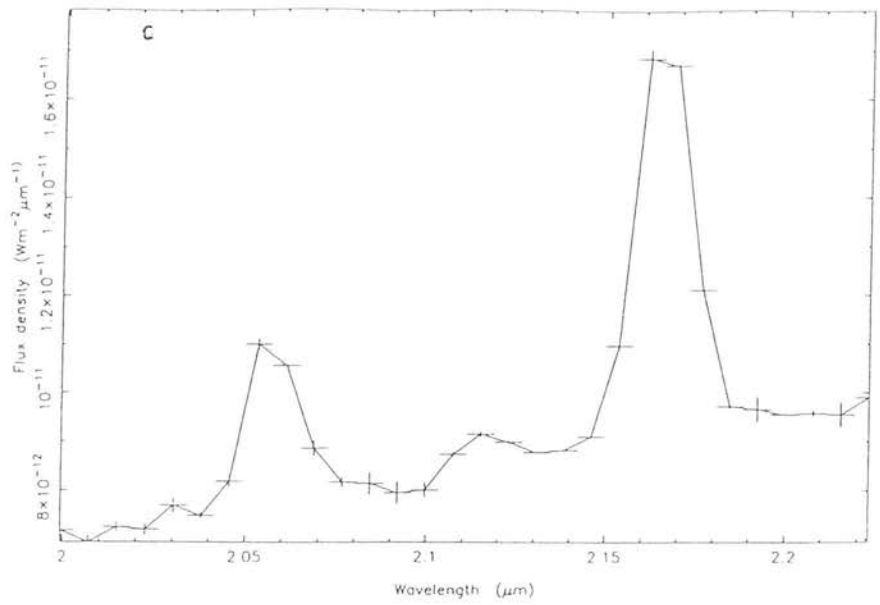

G37.874

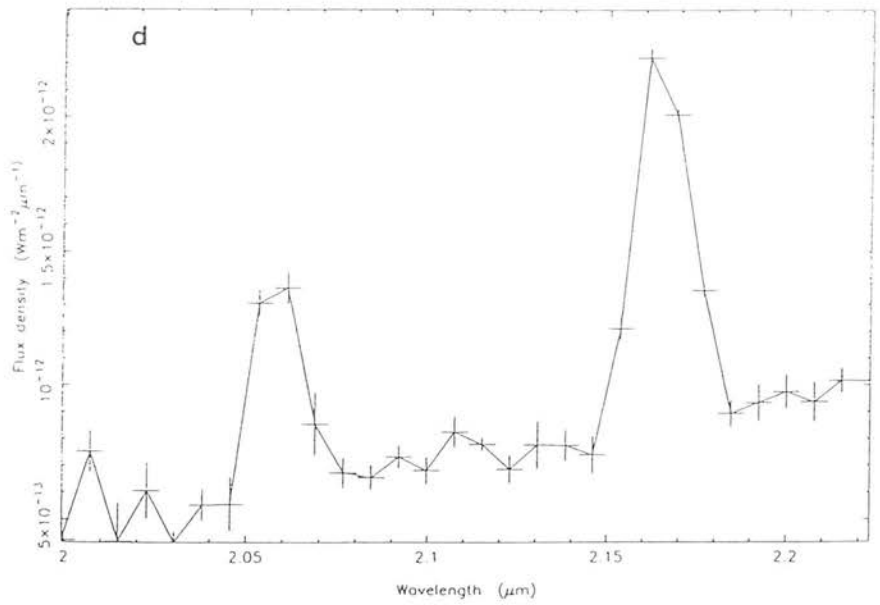

G45.454

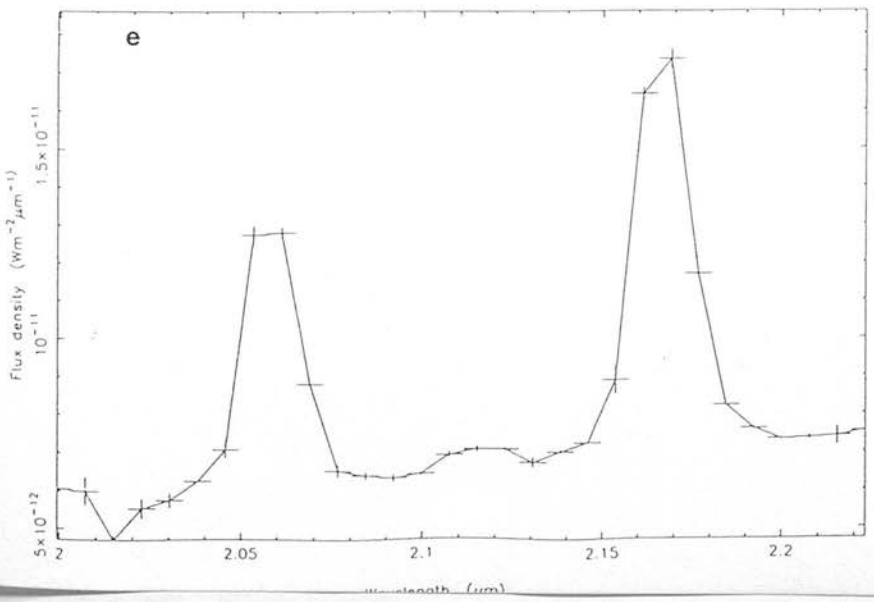

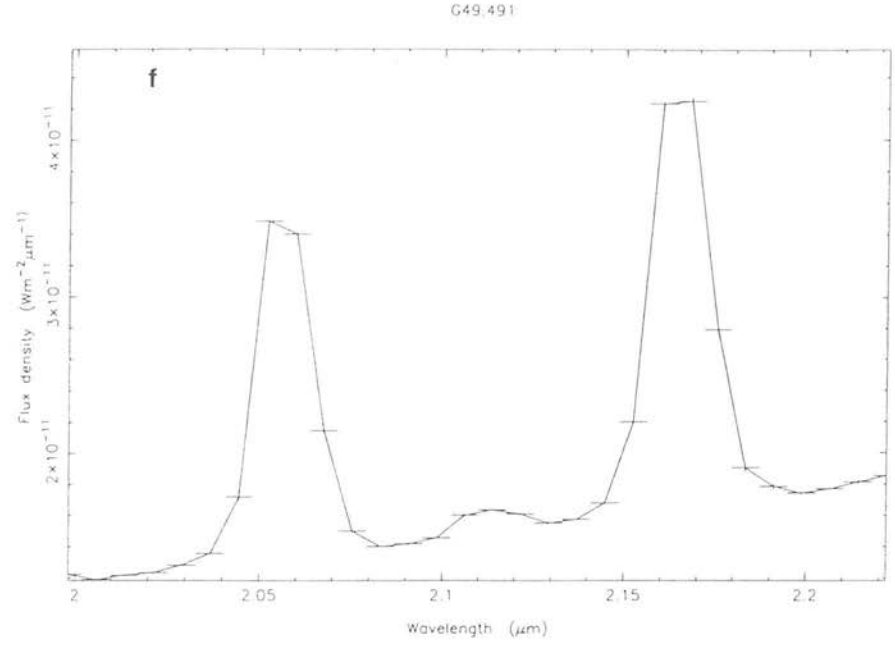
G49.491
f
Flux density (Wm^{-2}μm^{-1})
4×10^{-11}
3×10^{-11}
2×10^{-11}
2
2.05
2.1
2.15
2.2
Wavelength (μm)

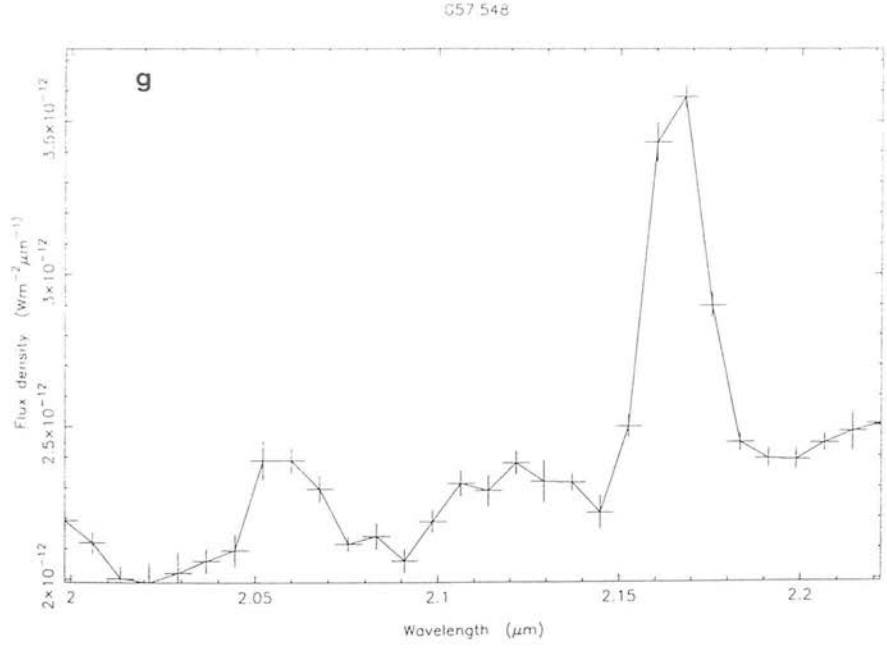
G57.548
g
Flux density (Wm^{-2}μm^{-1})
3.5×10^{-12}
3×10^{-12}
2.5×10^{-12}
2×10^{-12}
2
2.05
2.1
2.15
2.2
Wavelength (μm)

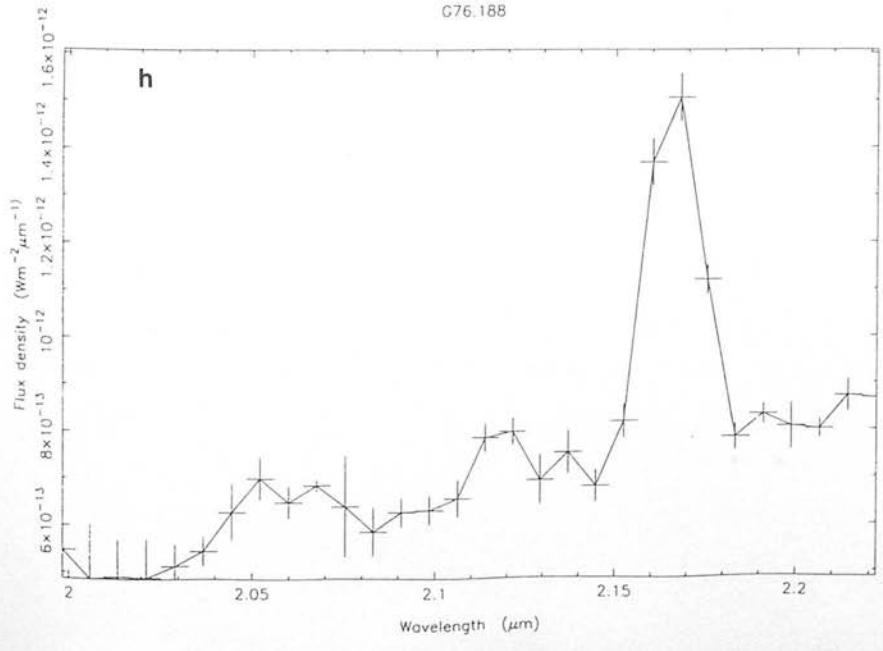
G76.188
h
Flux density (Wm^{-2}μm^{-1})
1.6×10^{-12}
1.4×10^{-12}
1.2×10^{-12}
10^{-12}
8×10^{-13}
6×10^{-13}
2
2.05
2.1
2.15
2.2
Wavelength (μm)

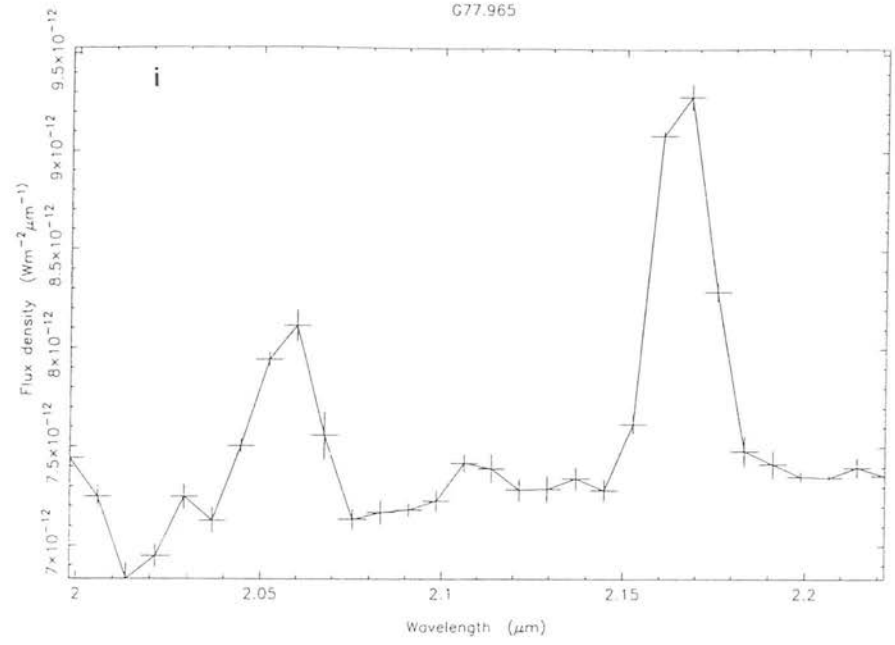
G77.965
i
Flux density (Wm$^{-2}\mu$m^{-1})
7×10^{-12}
7.5×10^{-12}
8×10^{-12}
8.5×10^{-12}
9×10^{-12}
9.5×10^{-12}
2
2.05
2.1
2.15
2.2
Wavelength (μm)

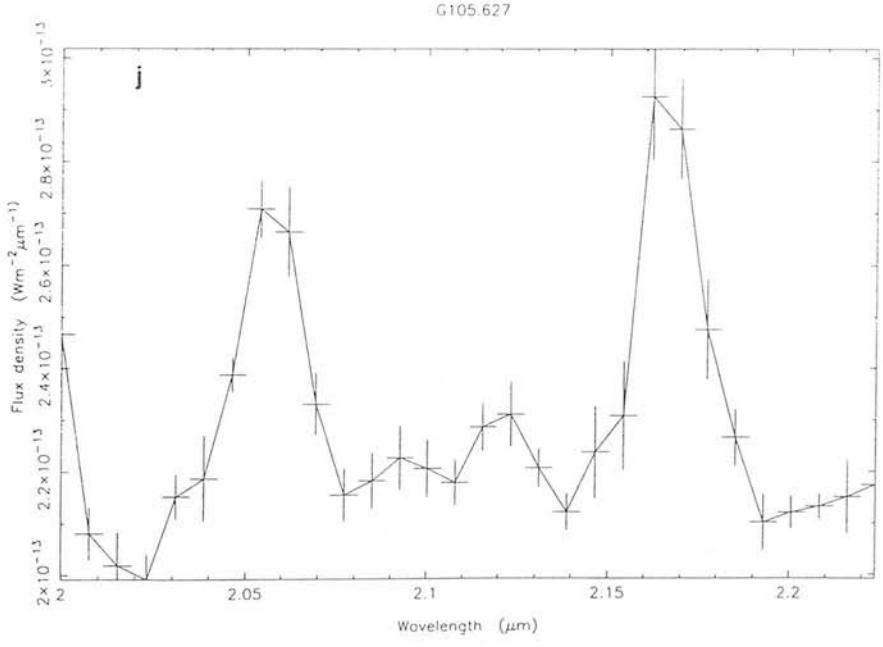
G105.627
j
Flux density (Wm$^{-2}\mu$m^{-1})
2×10^{-13}
2.2×10^{-13}
2.4×10^{-13}
2.6×10^{-13}
2.8×10^{-13}
2
2.05
2.1
2.15
2.2
Wavelength (μm)

established for the UCHII regions observed with CGS2. This was not so important for the UCHII regions observed with CGS4, since a suitable sky position could be identified at a spatial location within the $90\widehat{''}\times3\widehat{''}$ long slit. However, for UKT9 with its single aperture it is essential to firstly obtain accurate sky positions. The near infrared camera IRCAM on UKIRT was used on the nights of the 16, 17, 23 and 24 October 1991 in order to map the surrounding sky around each HII region. IRCAM is an infrared 1–5 μm imaging device with a 62×58 InSb array. The $1.2\widehat{''}$ per pixel mode was employed with the narrow band Brγ filter. A 3 or 5 point mosaic of the sky was made by moving the telescope $66\widehat{''}$ EW or NS, or NSEW respectively. For data reduction purposes dark frames (section 2.2.1) were taken.

Each object was then divided by a flatfield to cancel out the pixel to pixel gain variations across the detector. The flatfield was created from a stack of sky frames observed fairly close in time to the object frame, usually 5 or 6 frames were stacked. The median value in the stack was then found for each pixel in the array in order to obtain a flatfield frame which is free from starlight emission. A mean value would be biased towards anomalously high pixel values if stars were present in the frames and would not reflect true sky pixel values. The frame was then normalised to obtain a map of the sensitivity of each pixel across the array– a flatfield.

Bad pixels were removed by interpolation where each bad pixel value was replaced by the mean value of the surrounding pixels in a 3×3 box.

The final frames were combined spatially to form a mosaic from which "clean" patches of sky were targeted as offset positions for the telescope to nod onto for use with UKT9. The Brγ images are shown in fig 4.3a–j.

Flux Calibration

Possession of Brγ IRCAM images of the HII regions enabled an independent flux calibration method of the UKT9 spectra and a consistency check on the calibration discussed in section 4.2.1. Synthetic aperture photometry was performed to flux calibrate the HII regions. To mimic the UKT9 aperture the flux in a synthetic aperture of diameter 16

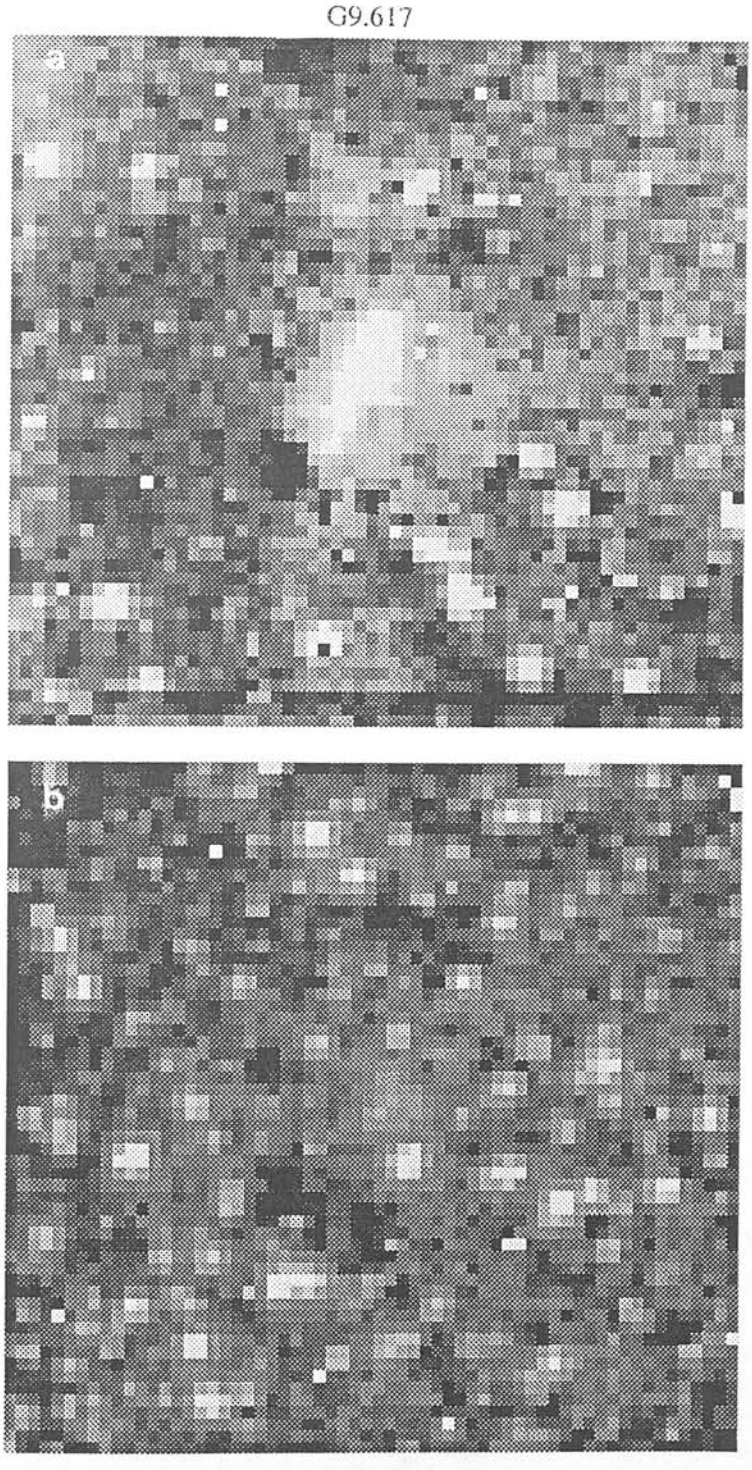

Figure 4.3: Brγ images of compact HII regions using IRCAM.

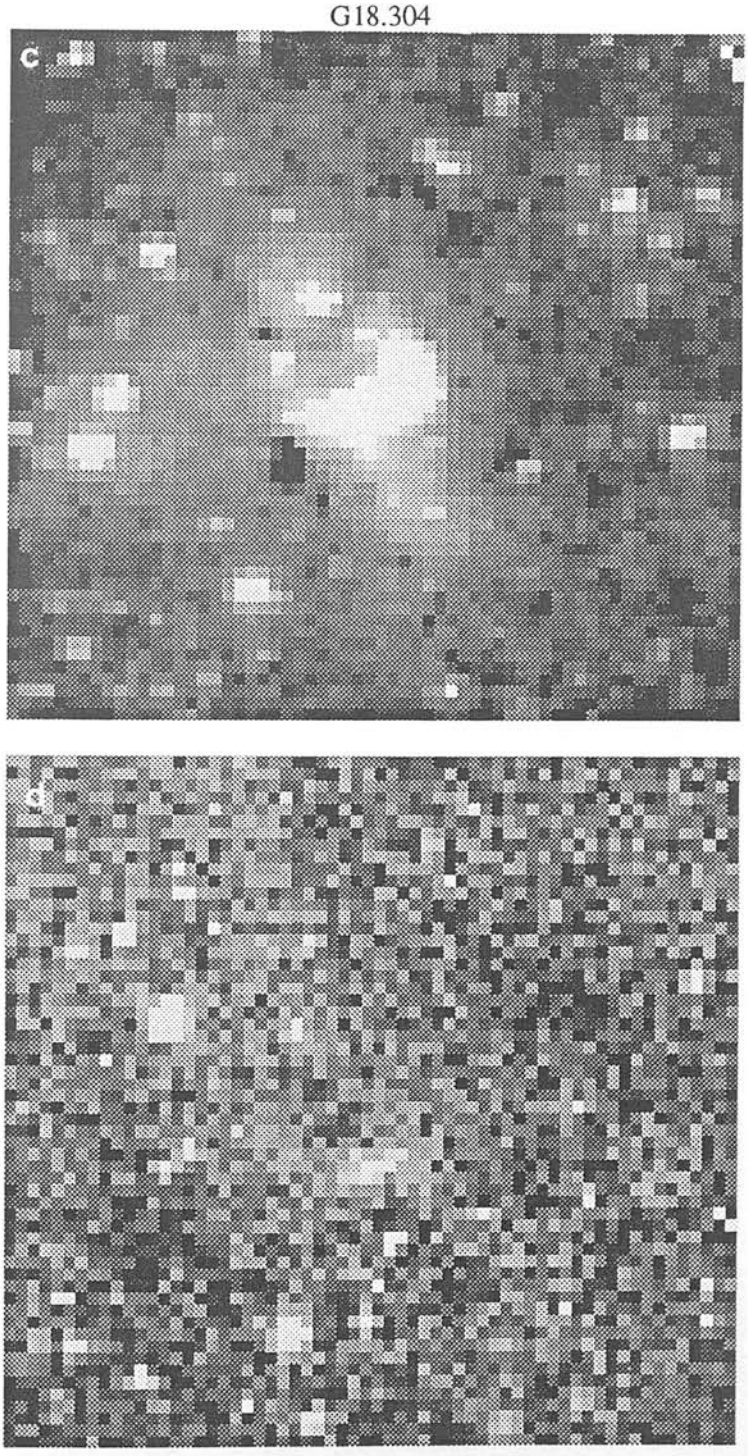
G18.304
c
d
G37.874

G45.454

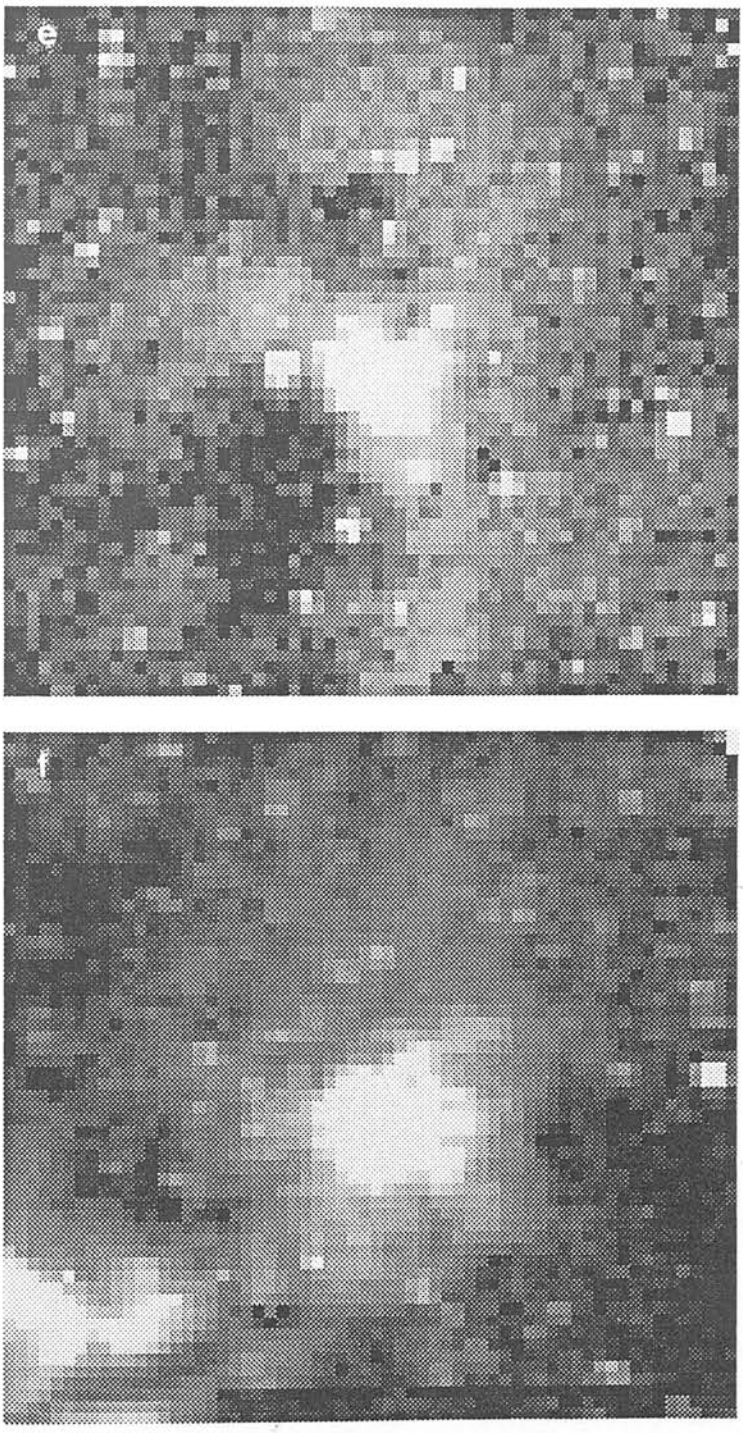

G49.491

G57.548

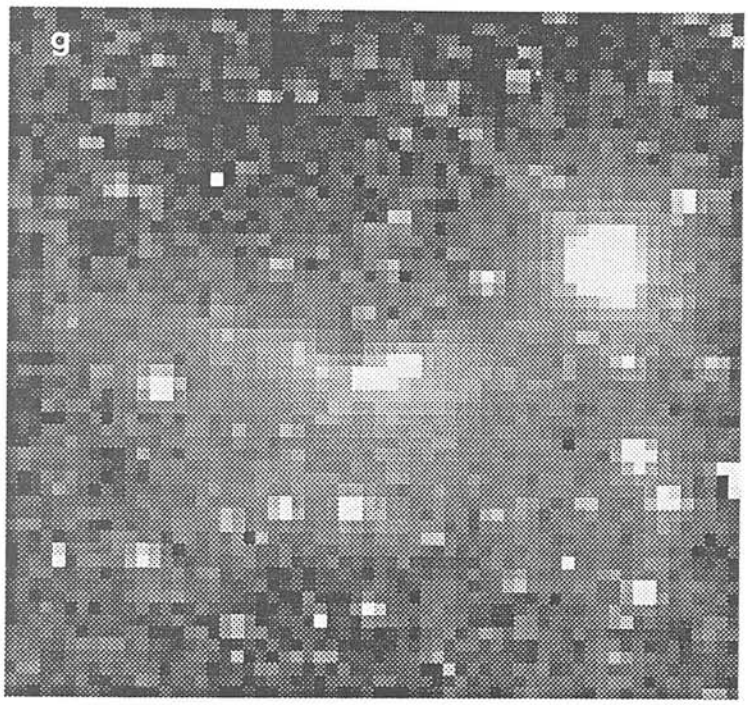

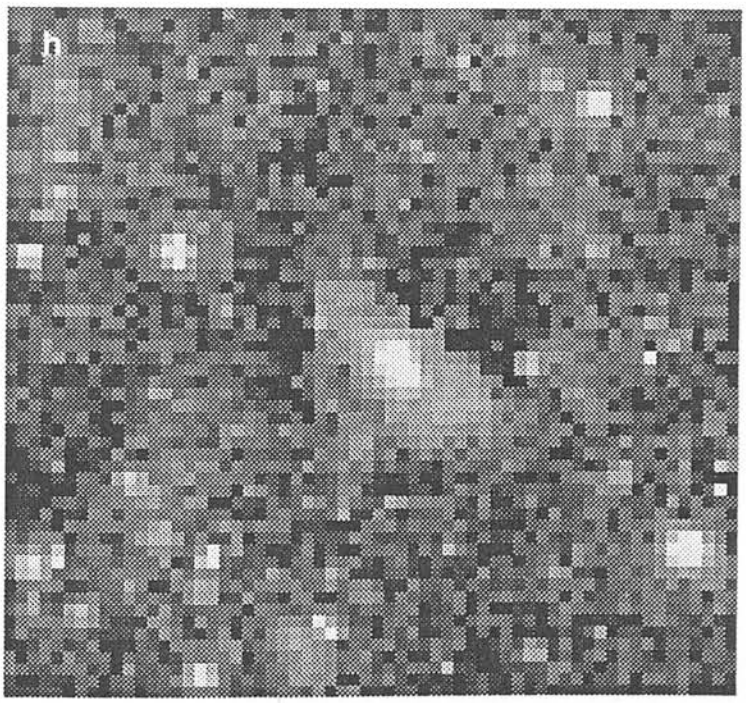

G76.188

G77.965

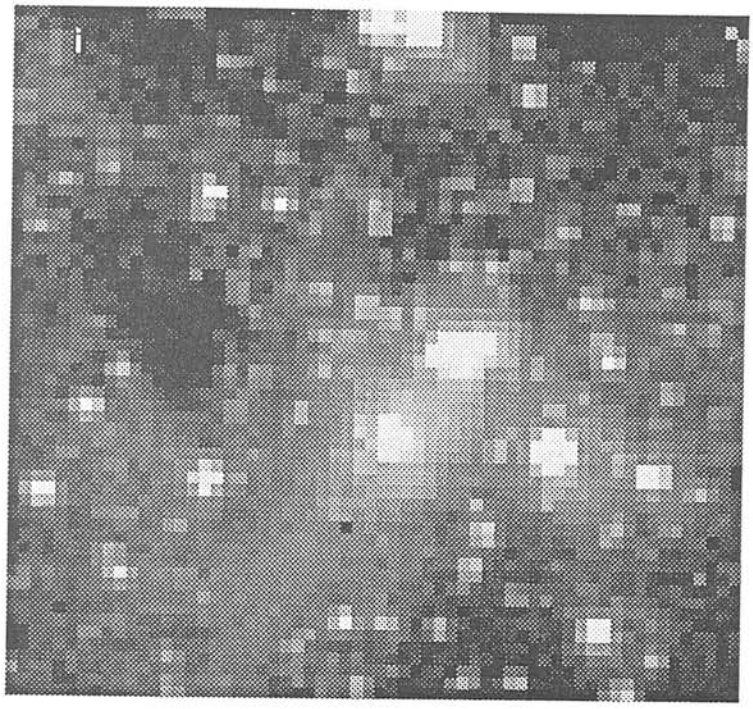

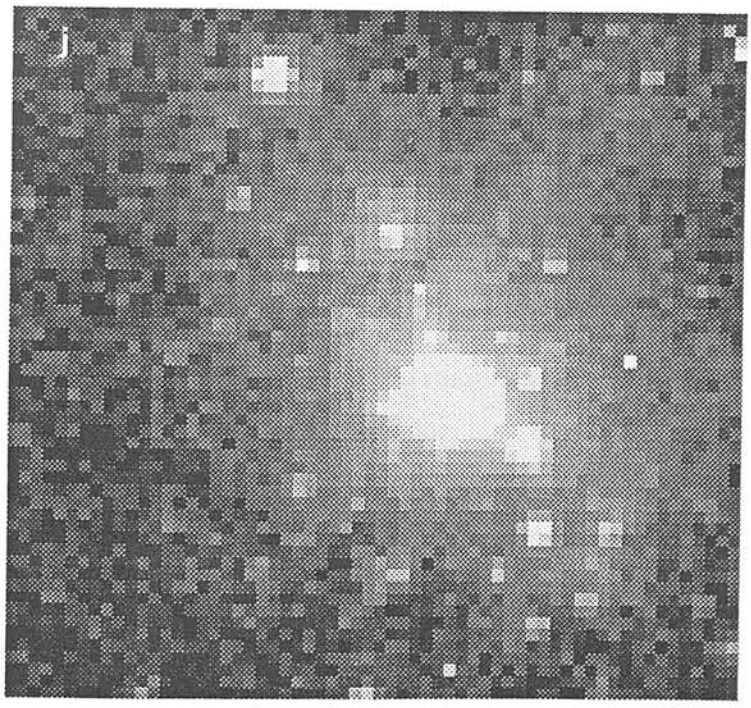

G105.627

pixels ($19.2\widehat{''}$) around the object was summed and the number of pixels recorded. In the same object frame the mean value for the sky/pixel was ascertained and thus the contribution of the sky to the summed flux was removed . Unfortunately two out of the four nights were not photometric and the data from these two nights was not usable.

The imaged HII regions were flux calibrated using eqn 4.2 and multiplication by the bandwidth which for the narrow band Brγ filter was 1%. Assuming the Rayleigh-Jeans approximation for stellar spectra $F_\lambda \propto \lambda^{-4}$ the difference between the magnitude at 2.165μm and 2.2μm is a factor of 1.06 and this was corrected for.

The difference between the instrumental magnitude (-2.5logC_K), where C_K is again the counts at 2.2μm, and the tabulated broad band K magnitude, is defined as the zero point. The zero points at 2.2μm of the standard stars used for calibration purposes were compared, to test the stability of the flux calibration. The scatter on the zero points was no more than ~10%. The derived flux is the total flux in the Brγ filter *i.e.* line + continuum, hence the contributions from the line and continuum must be separated. To do this the UKT9 spectrum was used for each object.

Line and continuum fitting

The IRCAM Brγ 1% filter covers a wavelength range 2.156–2.176μm. Initially a first order polynomial was used to fit the continuum in the UKT9 data which was then removed from the spectra. The residual line was then fitted with a gaussian and the line flux calculated.

The line fit was then removed from the continuum and the flux *i.e* the area under the continuum calculated, by resampling and binning the data for computational ease. The ratio of the line to line + continuum was then calculated over the wavelength range and the Brγ line flux determined, enabling the line flux to be calculated from the IRCAM data.

4.2.3 Comparison of UKT9 and IRCAM fluxes

The two sets of derived fluxes are given in table 4.3. There is a systematic error of $\sim 30\%$ between the two measurements. Explanations such as uncertainty in the flux calibration and the observing conditions on the different nights and the use of two different instruments can be invoked. Another possible difference could be due to the different spectral types used (see table 4.2) for spectral and flux calibration by UKT9 (predominantly K stars) and IRCAM (A stars), coupled with the approximation that the broad band K magnitude will be the same as the narrow band magnitude. Errors of approximately 10–20% are plausible because of this effect.

The errors in the uncertainty of the line fitting and the photon noise will be small in comparison. The actual scatter between the ratios of the two data sets is $\sim 5\%$, hence the actual error is dominated by the systematic error. If the scatter within systematic errors was large this would be indicative of inaccurate UKT9 flux calibration. Hence, the UKT9 measurements were used with confidence once 30% errors were assigned to each measured flux. IRCAM fluxes were not used because continuum K band measurements were not taken and extra errors are bound to be introduced on determining the continuum component from a different instrument. For line ratios only the internal errors due to line fitting and photon noise apply.

4.3 Corrections to observations

The derived fluxes need to be corrected for atmospheric absorption effects and extinction towards the HII region. Atmospheric correction factors were calculated as described in section 2.3 and are given in table 4.4.

Following the same principles as for section 2.4 the extinction was calculated by comparison of the observed Brγ fluxes with those derived from radio flux densities (eqn 2.1).

Zoonermatkerani *et al.* (1990) give radio flux densities at 1.4GHz. At this frequency, the radio continuum is typically near the turnover in the free-free spectrum; for an

Object	Brγ flux		Br$\gamma(\frac{\text{UKT9}}{\text{IRCAM}})$
	UKT9 (Wm^{-2})	IRCAM (Wm^{-2})	
G9.617	6.35×10^{-16}	8.5×10^{-16}	0.74
G10.965	1.30×10^{-16}	1.9×10^{-16}	0.68
G18.304	1.60×10^{-15}	2.2×10^{-15}	0.72
G38.874	3.09×10^{-16}		
G45.454	1.83×10^{-15}		
G49.491	6.00×10^{-15}	9.2×10^{-15}	0.65
G57.548	2.84×10^{-16}	4.3×10^{-16}	0.65
G76.188	1.50×10^{-16}		
G77.965	4.63×10^{-16}		
G105.627	2.14×10^{-15}		

Table 4.3: Comparative Brγ Fluxes.

Object	Velocities (kms^{-1})		Overall HeI flux correction
	LSR	Geocentric	
G9.617	4.1	-17.9	1.01
G10.965	18.5	-4.2	1.57
G18.304	32.7	7.2	1.29
G37.874	60.8	30.1	0.93
G45.454	55.9	24.2	0.96
G49.491	60.9	58.6	0.88
G57.548	2.8	-3.1	1.59
G76.188	-3.0	-15.7	0.97
G77.965	-5.5	-19.1	1.07
G105.627	-40.9	-48.4	0.87

Table 4.4: Atmospheric Corrections to HeI 2.058μm/Brγ ratio.

HII region with n_e=10^3cm^{-3}, T_e=10,000K and a diameter of 1pc then theoretically the continuum optical depth at 1.4GHz is 0.16, whilst at 15GHz it decreases to 0.001. For n_e=10^4cm^{-3} the 1.4GHz value increases to 16 and the 15GHz value to 0.1, therefore for these conditions the radio continuum seems to be generally optically thick at 1.4GHz, and turns over to become optically thin by 15GHz. A thermal Bremsstrahlung spectrum (see section 1.2.1) is given by:

$$S_\nu = B_\nu(1 - e^{-\tau_\nu}) \tag{4.3}$$

where S_ν is the radio flux density, B_ν is the Planck function which is proportional to ν^2 at radio frequencies. τ_ν is the optical depth in the radio continuum at a given frequency ν, $\tau_\nu \propto \nu^{-2.1}$ at radio frequencies (see section 1.2.1). This equation for S_ν can be written:

$$S_\nu = a(1)\nu^2(1 - e^{-a(2)\nu^{-2.1}}) \tag{4.4}$$

where a(1) and a(2) define the normalization and turnover in the spectrum. For the UCHII region sample, by iteration of eqn 4.4, using the radio flux densities at 5 and 15 GHz by Wood and Churchwell (1989), the continuum optical depth at 15GHz, $\tau_{15\mathrm{GHz}}$, was found and the inferred Brγ flux calculated from eqn 2.2. $\tau_{15\mathrm{GHz}}$ values were in the range 0.1–0.7. Although these values may be rather high they illustrate that $\tau_{1.4\mathrm{GHz}}$ values will not be small ($\ll$1), thus assuming an optically thin radio continuum is unlikely to be valid at this frequency. Inclusion of lower frequency radio measurements available for several of the UCHII regions and using the fitting routine described below suggest values for $\tau_{15\mathrm{GHz}}$ nearer $\sim$0.1 for several of the UCHII regions. Fortunately, the differential extinction factor C_K changes by no more than a few per cent in this case.

To obtain differential extinction estimates for the compact HII regions of this present study, one or more further flux measurements are needed in order to estimate a radio continuum optical depth and hence an optically thin radio flux. Literature concerning these objects has been scoured to obtain other radio measurements for these HII regions at higher and lower frequencies. Table 4.5 depicts the frequency, the observed flux density and cites the authors and beam sizes used. As pointed out by Kurtz *et al.* (1994), care is needed in interpretation of these different measurements. As already shown in section

4.2.3 there will be large systematic errors involved when using different instruments. HII regions located in crowded fields are subject to error because different objects in the same field may be viewed as the same region due to the finite resolution of the instrument. Some instruments will have aperture sizes that vary at different frequencies. Most importantly perhaps, many of these were single dish measurements which are of low resolution and may be contaminated by diffuse extended emission around the source. Consequently, single dish, large beam measurements were only used if there was at least one other small beam measurement at the same frequency for comparison, so that an appropriate scaling factor could be derived and applied to the other single dish measurements for that object. However, there will also be internal disagreement between small scale measurements, since different instruments and their configurations are sensitive to structure on different scales, thus flux measurements will reflect these differences. The scale size to which different small beam measurements in table 4.5 are sensitive, between $10\widehat{''}$ and $1\widehat{'}$, are given there.

Nevertheless, from comparison of small beam measurements by Kurtz *et al.* (1994) at 8.4 and 15GHz in cols 9 and 12 of table 4.5, the radio spectrum appears flat and hence it appears 15GHz continuum fluxes should be optically thin. From table 4.5, it should be possible to make use of all the data collated to model the radio spectrum between 0.365 and 15GHz and determine $\tau_{15\mathrm{GHz}}$ and hence an optically thin S_ν at 15GHz. For this purpose, a free-free radio spectrum of the form given in eqn 4.4 was fitted to the data and a minimum χ^2 method used to solve for the best fit for the unknown parameters a(1) and a(2) in order to tie down the scaling factor and the turnover of the radio spectrum. This involves minimizing the sum:

$$\chi^2 = \sum_{i=1}^{n} \left(\frac{y_i - y(x_i; a1, a2)}{\sigma_i} \right)^2 \tag{4.5}$$

Each data point (x_i,y_i) has an associated error σ_i, y is the non-linear model with the variable parameters a(1) and a(2). The routine uses Marquart's method (Press *et al.* 1986). From the best fit model the 15GHz flux was extrapolated and the continuum optical depths $\tau_{1.4\mathrm{GHz}}$ and $\tau_{15\mathrm{GHz}}$ were derived. Due to different errors associated with each radio measurement at a given frequency, (*e.g.* the difference in 1.4GHz values given in cols 2 and 3 of table 4.5 is not obviously explicable), errors on derived optically thin

Table 4.5: Compact HII region radio flux densities in mJy.

Object	0.365GHz	1.4GHz		5.0GHz					8.4GHz	10GHz	15GHz	
	(1)	(2)	(3)	(4)	(5)	(6)	(7)	(8)	(9)	(10)	(11)	(12)
		$20''$	$30''$	$1'$	$10''$				$18''$			$10''$
G9.617		895	407	297.4			1150	1300	965.8		1150	2953.5
G10.965		275	98	73.8				720				
G18.304	345	1397		967.3			1500	1420	90.3		1620	80.7
G37.874	266	1345		2202.4	1100[1]			5500	2342.8			3067.1
G45.454		2207	548		417.6		8500	714		356.2		
G49.491	661	4885										
G57.548		195				900						
G76.188		417	328						109.1			67.6
G77.965	320	174	100						12.2			34.2
G105.627	208	408				584						

[1] Flux density from Churchwell (1978).

(1) Douglas *et al.* (1980) $30''$, (2) Zoonermatkerani *et al.* (1990) $5''$. (3) Garwood *et al.* (1990) $4''$. (4) Becker *et al.* (1994) $4''$ (5) Wood & Churchwell (1989) $0.4''$. (6) Becker *et al.* (1991) $3.5'$. (7) Wink *et al.* (1982) $2.6'$, (8) Downes *et al.* (1980) $2.6'$. (9) Kurtz, Wood & Churchwell (1994) $18''$. (10) Handa *et al.* (1987) $2.6'$. (11) Wink *et al.* (1982) $2.6'$. (12) Kurtz, Wood & Churchwell (1994) $10''$.

radio fluxes were of the order 30–100%. However τ_{15GHz} was not greater than 0.15 for these compact HII regions, therefore the small beam 15GHz flux values given in col 12, table 4.5 were used and the optically thin assumption at this frequency validated. Where high frequency data were not available or solely in the form of single dish measurements, then the 1.4GHz value was extrapolated to an optically thin value as in eqn 2.2 using a mean value for $\tau_{1.4GHz}$ obtained from the rest of the data.

The 15GHz radio flux density was converted into a Brγ flux (equation 2.1) and by comparison with the observed Brγ fluxes the extinction towards the HII region was determined (eqn 2.3). The error on the observed Brγ flux was the systematic error discussed in section 4.2.3, whilst errors on radio fluxes were those taken from the best fit to the radio data. The optical depth at Brγ, $\tau_{Br\gamma}$, ranged between 0.1 and 4.3 which corresponds to visual extinctions A_v of 1–40. The correction factor due to differential extinction, C_k, described in section 2.4, eqn 2.4, for each HII region is given in col 2 of table 4.6 along with the inferred Brγ fluxes (col 3) derived from the radio flux densities.

The errors on the final derived ratios will be the sum of the errors added in quadrature from the atmospheric and extinction correction factors (tables 4.4 and 4.6 respectively). The resultant ratios and their corresponding errors are given in the final column of table 4.6.

4.4 Models

The standard models used in chapters 2 and 3 of the empirical HeI 2.058μm/Brγ ratio *vs.* stellar effective temperature adapted from DPJ (hereafter referred to as chapter 2 models) is shown in fig 4.4 . Two electron densities are depicted, $n_e=10^2$ and 10^4 cm^{-3} (solid lines). The introduction of dust, discussed by DPJ, has no effect on the low density $n_e=10^2 cm^{-3}$ model, but the dashed line is representative of a dusty model at $n_e=10^4 cm^{-3}$. An electron temperature of T_e=10,000K is assumed throughout.

As discussed in section 2.5.1, a detailed photoionization model of the HeI 2.058μm/Brγ ratio *vs.* effective temperature has recently been computed by Shields. He uses the photionization code CLOUDY (see Ferland 1993), and thus makes no assumptions about

Object	C_k	Brγ radio flux $\times 10^{-16}$Wm^{-2}	HeIλ2.058/Brγ ratio Observed	Corrected
G9.617	1.36	189.7	0.51	0.70±0.05
G10.965	1.42	66.8	0.26	0.58±0.23
G18.304	1.03	21.2	0.40	0.53±0.03
G37.874	1.47	227.8	0.62	0.84±0.10
G45.454	1.09	46.4	0.66	0.69±0.05
G49.491	1.23	577.8	0.79	0.85±0.06
G57.548	1.41	13.3	0.29	0.65±0.08
G76.188	1.15	7.31	0.11	0.17±0.05
G77.965	1.02	5.5	0.49	0.52±0.04
G105.627	1.07	43.9	0.68	0.64±0.08

Table 4.6: The HeI 2.058μm/Brγ ratio in UCHII regions.

case A or B (or deviations from either case) but solves the radiative transfer equation iteratively for thermal equlibrium at each point in the nebula, to compute total HeI 2.058μm and Brγ line strengths. Kurucz (1979) stellar atmosphere models are used in CLOUDY. The electron density is constant throughout the nebula within the ionization front. The electron temperature is a function of radius in these models; mean electron temperatures vary from between T_e=7,500–10,000K. These models are also shown in fig 4.4 (dashed lines) for $n_e=10^2$ and 10^4cm^{-3}.

Both models show the HeI 2.058μm/Brγ ratio to increase with stellar temperature to a maximum near T_{eff}= 38,000K. The model in chapter 2, for $n_e=10^2$cm^{-3}, then saturates at a value of 0.80, whereas the Shields model reaches a maximum value of 0.5 at this temperature. This can possibly be explained because the models of chapter 2 use a correction factor of 2/3 to the case B recombination coefficients given by Smits (1991a). Also different atomic data were used. Shields (private communication) points out this factor will be dependent on details on the ionization structure throughout the

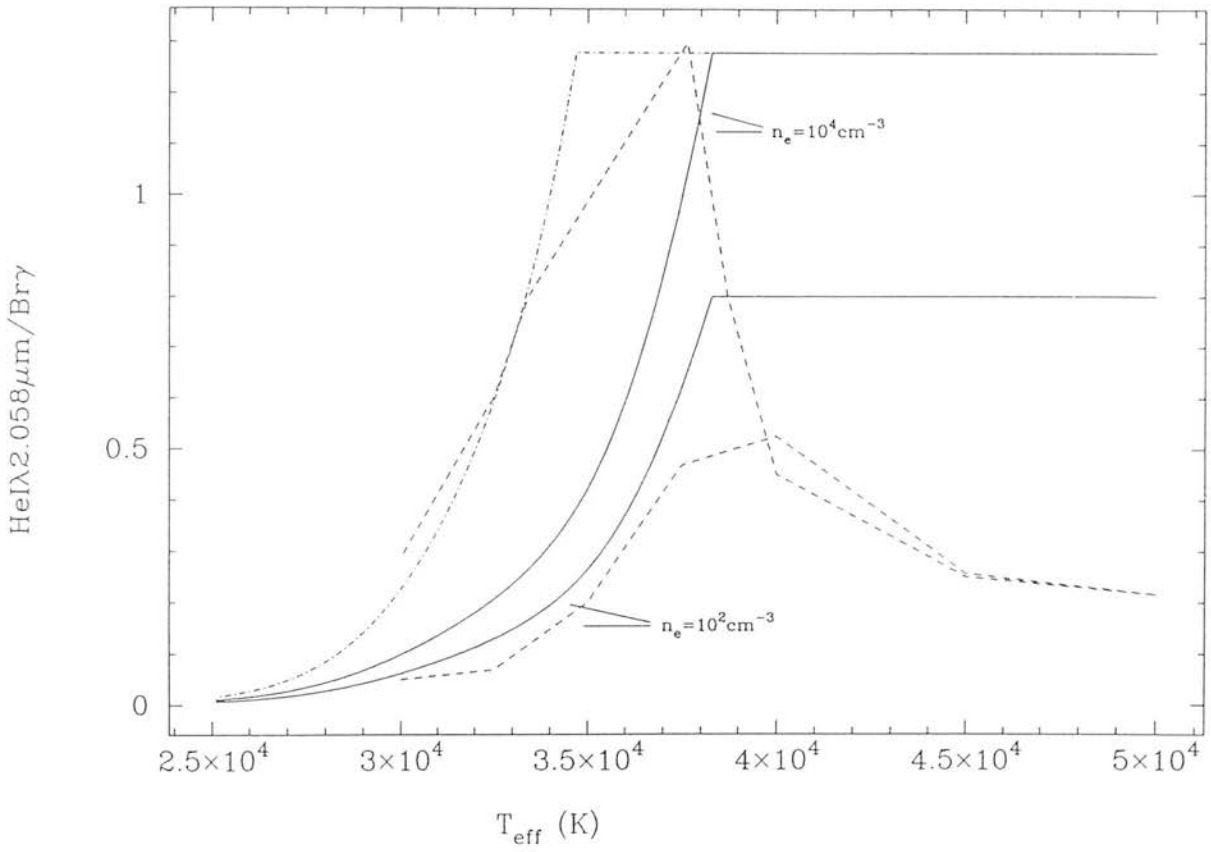

Figure 4.4: The HeI 2.058μm/Brγ ratio *vs.* stellar effective temperature. Solid curves depict the chapter 2 models for T_e=10,000K and n_e=10^2 and 10^4cm^{-3}. Dashed curves represent models by Shields for mean T_e values in the range 7,500–10,000K, for n_e=10^2–10^4cm^{-3}.

cloud, thus can only be calculated from a sophisticated photoionization code. However, for n_e=10^4cm^{-3}, the models of chapter 2 show good agreement with the Shields model using this correction factor of 2/3, in that a maximum value of 1.3 is attained in both these models.

Above T_{eff}=40,000K the models differ significantly. The model HeI 2.058 μm/Brγ ratio derived in chapter 2, remains constant at the maximum value whereas in the Shields model the HeI 2.058 μm/Brγ ratio then decreases as effective temperature increases. This decrease is predominantly a result of the decrease in the neutral helium to hydrogen fraction with increasing temperature.

Apart from the fact that the models of chapter 2 are approximate calculations (in that they use the OTS assumption to solve for radiative transfer through the HII region), and the Shields models are detailed photoionization and radiative transfer solutions, the major difference between the two sets of models concerns the neutral helium to hydrogen fraction assumed. This difference can be highlighted by examining equation (1) of Shields which is the ratio of 2.058 μm emission to 0.0584 μm absorption.

$$\frac{P(2.06\,\mu\text{m emission})}{P(\lambda 584\text{ destruction})} = \frac{40000 y^0 \xi_H}{2000\xi_H + 1} \tag{4.6}$$

where y^0, the ratio of neutral He to H by number is:

$$y^0 = y\xi_{He}/\xi_H$$

y is the helium abundance and ξ_{He} and ξ_H are the neutral He and H fractions in the He^+ zone. Equation 4.6 includes destruction by dust (the factor +1 in the denominator) as a competitive mechanism for destruction of 2^1P–1^1S 0.0584 μm photons. In section 2.5.3 from comparison of the relative mean free path of a 0.0584 μm photon before absorption by a hydrogen atom or a dust particle, dust absorption is found to be insignificant. As Shields points out this will be true so long as the hydrogen neutral fraction $\geq 5\times10^{-4}$ and establishes that that the hydrogen neutral fraction $> 10^{-4}$ throughout most of the HII region in his calculations, hence the assertion is in general valid. Therefore, eqn 4.6, becomes the ratio of HeI 2.058 μm emission to HI 0.0584 μm absorption and, is a

function of the HeI absorption cross-section and HI photoionization cross-section at that wavelength.

DPJ find a value of 2/3, at T_e=10,000K, for eqn 4.6 which is discussed in section 2.5.1. DPJ discuss in the text that the fraction of neutral helium to hydrogen atoms in the He^+ zone will affect the ultimate probability of the conversion of 2^1P into 2^1S photons, but assume as do the models of chapter 2, that the neutral helium and hydrogen fractions are equal, hence in the chapter 2 calculations, the ratio of HeI 2.058 μm emission to HI 0.0584 μm absorption scales with y rather than y^0.

However, Shields detailed models show that y^0 decreases with T_{eff} due to the increasing hardness of the radiation with T_{eff}. Since the HeI 2.058 μm line is pumped by resonant 1^1S–2^1P, 0.0584 μm photons, a slight decrease in y^0 will have an exaggerated effect on the HeI 2.058 μm/Brγ ratio. Thus the 2.058 μm/Brγ ratio drops off rapidly above a high enough effective temperature.

The observed HeI 2.058 μm/Brγ ratios are plotted in figs 4.5 and 4.6 for comparison with these models.

4.5 Observational Results

4.5.1 Comparison of Compact and UCHII region samples

In fig 4.5, the data is plotted against the theoretical models of chapter 2 for electron densities of n_e=10^2 and $10^4 cm^{-3}$ and electron temperatures of T_e= 10,000K (solid lines) and 5,000K (broad dashed lines) with the dusty n_e=$10^4 cm^{-3}$ models shown as narrow dashed and dot-dashed lines for the higher and lower T_e respectively. In fig 4.6, the same data is plotted against the Shields models for n_e=10^2 and $10^4 cm^{-3}$. Spectral type estimates for the compact HII regions are discussed shortly and depicted as described in section 2.6.

The HeI 2.058 μm/Brγ observations are consistent with both the models of chapter 2 or Shields *c.f.* fig 4.5 and fig 4.6. As a general trend, these ratios are lower than

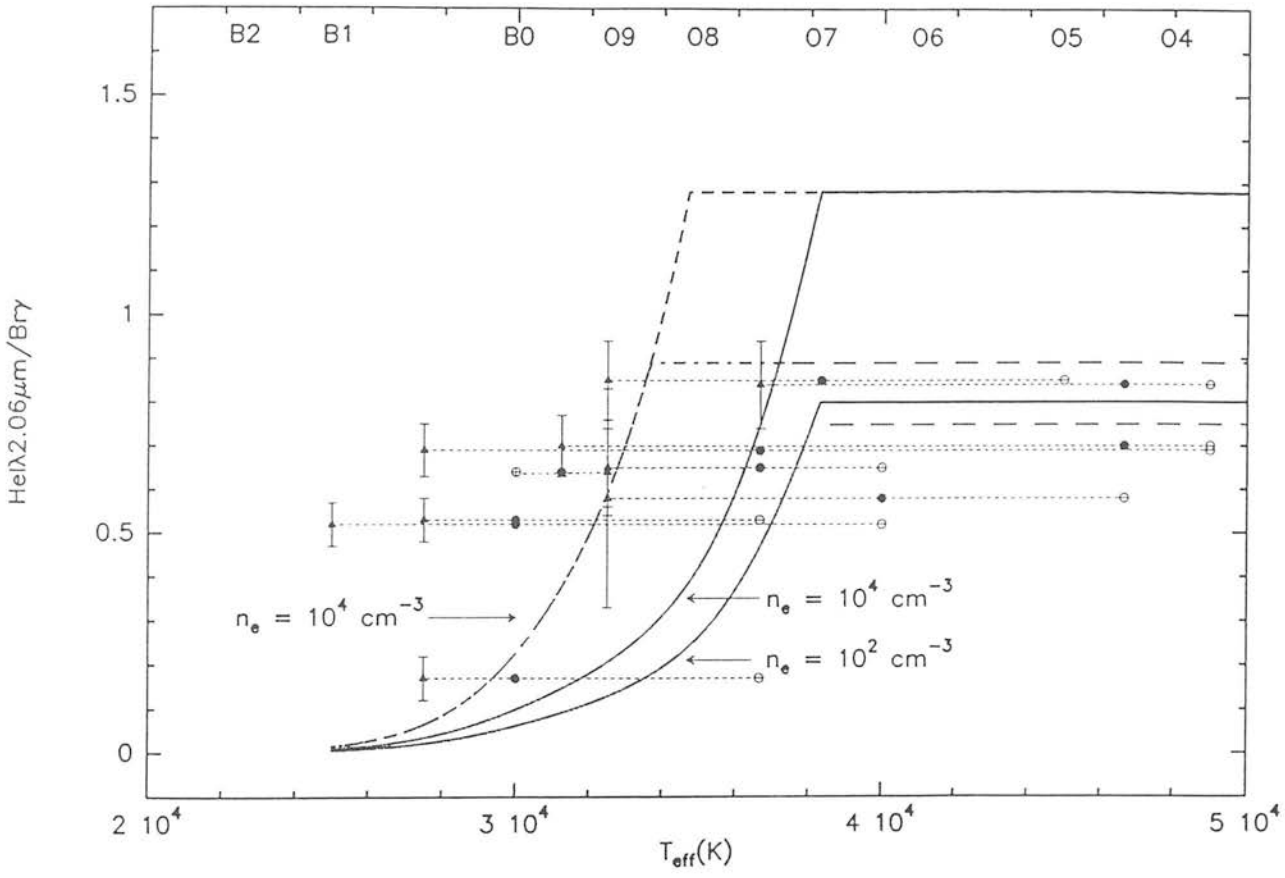

Figure 4.5: The dusty and non-dusty models of chapter 2 for T_e=5,000K (broad dash lines and dot-dash lines) and T_e=10,000K (solid and dashed lines) for n_e=10^2 and 10^4cm^{-3}. Data symbols are as described in fig 2.2.

those of the UCHII regions of chapter 2 *c.f.* figs 4.5 and 2.2. One of two obvious conclusions can be drawn. Either the electron densities are lower for these objects or the stellar temperatures are lower (or higher too in Shields models, see fig 4.6). A lower electron density is expected for larger HII regions which expand uniformly. Consequently, collisional excitation of the HeI metastable 2^3S level does not contribute significantly to the 2^1P population or thus enhance the 2.058μm line strength.

In chapter 2, comparison between UCHII region observations and models based on the calculations of DPJ were made. The observed ratios were compared with the saturated dusty curve for an electron density of n_e=10^4cm^{-3}, and effective temperatures greater than 35,000K were assumed for all UCHII regions bar one. Thus, stellar temperatures were considered to be higher than cluster temperatures in these UCHII regions (fig 2.2). For the present HII regions, four objects have radio single star temperatures that are consistent with lower effective temperatures than observed generally for the UCHII region sample; for the remaining compact HII regions only cluster temperatures are in agreement with lower stellar temperatures.

From Shields' models the effective temperature range for a given HeI 2.058μm/Brγ ratio is confined to a much narrower range (fig 4.6), since for effective temperatures greater than 40,000K, HeI 2.058μm/Brγ ratios are predicted to decrease. Therefore, in Shields' models lower observed ratios could result from higher effective temperatures in this compact HII region sample. For this to be the case, UCHII region effective temperatures would need to lie in the range 33–39,000K, which is in good agreement with predictions made from fine structure lines (see section 5.1), and compact HII region temperatures would have to be higher than 39,000K. However, IRAS spectroscopic measurements, of the [SIV] 10.5μm line are available for the compact HII regions G9.617, G45.454 and G105.627 (Simpson and Rubin 1990). S^{+++} was not detected in any of these objects. Stellar temperatures greater than T_{eff} ~40,000K are needed for S^{+++} to be produced in significant quantities, therefore it is unlikely that the compact HII regions have effective temperatures above T_{eff}=40,000K. Furthermore, the ionizing source(s) in an HII region with effective stellar temperature greater than ~40,000K is required to be a single star with mass greater than 30 $M_\odot$ or a stellar cluster where the most massive star is greater than 90 $M_\odot$. The likelihood of observing a star with effective temperature,

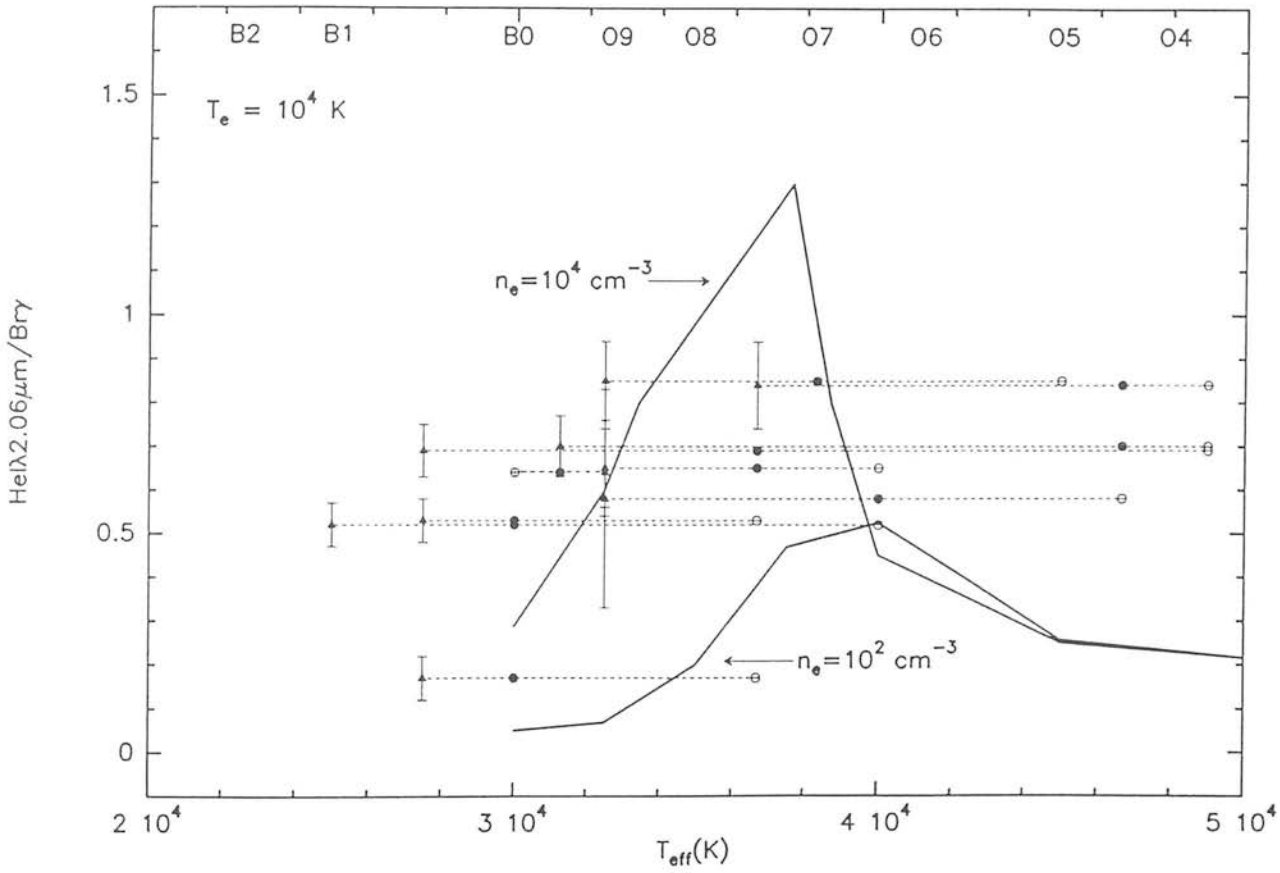

Figure 4.6: Shields' models for mean T_e values in the range 7,500–10,000K for n_e=10^2 and 10^4cm^{-3}. The same data is plotted as in fig 4.5.

T_{eff}, greater than 40,000K or 30 $M_{\odot}$ is 0.3 times that of observing an O8 or 20 $M_{\odot}$ star and 0.04 times that of observing a B0 or 10 $M_{\odot}$ star.

In addition to the two conclusions namely lower electron densities or effective temperatures, discussed above, if the same electron density and effective temperature range is appropriate for the UCHII region and compact HII region sample, either larger microturbulent velocities or comparable microturbulent velocities and lower electron temperatures than those observed in the UCHII regions, would produce lower resultant HeI 2.058μm/Brγ ratios. Microturbulent velocities greater than those found for the UCHII region sample, given in table 3.3, are not evident *c.f.* Downes *et al.* (1980). Moreover, one would not expect greater microturbulent velocities in this compact HII region sample since they are in general larger lower density HII regions than the UCHII region sample (Garay and Rodríguez 1983). From section 2.6, a HI broadened line with FWHM of 35 kms^{-1} corresponds to a microturbulent FWHM velocity of 28 kms^{-1} at T_e=10,000K, which reduces the maximum value of the HeI 2.058μm/Brγ ratio at $n_e=10^4 cm^{-3}$ to ~0.84. The observed HeI 2.058μm/Brγ ratio for the compact HII regions G37.874 and G49.491 are in good agreement with this value. Considering the same HI line width and electron density for a plasma with an electron temperature of T_e=5,000K, the maximum value of the HeI 2.058μm/Brγ ratio would be reduced from 0.89 (no turbulence) to ~0.50. These two ratios, for turbulent model HII regions, encompass the observed HeI 2.058μm/Brγ ratios observed in all these compact HII regions, bar G76.188. Therefore, if turbulent motions are evident in the UCHII regions and those objects are best represented by an electron temperature of T_e=10,000K (as was found to be the case for half the UCHII region sample), then if comparable microturbulence is present in the compact HII regions generally lower electron temperatures would also explain the predominantly lower observed HeI 2.058μm/Brγ ratios. However, systematically lower electron temperatures would only be expected if these compact HII regions have smaller Galactocentric radius than the UCHII regions. This is a result of the abundance gradient in the Galaxy which implies a lesser fraction of coolant metals further out from the Galactic Centre. Galactocentric radii values obtained for several UCHII and compact HII regions from Downes *et al.* (1980) provide no evidence for this to be the case.

4.5.2 Comparison with models

Comparison of the observations with the models of chapter 2 (fig 4.5) and those of Shields (fig 4.6) and the different implications are now discussed separately. Deriving spectral type estimates from radio and FIR measurements, representing a single star ionizing source and a cluster of stars, is described in section 2.6, and applied here.

To proceed with examination of fig 4.5:

a) first consider the exciting source to be a single star, for which the stellar effective temperature of the star falls between the temperature deduced from the IRAS and radio flux measurements (fig 4.5). From comparison with the models (fig 4.5), all the observed ratios, except G105.627, for a single star, fit the $n_e=10^2 cm^{-3}$ models which describe either a dusty or non dusty model, within the 1σ observational errors. The difference in the saturation value of the HeI 2.058μm/Brγ ratio between T_e=5,000–10,000K is only 0.05 at this electron density, equivalent to 1σ error bars on the observed ratios (table 4.6), thus it is impossible to determine a preferred electron temperature in this range. The single star measurements for G37.874 and G49.491 are also consistent with the higher electron density $n_e=10^4 cm^{-3}$ dusty or non dusty model for the lower electron temperature of T_e=5,000K. The four compact HII regions G18.304, G76.188, G77.965 and G105.627, have single radio star measurements in good agreement with the standard dusty HII region models for $n_e=10^4 cm^{-3}$.

b) If a cluster of stars is deemed to be more appropriate then several objects are consistent with the standard dusty models for $n_e=10^4 cm^{-3}$ between either end of the electron temperature range. From fig 4.5, many of the derived cluster temperatures are too low for HeI ionization, thus the HeI 2.058μm line would not have been observed if the effective temperature of the exciting source was this low. It is important to remember that cluster temperatures are lower limits, as discussed in section 2.6, thus realistic effective temperatures lie between single star and cluster estimates.

c) If the effective temperature of the source does lie between that of the single star estimate and the cluster temperature, most of the observed ratios, besides being consistent with the low density models, also then are in good agreement with the higher

density non-dusty models at $n_e=10^4 cm^{-3}$ (for both electron temperatures) or, equivalently a dusty model with less dust content with respect to that observed in the general interstellar medium (less than 10^{-2}) at this electron density (fig 4.5). Thus, models with densities between $n_e=10^2$ and $10^4 cm^{-3}$ are also consistent with all the compact HII region observations. The four sources G18.304, G76.188, G77.965 and G105.627 fit the dusty model for this higher electron density.

Hence, all the observed HeI 2.058μm/Brγ ratios in these compact HII regions are broadly consistent with some or all of the models in fig 4.5 and firm conclusions are hard to draw. Inclusion of microturbulence complicates the issue further. Comparison of the observed ratios with model predictions shows no evidence for turbulent motions, since most observations fit the rising or falling parts of the $n_e=10^2$ or $10^4 cm^{-3}$ curves. In contrast, there is no evidence to rule out turbulent motions without knowledge of accurate electron densities or effective temperatures. Microturbulence is now investigated further to examine whether the above predictions are altered. H110α RRL measurements were found from Downes *et al.* (1980) for four of the HII regions. It must be noted that these measurements are big beam measurements, thus broadened RRL's may also be attributed to velocity gradients.

Microturbulent FWHM velocities of 15–30 kms^{-1} are predicted from these measurements for T_e=10,000K, consistent with the turbulent FWHM value of 28 kms^{-1} discussed in section 4.5.1, in which the ratio has a maximum of 0.84. Such microturbulent velocities bring the $n_e=10^4$ cm^{-3} curve to be coincident with the $n_e=10^2 cm^{-3}$ curve for purely thermal motions at T_e=10,000K. Similarly, for the same RRL measurements, at T_e=5,000K, as discussed in section 5.1, the HeI 2.058μm/Brγ ratio decreases to $\sim$0.50 and these two values span the observed HeI 2.058μm/Brγ ratios.

Furthermore, if turbulent motions comparable to those in UCHII regions are present in these compact HII regions it is only the higher electron density models (except for G76.188 which is consistent with any n_e model) that are compatable with observed ratios.

Shields' models are shown in fig 4.6. His model for $n_e=10^2 cm^{-3}$ has a lower peak value for the HeI 2.058μm/Brγ ratio than the equivalent model in chapter 2. Shields' models are calculated to have mean electron temperatures in the range T_e=7,500–

10,000K. Comparison of both sets of models in fig 4.4 show quantitative agreement up to T_{eff}=38,000K. Then Shield's models reveal a flaw in the models of chapter 2 which is the assumption that relative neutral helium to hydrogen fraction, y^0, is constant with T_{eff} leading to the disagreement between the models above T_{eff}=38,000K. Fortunately, as discussed in section 4.5.1 it is unlikely that any compact HII regions have such high effective temperatures. Again, conclusions can be drawn by consideration of spectral types. a) Assuming single star effective temperatures then the HII regions G77.965 and G76.188 are in agreement with his $n_e=10^2 cm^{-3}$ model, but the rest of the HII regions are consistent with the higher $n_e=10^4 cm^{-3}$ electron density model. b) For cluster temperatures the same few HII regions that agree with the dusty HII region model of chapter 2 at $n_e=10^4 cm^{-3}$, also agree with the equivalent model by Shields. c) For the most realistic effective temperature estimates *i.e* that single star estimates are upper limits and cluster temperatures lower limits, then all compact HII regions (except G76.188) are solely consistent with the higher electron density model. From fig 4.6, it can be seen that there is a range of electron density models between $n_e=10^2$ and $10^4 cm^{-3}$, that would also be in agreement with the compact HII region observations. Inclusion of microturbulence in these models will not change the above conclusions except that G77.965 will no longer be in agreement with the lower density model. Thus, Shields' models incorporating microturbulence, for $n_e=10^4 cm^{-3}$, remain consistent with the observed HeI 2.058μm/Brγ ratios. The stellar temperature range is constrained further in this case by the downward displacement of the $n_e=10^4 cm^{-3}$ curve, as a result of microturbulence, evident from fig 4.6.

Clearly, to establish the accuracy of these models with observations both the effective temperatures of the ionizing sources in these HII regions needs to be further constrained and the electron density determined accurately by other means for these objects. The aim of this last section is to try to investigate effective temperatures, and in chapter 5, a discussion of electron density and detailed calculations will be carried out.

It is appropriate here to discuss Shields' models with reference to the UCHII regions in chapter 2. These models have mean electron temperatures close to the high electron temperature T_e=10,000K models of chapter 2. The conclusions of chapter 2 for the higher electron temperature model were: a) effective temperatures are all less than

T_{eff}=38,000K in the UCHII regions and span a narrow range of T_{eff}=32–36,000K. In this case the dust-to-gas mass ratio is less in at least some of these UCHII regions, or b) UCHII region effective temperatures are greater than T_{eff}=38,000K and microturbulence must be present. These conclusions remain unchanged, however an additional conclusion from Shields' models is that effective temperatures T_{eff} of all UCHII regions may be greater than 38,000K, and tightly constrained to T_{eff}=39,000±500K. As discussed in section 2.6, the likelihood of observing so many UCHII regions all within one spectral type is unlikely. Furthermore, the [SIV] 10.5μm line was not significantly detected in these UCHII regions either (Simpson and Rubin, 1990).

The implications of Shields models with reference to the observations in chapter 3 are discussed in section 4.5.4.

4.5.3 Spectral type classification

In order to differentiate between any model the spectral types of the exciting stars must be constrained further. The three estimates of spectral types used here are discussed in detail in section 2.6. Two of these are based on the assumption that the emission emanates from a single source; IRAS and the radio flux values can be utilized in this circumstance to give upper and lower limits to the spectral types respectively. A third estimate is derived from the ratio of the above two fluxes *i.e.* N_{Lyc}/L_{IR} and is dependent only on the effective temperature whether from a single star or a cluster of stars. These three estimates are given in table 4.7. Fig 4.7 shows predicted values of log L_{IR} *vs* log N_{Lyc} for a given spectral type (fig 4.7a) and mass (fig 4.7b), these values are derived from Puxley (1988) and DPJ. The lower two curves depict values for a single star for a non dusty (solid curve) and dusty (dashed curve) HII region. The dotted curve joins values for a cluster of stars assuming the spectral type (fig 4.7a) or mass (fig 4.7b) labelled is the most massive star in the cluster. The calculation was insensitive to a lower mass cut off less than 10 $M_{\odot}$ for stars with upper mass cut offs greater than $\sim$ 30 $M_{\odot}$. A mass function with spectral index -2.85 was used. The model used is described by Puxley (1988). The data is plotted against these curves in figs 4.7a,b. Only G105.627 lies below the solid line. If the exciting source is a single star then all three estimates of spectral

Object	IRAS (L_{IR}) (single star)	Radio (N_{Lyc}) (single star)	N_{Lyc}/L_{IR} (cluster)
G9.617	>O4	O4.5	O9.5
G10.965	O4.5	O6.5	O9.5
G18.304	O7.5	B0	B0.5
G37.874	>O4	O4.5	O7.5
G45.454	>O4	O7.5	B0.5
G49.491	O5	O7	O9
G57.548	O6.5	O8	O9.5
G76.188	O7.5	B0	B0.5
G77.965	O6.5	B0	B1
G105.627	B0	O9.5	O9

Table 4.7: Spectral type estimates for HII regions.

type should be similar, as is the case for G105.627.

Conversely, HII regions G9.617, G45.454 and G77.965 all lie close to the cluster model curve. However, cluster temperatures for these objects are in disagreement with observed HeI 2.058μm/Brγ ratios, since these temperatures are too low for HeI ionization in the nebula. At the other extreme, G9.617 and G45.454 both have infrared luminosity, L_{IR}, values greater than that for a single O3.5 star, therefore it is statistically unlikely that two HII regions powered by such massive stars ($\geq 100\,M_{\odot}$) would be observed. The difference in spectral types inferred for a single star for G77.965 is more than three classes again suggesting that infrared luminosity predicted is too high. For these three objects errors due to distance ambiguities may be responsible for these large L_{IR} values, which would move the data points in figs 4.7a,b into the regime between the model curves predicted for clusters and single stars. Kinematic distances are calculated from radial velocities, using the equations for the Galactic rotation curve:

$$V_R = -30(R - R_0)\sin l \cos b \tag{4.7}$$

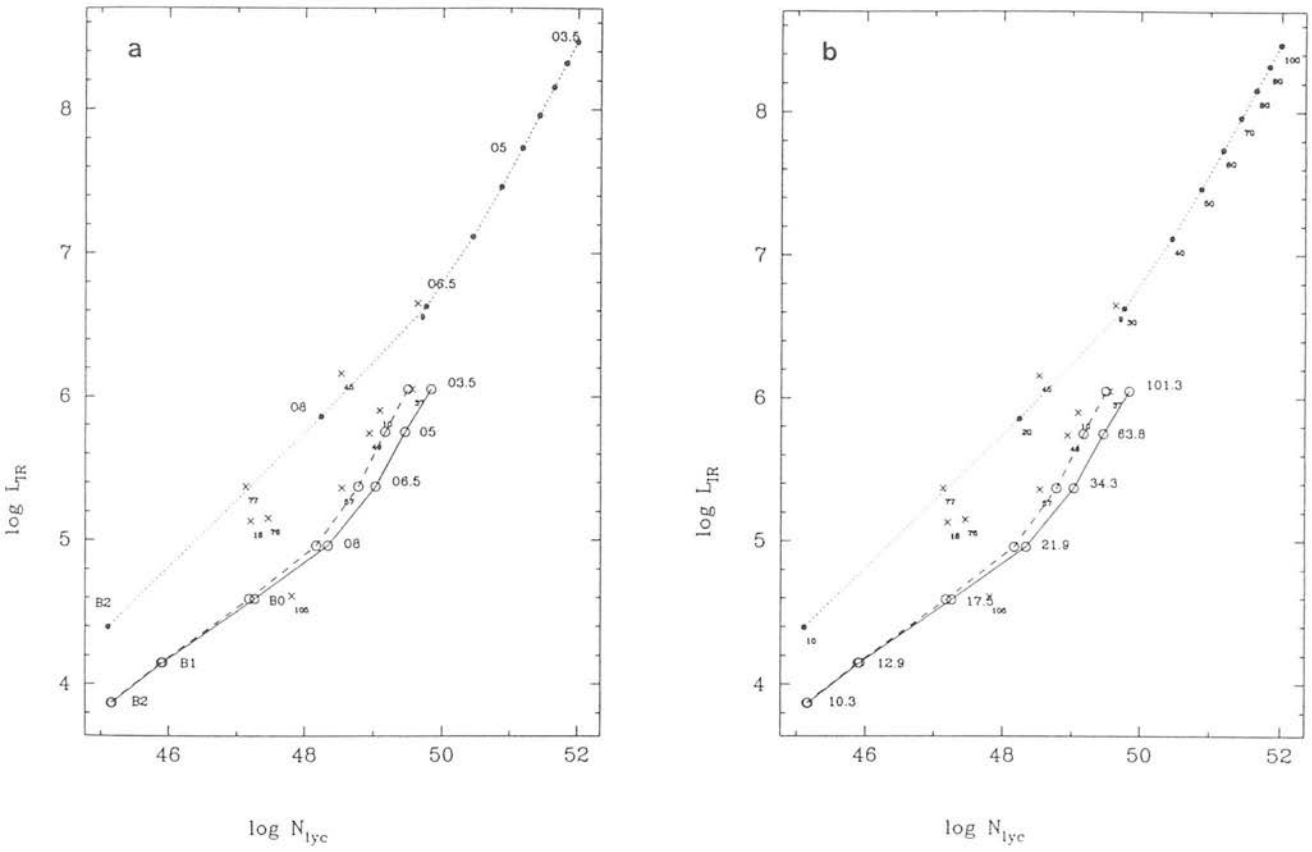

Figure 4.7: Log L_{IR} *vs.* log N_{Lyc} for (a) spectral types and (b) masses of stars. The lower two curves depict values for a single star for a non-dusty (solid curve) and dusty (dashed curve) HII region. The dotted curve joins values for a cluster of stars assuming the spectral type (fig 4.7a) or mass (fig 4.7b) labelled is the most massive star in the cluster.

$$R^2 = R_0^2 + D^2 - 2R_0 D\cos l \tag{4.8}$$

where V_R is the radial velocity with respect to the sun, R is the distance of the object from the Galactic centre, R_0 is the distance of the sun from the galactic centre and l and b are the Galactic longtitude and latitudes respectively, of the source. The factor 30 is taken from Oorts' constants which describe differential Galactic rotation. From this quadratic equation, for R less then R_0 two distances are derived, near and far distances. The best distance estimate is then inferred by a number of techniques *e.g.* from positions with respect to the 3kpc spiral arm, from optical luminosities or from RRL velocities on the premise that the cloud velocity exceeds the recombination line velocity, see Downes *et al.* (1980) for a discussion; disagreement in preferred distances between authors is common. Indeed for G9.617, the far distance of 19.1kpc was used, the near distance of 0.6kpc may be more realistic.

The rest of the objects plotted in figs 4.7a,b fall into the region between curves for single stars and clusters of stars. Deviations from either curve can be explained if the powering source consists of two or more stars of the same temperature or mass. However, a distribution of star masses is more probable. In this case, a further explanation is possible because the IMF is only a statistical description of the stellar population. Hence, in any real young cluster of stars the numbers of stars may be quite small and quantization noise may be significant.

Therefore, the ionization structure of these HII regions cannot be established conclusively, and the best estimates remain that the effective temperature of the source will lie between the single star and cluster temperature limits as calculated in section 2.6, and some other method is needed to differentiate between a single star or a cluster of stars as the powering source. Many authors use fine structure lines in the far–infrared to determine effective temperatures (Lacy *et al.* 1982, Hoare *et al.* 1991 and Simpson and Rubin 1984). By measuring pairs of line ratios, electron temperatures and densities in the HII region are estimated (section 1.2.3) and then compared with predicted line ratios from stellar atmosphere models to obtain the best fit estimate for the stellar temperature. However, for the complex heavier elements the atomic data are much more uncertain and many more approximations need to be included into photoionization codes for such

atoms than for the simpler two electron helium atom.

Interestingly, effective temperatures obtained by these authors who have studied one or more HII regions in detail lie in the range 33-38,000K. This result is suggestive of a sampling bias of HII regions with effective temperatures not greater than 40,000K, thus Shields' models may prove difficult to verify.

4.5.4 HeI 2.113 μm blend

To try to place further constraints on the parameters n_e, T_{eff} and microturbulence in these compact HII regions, the HeI 2.113μm blend was measured. This blend was detected convincingly in G45.454 and G49.491, *i.e.* the measured signal was greater than 3 times the 1σ errors and the best χ^2 fit was credible. The blend was not detected in any of the other objects, mainly because of the poor resolution with UKT9. The fitting procedure was the same as described in section 3.2. Observed ratios for HeI 2.113μm/Brγ are 0.029±0.010 and 0.035±0.007, and for HeI 2.113/HeI 2.058μm are 0.052±0.012 and 0.042±0.008 respectively. Theoretical ratios for HeI 2.113μm/Brγ are 0.040 (T_e=10,000K) and 0.027(T_e=5,000K) so long as stellar temperatures are greater than 38,000K (non dusty models), and greater than 35,000K (dusty models), see section 3.3. This assumption is valid if single star temperatures are appropriate for these two HII regions which appears to be the case (see fig 4.5, fig 4.6). Theoretical HeI 2.113/HeI 2.058μm ratios are 0.050(T_e=10,000K) and 0.039(T_e=5,000K) for $n_e=10^2 cm^{-3}$ and 0.032 for $n_e=10^4 cm^{-3}$ (section 3.3).

As discussed in section 3.3.3, optical depth effects in the HeI 2.113μm line need to be accounted for. The results for the two electron densities are now considered. Assuming these objects to be lower density, nearer $n_e=10^2 cm^{-3}$, then the optical depth in the 3889Å line, τ(3889) is small and optical depth effects negligible. The HeI 2.113μm/Brγ and HeI 2.113/HeI 2.058μm ratios of these two objects observed would then be consistent with an electron temperature model in the range T_e=5–10,000K and turbulent motions are not evident. Electron temperatures from Downes *et al.* (1980) are 7400±3000K for G45.454 and 7000±3000K for G49.491 in good agreement with these predictions.

For G45.454, a H110α radio recombination line FWHM velocity of 28 kms^{-1} is listed by Downes *et al.* (1980). This implies a microturbulent FWHM velocity of $\sim$ 20 kms^{-1} at T_e=10,000K if this broadening is purely because of microturbulence. This velocity would increase theoretical HeI 2.113/HeI 2.058μm ratios to 0.069(T_e=10,000K) for $n_e=10^2$cm^{-3} and a corresponding value of 0.063 for T_e=5,000K. Only the latter value is consistent with observations. The observed HeI 2.113/HeI 2.058μm ratio presents no evidence for microturbulence in G49.491.

Meanwhile, for a density nearer $n_e=10^4$cm^{-3}, values for τ(3889) are larger for the compact HII regions since they are generally larger sources than the UCHII regions. Therefore, an enhancement of 1.4–1.5 is expected (see section 3.4.1) bringing expected theoretical values for these two compact HII regions to be HeI 2.113μm/Brγ $\geq$ 0.056 (T_e=10,000K), 0.038 (T_e=5,000K) and HeI 2.113/HeI 2.058μm $\geq$ 0.045. The HeI 2.113μm/Brγ ratio for G45.454 is too high for this density, thus a lower electron density must be attributed to G45.454. Only the lower electron temperature value is in agreement the observed HeI 2.113μm/Brγ ratio for G49.491 at this electron density. This result agrees with the the observed HeI 2.058μm/Brγ ratio for G49.491 (section 4.5.2). With the addition of a microtubulent FWHM velocity of 20 kms^{-1} the HeI 2.113/HeI 2.058 increases to 0.062 and is too high for G49.491.

Therefore it is possible to conclude that in G45.454 the electron density is lower than $n_e=10^4$cm^{-3} and microturbulent velocities may be present, in quantitative agreement with RRL observations. In G49.491, either the electron density is nearer $n_e=10^2$ cm^{-3} and the electron temperature has a value in the range T_e=5,000–10,000K, consistent with RRL electron temperature predictions or, the electron density is higher and the electron temperature is nearer T_e=5,000K. Both conclusions are in agreement with the HeI 2.058μm/Brγ observations of G49.491. It should be noted that the observed HeI 2.058μm/Brγ ratio is the largest in the sample and does not represent general observed HeI 2.058μm/Brγ ratios in the compact HII region sample.

Therefore it does seem possible to conclude that the general case of lower electron densities is correct as suggested from the HeI 2.058μm/Brγ observed ratios of these objects from the models of chapter 2. However, to be consistent with the models of

Shields the electron densities need to be higher than $n_e=10^2 cm^{-3}$.

This discussion is continued in the general case, in light of predictions from Shields' models, namely the decrease in the neutral helium fraction with increasing T_{eff}. For the HeI 2.113μm/Brγ ratio, the ratio would not be expected to drop off rapidly at higher T_{eff}, since the decrease in neutral helium to hydrogen fraction with higher stellar effective temperatures would not be amplified by resonant effects in HeI. Therefore, if models of the HeI 2.113μm/Brγ ratio were produced by Shields, using the same formulism as for the HeI 2.058μm/Brγ, they would also be expected to saturate. Another test of Shields models would be to examine the HeI 2.113/HeI 2.058 μm ratios in HII regions with effective temperatures greater than 40,000K, or indeed planetary nebulae (see also chapter 6), to look for a correlation between higher temperatures and increasing ratios. Again, from the observations in chapter 3 and 4 no evidence of such a relation is apparent, but further constraints on effective temperature are needed to conclusively affirm this prediction. Therefore either the effective temperature is less than T_{eff}=40,000K for all the compact and UCHII regions observed, or the dramatic drop off of the HeI 2.058μm/Brγ ratio for T_{eff} >38,000K predicted from Shields' models is too steep.

It would be useful to summarize the conclusions for each compact HII region at this stage; however for observations of all these HII regions both single star temperatures and cluster temperatures (excluding unphysical values) are in agreement with the models of chapter 2 for the two electron densities and also in agreement with the model by Shields for $n_e=10^4 cm^{-3}$, except for G105.627. The predicted model for G105.627 is a single star dusty HII region model (see fig 4.5, fig 4.7) for $n_e=10^4 cm^{-3}$ with an effective temperature T_{eff} ~32,000K. In section 4.5.1, evidence from S^{+++} observations (Simpson and Rubin, 1990,) of a number of compact HII regions suggests that effective temperatures are less than T_{eff} ~40,000K in these objects. G37.874 is the only compact HII region where such an effective temperature is consistent with the lower limit cluster temperatures (table 2.7).

From RRL measurements, microturbulence is possible in some or all of the HII regions. Results from comparison of observations with Shields' models are generally unchanged with the addition of microturbulence, *i.e.* the $n_e=10^4 cm^{-3}$ model still remains

in agreement with observations. However, including microturbulence into the models of chapter 2 suggests electron densities must be greater than n_e=10^2cm^{-3}. It is clear that at least one of n_e, T_{eff} and V_{Turb} must be constrained in order to make any accurate predictions about the other physical parameters.

4.6 Conclusions

Observations of the HeI 2.058μm, HeI 2.113μm and Brγ lines were made for HII regions selected on the premise of larger source sizes than the UCHII region sample of chapters 2 and 3. The observed HeI 2.058μm/Brγ ratios are consistent with lower electron densities $n_e \geq 10^2$cm^{-3} than those of the UCHII region sample, suggesting that these larger sources have expanded to lower electron densities, and hence collisonal excitation is not an important process.

Another plausible reason why lower HeI 2.058μm/Brγ ratios are observed in these objects is lower effective temperatures. From single star temperatures derived from radio flux measurements this seems to be the case for four objects in fig 4.5. Examining the observed ratios against both the models of chapter 2 suggests that if single star temperatures are upper limits and cluster temperatures lower limits to the actual temperature in a nebula, then all compact HII regions, except G105.627, can be represented by an electron density model in the range n_e=10^2–10^4cm^{-3} with any electron temperature in the range T_e=5,000–10,000K, the higher density model being an upper limit. G105.627 agrees with an HII region model for n_e=10^4cm^{-3} and a single star of T_{eff} ~32,000K. The inclusion of a microturbulent FWHM velocity of ~28 kms^{-1}, as proposed for the UCHII regions in chapter 2, rules out this lower density model. In this case, the lower ratios must be attributed to slightly lower effective temperatures in this sample than in the UCHII region sample. Thus the HeI 2.058μm/Brγ ratios lie on the rising part of the model curves.

Shields' models reveal a probable error in the models of chapter 2 which is the result of the neutral helium to hydrogen fraction decreasing with increasing T_{eff}. This does not present any discrepancies in interpreting the results from the two sets of models in

these compact HII regions, since effective temperatures are probably not greater than 38,000K in these objects, the value above which the Shields' models turn over. Shields' models calculated for mean electron temperatures T_e=7,500–10,000K, where the electron temperature varies with radius, also rule out the lower density model, except for G76.188 and G77.965. Densities greater than this would be consistent with the observations. The inclusion of microturbulence requires G77.965 to have an higher electron density.

The HeI 2.113μm blend has been detected in two objects, and these observations suggest that lower density models than $n_e=10^4 cm^{-3}$ are indeed plausible in the general case. It is clear that electron densities and/or effective temperatures need to be constrained further to establish any firm conclusions. However, it appears that lower electron densities coupled with lower effective temperatures provide the explanation of lower HeI 2.058μm/Brγ ratios in this compact HII region sample. Effective temperatures may be measured from far-infrared fine structure lines and model atmosphere codes. Electron densities are studied in detail in chapter 5.

Chapter 5

Electron density determination in HII regions

5.1 Introduction

The HeI 2.058 μm/Brγ ratio has been studied in UCHII regions and compact HII regions in the previous chapters. All the models used for comparison with observations have been formulated on the pretext that a constant density is appropriate for these objects. Electron densities are generally presumed to be of the order n_e=10^4cm^{-3} for UCHII regions and lower for compact HII regions. These values are based on electron densities calculated from radio fluxes using either flux densities integrated over the source or peak flux densities per beam multiplied by the source size. Constant electron densities inferred from He^+/H^+ ratios, specifically the HeI 2.058 μm/Brγ ratio, may not necessarily reflect the same density values, particularly if the HII region is not homogeneous. In section 5.2, an in depth discussion of different methods and associated caveats in calculating electron densities is performed.

The aims of this chapter are twofold, firstly to calculate electron densities for the HII regions studied to date, to test whether the initial assumption, of electron densities of the order n_e=10^4cm^{-3} for UCHII regions and lower for compact HII regions, is valid here. Radio continuum measurements calculated for the objects in chapters 2 and 4 are used for

these calculations in section 5.3. Comparison of electron densities deduced from observed HeI 2.058μm/Brγ ratios and those calculated from radio continuum measurements for the HII regions is carried out in section 5.3.1.

Secondly, in previous chapters it has been shown that local conditions and physical processes affect the HeI 2.058μm/Brγ and other He^+/H^+ ratios. Thus, general HII region recombination line models have to be refined for each HII region. A next stage in modelling line ratios in HII regions is to substitute appropriate density distributions into individual models. Crude density gradient models reflecting different HII region morphologies are constructed in section 5.4 along with more detailed density gradient models of two UCHII regions obtained from Simpson and Rubin (1984) and Colgan *et al.* (1991). From this modelling some insight can be gained into the accuracy of assuming constant electron densities; in particular to address whether discrepancies between observed HeI 2.058μm/Brγ ratios and those from constant model predictions may be attributable to the constant density approximation, rather than microturbulence. Conclusions are then drawn in section 5.5.

5.2 Electron Densities

Two different methods are widely used to determine electron density. The electron density of a HII region is commonly calculated from either radio continuum measurements or fine structure line ratios. The advantages and disadvantages of both methods are discussed in detail below.

The advantage of deriving electron densities from radio measurements ~~are~~ is that these measurements are unaffected by interstellar extinction and the density derived is only weakly dependent on electron temperature (eqn 5.1). However, the distance to the source and the source size must be known (eqn 5.1); both parameters are subject to uncertainties. Distance ambiguities are discussed in section 4.5.3, and disagreement in source size is rife between different authors and papers *c.f.* source sizes by Zoonermatkermani *et al.* (1990) and Wood and Churchwell (1989). This may be partly because the resolution of the instrument varies with frequency. The resultant density will be an rms density

averaged over the nebula.

Alternatively, fine structure line ratios, *i.e.* the ratio of a pair of lines which are emitted by an excited atom from two levels with nearly the same energy, are often used. By examining collisional effects in detail the electron density in a nebula may be inferred.

Figs 5.1A and B show the dependence of the far-infrared fine structure line pair ratios of [OIII] 51.81/88.33μm and [SIII] 18.7/33.6μm respectively, on electron density. To understand the curves and their asymptotic behaviour it is necessary to consider two limits. In the low density case, every collisional excitation is followed by radiative decay and emission of a line photon. In this scenario, the line pair ratio is purely the ratio of the collision strengths which for a pair of lines with a small energy difference, is governed by the statistical weights of the two upper levels. The intercept on the y axis, which represents the line ratio in the low density limit, is thus a measure of the statistical weights. Collision strengths vary slightly with electron temperature as shown by the dotted lines (see section 1.2.3). The critical density, n_c of a transition is defined as the density at which collisional de-excitation becomes equally as important as spontaneous decay. Critical densities are $n_c = 3.8\times10^3$ and $1.7\times10^3 cm^{-3}$ for the [OIII] 51.8 and 88.3μm lines and $n_c = 2\times10^4$ and $6.5\times10^4 cm^{-3}$ for the [SIII] 18.7 and 33.6μm lines. Thus, as electron density increases collisional de-excitation becomes more important. In the high density case, there is a large probability of collisional de-excitation, thus significant level populations are built up in the two levels. Only after a number of repeated collisional excitations and de-excitations will a spontaneous transition occur, resulting in a line photon. In this case, the fine structure line pair ratio is a function of the two level populations, which are in turn given by the relative statistical weights, multiplied by the relative transition probabilities of radiative transitions from the two upper levels. Thus the line ratio will saturate as shown in figs 5.1A,B.

In the intermediate case, it is between the two critical densities of the two line transitions concerned, that the fine structure line ratio is most sensitive. Different line pairs in different species are sensitive to different density ranges. Examples of a number of fine structure lines and their corresponding sensitivities are given by Rubin *et al.* (1994).

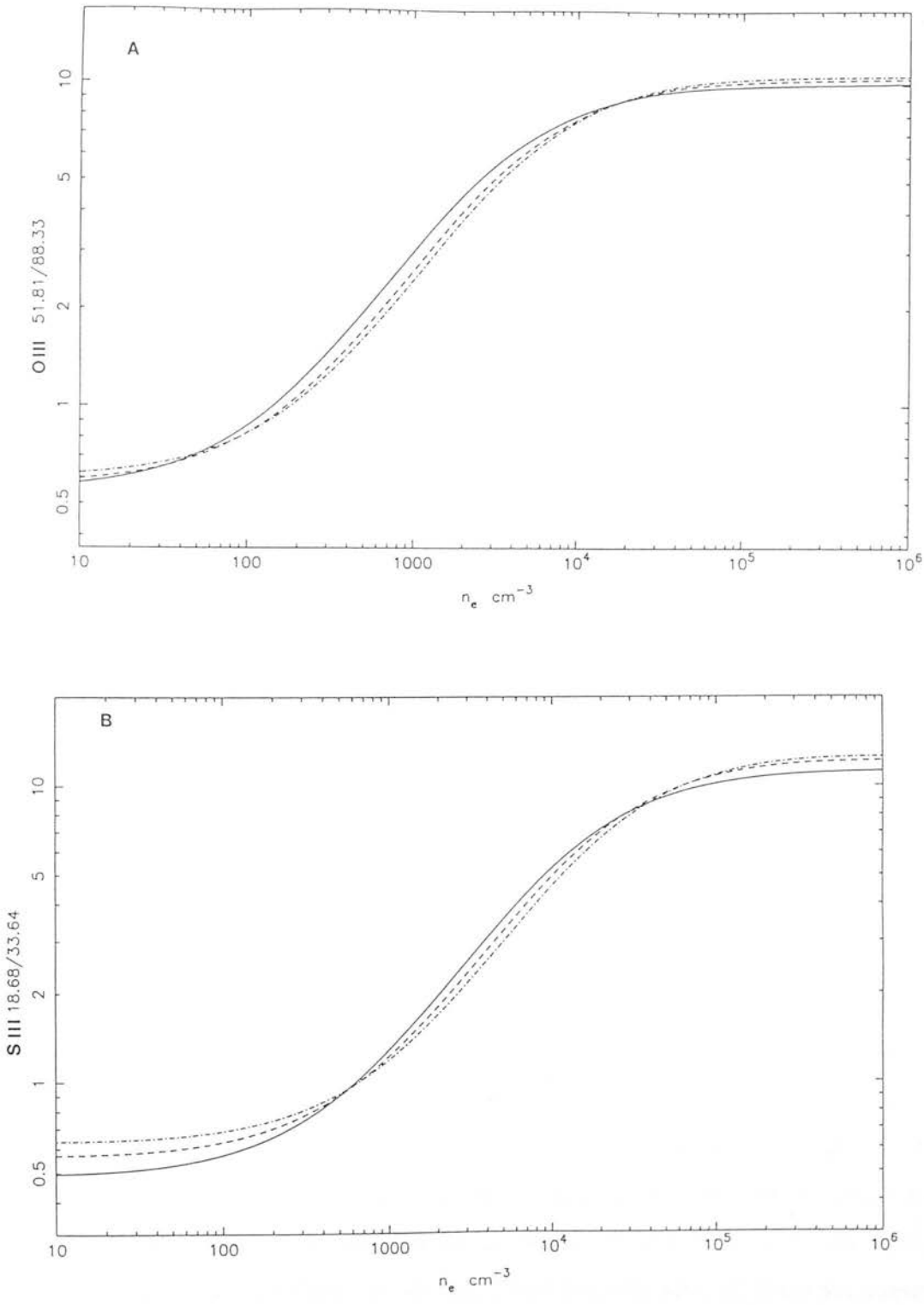

Figure 5.1: (A) the [OIII] 51.8/88.3μm and (B) [SIII] 18.7/33.6μm forbidden line ratios as a function of n_e.

This electron density determination is independent of size of and the distance to the nebula. Far-infrared fine structure line ratios are fairly insensitive to electron temperature (fig 5.1A,B) and extinction.

In contrast to the density inferred from the radio which is a global average, the fine structure line ratio is a particular measure of the density in the ionized zone of the ion concerned. Thus for example, if the density in the ionized zone is well above the critical density of the two fine structure lines measured, the line ratio will just reflect the saturated value. Differences in densities derived from the two methods may reflect small scale structure *i.e.* clumping in the ionized gas.

Wood and Churchwell (1989) observe different geometries resembling the structure of compact HII regions. Cometary, core–halo, shell, spherical and irregular or multiply peaked morphologies are established from their appearance in radio maps at 5 and 15 GHz. The difference in the densities derived from radio continuum measurements and those inferred from fine structure line calculations should be highlighted when considering core-halo sources where the emission from the O[III] and S[III] ionized species may be dominated by the greater volume of diffuse emission.

The HeI 2.058μm recombination line becomes dominated by collisional de-excitation from the 2^3S to the 2^1P level above n_c $\sim 5\times10^3 cm^{-3}$ (Osterbrock 1989). Therefore like the far infrared O[III] and S[III] lines, the HeI 2.058μm/Brγ ratio is potentially an indicator of electron density also. However, this is not the case unless the effective temperature T_{eff} is accurately known, since the HeI 2.058μm/Brγ ratio is highly sensitive to stellar effective temperature, below 38,000K for the models of chapter 2 and for all temperatures for Shield's models, discussed in chapter 4. This ratio is heavily influenced by optical depth effects in the resonant 1^1S–2^1P level which is affected by local conditions. Physical conditions which affect the ratio are the relative neutral helium to hydrogen fractions, microturbulence in the nebula and also to a lesser extent electron temperatures and helium abundance. Therefore, only after all these parameters are ascertained can any reliable electron density estimate be made.

Consequently, radio measurements, although subject to distance and source size estimate errors, present a much more reliable estimate of the electron density than densities

inferred from HeI 2.058 μm/Brγ ratios.

5.3 Integrated electron density calculations

On the basis of the previous discussion, best estimates of electron densities are now calculated individually for the UCHII and compact HII region samples of chapters 2 and 4. The rms electron density can be calculated from an optically thin radio flux density, S_ν, using the equations of Panagia and Walmsley (1978):

$$n_e = 311.2 \left(\frac{S_\nu}{Jy}\right)^{0.5} \left(\frac{T_e}{10^4 K}\right)^{0.25} \left(\frac{D}{kpc}\right)^{-0.5} b(\nu, T_e)^{-0.5} \theta_R^{-1.5} \tag{5.1}$$

where $b(\nu, T_e)$ is a form of the Gaunt factor. Assuming an electron temperature of T_e=10,000K and S_ν as the 15GHz integrated flux density, eqn 5.1 can be written:

$$n_e = 167064 \times \left(\frac{S_\nu}{Jy}\right)^{0.5} \left(\frac{D}{kpc}\right)^{-0.5} \theta_R^{-1.5} \tag{5.2}$$

The underlying assumption in this equation is that the continuum is optically thin at 15GHz, for the HII regions studied. Optical depths estimated for the compact HII regions in section 4.3 seem to corroborate this assumption. For the UCHII regions optical depth values given in table 2.4 suggest that the radio continuum may not be completely optically thin at 15GHz, therefore the 15GHz values were corrected for optical depth effects analogous to to the correction applied in eqn 2.2.

Distances for the UCHII regions are given by Wood and Churchwell (1989) who take these values from various authors, *e.g.* Downes *et al.* (1980) and Wink *et al.* (1982). Downes *et al.* (1980) also provide distances for several of the compact HII regions. For the rest of the sample the distances were derived from local standard of rest (LSR) velocities given by Lockman *et al.* (1989) or estimated from CO maps by Sanders *et al.* (1986) from eqns 4.7 and 4.8. The LSR velocities were transformed into radial velocities w.r.t. the sun using the Starlink program RV. These distances are given for each HII region in table 5.1.

θ_R is the source radius in arcsec, estimates of which vary from paper to paper. For the compact HII region sample, source sizes from Zoonermatkermani *et al.* (1990) were initially considered, and source sizes from other authors were used in the density calculations in cols 6,7 and 9 of table 5.1 for comparison. Likewise, for the UCHII region sample, Wood and Churchwell (1989) source sizes were used and electron densities from different source sizes given in cols 7–9 of table 5.1. The source radii from the two named authors are given in column 4 of table 5.1. For the Zoonermatkermani *et al.* (1990) objects, the source size listed in table 5.1 is the geometrical mean radius determined from FWHM values obtained from gaussian fits to the major and minor axes of the source. Wood and Churchwell (1989) have different definitions of source size dependent on their morphological classification. The morphology types for the HII regions classified by Wood and Churchwell (1989) and Kurtz *et al.* (1994) are given in table 5.1. For cometary sources the geometrical mean diameter was ascertained as described above and the radius value, taken from table 11, Wood and Churchwell (1989), is given in table 5.1. For core-halo sources the source radius in table 5.1, comes from the mean value of the minimum and maximum halo diameter listed by Wood and Churchwell (1989) at the 10% level. Finally, for the HII regions designated as spherical sources the radius of the source in table 5.1 is taken from table 16 (Wood and Churchwell 1989). Several UCHII regions have also been catalogued in the Zoonermatkermani *et al.* (1990) survey. These source sizes are 1–3 times smaller than those quoted by Wood and Churchwell (1989). Recently, Kurtz *et al.* (1994) and Becker *et al.* (1994) have published further observations of the compact HII regions at 8 and 15GHz, and compact and UCHII regions (according to their classification in chapters 2 and 4) at 5GHz respectively, which give different values for source sizes previously quoted for these objects. Immediately it is obvious that there is disagreement between authors and papers, which as described in section 5.2 is at least partly due to the dependence of the resolution of the instrument on frequency.

Considering the errors on the aforementioned three parameters, namely uncertainties in optical depths and thus 15GHz fluxes, distance ambiguities and differing source sizes, the derived electron densities should be considered qualitative and not definitive. Electron densities calculated from eqn 5.1 are listed in cols 6–9 in table 5.1 under the author and year from which the source radius was obtained. Distance and 15GHz flux

Object	S_{15GHz} Jy	Distance kpc	θ_R $\widehat{''}$	MT[1]	Integrated radio n_e (cm^{-3}) W&C	K, W& C	Z	B	peak/beam W& C
G9.617	1.754	19.1	7.5	I		2.95×10^3	2.46×10^3	4.66×10^3	
G10.965	0.617	18.3	7.8				1.41×10^3	4.79×10^3	
G18.304	0.084	4.5	7.75	MP		6.25×10^3	1.06×10^3	1.36×10^3	
G37.874	2.105	11.5	4.9	C		2.23×10^4	6.56×10^3	1.11×10^4	
G45.454	0.428	9.7	8.75	C	4.95×10^3		1.36×10^3		2.1×10^4
G49.491	5.340	4.1	8.85				7.27×10^3		
G57.548	1.230	11.6	5.0				4.89×10^3		
G76.188	0.068	6.6	4.1	MP		1.66×10^3	2.08×10^3		
G77.965	0.034	6.3	5.3	I		3.43×10^3	1.01×10^3		
G105.627	0.406	4.0	0.495				4.86×10^3		
G5.48	0.109	14.3	3.25	CH	2.78×10^3		1.20×10^3	1.37×10^3	1.3×10^4
G5.97	0.504	1.9	6.75	CH	5.49×10^3				3.7×10^4
G15.04	0.073	2.1	0.295	S	3.03×10^5				3.2×10^5
G29.96	2.161	9.0	3.35	C	1.35×10^4		8.12×10^3	1.32×10^4	4.4×10^4
G35.20	2.358	3.2	2.75	C	2.88×10^4				8.6×10^4
G43.89	0.455	10.3	1.75	C	1.42×10^4		8.57×10^3		2.3×10^4
G45.07	0.319	9.7	0.455	S	1.42×10^5				2.2×10^5
G45.12	2.415	9.5	1.95	C	3.71×10^4		8.52×10^3		1.1×10^5

Table 5.1: Integrated electron densities in HII regions.

[1] Morphological Type (Wood & Churchwell, 1989). C= cometary, CH=core halo, I=irregular, MP=Multiply Peaked, S=spherical.

W&C=Wood and Churchwell (1989). K,W&C=Kurtz, Wood and Churchwell (1994). Z=Zoonermatkerani *et al.*(1990). B=Becker *et al.* 1994.

uncertainities give errors of $\sim$ 100% on calculated electron densities. Electron densities calculated by Wood and Churchwell (1989) using peak flux densities per beam are given in col 10, table 5.1.

Consultation of table 5.1 reveals that despite source size uncertainties, electron densities obtained for the UCHII regions, using source sizes estimates from Zoonermatkermani *et al.* (1990), Becker *et al.* (1994) and Wood and Churchwell (1989), remain in the range n_e=10^3–10^5cm^{-3}. Excluding the objects G5.48 and G5.97 which have core-halo geometries, the values of n_e for UCHII regions are constrained to n_e=10^4–10^5cm^{-3}; these integrated electron density values are not less than 3 times the electron densities obtained from Wood and Churchwell (1989) using peak measurements per beam. Internal differences in integrated electron densities derived from Zoonermatkermani (1990) source sizes and those derived using Wood and Churchwell (1989) values are a factor of $\sim$ 2–4 (higher, using the latter values for the source size). For the core-halo sources the radio emission may be better represented by the core diameter rather than the mean of the core+halo diameter used here. This would lead to higher electron densities than those listed in table 5.1.

For the compact HII regions, using Zoonermatkermani *et al.* (1990) source sizes, electron densities are of the order n_e=10^3cm^{-3}. Recent measurements by Becker *et al.* (1994) at 5GHz, give smaller source sizes which result in electron densities 1–3 times higher than those found using previous source sizes. Kurtz *et al.* (1994) give source sizes a factor 1–3 smaller than the nominal Zoonermatkermani *et al.* (1990) source sizes, which results in electron densities a factor of 1–6 larger ($n_e \propto \theta_R^{-1.5}$).

It is still possible to conclude that for the compact HII regions, all these source size estimates yield electron densities which span the range n_e=10^3–10^4cm^{-3}. Thus the initial assumption that expected densities of the UCHII regions should be of the order n_e=10^4cm^{-3}, and that of compact HII regions lower, found here to be n_e<10^4cm^{-3}, is verified in general.

However, compact HII regions densities do not appear to be low as predicted from the HeI 2.058μm/Brγ ratio models proposed in chapter 2 and investigated for these objects in chapter 4, for which the n_e=10^2cm^{-3} model agrees with the observations.

Therefore microturbulence is also expected in compact HII regions if these models are to be credited. Alternatively, Shield's (1993) model for $n_e=10^4 cm^{-3}$ is consistent with the observations. Comparison of the electron densities derived in this section and electron densities inferred from HeI 2.058μm/Brγ observations are discussed in detail below.

5.3.1 Comparison of electron densities with HeI 2.058 μm/Brγ ratios

In fig 5.2 electron densities derived in section 5.3, are plotted against observed HeI 2.058μm/Brγ ratios and their 1σ errors. Source sizes from Wood and Churchwell (1989) for the UCHII regions, and Zoonermatkermani (1990) for the compact HII regions were used. The compact HII region data are represented by crosses and the UCHII region data by filled circles. Error bars on electron density estimates are not plotted, since different estimates are dominated by systematic errors, which cannot be accurately represented by formal error bars. There are two points to note, a) there does appear to be a trend that electron densities are higher for higher observed HeI 2.058μm/Brγ ratios in the compact HII region sample. From a least squares fit to the data, a correlation coefficient of 0.82 for 10 data points (99.8% significance) was found. b) a similar trend is not apparent amongst the UCHII regions (correlation coefficient of 0.09). The vertical error bars on the observed ratios bring all the data points to overlap, thus the UCHII regions may all have very similar HeI 2.058μm/Brγ ratios.

To understand why the electron density should vary so greatly for a given observed HeI 2.058μm/Brγ ratio one must return to model HeI 2.058μm/Brγ ratio predictions. Figs 2.2, 2.3 and 4.3 and 4.4 show that for a given electron density there are a range of theoretical HeI 2.058μm/Brγ ratios possible since the ratio is a function of stellar temperature, T_{eff}. Consideration of the models formulated in chapter 2 and those by Shields, reveals the HeI 2.058μm/Brγ ratio is possibly only constant above T_{eff}=38,000K (35,000K dense dusty models). Therefore only for this case would an obvious correlation between electron density and observed HeI 2.058μm/Brγ ratios be expected.

Fig 5.3 shows a plot which estimates a theoretical HeI 2.058μm/Brγ ratio as a function of constant electron density. This plot is based on the chapter 2 models for T_e=10000K (solid line) and T_e=5,000K (dashed line) assuming the stellar temperature

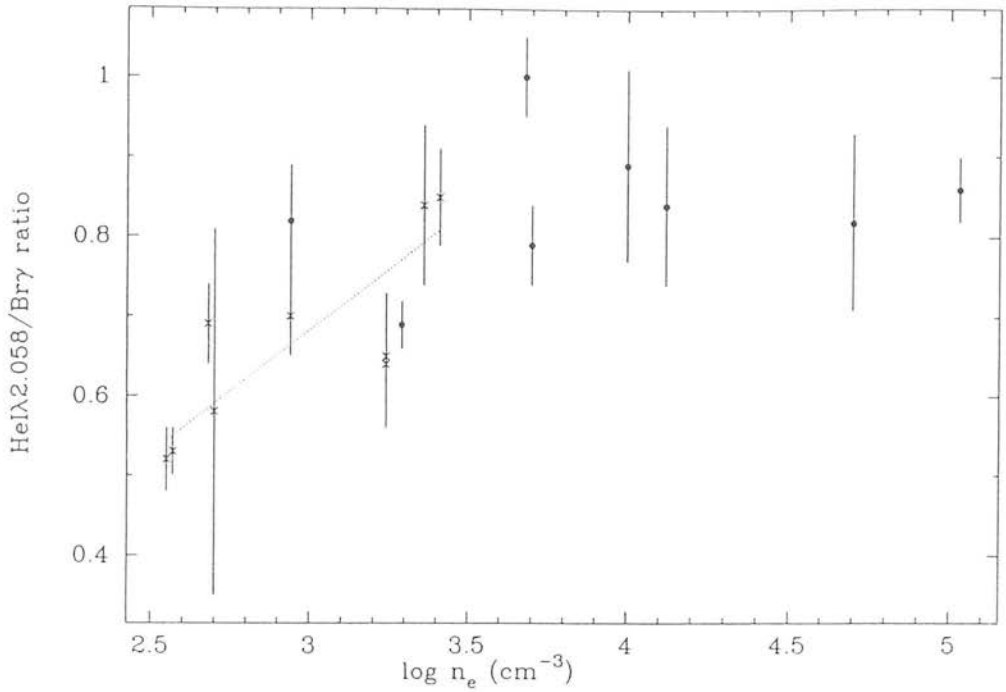

Figure 5.2: Observed HeI 2.058μm/Brγ ratio *vs.* electron density, n_e. n_e values are calculated from radio continuum measurements. The filled circles and crosses represent the UCHII region data and the compact HII region data respectively. The dotted line is the best fit to the compact HII region data.

T_{eff} is greater than 38,000K, thus the ratio can be represented by a single value for a given density. It is then easier to see how the ratio increases as electron density increases due to increased probability of collisional de-excitation from HeI 2^3S level to the 2^1P (section 2.5.2). The electron densities derived in section 5.3 infer the observed HeI 2.058μm/Brγ ratio to lie between 1.06 and 1.38 at T_e=10,000K, (0.82 and 0.95 T_e=5,000K) for the UCHII region sample and between 0.91 and 1.28 (0.78 and 0.89 T_e=5,000K) for the compact HII region sample (see fig 5.3). Observed HeI 2.058μm/Brγ ratios range between 0.68 and 1.00 for the UCHII regions (table 2.4) and 0.53 and 0.85 for the compact HII regions (table 4.6). The ratio for G76.188 is only 0.17, this value is much lower than that obtained for any other object and is not included in the following comparison since the effective temperature for this object is undoubtedly less than 38,000K (table 2.6).

If the model in fig 5.3 is considered valid, microturbulence is required for consistency with the observations for the T_e=10,000K models. Microturbulence is also required for agreement between some of the observed HeI 2.058μm/Brγ ratios for the T_e=5,000K

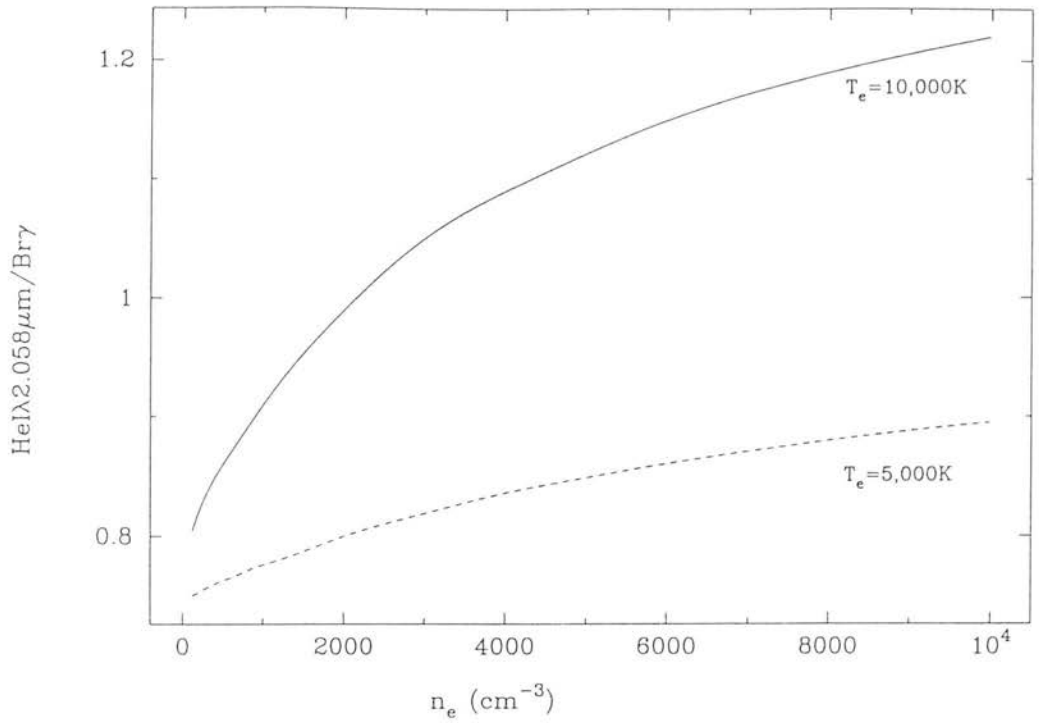

Figure 5.3: Predictions of the theoretical HeI 2.058μm/Brγ ratio as a function of n_e for T_e=5,000K and 10,000K.

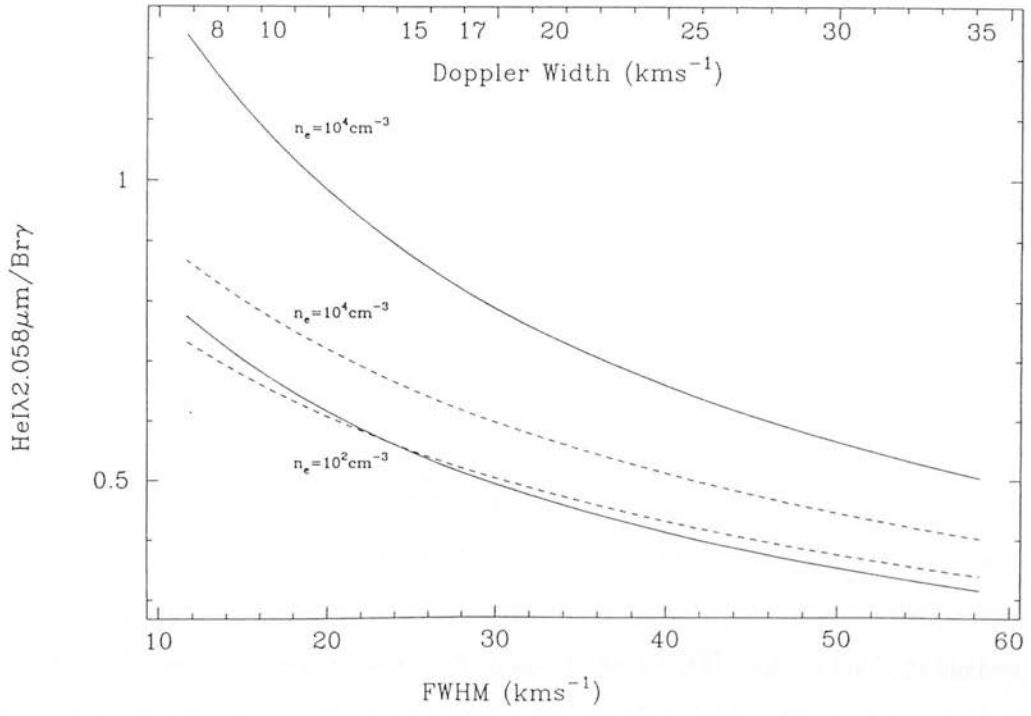

Figure 5.4: Predictions of the theoretical HeI 2.058μm/Brγ ratio with line width for T_e=5,000K (dashed line) and T_e=10,000K (solid line) and n_e=10^2 and 10^4cm^{-3}.

models. There is evidence for turbulent FWHM velocities of up to 50 kms^{-1} and on average 30 kms^{-1} in these HII regions *c.f.* Downes *et al.* (1980). Fig 5.4 depicts the decrease in the HeI 2.058μm/Brγ ratio with increasing microturbulence for the same physical conditions outlined in fig 5.3 for constant electron density values, ne=10^2 and $10^4 cm^{-3}$. From fig 5.4 it is clear that the addition of microturbulence into the appropriate electron density and temperature model can reproduce observed HeI 2.058μm/Brγ ratios.

Therefore observing HII regions with different effective stellar temperatures and varying amounts of microturbulence could mask any correlation between observed HeI 2.058μm/Brγ ratios and electron density. Alternatively, if a constant electron density is not an adequate representation of the density structure in the HII region and or an integrated density inferred from radio measurements is not compatible with the constant density assumed from HeI 2.058μm/Brγ ratios, then a correlatation between integrated or averaged radio values and observed HeI 2.058μm/Brγ ratios is not to be expected. This is the subject of section 5.4.

5.4 Density gradient modelling

Moving onto a detailed examination of electron densities as a function of radius as opposed to using rms and constant electron densities averaged over the source discussed previously, the aim in this section is to examine whether a constant density model is appropriate for HII regions and if turbulent motions are an essential component to model HeI 2.058μm/Brγ ratios.

Several models with different density profiles have been constructed to try to establish the accuracy of the HeI 2.058μm/Brγ ratio calculated with a constant density assumption, compared to the ratio derived using a realistic density distribution as evident from the different geometries observed. Two of the UCHII regions have published mapped density distributions; calculated HeI 2.058μm/Brγ ratios from these models should be a further test of the constant density models. It is worth noting at this point that the observed HeI 2.058μm/Brγ ratios have associated errors between 0.03 and 0.23

corresponding to errors in n_e of order a few hundred to a few thousand cm^{-3} respectively (see fig 5.3). Therefore, only if the difference in HeI 2.058μm/Brγ ratios calculated from constant and realistic density distributions is greater than the observational errors will accurate density calculations be advantageous over the constant density approximation.

Also as discussed above, constant electron densities derived from radio continuum measurements and those predicted from observed HeI 2.058μm/Brγ ratios will intrinsically be different if there is any clumping in the region. Calculating the HeI 2.058μm/Brγ ratio for a density gradient model should give more accurate results as long as the basic assumptions of the model remain valid.

5.4.1 Density distributions–Gaussian Models

In order to construct any electron density model some approximations need to be made. For the following calculations spherical symmetry was assumed and the model nebula divided into volume shells of constant electron density and size ΔR=0.01pc. Blister and bow shock models are discussed in section 1.4 and are favoured as more realistic models of HII regions by several authors. However these geometries are much more difficult to model, for this reason a further discussion of these geometries is refrained from. Next, some density distribution as a function of radius needed to be assumed.

Power law density distributions were initially considered, however a distribution of this type would have to be truncated to avoid an infinite density at the centre of the nebula radius=r_0. Due to the artifical cut off required in these power law models a Gaussian distribution is undoubtedly more physically realistic although still a crude approximation of any of these morphological types. This type of distribution is used as a first approximation. Broadly, a core-halo source can be represented by a very steep gaussian plus a broad shallow gaussian, a spherical source by a steep gaussian and a shell-like source by a gaussian with its centre offset, (*i.e.* a hole in the centre). Illustrative models are shown in fig 5.5 where the peak density is assumed to be $n_e=10^4 cm^{-3}$. Microturbulence was not incorporated into these models.

The integrated HeI 2.058μm/Brγ ratio was then calculated by summing the HeI

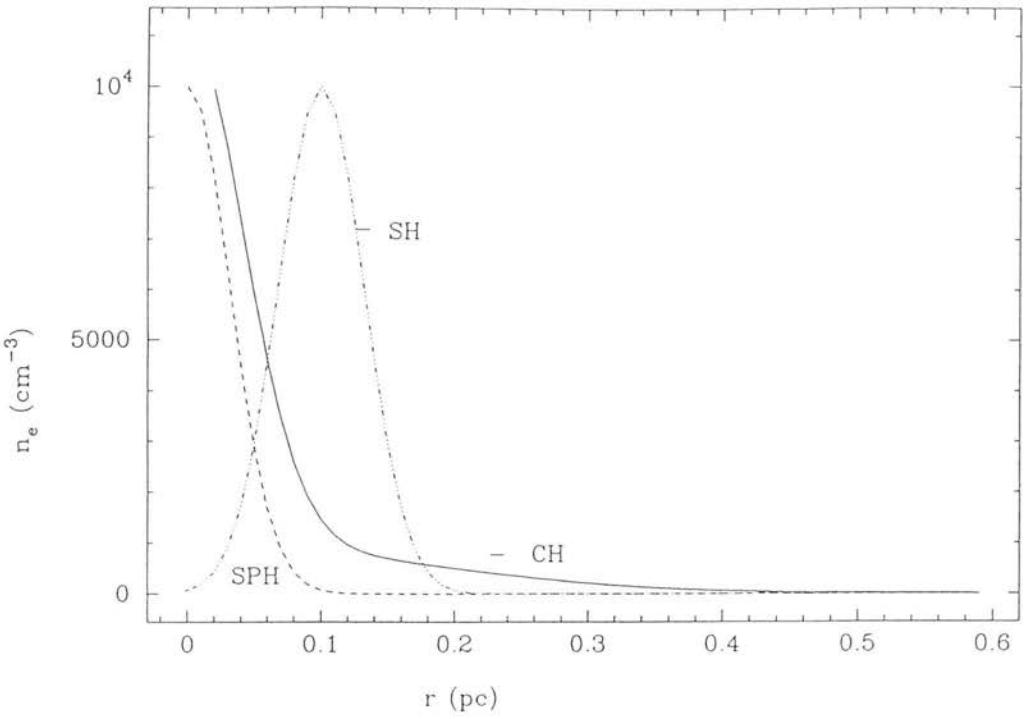

Figure 5.5: Modelled Gaussian density distributions for spherical, shell and core-halo sources as a function of radius.

2.058 μm and Brγ emission coefficients j_{HeI}, $j_{Br\gamma}$ in each volume shell:

$$\frac{I_{HeI}}{I_{Br\gamma}} = \frac{\sum_{i=1}^{n} j_{HeI} \Delta V}{\sum_{i=1}^{n} j_{Br\gamma} \Delta V} \tag{5.3}$$

equivalently,

$$\frac{I_{HeI}}{I_{Br\gamma}} = \frac{\sum_{i=1}^{n} n_e n_{He^+} \left(\frac{hc}{\lambda}\right) \alpha_{eff}(HeI) r^2 \Delta r}{\sum_{i=1}^{n} n_e n_{H^+} \left(\frac{hc}{\lambda}\right) \alpha_{eff}(Br\gamma) r^2 \Delta r} \tag{5.4}$$

Integrated HeI 2.058 μm/Brγ ratios can then be compared to the model HeI 2.058/Brγ ratios of the previous chapters and for an assumed stellar effective temperature and electron temperature a representative constant electron density can be inferred. This "constant" electron density can then be compared to radio peak and integrated electron densities and conclusions drawn.

For such comparisons, the models of chapter 2 with recombination coefficients calculated from Smits (1991a) were used since it is possible to approximately reproduce these HeI 2.058 μm/Brγ ratios as a function of density using eqn 2.7 and values from Osterbrock (1989), see section 2.5.2. Additionally, for these models an exciting temperature

greater than the saturation temperature of 38000K is assumed along with an electron temperature of T_e=10,000K initially. For these conditions the HeI 2.058μm/Brγ ratio has a value of 1.28 for a constant density $n_e=10^4 cm^{-3}$.

For gaussian density distributions for the spherical and shell-like sources given in fig 5.5 peak electron densities of $n_e=10^4 cm^{-3}$ were taken as representative of the peak values per beam given by Wood and Churchwell (1989) in their table 17, and the gaussian distribution of FWHM 0.1pc was chosen as representative of values for spherical and shell-like sources given by table 16, Wood and Churchwell (1989). For the core halo source a gaussian with peak electron density of $n_e=10^3 cm^{-3}$ and much larger FWHM of 0.4pc (representative of halo diameters for the latter half of table 13, Wood and Churchwell 1989) was added to the spherical gaussian model described above. For these three density models in fig 5.5 labelled SPH, SH and CH, representative of spherical, shell and core-halo morphologies, HeI 2.058μm/Brγ ratios of 1.01, 1.07 and 0.95 were found. These values correspond to constant densities of $\sim 2.5\times10^3$, 3.5×10^3 and $1.5\times10^3 cm^3$ respectively.

The integrated ratios are fairly insensitive to the outer radius, *i.e.* the size of the HII region, and the FWHM for these distributions as long as the gaussian is not truncated. The scaling factor which gives the peak density is an important parameter. It is instructive to know for the geometries considered whether the HeI 2.058μm/Brγ ratio is dominated by the peak density, reflects some averaged density over the region or is dominated by lower densities due to extended emission, if applicable, as given from radio continuum measurements.

Firstly considering the spherical and shell like distributions, peak density values were varied between 10^3–$10^5 cm^{-3}$. The integrated HeI 2.058μm/Brγ ratios for the spherical and shell-like density models remained lower than the ratio obtained for an HII region with constant density corresponding to the peak value of that distribution. Equivalently, the constant density corresponding to the integrated HeI 2.058μm/Brγ ratio, is appreciably less than the peak density for the gaussian disributions representing spherical and shell-like HII regions, from which the integrated HeI 2.058μm/Brγ ratio was deduced. Thus the HeI 2.058μm/Brγ ratio represents some average density in the

nebula.

For the core-halo source, the greater the emission in the halo, *i.e.* the larger the peak value of a realistic halo gaussian or equivalently the wider the core distribution for a given halo distribution, the lower the integrated HeI 2.058 μm/Brγ ratio. From the integrated value for this distribution it is apparent that the greater volume of extended emission in the halo is responsible for the electron density deduced from the HeI 2.058 μm/Brγ ratio. Examination of fig 2.2 reveals that the enhancement factor of the HeI 2.058 μm/Brγ ratio varies only by a factor of two with changes in density of over four orders of magnitude n_e=10^2–10^6cm^{-3}. Therefore the ratio is most sensitive to the density occupying the largest volume. Thus any density distribution with a halo volume greater than the core volume will reflect the density in the halo.

In order to examine this effect in more detail, realistic reconstructed mapped density distributions, as opposed to model density distributions, are now considered for two UCHII regions for which detailed density distributions are available in the literature.

5.4.2 Case studies–two UCHII regions

Detailed density distributions have been mapped by Simpson and Rubin (1984) and Colgan *et al.* 1991 for the UCHII regions G29.96 and G45.12 from radio continuum brightness maps. These authors assumed spherical symmetry. It should be noted that spherical symmetry is a first approximation to the actual three dimensional source structure, which may be somewhat complex. Indeed, for this reason, Hoare *et al.* (1991) decided a constant density approximation was as physically realistic as the models of Colgan *et al.* (1991) for G45.12. Furthermore, both G29.96 and G45.12 have designated cometary morphologies by Wood and Churchwell (1989), so spherical symmetry is certainly a rough approximation in these cases.

By replacing each surface brightness contour on the radio map with a circular contour the emission was determined by solving the radiative transfer equation for the brightness temperature:

$$T_{b\nu} = T_e(1 - e^{\tau_\nu}) \tag{5.5}$$

Assuming an optically thin nebula:

$$n_e^2(r)dr = \nu^{2.1} T_e^{0.35} T_{b\nu}(r)dr \tag{5.6}$$

The technique is described by Megeath *et al.* (1990).

The density distributions for G29.96 and G45.12 are given in figs 5.6 and 5.7. For both UCHII regions, conclusions in chapter 3 suggest an electron temperature of T_e=10,000K is representative for these two objects (section 3.4.2). Thus for subsequent conversion of integrated ratios to "constant" electron densities, only the constant density model of chapter 2 for T_e=10,000K is considered.

G29.96

The observed HeI 2.058μm/Brγ ratio for G29.96 is 1.00±0.05 (table 2.4). The density distribution by Simpson and Rubin (1984) is given in fig 5.6, who approximate the asymmetrical structure by circular contours to obtain a shell structure with a hole in the centre and a peak density of n_e=8.5×10^{3}cm^{-3}. From later radio measurements by Wood and Churchwell (1989) in contrast, a peak density per beam of n_e=4.4×10^{4}cm^{-3} was found. Therefore the Simpson and Rubin (1984) distribution may well lead to an underestimated integrated HeI 2.058μm/Brγ ratio. For this given density distribution in fig 5.6, the predicted HeI 2.058μm/ Brγ ratio is 0.98, which corresponds to a constant electron density of n_e~2×10^{3}cm^{-3}. This density reflects the diffuse component for G29.96 shown in fig 5.6. In table 5.1, integrated electron densities of n_e= 8×10^3–1.3 ×10^{4}cm^{-3} were calculated for G29.96 using 15GHz radio continuum measurements (col 4 table 5.1) and the appropriate source size quoted by each author. These values are a factor of 3–5 times less than the peak value from Wood and Churchwell (1989), given in col 8 of table 5.1 and comparable to the peak density of the Simpson and Rubin (1984) density distribution. On the basis of these values alone, microturbulence would be expected (see fig 5.4) to bring the HeI 2.058μm/Brγ ratio for these constant electron densities into agreement with the observed ratio of 1.0. However, for a density distribution like that in fig 5.6 the predicted volume shell integrated HeI 2.058μm/Brγ ratio is consistent with the observed ratio for G29.96 without microturbulent induced HeI line broadening.

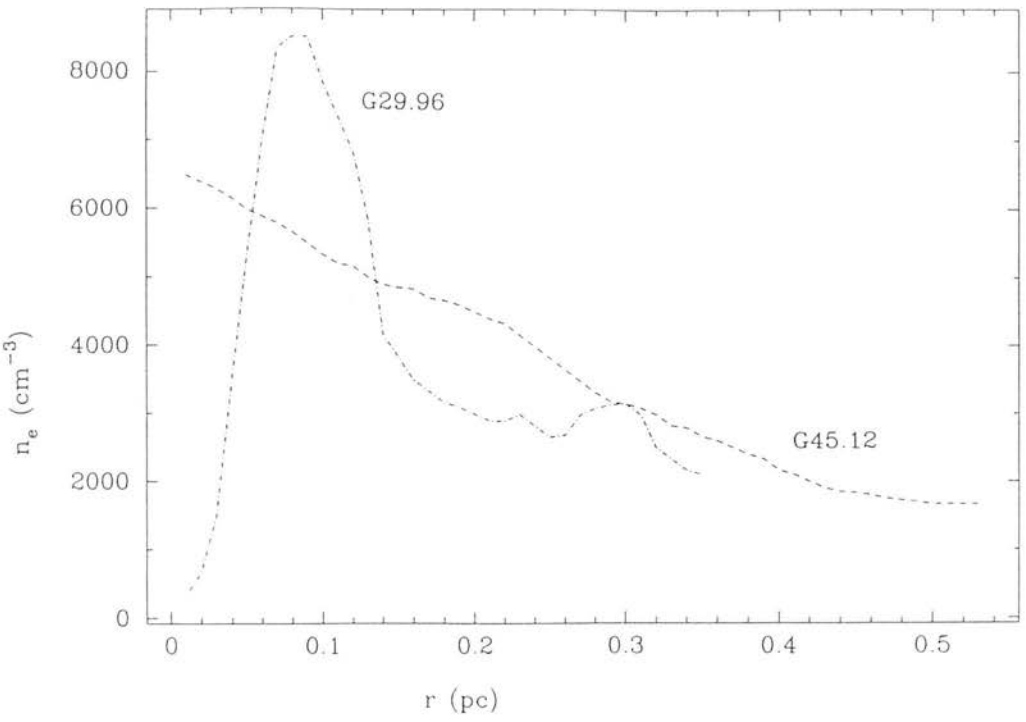

Figure 5.6: Model density distributions by Simpson and Rubin (1984) for G29.96 and G45.12 as a function of radius.

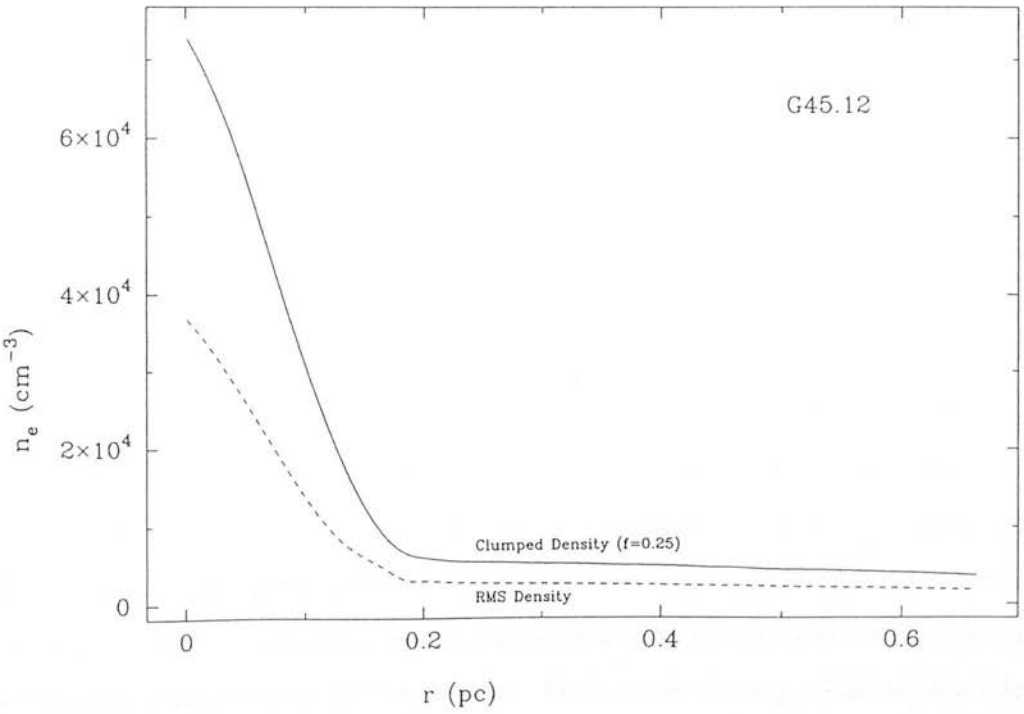

Figure 5.7: Model density distributions by Colgan *et al.* (1991) for G45.12 as a function of radius.

Therefore to explain observed high resolution HI and HeI line widths (see section 2.6) and the RRL line widths measured for G29.96 there are two possible explanations. Either spherical symmetry is too crude an approximation leading to lower integrated HeI 2.058μm/Brγ ratios for a microturbulent HII region than actually observed. Evidently a full integration over the realistic source geometry would be necessary. Or, the observed FWHM velocities must be attributed to turbulent motions on scales larger than 10^{12}cm (HeI 0.0584μm photon mean free path, section 2.6) or large scale expansion velocities. In this case a spherically symmetric density model for the distribution of G29.96 is a good first approximation.

G45.12

The observed HeI 2.058μm/Brγ ratios for G45.12 range from 0.80±0.04 to 0.93±0.04 (table 2.4, CGS2 and CGS4 measurements respectively).

Three circularized distributions are given in figs 5.6 and 5.7 for G45.12 the first of which differs rather dramatically from the other two. The first, by Simpson and Rubin (1984), can be approximated by a straight line with a maximum n_e=6.5×10^{3}cm^{-3} (fig 5.6). The second and third model distributions (fig 5.7) discussed by Simpson and Rubin (1984) and updated and revised by Colgan *et al.* (1991) resemble core-halo structures with peak rms electron densities of n_e~4–7×10^{4}cm^{-3} per beam for rms and clumped model distributions respectively, which they claim to be consistent with the Wood and Churchwell (1989) VLA map. A peak value per beam of n_e~1.1×10^{5}cm^{-3} is calculated by Wood and Churchwell (1989). The integrated HeI 2.058/Brγ ratios for these three model distributions are 0.95 and 1.00(rms) and 1.06(clu). Interestingly, although these density distributions are profoundly different the ratios obtained are not too discrepant when errors on observed HeI 2.058μm/Brγ ratios are taken into account. These integrated ratios imply constant densities of n_e ~1.5–3.5×10^{3}cm^{-3}, *c.f.* fig 5.3, considerably lower than peak density estimates, again a reflection of the broad halo extending outwards from r=0.2pc, shown in figs 5.6 and 5.7. These latter density estimates are fairly consistent with predicted electron densities by Colgan *et al.* 1991 from the far-infrared [OIII] 52/88μm line ratio.

Again using the 15GHz integrated flux densities calculated in chapter 4 and the different source sizes quoted in table 5.1, integrated electron densities of $n_e \sim 8\times10^3 cm^{-3}$ and $3.7\times10^4 cm^{-3}$ were found, the latter value comparable to peak densities used in the Colgan *et al.* (1991) models. If these estimates of the electron density were considered representative of a "constant" electron density in G45.12, HeI 2.058μm/Brγ ratios of 1.19 and 1.32 respectively, would be expected. To explain the observed HeI 2.058μm/Brγ ratios in this case, microturbulent motions resulting in broadened lines of FWHM 35 kms^{-1} corresponding to FWHM turbulent velocities of 28 kms^{-1} are proposed.

With the density distributions described above for a non-tubulent HII region, the CGS4 observed HeI 2.058μm/Brγ ratio of 0.93±0.04 agrees to within 2σ with the integrated HeI 2.058μm/Brγ ratios derived from the straight line and rms core-halo distributions, but the value derived from the clumped core-halo distribution is greater than all three observed ratios for G45.12 and microturbulent FWHM velocities of 15–21 kms^{-1} are required.

For G45.12, RRL FWHM velocities of 48 kms^{-1} by Downes *et al.* (1980) and 30–42 kms^{-1} by Wink *et al.* (1982) have been measured. For the density gradient models less microturbulence is required for the predicted HeI 2.058μm/Brγ ratios to be consistent with observations than if the radio integrated electron densities are assumed, and the HeI 2.058μm/Brγ ratios predicted from the constant density model.

5.5 Conclusions

To summarize the results of this investigation into electron density strucure in HII regions:

a) the assumptions of previous chapters that the average electron density expected for UCHII regions is of the order $n_e=10^4 cm^{-3}$ and lower for compact HII regions is verified. From radio continuum measurements, electron densities were found to be in the range $n_e=10^4$–$10^5 cm^{-3}$ for UCHII regions and $n_e=10^3$–$10^4 cm^{-3}$ for compact HII regions. The results of chapter 4 do not change in light of the higher electron densities found for the compact HII regions than the expected densities of $n_e=10^2 cm^{-3}$, since generally lower

electron densities are found in the compact HII region sample. However, electron densities inferred from radio continuum measurements and the HeI 2.058 μm/Brγ ratio will not be the same unless the density structure is homogeneous throughout the HII region.
b) Density gradient distributions calculated from radio maps can be used to determine a more accurate prediction of the HeI 2.058 μm/Brγ ratio for an HII region, however all models assume spherical symmetry which is only a first approximation and may not be valid.
c) A diffuse halo will dominate the HeI 2.058 μm/Brγ ratio. Otherwise, the ratio appears to represent some averaged density in the nebula, probably lower than the integrated density predicted from radio continuum measurements.
d) Differences between theoretical HeI 2.058 μm/Brγ ratios, for the UCHII regions G29.96 and G45.12, calculated from constant density and density gradient models are greater than the errors on the observed ratios for these objects. Ideally, rather than assuming spherical symmetry, the HeI 2.058 μm/Brγ ratio should be calculated for the most realistic source geometry.
e) From density profile models of the UCHII regions G29.96 and G45.12 it was found that integrated HeI 2.058 μm/Brγ ratios derived from these models are less than predicted HeI 2.058 μm/Brγ ratios derived from a constant density model, where the constant density is inferred from radio continuum measurements integrated over the source. Thus, whereas microturbulence may be needed to explain observed HeI 2.058 μm/Brγ ratios in the latter model, less or no microturbulence would be required in the former model.

Chapter 6

Starburst Galaxies

6.1 Introduction

Starburst galaxies are sites of massive star formation, characterized by their far–infrared excess, the result of reradiation of UV photons from newly formed hot OB stars to longer wavelengths by dust particles. These galaxies are currently forming stars at a rate which is thought to be so high that it could not have been sustained throughout the lifetime of the galaxy, although uncertainties in the IMF make this difficult to quantify.

In starburst galaxies, star formation occurs in sporadic (t=10^7–10^8yr, *e.g.* Telesco and Gatley, 1984) and (speculated) recurring bursts and therefore one should see the whole range of HII region evolution from UCHII regions, to compact HII regions, to diffuse, also termed as extended or giant, HII regions in these galaxies (see table 1.1). As giant HII regions contain a much greater volume of ionized gas, integrated He^+/H^+ emission line ratios from starburst galaxies, should in general reflect the physical properties of giant HII regions, *i.e.* low electron densities and less microturbulence. This should be true provided that the chosen He^+/H^+ ratio is not unduly sensitive to any high density components or, unless the galaxy is experiencing its first burst of star formation *i.e.* it only contains young UCHII and compact HII regions.

The aim of this chapter is to use the HeI 2.058μm/Brγ ratio diagnostics developed in earlier chapters to examine stellar populations and effective temperatures, T_{eff}, in

the widest possible range of actively star forming galaxies. A sample has thus been constructed which includes a wide range of luminosities and contains giant HII regions in other galaxies, dwarf galaxies, normal spirals, and ultraluminous IRAS galaxies. (Hereafter, this sample is referred to as a starburst galaxy sample even though it contains giant HII regions). In all of these categories, the precise physical mechanism for triggering star formation is controversial, but these different mechanisms are highly diverse. Clearly, any detailed discussion of these effects is well beyond the scope of this chapter. However, from HeI 2.058 μm/Brγ ratios it should be possible to investigate whether these different environments have any effect on the nature of the resulting stars formed *i.e* T_{eff}, and their HII region properties *i.e.* electron densities.

The initial aim of this work was to examine T_{eff} and hence masses of exciting stars in starburst galaxies, and thus make some predictions about the upper mass limit M_u of the IMF in these galaxies (see section 2.1). There is mounting evidence (*e.g.* see review by Scalo 1989,) that the IMF in some starburst galaxies is inconsistent with that in the solar neighbourhood; the lower mass cut off being markedly higher $\sim$ 3–6 $M_\odot$. As Scalo concludes, this result is invalid if the upper mass limit of the starburst IMF has been underestimated, because the upper and the lower mass limits are dependent parameters. If M_u is increased sufficiently, then M_l can be decreased to the extent that an IMF with M_l comparable to the solar neighbourhood value of 0.1 $M_\odot$ is perfectly plausible in these starburst galaxies. From studies by DPJ, the HeI 2.058 μm/Brγ ratio was predicted to be a reliable estimate of M_u for ratios less than $\sim$0.5, corresponding to an upper mass limit $M_u \leq 40\,M_\odot$. A number of galaxies in his sample were found to have HeI 2.058 μm/Brγ ratios $\leq$0.5, suggesting $M_u \leq 40\,M_\odot$. Such low upper mass limits suport the hypothesis of lower mass cut offs of a few solar masses in these galaxies.

From the studies in this thesis so far, however, the HeI 2.058 μm/Brγ ratio is complex and predominantly a function of local conditions, therefore unless all plasma variables are known, this ratio in itself is not an accurate indicator of effective stellar temperature T_{eff} or mass. However, in combination with optical HeI measurements a new method is suggested by which estimates of T_{eff} can be deduced.

In section 6.2, a brief description of the galaxy types and properties is given. Note

that the giant HII regions are referred to as a galaxy category here. In section 6.3, the observations are described and the spectra shown. Traditional extinction corrections are described in section 6.4. The results from the HeI 2.058 μm/Brγ ratio observations, and conclusions inferred from models discussed in previous chapters are presented in section 6.5. In section 6.6, optical data for these galaxies is reviewed and relevant conclusions drawn, and in section 6.7 the infrared and optical data are combined to enable further constraints on T_{eff} in starburst galaxies. Conclusions are presented in section 6.8.

6.2 Starburst galaxy sample selection

Table 6.1 gives the common names of the objects observed in April 1992. The IRAS designation and its equatorial coordinates are given in cols 3 and 4. Table 6.2 gives the far-infrared luminosity and the galaxy classification according to the categories below, as well as the observed HeI 2.058 μm/Brγ ratio. Previous observations of HeI 2.058 μm/Brγ ratios in a number of starburst galaxies have been made by DPJ. Table 6.3 is laid out in a similar format to table 6.2 for these objects. Recent measurements of NGC 5253, by Lumsden, Puxley and Doherty (1994) are included here.

All the galaxy sample are IRAS sources. The sample in table 6.2 was chosen to encompass a wide range of luminosities from fairly modest luminosities, L$\sim 10^7$–10^8 $L_\odot$, found in the giant HII regions NGC 5461 and NGC5471 in M101, to L$\sim 10^{12}$ $L_\odot$, found in the ultraluminous IRAS galaxies.

The far–infrared flux F_{IR} is defined in *Catalogued Galaxies & Quasars in the IRAS Survey* (1985) as:

$$\left(\frac{F_{IR}}{Wm^{-2}}\right) = 3.25 \times 10^{-14}\left(\frac{S_{60}}{Jy}\right) + 1.26 \times 10^{-14}\left(\frac{S_{100}}{Jy}\right) \qquad (6.1)$$

This is effectively the flux measured through an 80 μm wide filter centred at 80 μm and has been widely used as a representation of F_{IR}. L_{IR} was then derived using the recession velocity of the Galaxy given by the NASA/IPAC Extragalactic Database (NED) and H_0=75 kms^{-1} Mpc^{-1}. Values are given in table 6.2.

Galaxy	Other name	IRAS[1] name	Equatorial coordinates	
			α(1950)	β(1950)
II Zw 40		IRAS 05530+0323	05 53 05.0	03 23 05
HARO 1	Arp 136	IRAS 07336+3521	07 33 39.7	35 21 18
NGC 2623	Arp 243	IRAS 08354+2555	08 35 25.3	25 55 35
NGC 2903		IRAS 09293+2143	09 29 19.9	21 43 19
HARO 2	Mrk 33	IRAS 10293+5439	10 29 22.2	54 39 23
NGC 3310(HII)	Arp 217	IRAS 10356+5345	10 35 40.6	53 45 50
NGC 3310(NUC)			10 35 39.8	53 45 44
NGC 3310(B)			10 35 40.8	53 45 43
HARO 3	Mrk 35, NGC 3353	IRAS 10422+5613	10 42 16.5	56 13 20
NGC 3504		IRAS 11004+2814	11 00 28.1	28 14 35
NGC 3690A	Mrk 171	IRAS 11257+5850	11 25 44.2	58 50 23
NGC 3690B			11 25 44.2	58 50 23
NGC 3690C			11 25 44.2	58 50 23
NGC 4102		IRAS 12038+5259	12 03 51.6	52 59 23
NGC 4385	Mrk 52	IRAS 12231+0051	12 23 09.0	00 51 00
HARO 9	Arp 163, NGC 4670	IRAS 12428+2724	12 42 49.8	27 23 58
Mrk 59		IRAS 12566+3507	12 56 40.3	35 07 56
Arp 193		IRAS 13183+3423	13 18 17.0	34 24 04
NGC 5135		IRAS 13229−2934	13 22 57.0	−29 34 24
NGC 5461		IRAS 14017+5434	14 01 42.7	54 34 09
NGC 5471		IRAS 14027+5438	14 02 42.7	54 38 08
NGC 5713		IRAS 14376−0004	14 37 37.6	-00 04 35
II Zw 70	Mrk 829	IRAS 14489+3546	14 48 55.1	35 46 36
Arp220		IRAS 15327+2340	15 32 47.3	23 40 06
I Zw 123	Mrk 487	IRAS 15358+5525	15 35 48.4	55 25 34
NGC 6090	Mrk 496	IRAS 16104+5235	16 10 24.0	52 35 00

[1]Catalogued in both IRAS point and Faint source catalogues except NGC 5461.

Table 6.1: The starburst galaxy sample and co-ordinates.

The galaxy sample can generally be divided into morphological subsets.

a) Giant HII regions– these are isolated evolved external HII regions, powered by hot OB stars. Optical studies by Evans *et al.* (1986) and Torres–Peimbert, Peimbert and Fierro (1989) suggest that the two giant HII regions in this sample, NGC 5461 and NGC 5471, have helium abundances close to the primordial value.

b) Dwarf galaxies, which are small irregular isolated galaxies. They exhibit intense UV emission reminiscent of massive star formation. These objects are generally metal poor; it is thought that these galaxies are young and have not undergone numerous recurrences of star formation activity thus population II stars are not so plentiful. Stochastic self propagating star formation (Hunter and Gallagher, 1989), has been proposed as the star formation mechanism in these galaxies. All Haro objects fall into this category of galaxies. NGC 5253, is dwarf-like in that it is a small young metal poor irregular galaxy, but it is not isolated. Indeed, it has been proposed that star formation in this galaxy was initially caused from a past interaction with M83 (van den Bergh, 1980). M82, the other exception to this category, is also a dwarf galaxy in that it is a small, irregular galaxy, and is one of the earliest "classical" starburst galaxies observed. It is not however metal poor (having an approximately solar abundance; McCarthy, Heckman and van Breugel 1987), and it is known to have an older stellar population. Similarly, star formation is thought to result from a past interaction with M81 (Larkin *et al.* 1994).

c) Spiral galaxies, *e.g.* NGC 3310, NGC 5713 whose abundance is assumed Galactic. Unlike dwarf galaxies, their structure is organised. Spiral density waves in spiral discs (Elmegreen and Elmegreen, 1983) are thought to be the mechanism that induces star formation in some of these galaxies. All the spiral galaxies in this sample are classified as barred galaxies, although most have weak bars (SAB type morphology). Star formation is also proposed to be initiated from funnelling of molecular gas in the bar potential (Combes and Gerin 1985), *e.g.* NGC 253, the other classical starburst.

d) Ultraluminous galaxies, all of which are observed to have large IRAS luminosities, $L \sim 10^{12} L_{\odot}$. The luminosities of these powerful emission sources can be attributed to a number of processes. One way in which the gas in a molecular cloud can be compressed to a critical density for star formation to proceed, is the collapse of massive (10^8–$10^9 M_{\odot}$) clouds of molecular gas funnelled into the centres of mergers (Scoville and Norman, 1988).

Galaxy	HeI 2.058 μm/Brγ ratio	FIR L/ $L_{\odot}$	Morphology
HARO 1	0.990±0.320	10.55	BCD
NGC 2903	0.219±0.142	9.57	SP
HARO 2	0.584±0.029	9.42	BCD
NGC 3690A	0.557±0.049	11.41	UL
NGC 3690B	0.369±0.066	11.41	UL
NGC 3690C	0.536±0.056	11.41	UL
NGC 4102	<0.119	9.96	SP
NGC 5135	<0.355	10.92	SP
II Zw 70	0.340±0.046	8.52	BCD
Arp 220	<0.591	11.89	UL
II Zw 40	0.306±0.015	8.99	BCD
NGC 2623	0.417±0.038	11.28	UL
NGC 3310(HII)	0.505±0.038	9.93	GHII
NGC 3310(NUC)	0.565±0.111	9.93	SP
NGC 3310(B)	0.628±0.071	9.93	SP
NGC 4385	0.493±0.040	9.76	BCD
Arp 193	0.445±0.048	11.33	UL
NGC 5461	0.644±0.025	8.41	GHII
NGC 5471	0.369±0.053	7.64	GHII
NGC 6090	0.641±0.018	11.15	UL
HARO 3	0.529±0.025	9.09	BCD
NGC 3504	0.272±0.046	10.13	SP
HARO 9	0.509±0.069	8.91	BCD
Mrk 59	0.371±0.026	8.54	BCD
NGC 5713	0.317±0.049	10.33	SP
I Zw 123	0.511±0.088	7.74	BCD

Table 6.2: Observed HeI2.058 μm/Brγ line ratios in Starburst Galaxies (this chapter).

Galaxy	HeI 2.058 μm/Brγ ratio	FIR L/ $L_{\odot}$	Morphology
NGC 3690A	0.65±0.08	11.41	UL
NGC 3690B	0.28±0.05	11.41	UL
NGC 3690C	0.48±0.05	11.41	UL
He 2-10	0.64±0.09	9.64	BCD
NGC 1614	0.55±0.05	11.27	UL
NGC 253	0.38 ±0.08	10.11	SP
NGC 2798	0.60 ±0.08	10.26	SP
NGC 3256A	0.33 ±0.04	11.26	UL
NGC 3256B	0.71±0.15	11.26	UL
M82	0.34 ±0.02	10.07	BCD
NGC 5253	0.48±0.06	9.09	BCD

Table 6.3: Observed HeI2.058 μm/Brγ line ratios in Starburst Galaxies.

NGC 3690 is known to be a merging galaxy (Friedmann *et al.* 1987). Alternatively, the presence of an AGN may explain the observed L_{IR} without massive OB star formation occurring.

6.3 Observations

This data set comprises one of the largest samples of spectroscopic near infrared observations of starburst galaxies to date.

The observations were made using CGS4, (Mountain *et al.* 1990) discussed in section 2.2. Observations of 26 starburst galaxies were made in only 3 nights including calibration overheads (17–19 April 1992), of good observing conditions.

The observational configuration is the same as described in section 2.2. The 75lines/mm grating and the 150mm short camera results in complete coverage of the K window with

a resolution of ~900 kms^{-1} at 2.2 μm. The spectra were sampled 4 times over two pixels.

The detected emission from these galaxies was confined spatially to one central row ($3.1\widehat{''}$) for most sources, and in all cases was not observed over more than 3 detector rows. Thus, it was possible to obtain sky spectra by sliding typically 10 rows ($31\widehat{''}$) along the slit. Argon and krypton lamps were used for wavelength calibration; the accuracy of this calibration was ~0.0002 μm. Total galaxy integration times were between 20 and 45 minutes. Standard stars were observed both before and after galaxy observations, to monitor any variation in flux levels between standard observations, and the average of the two reduced spectra used for flux calibration. The standard stars observed, their equatorial coordinates and their spectral types are given in table 6.4. Detailed CGS4 reduction methods are described in section 2.2.1.

The HeI 2.058 μm and Brγ line fluxes in the final calibrated spectra were determined from the best fitting triangular profile for the two lines. The instrumental FWHM (6.5×10^{-3} μm at 2.2 μm) closely matched the FWHM ($6.1\text{–}6.7\times10^{-3}$ μm) of the measured profiles for the CGS4 observations. The spectra are shown in fig 6.1a–z and the raw ratios given in table 6.2.

6.4 Extinction in starburst galaxies

In previous chapters extinction corrections were made by utilizing radio continuum fluxes via conversion to an ionizing photon rate, N_{Lyc} (section 2.4). This calculation assumes that the radio continuum is entirely due to free-free emission from the ionized gas in the star forming regions; a valid assumption for young HII regions ionized by OB stars. However, in starburst galaxies the emission arises from an ensemble of stars in different evolutionary stages, and the radio continuum emission is likely to comprise two components– a free-free thermal component and a synchrotron non-thermal component. The latter, which results from relativistic particles gyrating in a magnetic field *e.g.* as occurs in supernova remnants, may well dominate the total radio flux (Gioia, Gregorini and Klein 1982). Therefore extinction estimates cannot reliably be derived from radio continuum fluxes. It is also possible to use radio or millimetre recombination lines from

Standard	Equatorial coordinates α(2000)	β(2000)	K mag	Spectral type
BS 2124	06 02 23.0	09 38 51		A2V
BS 2931	07 39 11.9	24 13 21		A2V
BS 3420	08 37 52.1	−26 15 18		A0V
BS 3474	08 46 40.0	28 45 55		A3V
BS 3711	09 21 15.3	15 22 16		A1V
BS 4131	10 33 43.5	53 29 50		A1V
BS 4295	11 01 50.4	56 22 56		A1V
BS 4332	11 08 49.0	24 39 30		A3IV
BS 4550	11 52 58.7	37 43 08	4.40	G8V
BS 4660	12 15 25.5	57 01 57		A3V
BS 4799	12 36 47.3	−05 49 55		A3V
BS 4869	12 49 17.4	27 33 08		A2V
BS 4875	12 50 10.6	37 31 01		A3V
BS 4948	13 06 10.1	29 01 46		A3IV
BS 5090	13 31 33.2	−28 06 46		A1V
BS 5191	13 47 32.3	49 18 48	2.37	B3V
BS 5280	14 02 59.6	50 58 18		A2V
BS 5501	14 45 30.1	00 43 02		B9.5V
BS 5569	14 55 58.6	32 18 01		A2V
BS 5793	15 34 41.2	26 42 53		A0V
BS 5818	15 35 57.0	54 37 50		A2V
BS 6092	16 19 44.3	46 18 48	4.30	B5IV
BS 6156	16 30 05.9	48 57 39		A1V
BS 6806	18 09 37.4	38 27 27	4.24	K2V

Table 6.4: Standard star list.

high n-levels in a similar manner (conversion to N_{Lyc}) to estimate the extinction in a star forming region. However, radio and mm recombination lines are very weak and have only been detected in a few bright nearby starbursts, *e.g.* M82 (Puxley *et al.* 1989). Therefore in starburst galaxies the extinction must be calculated by a different technique. The most common method for extinction correction utilizes observed values of the two brightest hydrogen emission lines Hα and Hβ.

The fundamental assumption used here is that the emission arises from a point source or a nucleus and the extinction is purely foreground. This method is outlined below:

$$\frac{I_{H\alpha}}{I_{H\beta}} = \frac{I_{H\alpha TH}}{I_{H\beta TH}} e^{-(\tau_{H\alpha}-\tau_{H\beta})} \tag{6.2}$$

where $I_{H\alpha}$ and $I_{H\beta}$ are the observed Hα and Hβ line intensities, $I_{H\alpha TH}$ and $I_{H\beta TH}$ the theoretical Hα and Hβ line intensities and $\tau_{H\alpha}$ and $\tau_{H\beta}$ the Hα and Hβ line optical depths. A convenient form of this equation used in optical astronomy is:

$$\frac{I_{H\alpha}}{I_{H\beta}} = \frac{I_{H\alpha TH}}{I_{H\beta TH}} 10^{-c(f(H\alpha)-f(H\beta))} \tag{6.3}$$

Therefore the optical depth dependence has been split into two components, c, which is an extinction measure particular to the physical conditions in the observed region, and f(λ), which is given by the interstellar extinction curve. The standard or Whitford (1958) extinction curve is normalized to f(Hβ). This extinction curve maps well onto the infrared extinction curve by Draine (1989), discussed in section 2.4. Assuming case B, the theoretical value for the ratio of Hα/Hβ is 2.85 for $n_e=10^2 cm^{-3}$ and T_e=10,000K (Hummer and Storey 1987). Hence, from line observations of Hα and Hβ, c can be solved for, from eqn 6.3, and is independent of wavelength. Thus, the differential extinction between any two pairs of lines in the same nebula can then be determined by further application of the interstellar extinction curve. Equivalently c can be quoted in terms of A_v or E_{B-V} where $c=0.97A_v$ or $3.2E_{B-V}$.

The underlying assumption of purely foreground extinction is obviously an approximation, valid if the observed emission stems from the galactic nucleus. However, it is equally or more plausible in some galaxies that the stars and dust are distributed

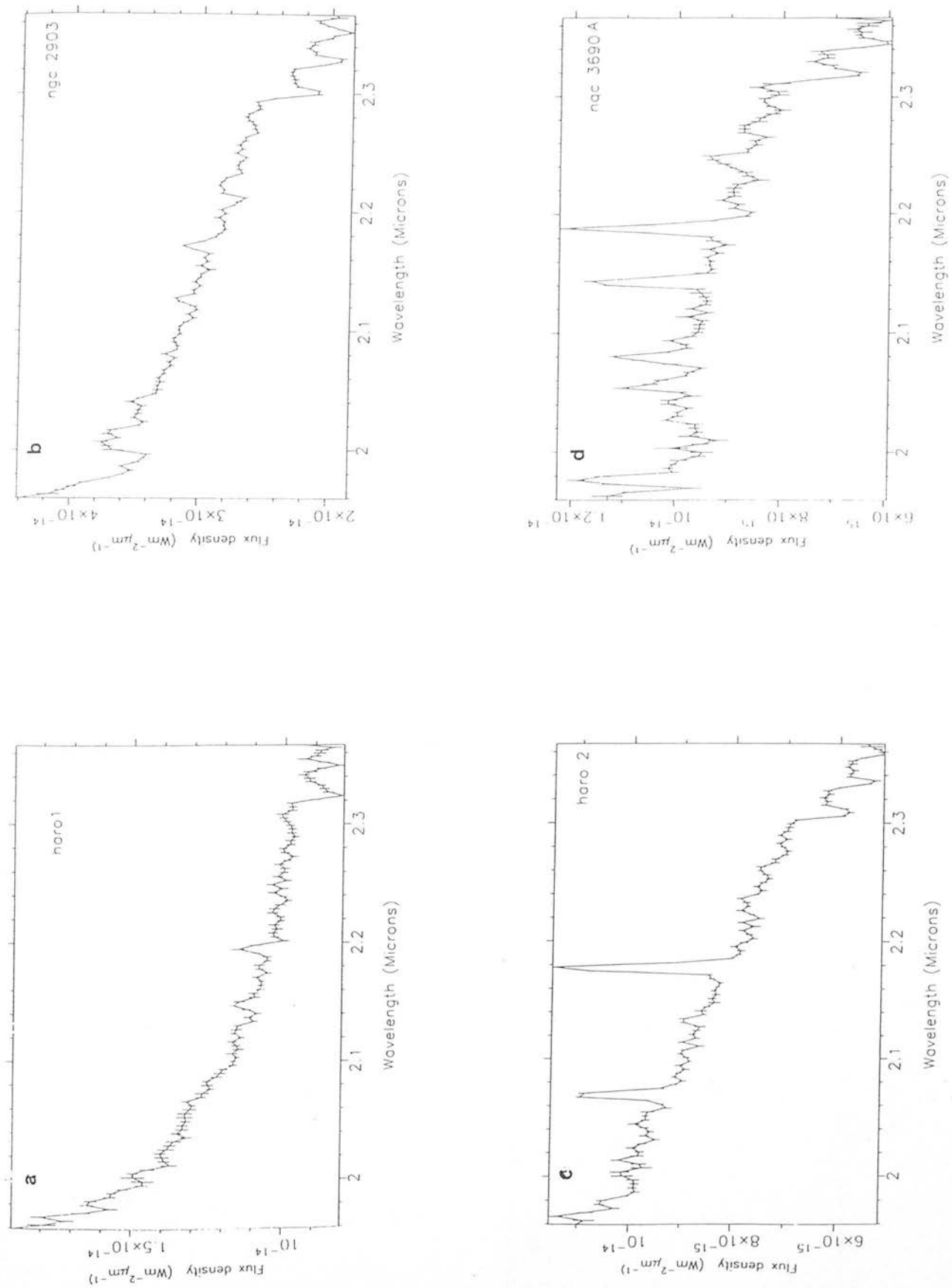

Figure 6.1: K-band spectra of 26 starburst galaxies and giant HII regions taken with CGS4.

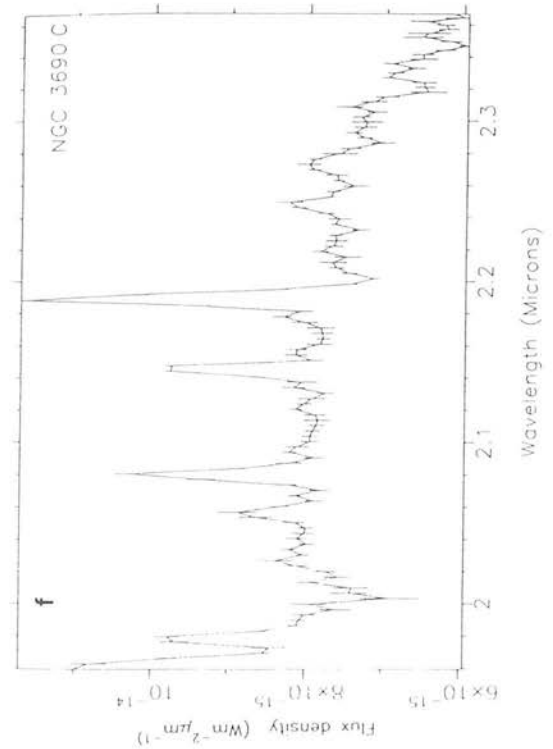
NGC 3690 C
f
Flux density (Wm$^{-2}\mu$m^{-1})
Wavelength (Microns)

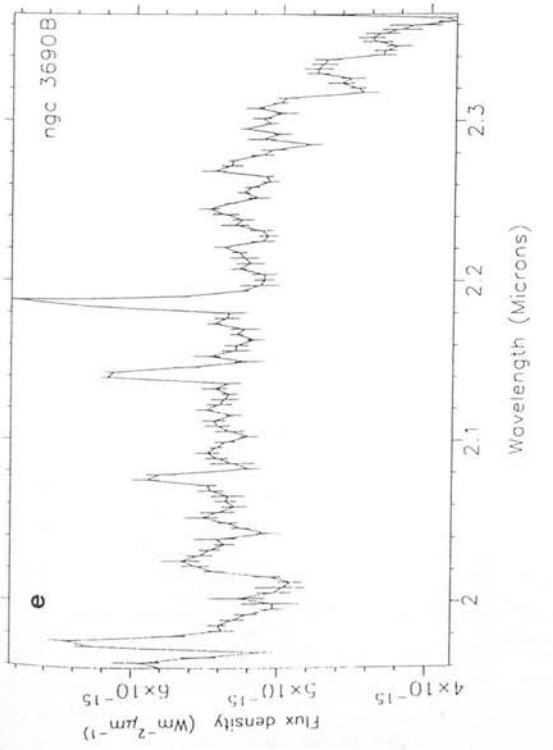
ngc 3690B
e
Flux density (Wm$^{-2}\mu$m^{-1})
Wavelength (Microns)

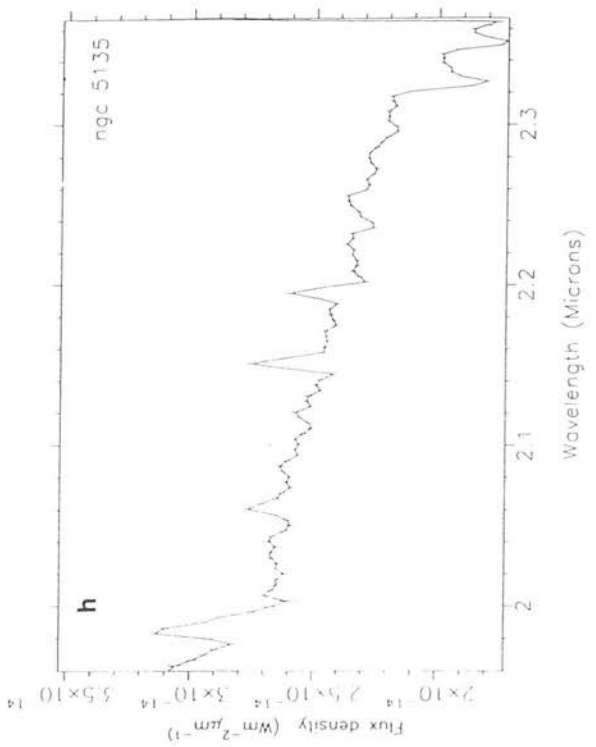
ngc 5135
h
Flux density (Wm$^{-2}\mu$m^{-1})
Wavelength (Microns)

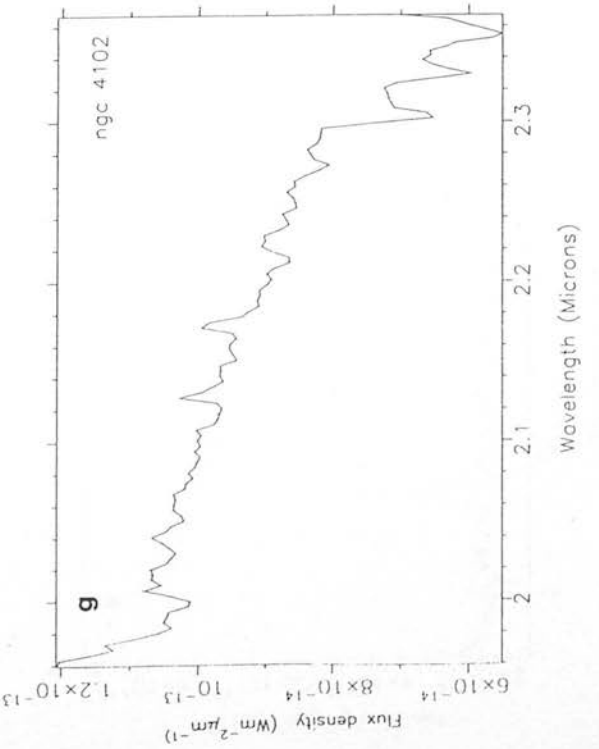
ngc 4102
g
Flux density (Wm$^{-2}\mu$m^{-1})
Wavelength (Microns)

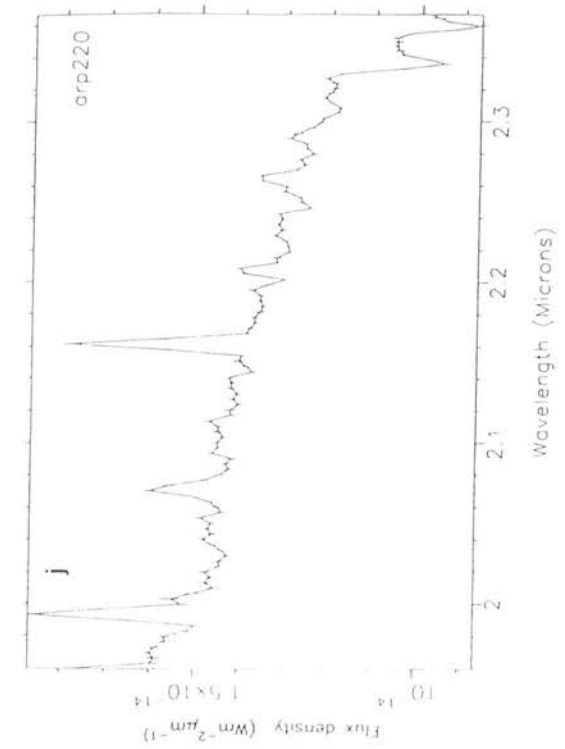
arp220
j
Flux density (Wm$^{-2}\mu$m^{-1})
Wavelength (Microns)

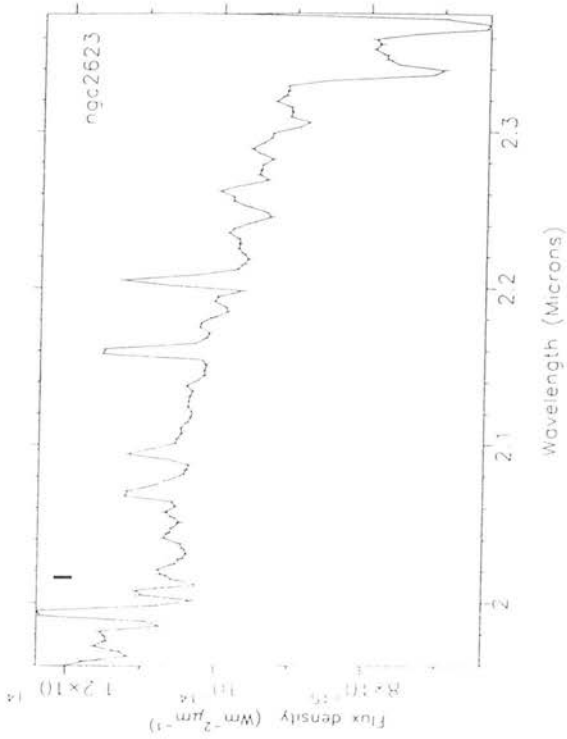
ngc2623
l
Flux density (Wm$^{-2}\mu$m^{-1})
Wavelength (Microns)

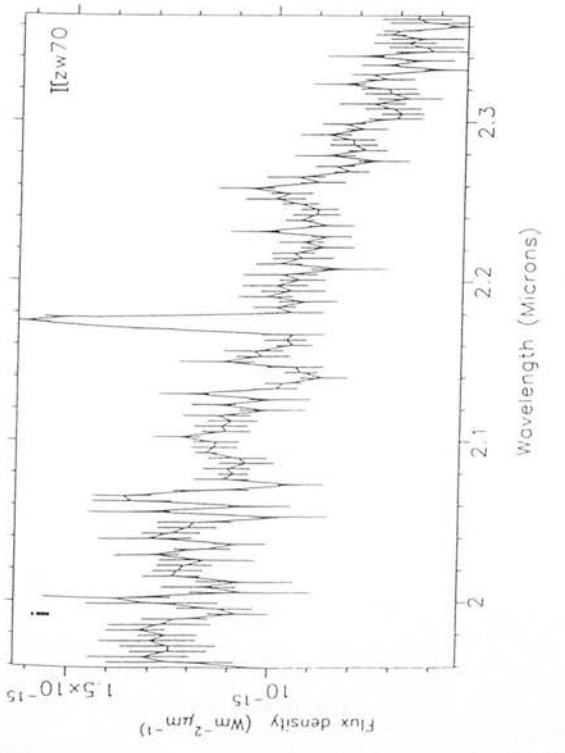
I[zw70
i
Flux density (Wm$^{-2}\mu$m^{-1})
Wavelength (Microns)

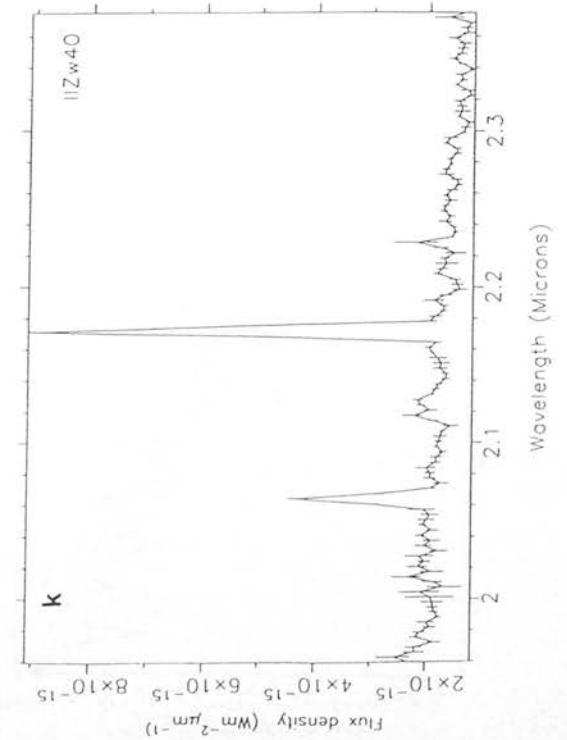
IIZw40
k
Flux density (Wm$^{-2}\mu$m^{-1})
Wavelength (Microns)

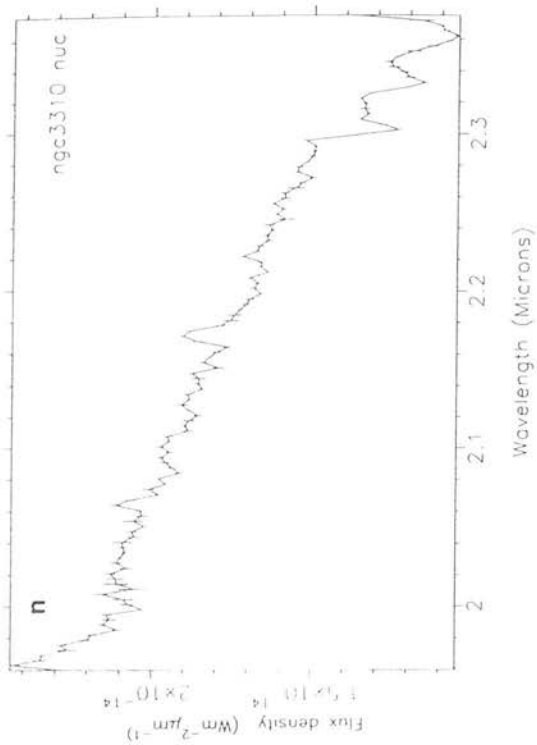
n
ngc3310 nuc
Flux density (Wm$^{-2}\mu$m^{-1})
Wavelength (Microns)

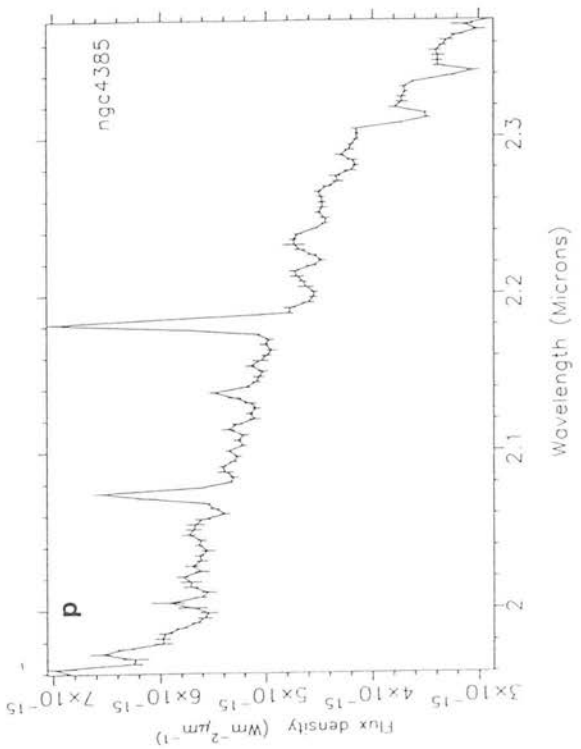
p
ngc4385
Flux density (Wm$^{-2}\mu$m^{-1})
Wavelength (Microns)

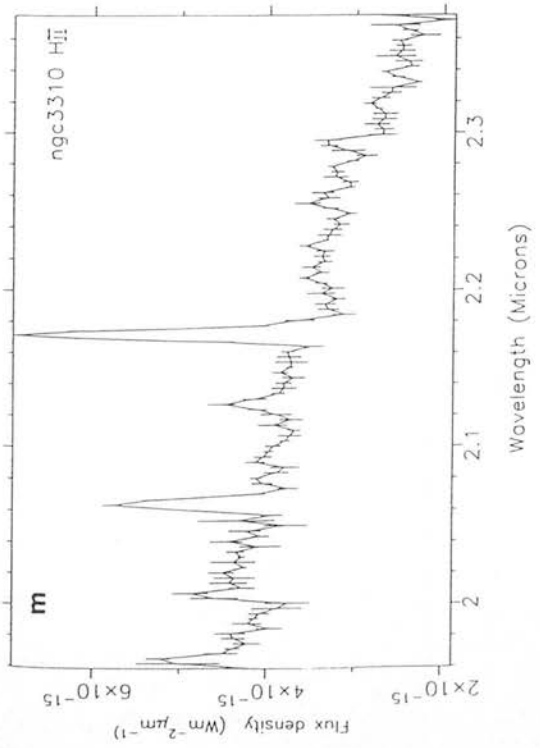
m
ngc3310 HII
Flux density (Wm$^{-2}\mu$m^{-1})
Wavelength (Microns)

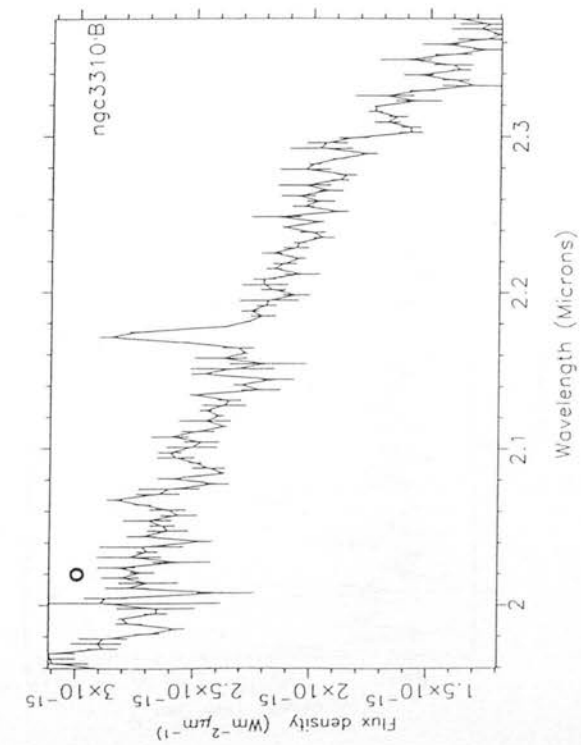
o
ngc3310B
Flux density (Wm$^{-2}\mu$m^{-1})
Wavelength (Microns)

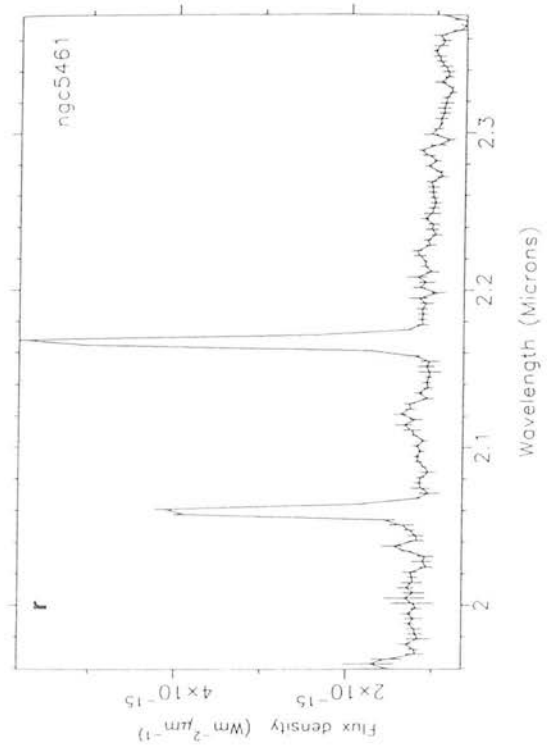
ngc5461
r
Flux density (Wm$^{-2}\mu$m^{-1})
2×10^{-15}
4×10^{-15}
2
2.1
2.2
2.3
Wavelength (Microns)

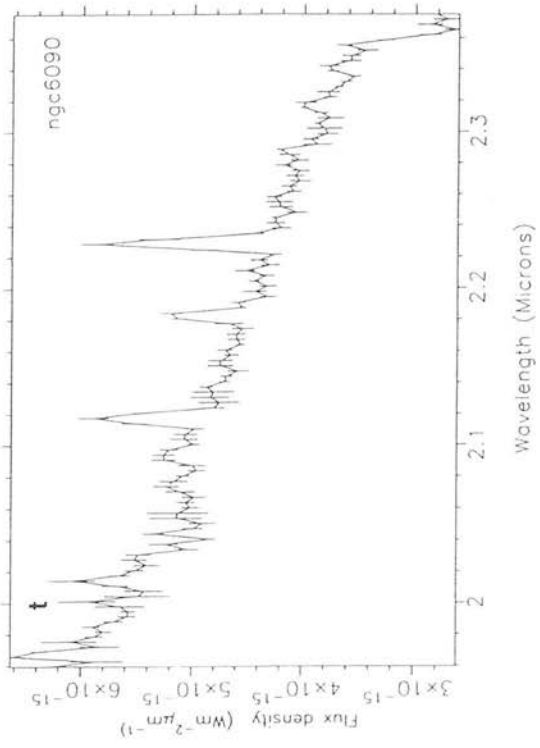
ngc6090
t
Flux density (Wm$^{-2}\mu$m^{-1})
3×10^{-15}
4×10^{-15}
5×10^{-15}
6×10^{-15}
2
2.1
2.2
2.3
Wavelength (Microns)

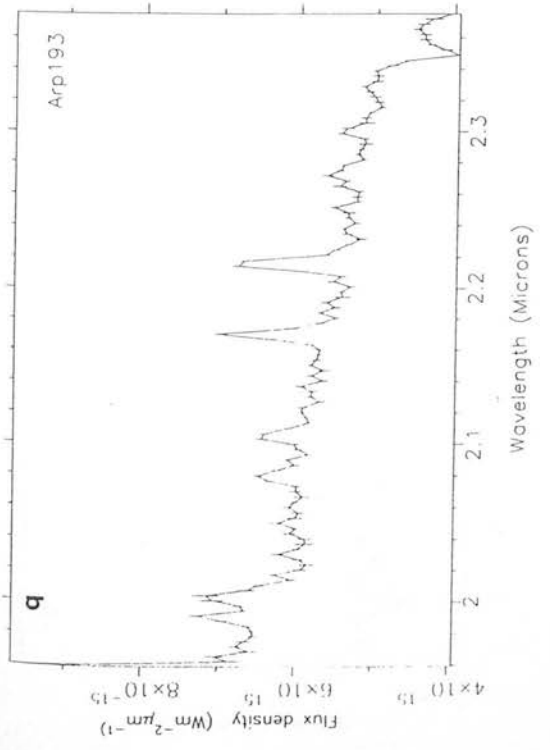
Arp193
q
Flux density (Wm$^{-2}\mu$m^{-1})
4×10^{-15}
6×10^{-15}
8×10^{-15}
2
2.1
2.2
2.3
Wavelength (Microns)

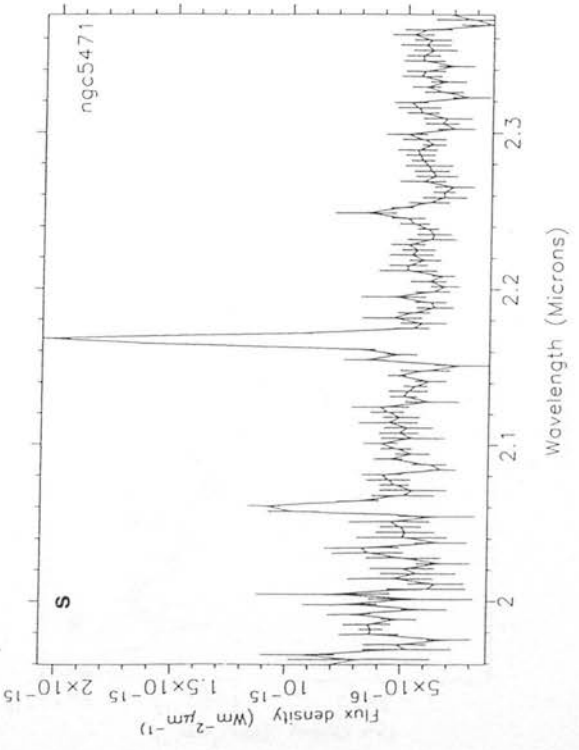
ngc5471
s
Flux density (Wm$^{-2}\mu$m^{-1})
5×10^{-16}
10^{-15}
1.5×10^{-15}
2×10^{-15}
2
2.1
2.2
2.3
Wavelength (Microns)

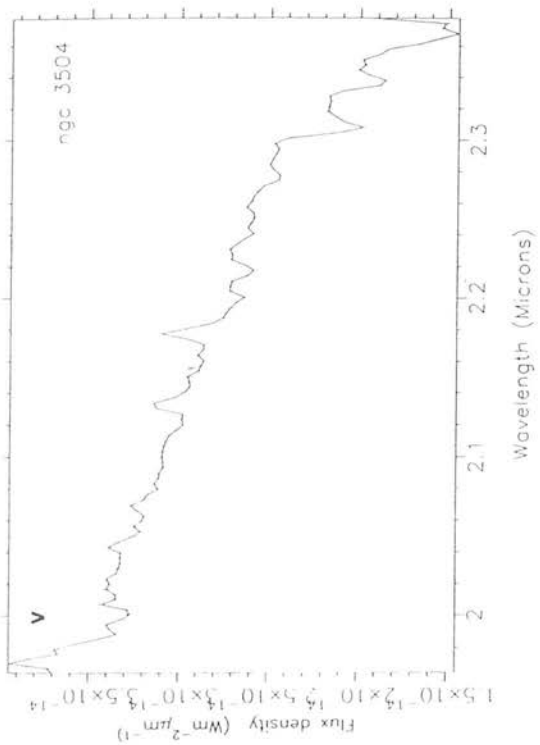
ngc 3504
v
Wavelength (Microns)
Flux density (Wm$^{-2}\mu$m^{-1})

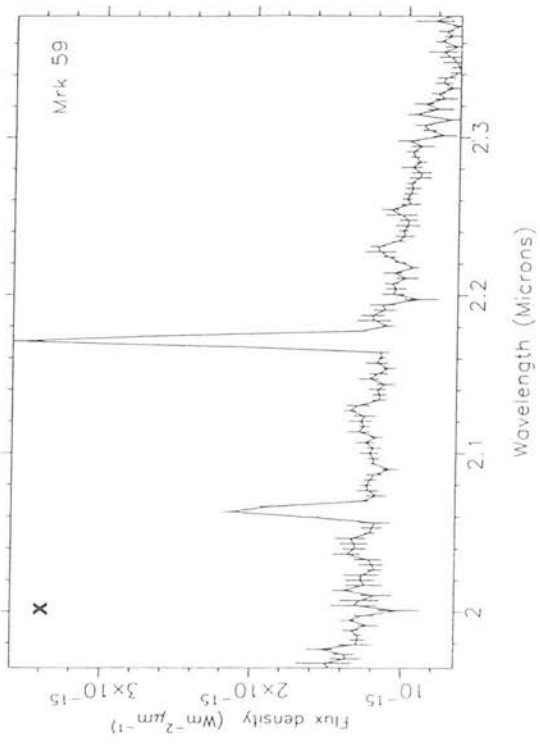
Mrk 59
x
Wavelength (Microns)
Flux density (Wm$^{-2}\mu$m^{-1})

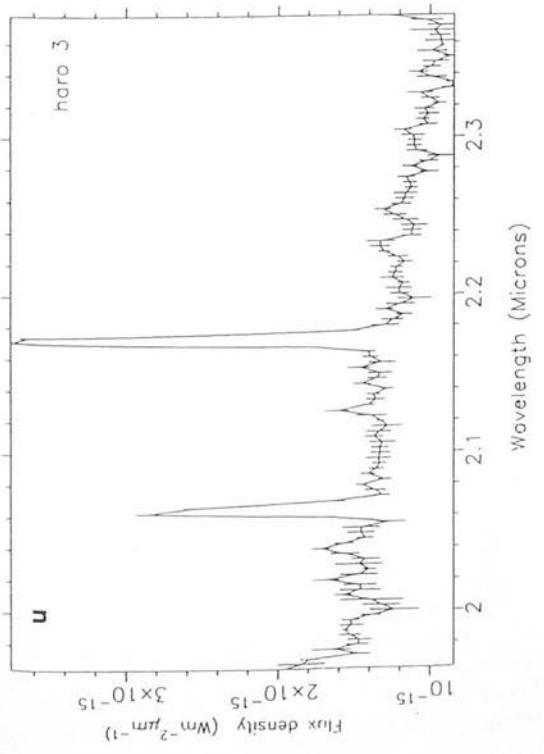
haro 3
u
Wavelength (Microns)
Flux density (Wm$^{-2}\mu$m^{-1})

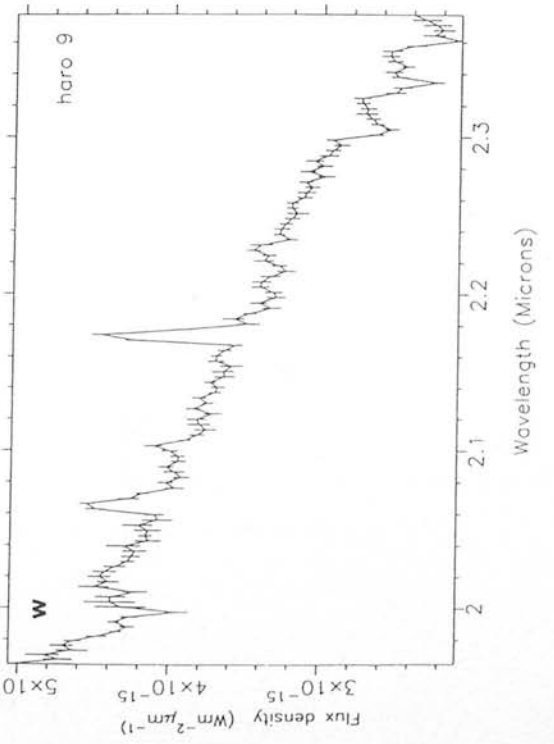
haro 9
w
Wavelength (Microns)
Flux density (Wm$^{-2}\mu$m^{-1})

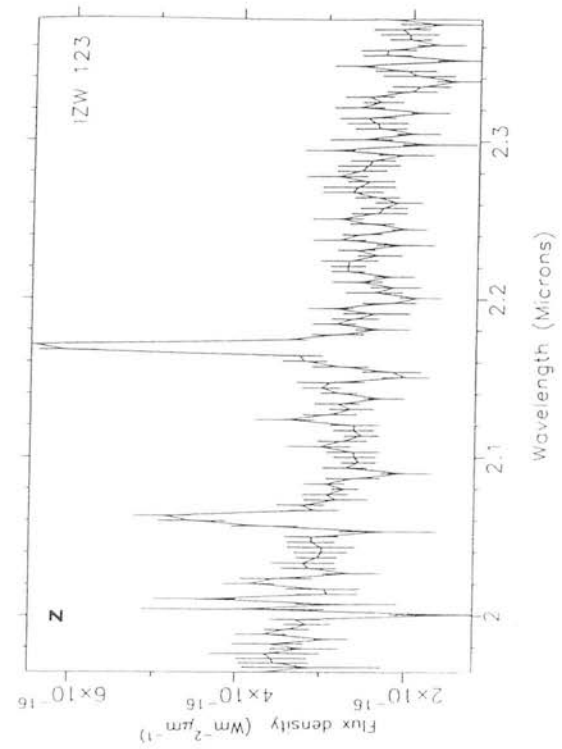
IZW 123
z
Flux density (Wm$^{-2}\mu$m^{-1})
2×10^{-16}
4×10^{-16}
6×10^{-16}
2
2.1
2.2
2.3
Wavelength (Microns)

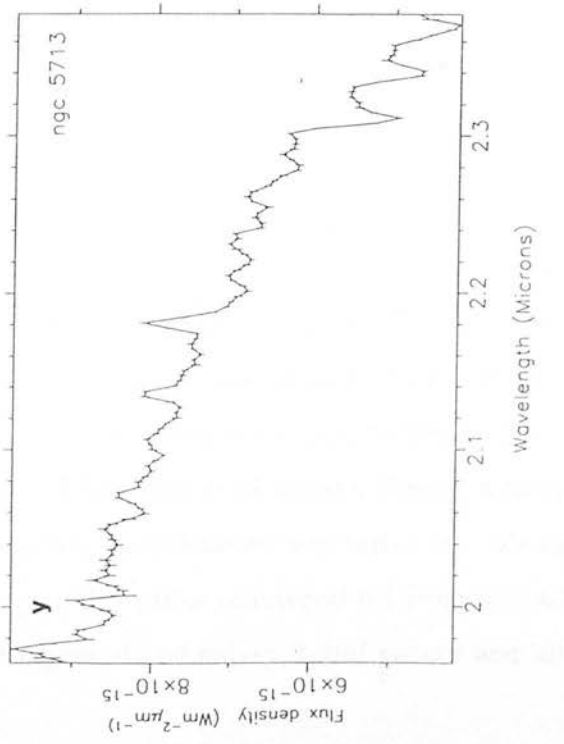
ngc 5713
y
Flux density (Wm$^{-2}\mu$m^{-1})
6×10^{-15}
8×10^{-15}
2
2.1
2.2
2.3
Wavelength (Microns)

homogeneously throughout the observed region. In this case, the extinction inferred from the foreground assumption is incorrect and likely to be an underestimate (Puxley 1988). Conversely, if extinction estimates from infrared measurements, *e.g.* the ratio of Brγ/Brα, are significantly higher than those inferred from optical data then it is expected that the stars and gas are distributed in a more homogeneous fashion.

The given A_v values in the literature are not greater than $\sim$10 (NGC 253, Davidge and Maillard 1990) and predominantly 1–2 (Leech *et al.* 1989, Vacca and Conti 1992, Torres–Peimbert *et al.* 1989, Pastoriza *et al.* 1993). A visual extinction of A_v=10 yields a correction of no more than 10% on the HeI 2.058μm/Brγ ratio. However, as noted above these A_v values are derived as in eqn 6.3, thus may be an underestimate. In reality, one might expect nuclear emission as well as that from stars and dust distributed throughout the galaxy, thus an accurate extinction measurement is difficult to determine. Nevertheless, uncertainties in the HeI 2.058μm/Brγ ratio due to differential extinction are unlikely to be large in starburst galaxies (unlike deeply embedded UCHII regions).

The HeI 2.058μm/Brγ ratios were not extinction corrected because a) c values were not available for all the objects and b), to reiterate, the foreground assumptions from which these c values were derived are liable to be an underestimate.

6.5 The HeI 2.058 μm/Brγ ratio in Starburst Galaxies

The raw observed HeI 2.058μm/Brγ ratios are given in table 6.2. Atmospheric absorption effects (section 2.3) were not problematic because galaxy emission lines are much broader, of the order of a few hundred kms^{-1} due to the galaxy rotation velocity, than equivalent emission lines from HII regions ($\leq$50 kms^{-1}). Also, for a large number of starburst galaxies the HeI 2.058μm line was redshifted away from the 2.06μm telluric absorption feature. Table 6.3 gives uncorrected HeI 2.058μm/Brγ ratios for starburst galaxies observed by DPJ and Lumsden *et al.* (1994). Firstly, a correlation between HeI 2.058μm/Brγ ratios and galaxy classifications was tested for. Histograms are shown in fig 6.2. Bins of HeI 2.058μm/Brγ ratios of interval 0.1 from 0 to 0.8 were constructed for each of the giant HII region, dwarf galaxy, spiral galaxy and ultraluminous galaxy

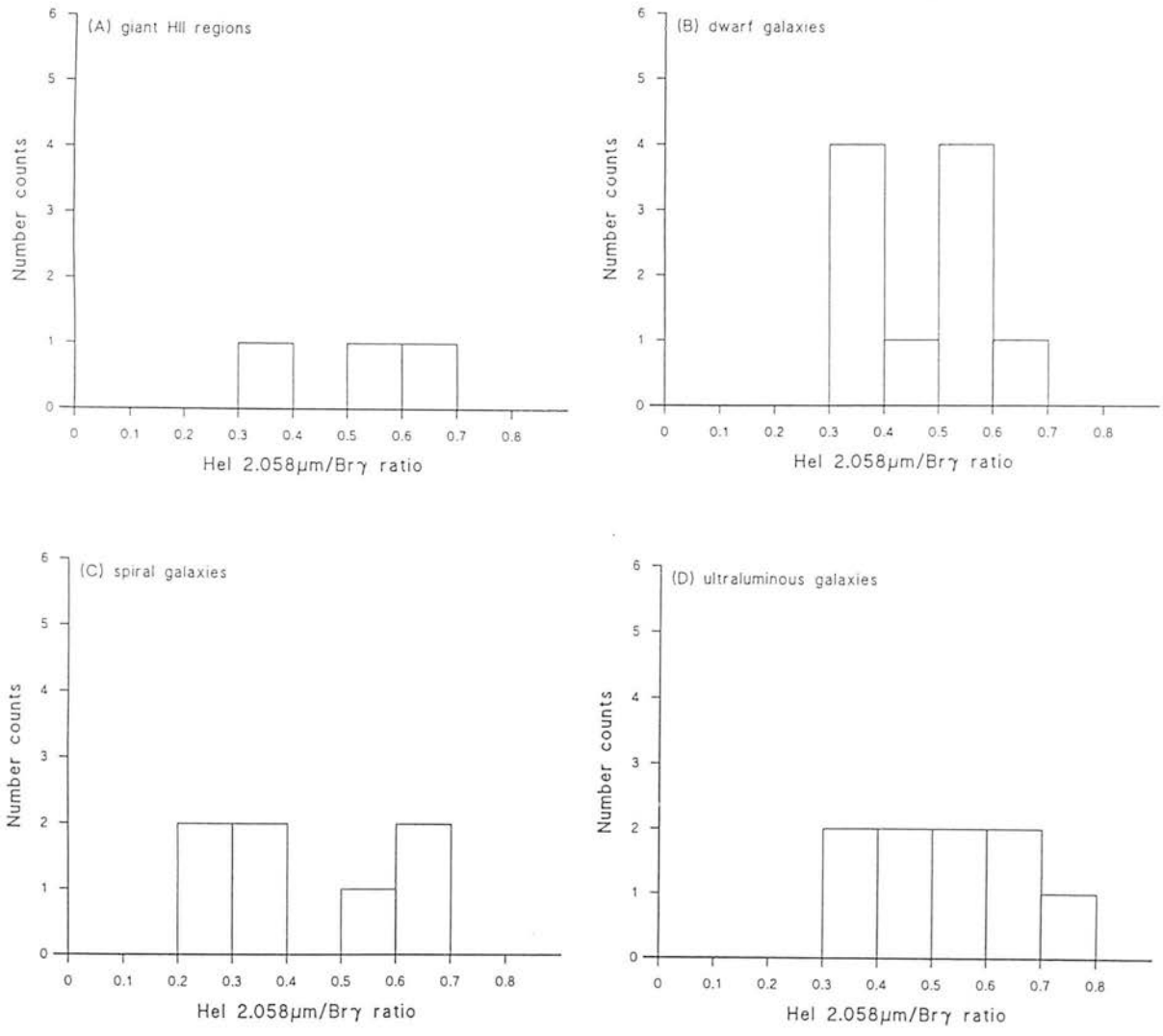

Figure 6.2: Histograms of HeI 2.058 μm/Brγ ratios for (A) giant HII regions, (B) dwarf galaxies, (C) spiral galaxies and (D) ultraluminous galaxies.

categories and each galaxy was binned accordingly. Kolmogorov-Smirnov (K-S) tests were performed between all pairs of these distributions. There was no evidence to suggest that any data set arose from a different parent distribution even at the 1σ level. Thus, since the HeI 2.058μm/Brγ ratio is a strong function of effective temperature and electron density it does not appear that either of these parameters are heavily influenced by their star forming environment. This lack of correlation suggests that the effective temperatures or electron densities for the classes of galaxies observed, as a whole, are all similar. Further, the lack of a clear indication of lower HeI 2.058μm/Brγ ratios in metal poor *i.e.* dwarf galaxies with primordial abundances, may stem from the fact that for the same stellar population a lower helium abundance implies a higher electron temperature (section 4.5.1). Thus, if similar stellar populations are found amongst galaxy categories, although a lower helium abundance decreases the ratio, the higher electron temperature increases the ratio. The combination of these two factors may mask the expected correlation between HeI 2.058μm/Brγ ratios and helium abundance.

The observed ratios and their 1σ errors given in table 6.2 and 6.3 lie in the range 0.22-0.64, excluding Haro 1. Haro 1 has an unusually steep sloping continuum, suggesting a large population of hot stars with not many older stars (fig 6.1a). The combination of this sloping continuum and the HeI 2.058μm/Brγ ratio of 0.99 ± 0.32 possibly suggests that this galaxy is undergoing its first burst of star formation and contains only high density UC and compact HII regions. This is a purely speculative conjecture since the continuum shape makes accurate line flux estimation difficult in this object (fig 6.1a).

Upper limit values are only available for NGC 4102, NGC 5135 and Arp 220, either integration times were not long enough or star formation is not occurring since there is no UV emission from hot OB stars to ionize helium atoms in the surrounding gas. 2σ upper limits are given for these galaxies in table 6.2. The upper limits for NGC 5135 and Arp 220 fall within the range of observed values of the HeI 2.058μm/Brγ ratio detected in other galaxies, whereas the upper limit for HeI 2.058μm in NGC 4102 is considerably smaller suggesting very little HeI ionization.

For the rest of the sample, the most striking fact is that the observed HeI 2.058μm/Brγ ratios are considerably lower than those of the compact and UCHII regions studied pre-

viously.

Fig 6.3 depicts the models of chapter 2 (solid lines) and those by Shields (dashed lines) both for $n_e=10^2 cm^{-3}$ assumed throughout further calculations, for Galactic ($N_{He}/N_H=0.1$) and primordial ($N_{He}/N_H=0.08$) abundances. An electron temperature of $T_e=10{,}000K$ is used in the chapter 2 models and for subsequent theoretical calculations, as used, by other authors for the galaxies discussed below. Electron temperature is a function of radius in Shields' models, mean T_e values increase from 7,500–10,000K as T_{eff} increases from 35–48,000K. Both sets of models are considered accurate up to T_{eff}=38–40,000K, but at higher effective temperatures the two sets of models disagree. There is a slight disagreement as to the effective temperature at which the HeI 2.058μm/Brγ ratio attains its maximum, T_{eff}=38,000K for chapter 2 models, and T_{eff}=40,000K for Shields' models. There is however, a large discrepancy between the maximum HeI 2.058μm/Brγ ratio values predicted by the two models– 0.8 (chapter 2 models and Smits' 1991a values) and 0.5 (Shields' models). Reasons for this discrepancy are not completely understood, although different atomic data and line transfer assumptions are supposed (section 4.4). Shields reveals a flaw in the models of chapter 2, in that the neutral helium to hydrogen fraction y^0 is not constant with T_{eff} but decreases with harder ionizing radiation *i.e.* higher T_{eff}. Shields' models show this decrease to be significant above $\sim$ 40,000K (fig 4.6).

All the observed ratios are lower than the maximum value (0.8) for the Galactic abundance model of chapter 2 (solid lines, fig 6.3) and lower than or equal to the primordial adundance model (0.61) for $n_e=10^2 cm^{-3}$. Furthermore, half of these ratios in tables 6.2 and 6.3 are lower than 0.5, the maximum value in the $n_e=10^2 cm^{-3}$ model from Shields (dashed lines, fig 6.3), for a Galactic helium abundance, and seven galaxies have ratios lower than 0.38, the maximum value of Shields' models for a primordial helium abundance.

These low values do seem to agree with the assumption that these measurements reflect lower electron density plasmas. However these ratios may also be attributed to lower or higher effective temperatures (see fig 6.3). A combination of the two effects is considered most likely for the galaxies with the lowest observed HeI 2.058μm/Brγ ratios.

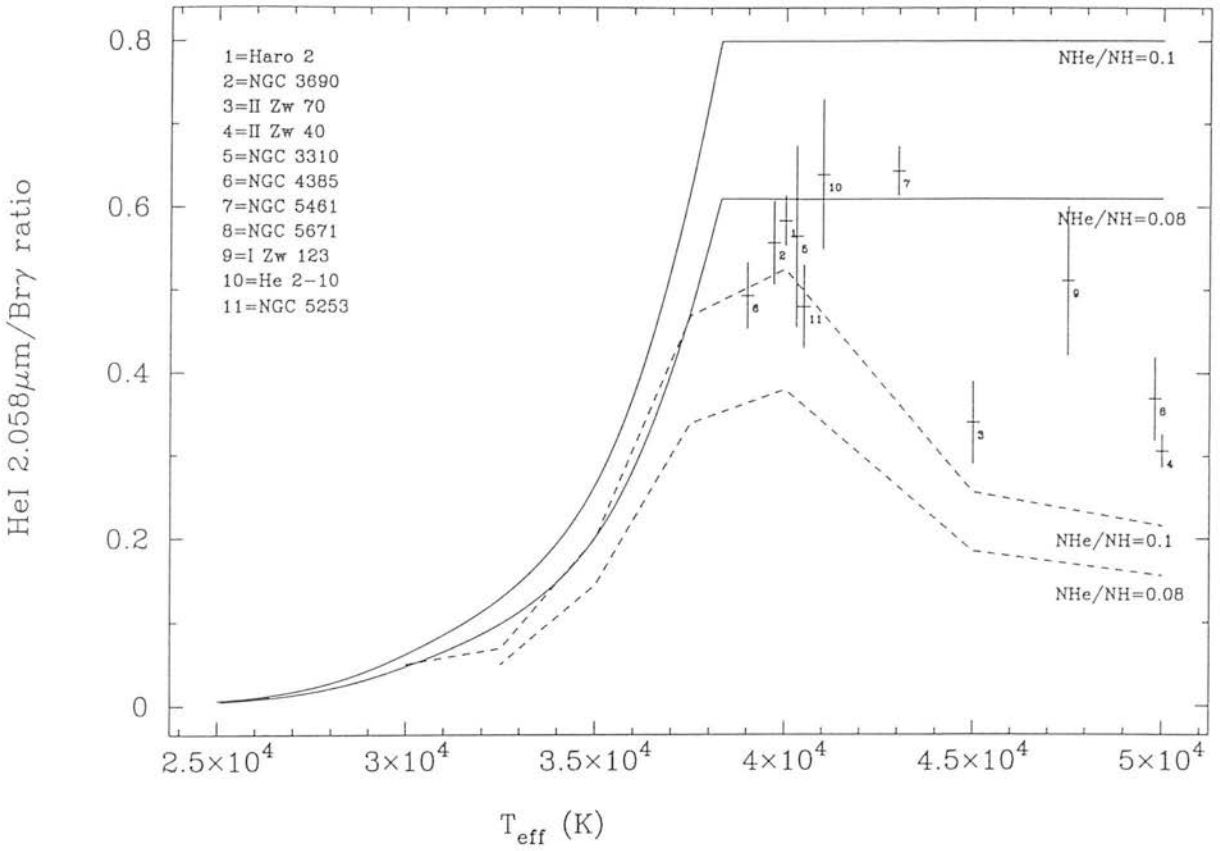

Figure 6.3: The HeI 2.058 μm/Brγ ratio *vs.* T_{eff} for $n_e = 10^2 cm^{-3}$. The models of chapter two are plotted as solid lines and Shields' model as dashed lines for Galactic and primordial helium abundances. Starburst galaxies or giant HII regions with optical HeI data are plotted with 1σ error bars.

However, consideration of observed HeI 2.058μm/Brγ ratios alone can only conclusively say that galaxies with observed HeI 2.058μm/Brγ ratios less than 0.33 (see below) are likely to have effective temperatures to either side of the maximum at T_{eff} ~40,000K, implying either low effective temperatures T_{eff}=35–37,000K or high effective temperatures T_{eff}=40–50,000K (see fig 6.3). This also means that the observations are in agreement with the rising part of a model curve for any given electron density. Therefore, the conclusions obtained from the HeI 2.058μm/Brγ ratio itself are no more constrained than for previous chapters.

In order to constrain these two parameters, literature pertaining to these starburst galaxies was searched through. From optical data electron densities and effective temperatures were found for a number of these galaxies. Far–infrared forbidden line ratios as electron density indicators have been discussed in section 5.2. The principle is the same for optical forbidden line ratios except these line ratios will be less accurate since in general, extinction corrections must be incorporated. Electron densities derived from the optical forbidden line ratio [SII]λ6716Å/[SII]λ6731Å have been found for half the sample of galaxies. The proximity of the two [SII] lines means that this ratio is independent of extinction. It should be noted that these two lines may not probe the same region as the HeI (2.058μm) and HI (Brγ) lines. However, from fig 5.3 of Osterbrock (1989), it can be seen that the [SII] flux ratio is sensitive to electron densities between the ranges $n_e=10^2$–$10^4 cm^{-3}$. The electron density values for starburst galaxies given in the literature range from $n_e=50 cm^{-3}$ to $n_e=1.2\times10^3 cm^{-3}$ (Armus, Heckman and Miley 1989, Kunth and Sargent 1983, Pastoriza *et al.* 1993, Vacca and Conti 1992, Torres-Peimbert *et al.* 1989 and Walsh and Roy 1989,1993). The one exception is the nucleus of NGC 3310 for which $n_e=8\times10^3 cm^{-3}$ is given by Pastoriza *et al.* (1993), a value much higher than for the HII regions observed in NGC 3310 ($n_e=2\times10^2 cm^{-3}$). Curiously, the observed HeI 2.058μm/Brγ ratios for the nucleus and two other observed regions in NGC 3310 do not reflect such a difference in electron density.

Thus, the electron densities measured from optical lines and the observed HeI 2.058μm /Brγ ratios (*c.f.* tables 6.2 and 6.3 and fig 5.3) are consistent with the inference that the HeI 2.058μm/Brγ emission from starburst galaxies is dominated by low density evolved giant HII regions. Furthermore, in such HII regions microturbulent motions

are expected to be less than in compact or UCHII regions of the order FWHM~10–15kms^{-1}, corresponding to a decrease in the HeI 2.058μm/Brγ ratio of ~10%. With the inclusion of microturbulence in Shield's low density model (dashed lines, fig 6.3), the maximum value of the HeI 2.058μm/Brγ ratio is 0.45 for a Galactic helium abundance and 0.33 for a primordial helium abundance. Equivalent maxima of the chapter 2 models (solid lines, fig 6.3) for this density and 10 kms^{-1} microturbulence are 0.64 (Galactic abundance) and 0.53 (primordial abundance). If the actual maximum value of the HeI 2.058μm/Brγ ratio for n_e=10^{2}cm^{-3} and microturbulent motions is considered to lie somewhere between 0.45 and 0.64 for a Galactic abundance and between 0.33 and 0.53 for a primordial abundance, then the lowest HeI 2.058μm/Brγ ratios (see fig 6.3) can only be explained by lower effective temperatures than T_{eff} ~38,000K (chapter 2 models, solid lines) or effective temperatures lower or higher than T_{eff} ~40,000K which corresponds to the maximum value of the ratio (Shields' models, dotted lines). (Hereafter, it will be assumed that the maximum value of the HeI 2.058μm/Brγ occurs at T_{eff} ~40,000K when discussing both models).

For all these galaxy categories, comparison of observed HeI 2.058μm/Brγ ratios with Shields' models show that effective temperatures can range from between T_{eff}=30,000–50,000K. T_{eff} could be calculated from infrared luminosities which are described in section 2.6, however assumptions about the initial mass function (IMF) would be needed; different assumptions lead to different T_{eff} values. A much neater method would be to look for [SIV] emission which characterizes T_{eff} greater than ~ 40,000K as discussed in section 4.5.1. Aitken *et al.* (1982) use a further sophisticated technique of measuring the high excitation fine structure [SIV] 10.5μm line in conjunction with the lower excitation [ArIII] 9.0μm and [NeII] 12.8μm lines to infer T_{eff} must be at least 40,000K in NGC 5253. Indeed such observed S^{+++} emission coupled with the observed HeI 2.058μm/Brγ ratios would verify Shields' models for effective temperatures greater than T_{eff} ~40,000K.

From the literature, T_{eff} predictions from various authors are given below. Kunth (1986) claims blue compact dwarf galaxies are very low density, n_e <100cm^{-3}, and extremely hot, T_{eff} >37,000K. T_{eff} values quoted are generally obtained from photoionization and radiative transfer models *e.g.* CLOUDY, (Ferland 1993, see section

4.4), and models by Evans and Dopita (1985) and Mathis (1982). A best fit T_{eff} model is derived from the observed lines of a number of ionized species. Pastoriza *et al.* (1993) find T_{eff} of $\sim$ 40,000K most appropriate for the nucleus and HII regions they observe in NGC 3310. Campbell (1988) derives $T_{eff} \sim$ 45,000K for NGC 5253 and 50,000K for II Zw 40. Both Mathis (1982) and Evans (1986) calculate very high T_{eff} for the giant HII regions NGC 5461 and NGC 5471. Mathis' (1982) models gives 40,000K$<T_{eff}<$50,000K and T_{eff}=50,000K for NGC 5461 and NGC 5471 respectively. Similarly Evan's results mimic those for NGC 5471 and quote T_{eff}=43,000K for NGC 5461. Finally, Sugai and Taniguchi (1992) claim $T_{eff} \sim$41,000K for He 2-10 and $T_{eff} \sim$39,000K for NGC 4385.

Naturally, there are many uncertainties in all the effective temperatures quoted above *e.g.* concerning the atomic data. Nevertheless, these values seem to imply that the majority of starburst galaxies for which optical data is available have T_{eff} greater than $\sim$40,000K, and thus the low observed HeI 2.058μm/Brγ ratios, in this subset, are evidence to support the behaviour of Shields' models at high T_{eff} (dashed lines, fig 6.3, see below). Furthermore, if the presence of Wolf Rayet stars are indicative of high T_{eff} then Haro 2, NGC 5253, He 2-10, II Zw 40 and NGC 1614 all fall into this category (Conti 1991, Vacca and Conti 1992).

To summarize from the optical data, evidence exists that:
a) the overall electron density measured from emission line ratios is of the order $n_e=10^2 cm^{-3}$. For this case microturbulence effects do not decrease the observed HeI 2.058μm/Brγ ratios by more than 10%.
b) effective stellar temperatures for the majority of the starburst galaxy subset for which optical data is available, are $T_{eff} \geq$40,000K. Observed HeI 2.058μm/Brγ ratios for these galaxies are in general agreement with predictions from Shields' models.

In previous chapters the HeI 2.113μm blend has been observed in all of the UCHII regions and some of the compact HII regions and further conclusions drawn. The relevance of further HeI line observations are twofold. First, as discussed in section 4.5.4, any He^+/H^+ recombination line ratio unaffected by resonance effects from the ground state will not have such a strong dependence on the neutral helium to hydrogen fraction y^0 *i.e* the ratio will reach a saturation value and not drop off rapidly above T_{eff}=40,000K.

Secondly, the ratio of the two helium lines will be abundance independent. This ratio will be constant up to T_{eff}=40,000K, and then decrease. Thus, the HeI 2.058μm/Brγ ratio (sensitive to all T_{eff} in the range 25–50,000K) in conjunction with another non-fluorescent HeI/HI line ratio (sensitive up to T_{eff} ~40,000K) or a HeI 2.058μm/HeI line ratio (sensitive above T_{eff} ~40,000K) should enable determination of effective temperatures in HII regions and Galaxies.

The uncertainties due to optical depth effects in the HeI 2.113μm line hindered more definite conclusions from the three sets of line ratios. Ideally, an additional HeI line free of optical depth or collisional effects would serve this purpose. Other than the complex 1.083μm line, the brightest most readily observable HeI line are optical transitions (see fig 6.4). There are several other weak HeI lines possibly observable with high resolution spectroscopic measurements *e.g.* the HeI 2.1615 and 2.1624μm 7F–4D blend, seen in NGC 5253 (Lumsden *et al.* 1994). Whether these lines would be detected in most of these more distant galaxies in the sample is speculative. It is for these galaxies where optical HeI and HI observations exist that further progress can be made. Optical HeI lines and their advantages and disadvantages are discussed below.

6.6 Starburst galaxy subset with optical data

An extensive literature search was performed to extract all optical HeI line measurements for the starburst galaxy sample given in tables 6.2 and 6.3. Optical HeI measurements were found for almost half of the galaxy sample. Predominantly, optical HeI lines have been studied in metal poor *i.e.* blue dwarf galaxies and giant HII regions in the context of helium abundance determination. In addition, detailed spectroscopic studies of NGC 3310 (Pastoriza *et al.* 1993) and NGC 3690 (Friedmann *et al.* 1987) have been carried out. Table 6.5 lists the galaxies for which optical HeI/HI measurements have been found.

6.6.1 Infrared HeI/HI line ratios

Before the optical HeI/HI data is discussed the observed HeI 2.058μm/Brγ ratios in this subset of galaxies are analysed. Returning to fig 6.3, in this current study the maximum

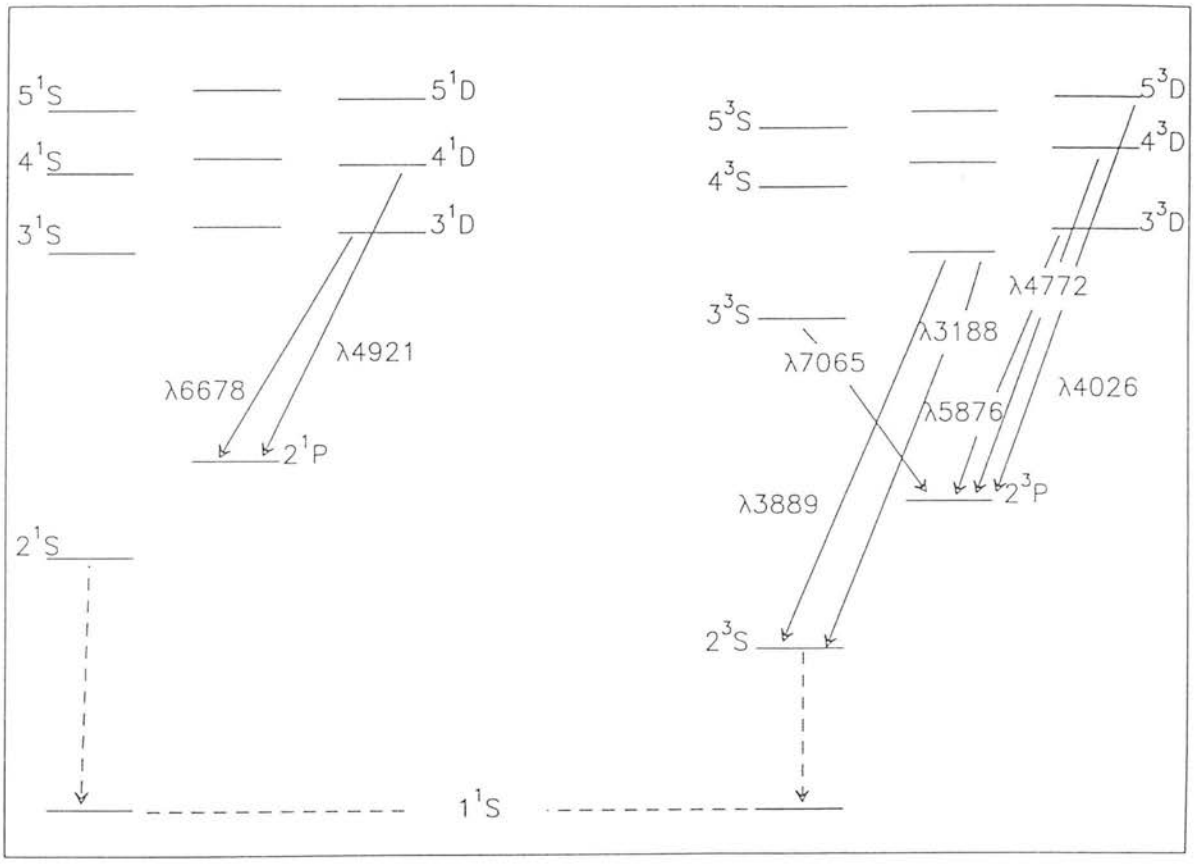

Figure 6.4: Partial energy-level diagram of HeI showing prominent optical transitions

value for the HeI 2.058μm/Brγ ratio at $n_e=10^2 cm^{-3}$, T_e ~10,000K is considered to lie between 0.38 (dashed lines, Shields' models for a primordial abundance) and 0.8 (solid lines, chapter 2 models for a Galactic abundance) and the ratio is assumed to turn over above T_{eff}=40,000K. Therefore for a given ratio two T_{eff} solutions are possible unless the ratio corresponds to the maximum value *i.e.* a value $\geq$ 0.38 implying T_{eff} ~40,000K for the object.

It should be noted that in previous chapters there was no observational evidence to confirm this turn over, but as discussed in section 4.5.4 this may be due to selection effects. If effective temperatures inferred from optical measurements are believed, then a number of galaxies are known to have $T_{eff} \geq$40,000K, thus this data also serves as a test of Shields' model predictions.

The objects for which optical data are available are plotted in fig 6.3. The only optical HeI lines tabulated for NGC 3690 were found for NGC 3690A. For NGC 3310, optical HeI measurements were found for the nucleus, the giant HII region and NGC 3310 (B), however most measurements agreed within the errors and a mean value was taken for each optical HeI line. T_{eff} values, discussed in section 6.5, from the literature were used for more than half the objects. For these and the remaining objects, theoretical diagrams of Evans and Dopita (1985) or others were used to obtain estimates of T_{eff}, from [OIII], [OII] and Hβ measurements elsewhere in the literature. If a number of sources have the same effective temperature then the data in fig 6.3 are spaced equally slightly to either side of this temperature for clarity. These effective temperature estimates are dependent on the atomic data used and a large number of other parameters and are probably accurate to a few 1000K, although the reliability of such models is difficult to determine.

Observed HeI 2.058μm/Brγ ratios for this subset of galaxies suggest the majority of these objects have effective temperatures T_{eff} of around 40,000K in agreement with the effective temperatures found from optical data. However, the ratio for I Zw 123 suggests a lower effective temperature than that obtained using optical data. The ratios lie on or between the solid curves for a primordial abundance as expected in dwarf galaxies and the dashed lines for a Galactic abundance. Effective temperatures for II

Zw 70, II Zw 40, and NGC 5471 are expected to be lower or higher from their lower HeI 2.058μm/Brγ ratios (see fig 6.3). Higher values are in qualitative agreement with the effective temperatures predicted from the optical data, and also qualitatively affirm the prediction of the behaviour of the HeI 2.058μm/Brγ ratio above T_{eff} ~40,000K. Examination of optical HeI/HI data should provide further evidence for this conclusion.

6.6.2 Optical HeI/HI line ratios

Table 6.5 gives a summary of the prominent HeI optical lines (see fig 6.4), and their strengths relative to Hβ, measured in these galaxies; the reference is given in the final column.

Assuming the physical conditions n_e=10^2cm^{-3}, T_e=10,000K and recombination coefficients from Hummer and Storey (1987) and Smits (1991a) the theoretical ratio of HeI 4472/Hβ is 0.049 for a Galactic abundance. Further theoretical HeI line strengths relative to Hβ are derived from Smits (1991a) who calculates HeI line strengths relative to HeI 4472Å (section 2.5.1). The first two rows of table 6.5 give maximum theoretical line strengths for Galactic and primordial helium abundances respectively. As discussed in section 6.6, primordial abundances are expected for most of this galaxy subset. As for any HeI/HI ratio, the HeI(opt)/Hβ ratio is a function of effective temperature, T_{eff}. Three processes which result from a large population in the n=2 metastable levels, as detailed in section 3.3, can further affect these HeI line strength measurements: collisional excitation, photoionization and optical depth effects. Studies in chapter 3 show that these effects are negligible in the 2^1S level and that photoionization effects are marginal. Although collisional effects are unimportant for the HeI 2.058μm and 2.113μm lines they may be of consequence for these HeI optical lines given in table 6.5. Each of the optical HeI lines and any potential physical processes which could affect the line strength are now discussed.

It is important to note that measurements of optical HeI line strengths by different authors for the same galaxy are in good agreement, with only one or two exceptions. Any anomalously high or low values have been neglected from the discussion below. The observed values have all been dereddened (section 6.4) by the given author, except NGC

Galaxy	λ3889	λ4026	λ4471	λ4921	λ5876	λ6678	λ7065	[1]Ref
TH(NHe/NH=0.1)	0.104	0.020	0.042	0.013	0.130	0.036	0.023	
TH(NHe/NH=0.06)	0.083	0.016	0.039	0.010	0.104	0.030	0.016	
HARO 2			0.034		0.096			Davidge
NGC 3690A					0.069	0.036		Friedmann
NGC 3690A					0.104			French
II ZW 70			0.011		0.104	0.036		Osterbrock
II ZW 70	0.132±0.009		0.044±0.003		0.084±0.004			French
II ZW 40	0.142±0.015		0.041±0.006		0.071±0.005	0.020 ±0.003	0.025±0.002	Campbell
II ZW 40		0.026±0.004	0.035±0.002	0.011±0.002	0.070±0.002	0.022±0.002		Pagel
II ZW 40			0.047		0.077	0.026	0.034	Walsh
II ZW 40				0.033	0.076	0.033	0.046	French
II ZW 40	0.181±0.016	0.023	0.041±0.002	0.011±0.003	0.083±0.004	0.028±0.009		Stephenson
II ZW 40			0.035±0.007		0.064±0.013			Kunth
NGC 3310(HII)	0.130±0.029		0.036±0.009		0.099±0.005	0.032±0.003		Terlevich
NGC 3310(NUC)					0.100±0.010	0.030±0.010		Pastoriza
NGC 3310(B)	0.100±0.020		0.030±0.005		0.130±0.010	0.030±0.006	0.019±0.006	Pastoriza
NGC 4385					0.122			Pastoriza
NGC 5461	0.191±0.018	0.017±0.002	0.041±0.002	0.013±0.002	0.129±0.009	0.035±0.004	0.027±0.004	Terlevich
NGC 5461			0.036		0.110	0.030	0.020	Torres
NGC 5461			0.036		0.093			Evans
NGC 5471	0.186±0.016	0.016±0.002	0.035±0.002	0.011±0.002	0.110±0.009	0.030±0.004	0.026±0.004	D'Odorico
NGC 5471			0.034		0.095	0.026	0.021	Torres
NGC 5471			0.035		0.077			Evans
I ZW 123			0.056		0.103	0.026	0.040	D'Odorico
HE 2-10			0.026±0.006		0.092±0.016			French
NGC 5253		0.013±0.002	0.036±40.002		0.099±0.002	0.025±0.002		Vacca
								Walsh

[1] Davidge=Davidge (1989). Friedmann=Friedmann et al. (1967). French=French (1980). Osterbrock=Osterbrock and Pogge (1987). Campbell=Campbell et al. (1986). Pagel=Pagel et al. (1992). Walsh=Walsh and Roy (1989, 1993). Terlevich=Terlevich et al. (1991). Stevenson=Stevenson et al. (1993). Kunth=Kunth and Sargent (1983). Vacca=Vacca and Conti (1992). Pastoriza=Pastoriza et al. (1993). Torres=Torres-Peimbert et al. (1989). Evans=Evans (1966). D'Odorico= D'Odorico et al. (1963).

Table 6.5: Optical HeI/Hβ lines ratios obtained from the literature for the starburst galaxy subset. Theoretical ratios for Galactic and Primordial abundances are given in the first two rows.

3690. The dereddened HeI line strength (relative to Hβ) for this object was calculated from eqn 6.2, using raw flux values from Friedmann *et al.* (1987).

Optical depth effects on the 2^3S–3^3P λ3889 line have been discussed in section 3.3.3. This line strength is heavily reduced by a large population in the 2^3S level, up to a factor of 15, (table 3, Robbins 1968). Comparison of theoretical values with observed values given for various galaxies reveal measured λ3889 values to be higher than those predicted. This is the result of contamination by the H8 line which has the same rest wavelength. Therefore predictions from observed values of the λ3889 line strength are unreliable and not considered further.

Three objects: II Zw 40, NGC 5461 and NGC 5471, all of which have predicted low or primordial helium abundances, have measured λ4026 line strengths. This 5^3D–2^3P transition is changed negligibly by any of the processes mentioned above. The observed λ4026 line strengths for NGC5461 and NGC 5471 (Torres-Peimbert *et al.* 1989) are in excellent agreement with predicted maximum values for a primordial abundance, suggestive of T_{eff} >38,000K. The values for II Zw 40 are slightly higher.

The λ4472 4^3D–2^3P line is the standard line; strengths of other HeI lines are often quoted relative to this line. This is one of the brightest observed HeI lines which is unaffected by collisions and only slightly affected by optical depth effects (no more than a few per cent, *c.f.* table 3, Robbins 1968).

Fig 6.5a depicts the ratio of HeI 4472Å/Hβ as a function of T_{eff} for n_e=10^2cm^{-3} and T_e=10,000K. Figs 6.5b and 6.5c show similar models for the HeI 5876Å and HeI 6678Å lines. These line ratios are discussed below; these three lines are the brightest uncomplicated HeI lines. These models are based on the formulated models in chapter 2 and Smits (1991a) calculations. In contrast to the HeI 2.058μm/Brγ ratio (fig 6.3), the decrease in the relative neutral helium to hydrogen fraction with T_{eff} will not produce an exaggerated decrease in the HeI 4472Å/Hβ ratio, or the other two line ratios, above T_{eff} ~40,000K, since no resonant processes to the ground state are involved (see section 4.5.4). As in table 6.4, Smits'(1991a) calculations and those of Hummer and Storey (1987) are used to calculate recombination coefficients for HeI 4472Å (also HeI 5876Å and HeI 6678Å), and Hβ respectively. These coefficients, unlike those of the HeI 2.058μm

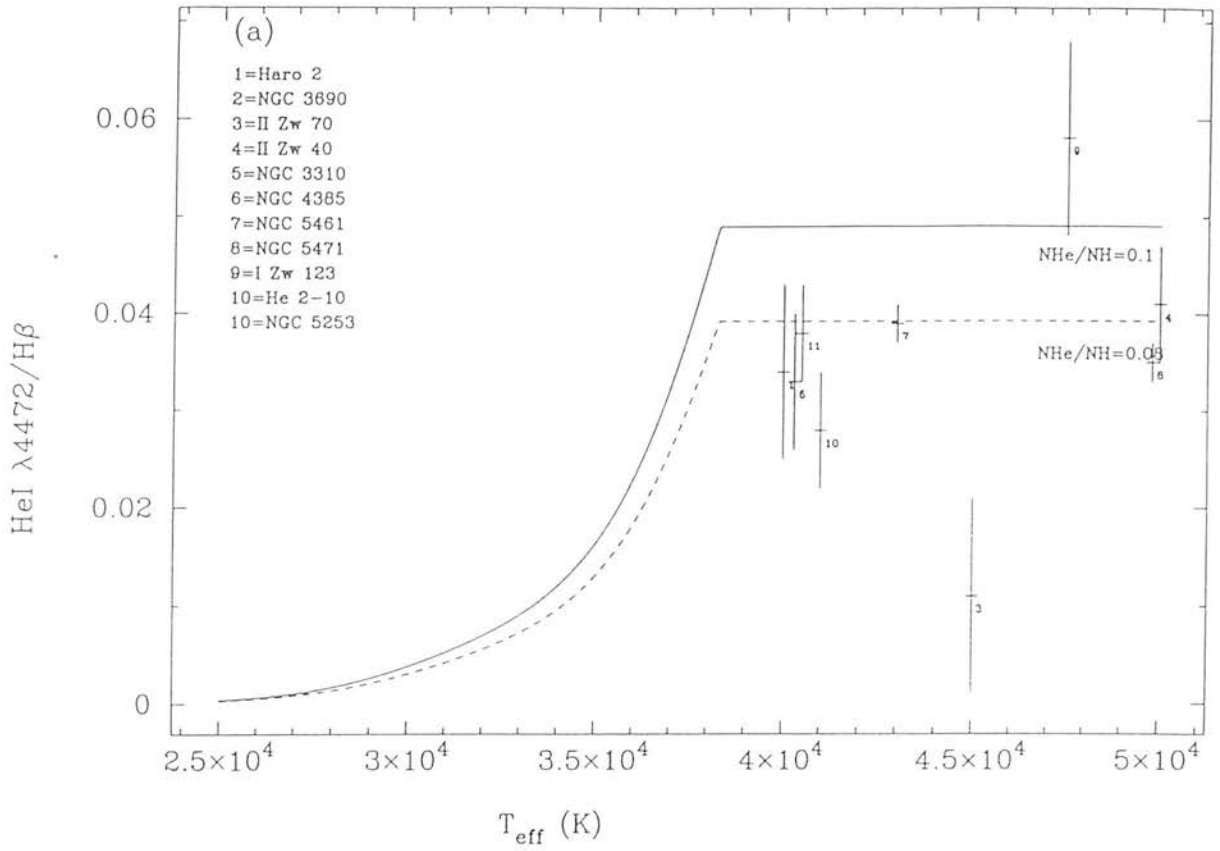

Figure 6.5: Optical HeI/Hβ line ratios *vs.* T_{eff} for the bright HeI 4472Å, 5876Å and 6678Å lines. Models are based on those formulated in chapter 2 and are calculated for Galactic and primordial helium abundances. Data for the same galaxies as in fig 6.3 are plotted with 1σ error bars.

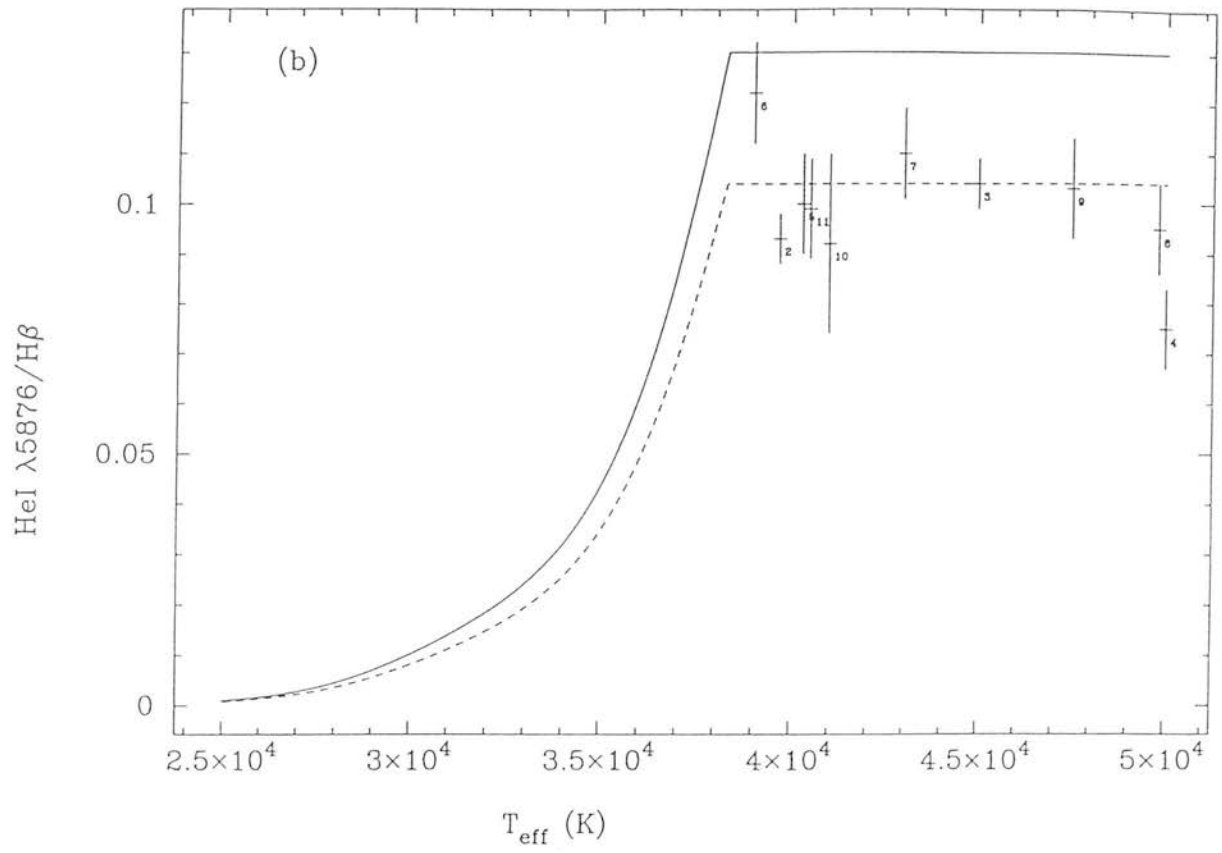
(b)
HeI λ5876/Hβ
0.1
0.05
0
2.5×10^4
3×10^4
3.5×10^4
4×10^4
4.5×10^4
5×10^4
T_eff (K)

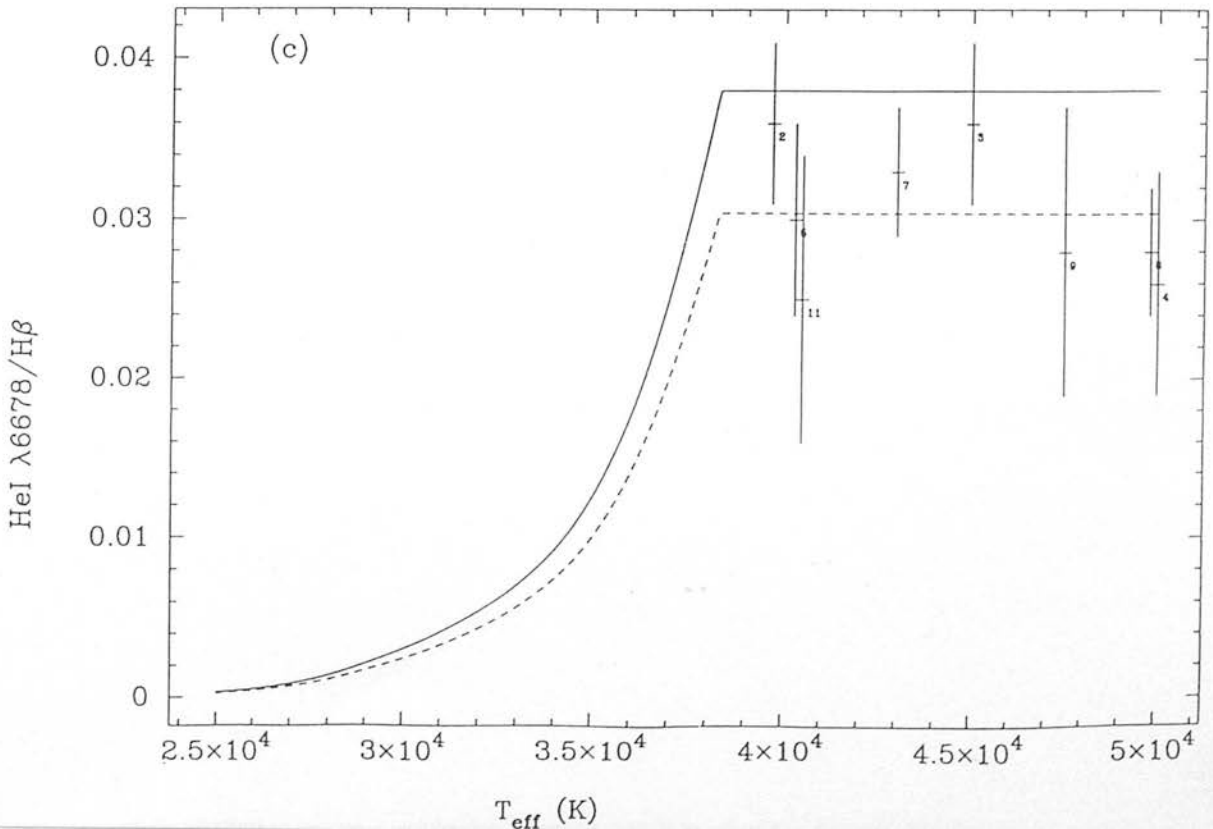
(c)
HeI λ6678/Hβ
0.04
0.03
0.02
0.01
0
2.5×10^4
3×10^4
3.5×10^4
4×10^4
4.5×10^4
5×10^4
T_eff (K)

line, appear untainted by optical depth and collisional effects, and thus there is no reason to expect any large error on the maximum value of these ratios, for the physical conditions known in these galaxies. Solid lines depict Galactic helium abundance predictions and dotted lines primordial abundance predictions. The optical data are plotted against this model (fig 6.5a) for the same T_{eff} values described in section 6.5. Most values are in agreement, within 1σ errors, with the primordial maximum value for this ratio. The ratios are consistent with the T_{eff} values inferred from photionization models discussed in section 6.5, except the ratio for II Zw 70. The value for II Zw 70 is considerably less than other values and inconsistent with predictions from other optical HeI lines.

Line strengths for λ4921 4^1D–2^1P are given in col 5, table 6.5 for II Zw 40, NGC 5461 and NGC 5471. All these values are in good agreement with the predicted primordial value and $T_{eff} > 38{,}000$K. No corrections for collisional or optical depth effects are necessary.

The 5876, 3^3D–2^3P transition, is the brightest observed optical HeI line. Collisional effects are unimportant for this line at low densities $n_e=10^2 cm^{-3}$ as long as T_e is not greater than 10,000K, but they modify the line strength dramatically at higher electron densities. Optical depth or fluorescent effects enhance the line strength by no more than 10% (table 3, Robbins 1968). From table 6.5 and fig 6.5b, a plot analogous to fig 6.5a for the λ5876 line, the observed values are fairly consistent with primordial abundances for $T_{eff} \geq 38{,}000$K, and the T_{eff} values assigned to the data, except the value for II Zw 40 which is somewhat lower. The yellow Na D interstellar sodium absorption line has a rest wavelength of 5893Å. The redshifted II Zw 40 5876Å falls at 5891Å (redshift from NED database), thus it appears that a considerable amount of the intrinsic line has been absorbed.

Optical depth effects are entirely negligible for the singlet series (section 3.3), and collisions are insignificant for the λ6678 3^1D–2^1P transition. From fig 6.5c, observed ratios imply $T_{eff} \geq 36{,}000$K; the values for II Zw 40 and NGC 5253 are the lowest.

Collisional effects are not more than 5% for the λ7065Å, 3^3S–2^3P, transition at this low density. With increasing electron density collisional effects become rapidly significant, *e.g.* at $n_e=10^4 cm^{-3}$ collisions produce the same line strength as recombinations

(C/R=1.02 section 3.3.1). Robbins' (1968) table 3, shows that fluorescent enhancement of the λ7065 2^3P–3^3S line by up to a factor of 4 is possible. Most of the observed HeI 7065Å/Hβ ratios in table 6.3 are considerably higher than the maximum predicted value of this ratio. Therefore it appears that the 7065Å line, like the 3889Å line, is difficult to model accurately and the results in col 8, table 6.5 are not analysed further.

To summarize, optical HeI/Hβ ratio models are sensitive to effective T_{eff} up to 38,000K and then saturate. Thus, this ratio in conjunction with the HeI 2.058μm/Brγ ratio provides a constraint on T_{eff}. Firstly, these results are in agreement with the lower electron densities $n_e=10^2 cm^{-3}$ predicted for ionized gas in these galaxies. For the ten galaxies, mainly dwarf galaxies and giant HII regions, in table 6.5, the optical HeI/Hβ data (with appropriate errors) from the literature agree with the assumption that for most of these galaxies $T_{eff} \geq$38,000K and agree with the T_{eff} values obtained from the literature, with a few exceptions. In II Zw 40, the HeI 5876Å line strength is less than for the other objects and considerably less the saturation value; however the redshifted wavelength of this line is coincident with the Na D interstellar absorption feature. The HeI 4472Å line strength for NGC3310 (B), NGC 5471 and He 2-10 implies a lower T_{eff} than the saturation value in contrast to the predictions from the other HeI line measurements for these objects. The HeI 4472Å line strength for I Zw 123 is somewhat higher than would be expected for a dwarf galaxy.

Thus the lower T_{eff} values found from the HeI 2.058μm/Brγ ratio for II Zw 70, II Zw 40 and NGC 5471, not seen in the optical data, confirms that these low HeI 2.058μm/Brγ ratios must be a result of higher effective temperatures than T_{eff} ~40,000K in these objects. This result strengthens the predictions of Shields' models above T_{eff} ~40,000K *i.e.* the HeI 2.058μm/Brγ ratio decreases above this temperature as a direct result of the decrease in the neutral helium to hydrogen fraction, y^0, with T_{eff}. By further comparison of the HeI 2.058μm/HeI (opt) observations it should be possible to examine the high effective temperature range T_{eff}=40–50,000K in more detail, since this ratio is expected to remain constant at all T_{eff} (chapter 2 models), or decrease above T_{eff} ~40,000K. Thus, the high T_{eff} predictions of Shields' models can be thoroughly tested, and this is the subject of the next section.

6.7 HeI 2.058 μm/HeI optical line ratio

As mentioned in section 6.5, the HeI 2.058 μm/HeI (opt) ratio is abundance independent. Table 6.6 combines the optical data in table 6.5 with the infrared observations in tables 6.2 and 6.3 as follows:

$$\frac{I_{HeI2.058}}{I_{HeIopt}} = \frac{I_{HeI2.058}}{I_{Br\gamma}} \times \left(\frac{I_{HeIopt}}{I_{H\beta}} \right)^{-1} \times \frac{I_{Br\gamma}}{I_{H\beta}} \tag{6.4}$$

To avoid beam size discrepancies, theoretical values were used for $I_{Br\gamma}/I_{H\beta}$. From Hummer and Storey (1987), $I_{Br\gamma}/I_{H\beta}$ =0.0275 for $n_e=10^2 cm^{-3}$ and T_e=10,000K. For this calculation, the c values (section 6.4) were employed to estimate the differential extinction between HeI 2.058 μm and Brγ 2.165 μm. This method is not detailed since the differential correction factor was no more than a few per cent.

The HeI 2.058 μm/HeI (opt) ratio should be independent of beam size, since each observed ratio on the RHS of eqn 6.4 represents an average ratio in the same beam. The only consideration to be noted is that the infrared measurements probe deeper into the ionized gas than the optical measurements, and the extinction correction assumes the two measurements sample the emission from the same source. With the dust and stars mixed in a homogeneous fashion however, the optical measurements sample the stars in the surface of the gas, whereas the infrared emission will also pick up emission from other stars more deeply embedded.

The HeI 2.058 μm/HeI (opt) values are plotted in figs 6.6a–c, for the same HeI 4472Å, HeI 5876Å and HeI 6678Å lines as displayed in figs 6.5a–c. The solid straight line represents the model ratio where the chapter 2 models are assumed and Smits' (1991a) line strengths used. The dotted line shows the ratio where Shields' models are used for HeI 2.058 μm line, and chapter 2 models and Shields' calculations used for the optical HeI line. An artificial dip at T_{eff}=32,500K would have been created in calculating ratios in the latter model. This dip was interpolated over.

The theoretical maxima (the ratio is assumed approximately constant up to $T_{eff} \sim$ 40,000K in the dotted model) for all the HeI 2.058 μm/HeI (opt) ratios in table 6.6 are given in the first two rows of table 6.6 for the models described above. An object is

Galaxy	HeI/λ4026	HeI/λ4472	HeI/λ4921	HeI/λ5876	HeI/λ6678	Ref.
TH(NHe/NH=0.1)[1]	0.581	0.283	1.050	0.105	0.368	
TH(NHe/NH=0.1)[2]	0.930	0.453	1.680	0.171	0.588	
HARO 2		0.482				Davidge
NGC 3690A				0.156		Friedmann
NGC 3690A		1.00		0.169	0.417	French
II Zw 70				0.089		Osterbrock
II Zw 70		0.855		0.090	0.261	French
II Zw 40		0.196		0.102		Campbell
II Zw 40		0.212		0.122	0.433	Pagel
II Zw 40	0.309	0.247	0.787	0.123	0.393	Walsh
II Zw 40		0.184		0.113	0.333	French
II Zw 40			0.262	0.114	0.262	Stephenson
II Zw 40	0.374	0.210	0.781	0.104	0.303	Kunth
II Zw 40		0.240		0.132		Vacca
NGC 3310(HII)		0.388		0.141	0.437	Pastoriza
NGC 3310(NUC)				0.152	0.508	Pastoriza
NGC 3310(B)		0.578		0.133	0.578	Pastoriza
NGC 4385				0.223		Terlevich
NGC 5461	1.055	0.438	1.380	0.139	0.513	Torres
NGC 5461		0.460		0.163	0.598	Evans
NGC 5461		0.050		0.192		D'Odorico
NGC 5471	0.638	0.292	0.928	0.092	0.340	Torres
NGC 5471		0.300		0.108	0.393	Evans
NGC 5471		0.293		0.133		D'Odorico
I Zw 123		0.244		0.108	0.506	French
He 2-10		0.632		0.192		Vacca
NGC 5253	1.015	0.347		0.133	0.528	Walsh

[1] Using Shields' models for HeI 2.058 μm.

[2] Using Smits' 1991a HeI line strengths and chapter 2 models.

Table 6.6: HeI (IR)/HeI (opt) line ratios in the starburst galaxy subset which have optical line fluxes.

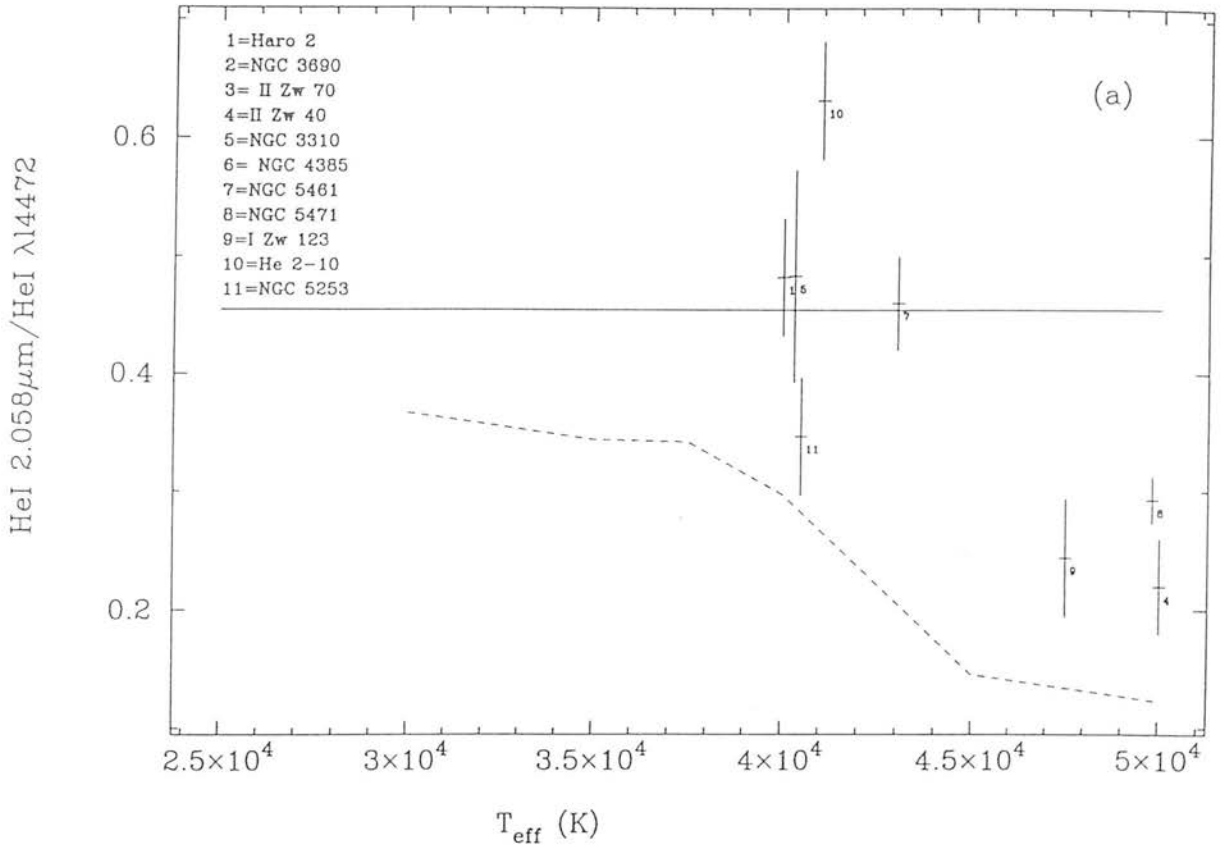

Figure 6.6: The HeI 2.058μm/HeI (opt) line ratios *vs.* T_{eff} for the bright optical HeI 4472Å, 5876Å and 6678Å lines. Solid lines combine the chapter 2 models shown in fig 6.3 (solid lines) and the models shown in fig 6.5. Dashed lines combine Shields' models (fig 6.3, dashed lines) and the models in fig 6.5. Data points are for the same galaxies as in fig 6.3, and plotted with 1σ error bars.

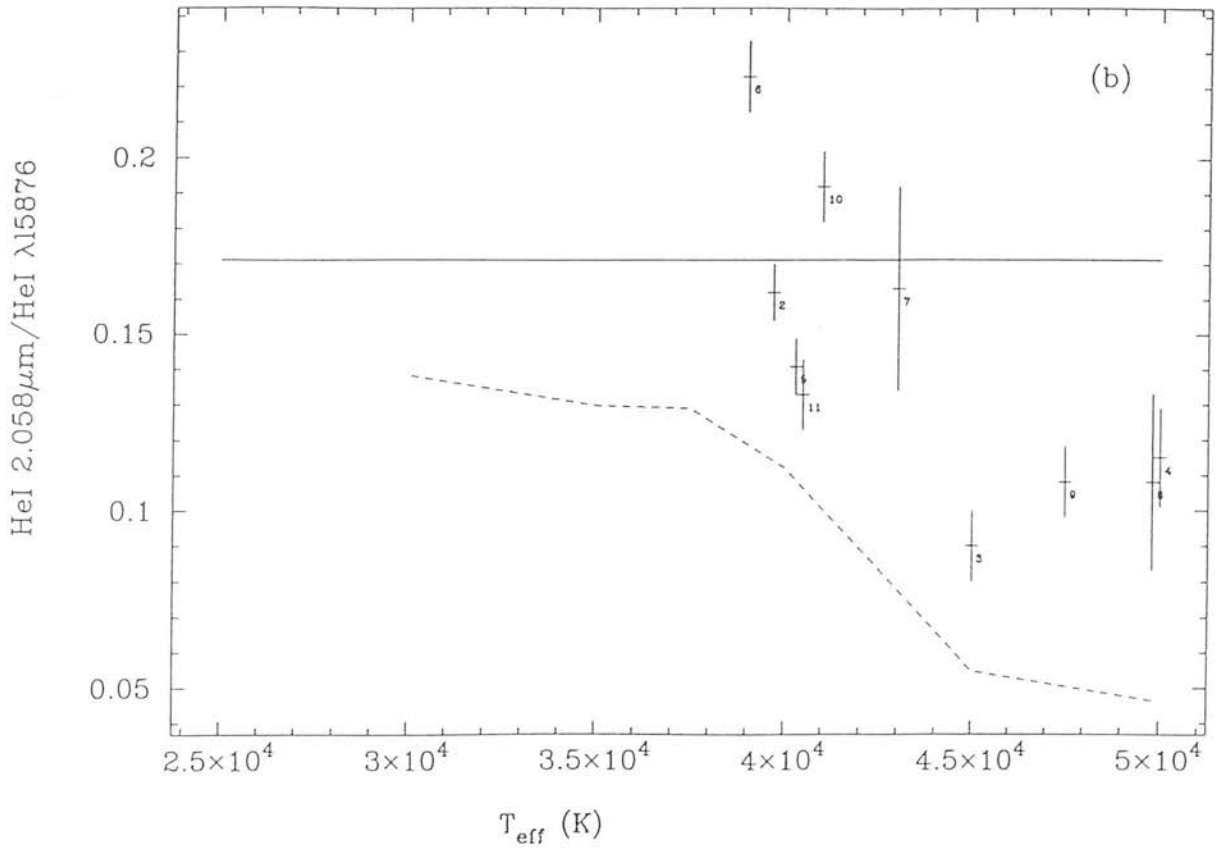
(b)
HeI 2.058μm/HeI λ15876
0.2
0.15
0.1
0.05
2.5×10^4
3×10^4
3.5×10^4
4×10^4
4.5×10^4
5×10^4
T_eff (K)

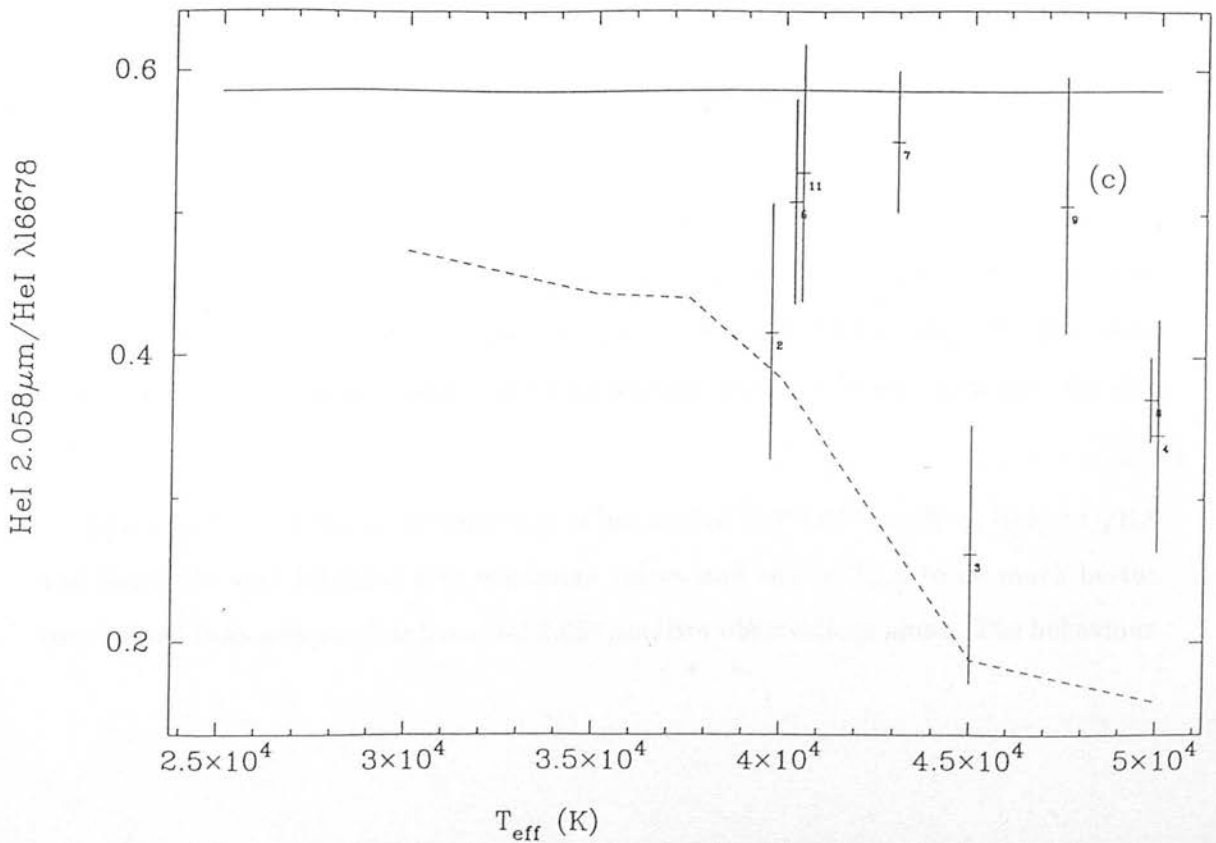
(c)
HeI 2.058μm/HeI λ16678
0.6
0.4
0.2
2.5×10^4
3×10^4
3.5×10^4
4×10^4
4.5×10^4
5×10^4
T_eff (K)

assumed to have an effective temperature of T_{eff}=40,000K if its given line pair ratio falls between or is higher than these values. This may underestimate T_{eff} in an object if Smits' (1991a) values are more accurate since the lower maximum value predicted using Shields' models also represents a hotter T_{eff} using Smits' (1991a) values and assuming a more realistic turnover in the solid line models of fig 6.6. Comparison of the entries in table 6.6 and figs 6.6a–c, imply an effective temperature T_{eff} ~40,000K for Haro 2, NGC 3690, NGC 3310, NGC 4385, NGC 5461, and He 2-10. For I Zw 123, the HeI 2.058μm/HeI 4472Å and HeI 2.058μm/HeI 5876Å ratios suggest T_{eff} >40,000K, consistent with the literature whilst the weaker HeI 2.058μm/HeI 6678Å and HeI 2.058μm/Brγ ratios predict a lower T_{eff} ~40,000K. In He 2-10 the HeI 2.058μm/HeI 4472Å and HeI 2.058μm/HeI 5876Å ratios are higher than the maximum theoretical values for these ratios given in table 6.6 and fig 6.6.

However, the effective temperatures from the literature (section 6.5) place all these galaxies to the right of where they are expected from the models in fig 6.6a–c. The effective temperatures assigned to the data points are derived from the [OIII], [OII] and Hβ lines using the diagnostic diagrams of Evans and Dopita (1985) (section 6.5) and or CLOUDY (Ferland 1993) models for the same ionized species. The effective temperature of NGC 5253 was found from [SIV] line measurements. This line has a similar ionization potential to [OIII], thus it would be expected to trace the same properties. The ionization potential of [OIII] is 35.1eV, much higher than that of HeI (24.6eV). The higher T_{eff} values from [OIII] measurements may be a reflection of the higher excitation in this smaller [OIII] zone compared to the HeI zone.

T_{eff} values >40,000K are inferred for II Zw 70, II Zw 40 and NGC 5471 from observed ratios in figs 6.6a–c. This is in qualitative agreement with the effective temperatures predicted from high excitation oxygen lines. However, the HeI 2.058μm/HeI (opt) ratios again reflect lower temperatures than those inferred from the [OIII], [OII] and Hβ line ratios.

Nevertheless, in general the three sets of line ratios: HeI 2.058μm/Brγ, HeI(opt)/Hβ and HeI 2.058μm/HeI (opt) give consistent values and enable T_{eff} to be much better constrained than was possible from HeI 2.058μm/Brγ observations alone. The behaviour

of the HeI 2.058μm/Brγ above T_{eff} ~40,000K as predicted from Shields' models has been validated, although the disagreement in maxima between the two sets of models in fig 6.3 suggests that the values in Shields' models may need to be re-examined. If the maximum value of the HeI 2.058μm/Brγ ratio were consistent for the two models, more accurate predictions of T_{eff} could be made. The one further test of these HeI 2.058μm/HeI (opt) models would be to examine the HeI 2.058μm/Brγ ratio in conjunction with optical HeI measurements for an object with T_{eff} known to be less than T_{eff}=38,000K.

6.8 Conclusions

Near–infrared spectroscopic measurements of the HeI 2.058μm/Brγ ratio are presented for a wide ranging sample of star forming galaxies: giant HII regions, normal spirals, dwarf galaxies and ultraluminous IRAS galaxies. From these near–infrared observations several inferences have been made:

a) The observed ratios showed no trend with galaxy category; possibly suggesting that different star forming environments do not change the nature of the stellar population.

b) Lower ratios were observed in this starburst galaxy sample than in individual UC or compact HII regions. This result is in agreement with the assertion that the HeI 2.058μm/Brγ emission results from evolved lower density giant HII regions.

c) Assuming in these studies that the maximum value of the HeI 2.058μm/Brγ ratio lies between the values predicted from chapter 2 and Shields' low density models, and both Galactic and primordial helium abundances are considered, then several galaxies must have effective temperatures which are either lower or higher than T_{eff} ~40,000K. This is due to the double-valued nature of the behaviour of the HeI 2.058μm/Brγ ratio with T_{eff}, below the maximum value of the ratio which corresponds to T_{eff} ~40,000K.

A subset of galaxies for which optical data was well documented in the literature was chosen. This sample was predominantly comprised of metal poor objects and the literature describes these galaxies as having effective temperatures $T_{eff} \geq$ 40,000K and electron densities of $n_e=10^2 cm^{-3}$. The observed HeI 2.058μm/Brγ ratios suggest that most of these objects have effective temperatures T_{eff} ≥40,000K. Three objects, II

Zw 40, II Zw 70 and NGC 5471, had comparatively lower HeI 2.058μm/Brγ ratios in qualitative agreement with Shields' models and the higher T_{eff} values given in the literature.

Optical HeI/Hβ models have been constructed with the same formulation as the models of chapter 2, adopting Smits' (1991a) HeI line strengths. Comparison of observed optical HeI/Hβ line ratios in general reaffirmed the prediction that these galaxies had effective temperatures $T_{eff} \geq$40,000K. Lower values were not generally found for the three galaxies named above, ruling out lower T_{eff} values for these objects. Infrared and optical measurements were combined and compared to models, confirming these results and further illustrating the behaviour of HeI 2.058μm/HeI (opt) ratios above $T_{eff} \sim$40,000K.

To summarize and generalize the results for this subset of galaxies:
a) This new method of combining infrared HeI/HI and optical HeI/HI measurements for the three sets of line ratios: HeI 2.058μm/Brγ, HeI(opt)/Hβ or HeI 2.058μm/HeI (opt) enables T_{eff} to be much better constrained than was possible from HeI 2.058μm/Brγ observations alone.
b) These results validate the predictions of Shields' models for the behaviour of the HeI 2.058μm/Brγ above $T_{eff} \sim$40,000K. Further, if the maximum value of the HeI 2.058μm/Brγ ratio were consistent for the two models, more accurate prediction of T_{eff} could be made.

One final suggestion is that there are a number of weak HeI lines in the K window which are the HeI 2.113μm blend (optical effects are not too important for low densities) and the 2.1615 and 2.1624μm 7F–4D blend. High resolution spectroscopic measurements may be able to determine line fluxes for these lines. The advantages are that these lines would probe to the same depth in the ionized gas as the HeI 2.058μm and Brγ lines, differential extinction corrections would be small, and there would be no systematic errors from observations made with different instruments.

Chapter 7

Conclusions

In this work, the aim has been to test theoretical models of the HeI 2.058μm/Brγ ratio as a function of effective temperature, T_{eff}, and so calculate spectral types of the hottest most massive stars present in HII regions. For this purpose, K band measurements of the HeI 2.058 μm and Brγ recombination lines were carried out for samples of ultracompact (UC) HII regions, compact HII regions and giant HII regions in, or the nuclei of, starburst galaxies.

Two detailed models of the HeI 2.058μm/Brγ ratio *vs.* T_{eff} have been published to date, by Doyon, Puxley and Joseph (1992) (DPJ), and Shields (1993). The former models use the on-the-spot (OTS) approximation to solve for radiative transfer whilst the latter models make use to the photoionization/radiative transfer code CLOUDY (Ferland 1993). Both models agree up to T_{eff} ~40,000K showing an increase in the HeI 2.058μm/Brγ ratio with T_{eff}. The major difference between the two models is that DPJ assume the neutral helium to hydrogen fraction is constant with T_{eff}, whereas Shields models show that this quantity decreases with increasing T_{eff}. This results in a turnover in Shields' models, whereas DPJ predicts the HeI 2.058μm/Brγ ratio to saturate, above T_{eff} ~40,000K. The models of DPJ have been updated to make use of recent atomic data from Smits (1991a), who gives HeI 2.058μm line strengths for electron densities of n_e=10^2, 10^4 and 10^6cm^{-3} and includes the effects of collisional excitation on the HeI 2.058μm line. Electron temperatures of T_e=5,000 and 10,000K

were considered. Shields' models were calculated for electron densities of $n_e=10^2$ and $10^4 cm^{-3}$. Electron temperatures are a function of T_{eff} and radius in the nebula, mean values are T_e=7,500–10,000K.

In chapter 3, theoretical HeI 2.113μm/Brγ and HeI 2.113/HeI 2.058μm ratios were constructed in order to further test the predictions of the HeI 2.058μm/Brγ ratio discussed in chapter 2. To determine theoretical values for the HeI 2.113μm line strength results from Smits (1991a) were used. Additional physical processes, the result of the metastability of the HeI 2S levels, were investigated, namely, collisional excitation from the HeI 2^3S level to n$\geq$3, photoionization from 2^3S, and optical depth effects in the 2^1S–n^1P, and 2^3S–n^3P transitions for n$\geq$3. Only the latter process was found to affect the HeI 2.113μm line strength. As optical depth is dependent on the source size, individual models were constructed for each UCHII region.

This thesis was centred around observations made to test the models in detail, and the results obtained. To compare results to theoretical predictions, independent measurements of effective temperatures were required. Radio continuum and IRAS luminosities were used to estimate effective temperatures, and spectral types, derived both for a single star and cluster of stars assumed as the powering sources(s) in compact and UCHII regions.

In chapter 2, observations of the HeI 2.058μm/Brγ ratio in UCHII regions were studied. In chapter 3, additional HeI 2.113μm data were analysed for the same UCHII regions. Observed HeI 2.058μm/Brγ ratios in compact HII regions were the subject of chapter 4. The latter objects were selected to fit this category by their listed source sizes from radio measurements. Model physical parameters were chosen which best represented the observations in these chapters, thus predictions relating to the physical conditions in compact and UCHII regions were made. Physical parameters– effective temperatures, electron densities and electron temperatures found to represent the emission from compact and UCHII regions are now discussed.

For the majority of the UCHII regions, effective temperatures were thought to be greater than ~35,000K, in agreement with further observations in chapter 3. Furthermore, dusty HII region models were preferred if radio or cluster stellar temperatures were

assumed for the UCHII regions. IRAS spectral observations, available for a number of these UCHII regions and compact HII regions, failed to detect any significant S^{+++} emission, which would be expected in stars hotter than T_{eff} ~40,000K. Thus, Shields models could not be tested above T_{eff} ~40,000K in chapters 2 or 4. The turnover seen in the HeI 2.058 μm/Brγ ratio above T_{eff} ~40,000K was not expected for the HeI 2.113 μm/Brγ ratio since the HeI 2.113 μm line is unaffected by the decrease in the neutral helium to hydrogen fraction with T_{eff}. Conversely, the HeI 2.113 μm/HeI 2.058 μm ratio would be expected to increase above T_{eff} ~40,000K. Such a trend was not displayed amongst the UCHII region sample, or the few compact HII regions in which the 2.113 μm blend was detected, further indicating that T_{eff} was not above 40,000K in any of these objects.

Generally lower observed HeI 2.058 μm/Brγ ratios were found in the compact HII regions. One explanation is that they have lower effective temperatures than UCHII regions. Shields' models and the dusty models of chapter 2, favour this interpretation. Single star temperatures derived from radio flux measurements, have shown this to be the case for four compact HII regions. Another possibility is that there are lower electron densities in compact as compared to UCHII regions. Radio continuum measurements were used to calculate electron densities in chapter 5. Electron densities were found to be in the range $n_e=10^4$–$10^5 cm^{-3}$ for UCHII regions and $n_e=10^3$–$10^4 cm^{-3}$ for compact HII regions. Therefore, for the remaining objects, lower electron densities are the most plausible explanation.

Electron temperatures of T_e=5,000K were consistent with UCHII region observations of the HeI 2.058 μm/Brγ ratio. However, such low electron temperatures imply smaller galactocentric radii values than are known for a number of UCHII regions, thus higher electron temperatures of T_e=10,000 K are appropriate in a number of UCHII regions. This introduced disagreement, in that predicted HeI 2.058 μm/Brγ ratios were higher than observed values, and therefore some additional mechanism or other effect must be present to produce a decrease in the ratio.

Microturbulence in the velocity field was thought to be the additional mechanism which was responsible for the lower observed HeI 2.058 μm/Brγ ratios than predicted from models in UCHII regions with electron temperatures of T_e=10,000K. As discussed

above, effective temperatures were not found to be greater than ~40,000K. Therefore, although effective temperatures greater than this turnover value in Shields' models are consistent with observations, this explanation is ruled out for the compact and UCHII regions studied in chapters 2–4. The effect of microturbulence is as follows. As the electron temperature is increased from T_e=5,000K, and the HeI 2.058μm/Brγ ratio increases, further broadening of the HeI 2.058μm line decreases the optical depth in this line, which produces a decrease in the HeI 2.058μm/Brγ ratio. The required microturbulent velocities are not greater than thermal velocities at T_e=5,000K and reach values of the order ~20kms^{-1} for T_e=10,000K, in agreement with the mean observed HeI 2.058μm/Brγ ratio for these UCHII regions. From observations in chapter 3, it was shown that almost half of the UCHII regions were in accord with only the higher temperature model, as microturbulence of order ~20kms^{-1} was required to explain observed HeI 2.113/HeI 2.058μm line ratios. For the remaining UCHII regions any model, within the range of parameters given above, would be consistent with observations.

RRL and high resolution HeI and HI measurements of the observed compact and UCHII regions are broadly consistent with microturbulent velocities of order 20kms^{-1} but small beam measurements of the HeI 2.058μm and Brγ line widths are needed, since large scale velocity motions would also explain the RRL measured line widths, but occur over scales which are too large to affect the HeI 2.058μm line.

In chapter 5, it was demonstrated that more accurate electron density or density gradients may be a substitute for microturbulence in HII region models for T_e=10,000K. It was noted however that integrated electron densities inferred from radio continuum measurements and the HeI 2.058μm/Brγ ratio will not be the same unless the density structure is homogeneous throughout the HII region. Therefore, lower electron densities predicted from radio measurements which would explain observed HeI 2.058μm/Brγ values may just be a reflection of local densities from which the different density indicators originate. A techinque using density gradient distributions calculated from radio maps was used to determine a more accurate prediction of the HeI 2.058μm/Brγ ratio in HII regions. Detailed studies were performed on two UCHII regions which revealed that the difference between HeI 2.058μm/Brγ ratio predicted for constant electron density and density gradient models was greater than observational errors. Such a density gradient

could be a plausible alternative to microturbulence. However, all density distribution models have been produced with the simplifying assumption of spherical symmetry. Therefore, appropriate density distributions need to be incorporated into any detailed HII region model and an integral over a realistic source geometry performed.

In chapter 6, HeI 2.058μm/Brγ observations focussed on starburst galaxies and giant HII regions in external galaxies. Near–infrared spectroscopic measurements of the HeI 2.058μm/Brγ ratio in a wide ranging sample of star forming galaxies, giant HII regions, normal spirals, dwarf galaxies and ultraluminous IRAS galaxies, were presented.

Since the HeI 2.058μm/Brγ ratio was shown to be dominated by regions of greater volume in chapter 5, lower density giant HII regions were expected to dominate the integated emission from starburst galaxies. The observed HeI 2.058μm/Brγ ratios were much lower than had been observed in compact and UCHII regions which upheld this assertion. Lower electron densities of order n_e=10^2cm^{-3} were found from optical collisionally excited forbidden lines, further evidence to validate the above assumption. However, even with the inclusion of microturbulence, the observed HeI 2.058μm/Brγ ratio in a number of galaxies were still lower than the peak value at T_{eff} ~40,000K. Therefore, effective temperatures somewhat lower, or additionally higher than the turnover at T_{eff} ~40,000K in Shields models were required for these objects.

A subset of galaxies for which optical data were well documented in the literature was analysed in more detail. This sample was predominantly comprised of metal poor objects. Such galaxies are expected to have effective temperatures $T_{eff} \geq$ 40,000K and electron gas densities of n_e=10^2cm^{-3}. Thus, these objects enabled the turnover predicted in Shields models to be tested. The observed HeI 2.058μm/Brγ ratios suggested that most of these objects have effective temperatures T_{eff} ~40,000K. Three objects had comparatively lower ratios in agreement with Shields' models above ~40,000K and the higher T_{eff} values given in the literature.

Additionally, optical HeI data were acquired from the literature and HeI/Hβ models were constructed with the same formulation as the models of chapter 2. Again, the decrease in the neutral helium to hydrogen fraction does not affect any HeI optical lines significantly. Comparison of observed optical HeI/Hβ line ratios in general reaffirmed the

prediction that these galaxies had effective temperatures $T_{eff} \geq 40{,}000$K. Lower values were not predominantly found for the three galaxies discussed above, ruling out lower T_{eff} values for these objects. Thus, whilst the HeI 2.058μm/Brγ or HeI(opt)/Hβ are each individually not very sensitive effective temperature indicators, the combination of optical and infrared HeI/HI ratios enables T_{eff} to be constrained using Shields models. If the discrepancy between the maxima of the HeI 2.058μm/Brγ ratios in chapter 2 and Shields' models could be resolved accurate effective temperatures could be deduced from this method. Thus the question of the masses of stars and the IMF in our own galaxies and other galaxies could be readdressed.

7.1 Future work

This final result confirms that the models used in this thesis may be useful for effective temperature determination. Rather, than comparison of HeI 2.058μm and Brγ lines with optical HeI and Hβ lines, where systematic differences between using different instruments may be significant and extinction corrections are vital, other infrared measurements of HeI lines in the K window would be advantageous. The HeI 2.1137 singlet 4^1S–3^1P line would be ideal if it could be separated from its equivalent triplet 2.1126μm line, shown to be complicated by optical depth effects, and the dominant component of the 2.113μm blend. A resolution of $\sim$150kms^{-1} would be required. This is possible to acheive with the 150 l/mm and the echelle gratings on CGS4. There are also weak HeI 7F-4D (the equivalent of Brγ) lines which have been detected in the spectrum of the UCHII region G29.96 as well as in the starburst galaxy NGC 5253 (Lumsden *et al.* 1994). These lines arise from sufficiently high transitions that optical depth effects are not important. The greatest advantage is that all such near-infrared lines would probe to the same depth in the ionized gas as the HeI 2.058μm and Brγ lines.

From chapter 6, it was shown that Shields' models correctly predicted the behaviour of the HeI 2.058μm/Brγ ratio with effective temperature. The discrepancy between the maxima of the HeI 2.058μm/Brγ ratios in chapter 2 and Shields' models must be resolved before such models can be used to determine accurate effective temperatures. It is important to be able to test the high temperature predictions of Shields' models

against simpler geometry less physically complex HII regions. Such HII regions could be selected from the sample of HII regions by Simpson and Rubin (1990), for objects observed to have significant S^{+++} emission. Observations of HeI 2.058μm/Brγ ratios in planetary nebula, by DePoy and Shields (1994), are in qualitative agreement with the predicted decrease in the HeI 2.058μm/Brγ ratio at high T_{eff}.

In chapter 4, it was seen how electron densities, effective temperatures and microturbulence remain uncertain parameters. Other methods to constrain electron densities, dealt with in chapter 5, represent a first step in extending the models to account for varying density distributions.

To investigate the effect of microturbulence on the HeI 2.058μm line in more detail, it would be necessary to examine the HeI line width over scales comparable to the mean free path over which absorption of helium atoms takes place. For 584Å photons, which are responsible for pumping the HeI 2.058μm line, this scale length is of the order of $10^{-4\widehat{m}}$ or less for the compact and UCHII regions studied in this work which have distances of 2–20kpc. Such resolutions are only possibly achievable with long baseline radio interferometers. However, RRl lines are weak even with sensitivities of $0.5^{\widehat{m}2}$ as can be seen from Wood and Churchwell (1991). Optical and infrared interferometry techinques have been proposed which would be capable of detecting brighter HeI lines *e.g.* E.S.O. VLT project in Chile. In principle, infrared interferometry could be used to investigate microturbulent velocity fields in obscured HII regions.

FIR collisionally excited lines can be used to determine effective temperatures. Several papers (*e.g.* Lacy *et al.* 1976, Lacasse *et al.* 1980, Pipher *et al.* 1984, and references therein) have been published which use the [NeII] (12.8μm), [ArIII] (9.0μm) and [SIV] (10.5μm) mid-IR lines observable from the ground to predict T_{eff}. Mid-infrared spectroscopic techniques can probe the youngest most obscured UCHII regions not even visible in the near-infrared. Such observations in starburst galaxies will be possible with the commissioning of the new mid-infrared spectrometer "Michelle" on UKIRT which will have a much greater spectral resolution than with the current mid-IR spectrometer CGS3. Since extinction generally decreases at longer wavelenths, mid-infrared emission will be measureable from regions nearer the nucleus of starburst galaxies than even

near-infrared measurements are able to sample.

Models of the far-infrared line ratios of [SIII] (19 μm)/[OIII] (52 μm) and [NIII] (57 μm)/[NII] (122 or 205 μm) as a function of T_{eff} have been constructed by Rubin *et al.* (1994). Only the [SIII] (19 μm) line is observable from the ground. New or forthcoming space observatories such as ISO and SIRTF present opportunities to detect FIR fine structure lines which are difficult or impossible to detect with ground-based telescopes. SOFIA is a new proposed infrared airborne observatory envisaged to replace the KAO. SOFIA is planned to contain a 2.5m telescope which will achieve far greater resolutions than the existing 91cm telescope on the KAO.

Evans and Dopita (1985) have similarly produced diagnostic diagrams of bright optical forbidden lines *vs.* T_{eff}. They have produced an extensive photoionization/radiative transfer code which would enable similar diagrams of forbidden infrared lines ratios as a function of T_{eff}. Such lines would be observable from giant, compact and UCHII regions and not as prone to large extinction corrections as optical transitions. CLOUDY (Ferland 1993) could be used to make similar predictions. Initially, model HeI 2.058 μm/Brγ ratios were constructed by DPJ to circumvent the problems associated with using FIR forbidden lines, namely the uncertainies in the atomic data and abundances for the heavier complex species. There is still a great need for accurate atomic data for heavier elements.

A combination of both effective temperatures determined from FIR forbidden lines which are fairly insensitive to electron density and temperatures and effective temperatures from the simpler HeI and HI atoms should enable effective temperatures to be determined in HII regions in our own and other galaxies. Theoretical modelling needs to be further developed before this can happen since complications arise in the interpretation of measurements of different ionized species in which the emission emanates from different volumes within the HII region (Rubin 1986).

References

Abbot, D.C., Hummer, D.G., 1985, ApJ, 294, 286

Aitken, D.K., Roche, P.F., Allen, M.C., Phillips, M.M., 1982, MNRAS, 199, 31p

Aller, L.H., 1942, ApJ, 95, 52

Armus, L., Heckman, T.M., Miley, G.K., 1989, ApJ, 347, 727

Baker, J.G., Menzel, D.H., 1938, ApJ, 88, 52

Baldwin, J.A., Ferland, G.J., Martin, P.G., Corbin, M.R., Cota, S.A., Peterson, B.M., Slettebak, A., 1991, ApJ, 374, 580

Balick, B., 1975, ApJ, 201, 705

Ball, R., Arens, J.F., Jernigan, J.G., Keto, E., Meixner, M.M., 1992, ApJ, 389, 616

Becker, R.H., White, R.L., Edwards, A.L., 1991, ApJS, 75, 1

Becker, R.H., White, R.L., Helfand, D.J., Zoonermatkermani, S., 1994, ApJS, 91, 347

Berrington, K.A., Kingston, A.E., 1987, J.Phys.B, 20, 6631

Bodenheimer, P., Tenorio-Tagle, G., Yorke, H.W., 1979, ApJ, 233, 85

Brocklehurst, M., 1972, MNRAS, 157, 211

Campbell, A., Terlevich, R., Melnick, J., 1986, MNRAS, 223, 811

Campbell, A., 1988, ApJ, 335, 644

Catalogued Galaxies and Quasars Observed in the IRAS Survey, 1985. Prepared by Lonsdale, C.J., Helou, G., Good, J.C., Rice, W., Jet Propulsion Laboratory.

Chini, R., Krügel, E., Kreysa, E., 1986, A&A, 167, 315

Chini, R., Krügel, E., Wargau, W., 1987, A&A, 181, 378

Churchwell, E., 1975, in Wilson, T.L., Downes, D., eds, HII Regions and Related Topics. Springer-Verlag, Berlin, p.245

Churchwell, E., Walmsley, C.M., 1975, A&A, 38, 451

Churchwell, E., 1990, A&AR, 2, 79

Churchwell, E., Wolfire, M.G., Wood, D.O.S., 1990, ApJ, 354, 247

Clegg, R.E.S., 1987, MNRAS, 229, 31p

Clegg, R.E.S., Harrington, J.P., 1989, MNRAS, 239, 869

Colgan, S.W.J., Simpson, J.P., Rubin, R.H., Erickson, E.F., Haas, M.R., Wolf, J., 1991, ApJ, 366, 172

Combes, F., Gerin, M., 1985, A&A, 150, 327

Conti, P.S., 1991, ApJ, 377, 115

Davidge, T.J., 1989, PASP, 101, 494

Davidge, T.J., Maillard, J.-P., 1990, ApJ, 351, 432

Davidson, K., Harwit, M., 1967, ApJ, 148, 443

DePoy, D.L., Shields, J.C., 1994, ApJ, 422, 187

D'Odorico, S., Rosa, M., Wampler, E.J., 1983, A&AS, 53, 97

Douglas, J.N., Bash, F.N., Torrence, G.W., Wolfe, C., 1980, The Texas Survey: Preliminary +18deg strip. Univ. Texas. Pub. Ast. No 17

Downes, D., Wilson, T.L., Bieging, J., Wink, J.E., 1980, A&AS, 40, 379

Doyon, R., Puxley, P.J., Joseph R.D., 1992, ApJ, 397, 117 (DPJ)

Draine, B.T., 1985, ApJS, 57, 587

Draine, B.T., 1989, in Kaldeich, B.H., ed., Proc. 22nd Eslab Symposium, Infrared spectroscopy in Astronomy. ESA Publications, p93

Dreher, J.W., Welch, W.J., 1981, ApJ, 245, 857

Eddington, A.S., 1934, MNRAS, 95, 2

Elmegreen, B.G., Elmegreen, D.M., 1983, MNRAS, 203, 31

Evans, I., Dopita, M.A., 1985, ApJS, 58, 125

Evans, I., 1986, ApJ, 309, 544

Ferland, G.J., 1980, PASP, 92, 596

Ferland, G.J., 1993, Univ. Kentucky Dept. of Physics and Astronomy Internal Report

Fich, M., 1993, ApJS, 86, 475

Forster, J.R., Caswell, J.L., Okumura, S.K., Hasegawa, T., Ishiguro, M., 1990, A&A, 231, 473

Friedmann, S.D., Cohen, R.D., Jones, B., Smith, H.E., 1987, AJ, 94, 1480

French, H.B., 1980, ApJ, 240, 41

Garay, G., Rodríguez, L.F., 1983, ApJ, 266, 263

Garay, G., Reid, M.J., Moran, J.M, 1985, ApJ, 289, 681

Garay, G., Rodríguez, L.F., van Gorkum, J.H., 1986, ApJ, 309, 553

Garay, G., 1989, in Gordon, M.A., Sorochenko, R.L., eds, Radio Recombination lines: 25 years of investigation. Kluwer, Dordrecht p.73

Garwood, R.W., Perley, R.A., Dickey, J.M., Murray, M.A., 1988, AJ, 96, 1655

Geballe, T.R., Krisciunas, K., Lee, T.J., Gatley, I., Wade, R., Duncan, W.D., Garden, R., Becklin, E.E., 1984, ApJ, 284, 118

Gioia, I.M., Gregorini, L., Klein, U., 1982, A&A, 116, 164

Gordon, M.A., Walmsley, C.M., 1990, ApJ, 365, 606

Handa, T., Sofue, Y., Nakai, N., Hirabayashi, H., Inoue, M., 1987, PASP, 39, 709

Harper, D.A., Low, F.J., 1971, ApJ, 165, L9

Herter, T., Helfer, H.L., Pipher, J.L., Forrest, W.J., McCarthy, J., Houck, R.J., Willner, S.P., Puetter, R.C., Rudy, R.J., Soifer, B.T., 1981, ApJ, 250, 186

Herter, T., Helfer, H.L., Pipher, J.L., 1983, A&AS, 51, 195

Hjellming, R.M., 1966, ApJ, 143, 420

Hoare, M.G., Roche, P.F., Glencross, W.M., 1991, MNRAS, 251, 584

Hollenbach, D., Johnstone, D., Shu, F., 1992, in Cassinelli, J.P., Churchwell, E.B., eds, Massive Stars: Their Lives in the Interstellar Medium. A.S.P. CONF. SER. Vol 35, p. 26

Hummer, D.G., Storey, P.J., 1987, MNRAS, 224, 801

Hunter, D.A., Gallagher, J.S. III., 1989, Science, 243, 1557

Icke, V., Gatley, I., Israel, F.P., 1980, ApJ, 236, 808

Israel, F.P., 1967, PhD thesis. Univ. Leiden

Jennings, E., 1975, in Wilson, T.L., Downes, D., eds, HII Regions and Related Topics. Springer-Verlag, Berlin, p.137

Jourdain de Muizon, M., Cox, P., Lequeux, J., 1990, A&AS, 83, 337

Keto, E., Proctor, D., Ball, R., Arens, J., Jernigan, J.G., 1992, ApJ, 401, L113

Kingdon, J., Ferland, G.J., 1991, PASP, 103, 752

Koorneef, J., 1983, A&A, 128, 84

Krügel, E., Mezger, P.G., 1975, A&A, 42, 441

Kunth, D., 1986, PASP, 98, 984

Kunth, D., Sargent.W.L.W., 1983, ApJ, 273, 81

Kurtz, Wood, D.O.S., Churchwell, E., 1994, ApJS, 91, 659

Kurucz, R.L., 1979, ApJS, 40, 1

Lacasse, M.G., Herter, T., Krassner, J., Helfer, H.C., Pipher, J.L., 1980, A&A, 86, 231

Lacy, J.H., Baas, F., Townes, C.H., Geballe, T.R., 1979, ApJ, 227, L17

Lacy, J.H., 1981, in Wynn-Williams, C.G., Cruikshank, D.P., eds, IAU Symposium No.96, Infrared Astronomy. Kluwer, Dordrecht, p237

Lacy, J.H., Beck, S.C., Geballe, T.R., 1982, ApJ, 255, 510

Landolt–Börnstein, 1982, in Schiaffers, K., Voigt, H.H., ed., Astronomy& Astrophysics, 2b, Stars & star clusters, p.31

Larkin, J.E., Graham, J.R., Matthews, K., Soifer, B.T., Beckwith, S., Herbst, T.M., Quillen, A.C., 1994, ApJ, 420, 159

Leech, K.J., Penston, M.V., Terlevich, R., Lawrence, A., Rowan-Robinson, M., Crawford, J., 1989, MNRAS, 240, 349

Lockman, F.J., 1989, ApJS, 71, 469

Low, F.J., Aumann, H.H., 1970, ApJ, 162, L79

Lumsden, S.L., Puxley, P.J., Doherty, R.M., 1994, MNRAS, 268, 821

Mac Low, M.-M., van Buren, D., Wood, D.O.S., Churchwell.E., 1991, ApJ, 369, 395

Mathis, J.S., 1971, ApJ, 167, 261

Mathis, J.S., 1982, ApJ, 261, 195

Mathis, J.S., 1986, PASP, 98, 995

Mathis, J.S., Rumpl, W., Nordsieck, K.H., 1977, ApJ, 217, 425

McCarthy, P.J., Heckman, T., van Brugel, W., 1987, AJ, 93, 264

Megeath, S.T., Herter, T., Gull, G.E., Houck, J.R, 1990, ApJ, 356, 534

Mezger, P.G., Henderson, A.P., 1967, ApJ, 147, 471

Mezger, P.G., Schrami, J., Terzian, Y., 1967, ApJ, 150, 807

Mountain, C.M., Leggett, S.K., Selby, M.J., Blackwell, D.E., Petford, A.D., 1985, A&A, 151, 399

Mountain, C.M., Robertson, D.J., Lee, T.J., Wade, R., 1990, in Crawford, D.L., ed, Proc. SPIE, Instrumentation in Astronomy VII, 1235, p25

Osterbrock, D.E., Pogge, R.W., 1987, ApJ, 323, 108

Osterbrock, D.E., 1989, Astrophysics of Gaseous Nebulae, University science books, p.29

Pagel, B.E.J., Simonson, E.A., Terlevich, R.J., Edmunds, M.G., 1992, MNRAS, 255, 325

Panagia, N., Walmsley, C.M., 1978, A&A, 70, 411

Pastoriza, M.G., Dottori, H.A., Terlevich, E., Terlevich, R., Díaz,A.I., 1993, MNRAS, 260, 177

Petrosian, V., Silk, J., Field, G.B., 1972, ApJ, 177, L69

Pipher, J.L., Helfer, H.L., Herter, T., Briotta, D.A. Jr., Houck, J.R., Willner, S.P., Jones, B., 1984, ApJ, 285, 174

Pottasch, S.R., 1962, ApJ, 135, 385

Press, W., Flannery, B., Teukolsky, S., Vetterling, W., 1986, Numerical Recipes, Cambridge University Press.

Puxley, P.J., 1988, PhD thesis, University of Edinburgh

Puxley, P.J., Brand, P.W.J.L., Moore, T.J.T., Mountain, C.M., Nakai, N., Yamashita, T., 1989, ApJ, 345, 163

Ramsay, S.K., Mountain, C.M., Geballe, T.R., 1992, MNRAS, 259, 751

Rank, D.M., Dinerstein, H.L., Lester, D.F., Bregman, J.D., Aitken, D.K., Jones, B., 1978, MNRAS, 185, 179

Rayo, J.F., Peimbert, M., Torres-Peimbert, S., 1982, ApJ, 255, 1

Reid, M.J., Haschick, A.D., Burke, B.F., Moran, J.M., Johnston, K.J., Swenson, G.W. Jr., 1980, ApJ, 239, 89

Robbins, R.R., 1968, ApJ, 151, 511

Roche, P.F., Aitken, D. K., 1984, MNRAS, 208, 481

Rubin, R.H., 1968a, ApJ, 153, 761

Rubin, R.H., 1968b, ApJ, 154, 391

Rubin, R.H., Hollenbach, D.J., Erickson, E.F., 1983, ApJ, 265, 239

Rubin, R.H., 1984, ApJ, 287, 653

Rubin, R.H., 1985, ApJS, 57, 349

Rubin, R.H., 1986, Péquignot, D., ed., in Workshop on Model Nebulae. Paris: Observatoire de Paris, p. 235

Rubin, R.H., Simpson, J.P., Lord, S.D., Colgan, S.W.J., Erickson, E.F., Haas, M.R., 1994, ApJ, 420, 772

Ryle, M., Downes, D., 1967, ApJ, 148, L17

Sanders, D.B., Clemens, D.P., Scoville, N.Z., Solomon, P.M., 1986, ApJS, 60, 1

Sarazin, C., 1977, ApJ, 211, 772

Scalo, J., 1989, in Renzini, A., Fabbiano, G., Gallagher, J.S., eds, Windows on Galaxies. Kluwer, Dordrecht, p.125

Scott, P.F., 1981, MNRAS, 194, L25

Scoville, N.Z., Norman, C., 1988, ApJ, 332, 163

Sharpless, S., 1959, ApJS, 4, 257

Shields, J.C., 1993, ApJ, 419, 181

Shortridge, K., 1991, Figaro–General Data Reduction & Analysis

Skillman, E.D., 1989, ApJ, 347, 883

Simpson, J.P. Rubin, R.H., 1984, ApJ, 281, 184

Simpson, J.P. Rubin, R.H., 1990, ApJ, 354, 165

Smits, D.P., 1991a, MNRAS, 248, 193

Smits, D.P., 1991b, MNRAS, 251, 193

Sorochenko, R.L., Berulis, J.J., 1969, Ap lett, 4, 173

Spitzer, L. Jr., Savedoff, M.P., 1950, ApJ, 111, 593

Stańiska, G., 1982, A&AS, 48, 299

Stevenson, C.C., McCall, M.L., Welch, D.L., 1993, ApJ, 408, 460

Strömgren, B., 1939, ApJ, 89, 526

Struve, O., Elvey, C.T., 1938, ApJ, 88, 364

Sugai, H., Taniguichi, Y., 1992, AJ, 103, 1470

Telesco, C.M., Gatley, I., 1984, ApJ, 284, 557

Tenorio-Tagle, G., 1979, A&A, 71, 59

Terlevich, R., Melnick, J., Masegosa, J., Moles, M., Copretti, M.V.F., 1991, A&AS, 91, 285

Thompson, R.I., Tokunaga, A.T., 1980, ApJ, 235, 889

Thronson, H.A., Jr., Harper, D.A., 1979, ApJ, 230, 133

Torres-Peimbert, S., Peimbert, M., Fierro, J., 1989, ApJ, 345, 186

Treffers, R.R., Fink, U., Larson, H.P., Gautier, T.N., III., 1976, ApJ, 209, 793

Turner, B.E., Matthews, H.E., 1984, ApJ, 277, 164

Vacca, W.D., Conti, P.S., 1992, ApJ, 401, 543

van den Bergh, S., 1980, PASP, 92, 122

Viner, M.R., Clarke, J.N., Hughes, V.A., 1976, AJ, 81, 512

Walsh, J.R., Roy, J.-R, 1989, MNRAS, 239, 297

Walsh, J.R., Roy, J.-R, 1993, MNRAS, 262, 27

Waltman, W.B., Waltman, E.B., Schwartz, P.R., Johnston, K.J., Wilson, W.J., 1973, ApJ, 185, L135

Whitford, A.E., 1958, AJ, 63, 201

Wiese, W.L., Smith, M.W., Glennon, M.M., 1966, NSRDS-NBS, No. 4

Wink, J.E., Altenhoff, W.J., Mezger, P.G., 1982, A&A, 108, 227

Wood, D.O.S., Churchwell, E., 1989, ApJS, 69, 831

Wood, D.O.S., Churchwell, E., 1991, ApJ, 372, 199

Wynn-Williams, C.G., Becklin, E.E., Matthews, K., Neugebauer, G., 1978, MNRAS, 183, 237

Yorke, H.W., Tenorio-Tagle, G., Bodenheimer, P., 1983, A&A, 127, 313

Yorke, H.W., Tenorio-Tagle, G., Bodenheimer, P., 1984, A&A, 138, 325

Yorke, H.W., 1986, ARA&A, 24, 49

Zanastra, H., 1951, B.A.N., 11, 341

Zoonermatkermani, S., Helfand, D.J., Becker, R.H., White, R.L., Perley, R.A., 1990, ApJS, 74, 181

Zuckerman, B., 1973, ApJ, 183, 863

Mon. Not. R. Astron. Soc. **266**, 497–510 (1994)

Spectroscopy of H II regions at 2 μm: ultracompact sources

Ruth M. Doherty,[1] Phil Puxley,[2] René Doyon[3] and Peter W. J. L. Brand[1]

[1]*Institute for Astronomy, University of Edinburgh, Blackford Hill, Edinburgh EH9 3HJ*
[2]*Royal Observatory, Blackford Hill, Edinburgh EH9 3HJ*
[3]*Université de Montréal, C.P. 6128, Succ. A., Montréal, Quebec, H3C 3J7, Canada*

Accepted 1993 September 17. Received 1993 August 27; in original form 1993 March 26

ABSTRACT

We have measured the line fluxes of He I 2.058 μm and Br γ 2.165 μm from ultracompact (UC) H II regions excited by stars of spectral types O4 to B1. The ratio of these two lines is compared with theoretical predictions of the dependence of this ratio on the effective temperature of the exciting star(s) for electron densities of $n_e = 10^2$, 10^4 and 10^6 cm^{-3}. From our observations, the He I 2.058 μm/Br γ ratio is approximately constant over this range of spectral types. Our observations are in good agreement with the theoretical model of Doyon, Puxley & Joseph for an electron temperature and density of $T_e = 5 \times 10^3$ K, $n_e = 10^4$ cm^{-3} and a Galactic helium abundance of 0.1. Alternatively, for an electron temperature and density of $T_e = 10^4$ K and $n_e = 10^4$ cm^{-3} the He I linewidth must be increased from its Doppler value of 6 km s^{-1} to about 17 km s^{-1}, e.g. by turbulent motions of the ionized gas, to be consistent with our observations.

We also consider the role of telluric CO_2 absorption on the He I recombination line at 2.058 μm. Because of the intrinsic narrowness of the He I line (20–40 km s^{-1}) the percentage of He I line flux removed varies as the Earth revolves. For the observations presented here, up to 36 per cent of the He I line is absorbed before it reaches the telescope.

Key words: H II regions – infrared: stars.

1 INTRODUCTION

The ratio of the infrared recombination lines of He I (2^1P–2^1S) 2.058 μm[1] and Br γ 2.165 μm[1] in H II regions has been modelled by Doyon, Puxley & Joseph (1992, hereafter DPJ). This ratio is a measure of the relative number of helium to hydrogen ionizing photons, which is strongly dependent on the effective temperature of the exciting source and hence on its mass. This strong mass dependence means that the He I 2.058 μm/Br γ ratio integrated over the stellar population should be a strong function of the upper mass limit, M_u, of the initial mass function (IMF), whilst remaining fairly insensitive to the lower mass limit, M_l (DPJ). There is mounting evidence (e.g., see the review by Scalo 1989) that the IMF in some starburst galaxies is inconsistent with that in the solar neighbourhood, the lower mass cut-off being markedly higher, ~ 3–6 $M_\odot$. As Scalo concludes, this result is invalid if the upper mass limit of the starburst IMF has been underestimated, because the upper and the lower mass limits are dependent parameters. If M_u is increased sufficiently, then M_l can be decreased to the extent that an IMF with M_l comparable to the solar-neighbourhood value of 0.1 $M_\odot$ is perfectly plausible in these starburst galaxies. Our aim in this series of papers is to examine the dependence of the He I 2.058 μm/Br γ ratio on effective stellar temperature for less complex, unevolved H II regions in our own Galaxy, and to quantify modifications to the ratio due to density, and line and continuum radiative-transfer effects.

Other transitions, such as the mid-infrared, fine-structure lines [S IV] λ10.52 μm, [Ar III] λ9.0 μm and [Ne II] λ12.8 μm (Aitken et al. 1982), and the optical fine-structure lines [O III] $\lambda\lambda$4959, 5007 and Hβ (Campbell, Terlevich & Melnick 1986), have been used as similar diagnostics to constrain stellar effective temperatures. Advantages of the He I 2.058 μm/Br γ line ratio are as follows: (i) both lines are close in wavelength and lie in the K window where dust extinction is an order of magnitude smaller than at visual wavelengths, (ii) the lines are intrinsically bright, the He I 2^1P level being boosted by the 1^1S–2^1P 0.0584-μm resonance-line transition, and (iii) the variation in the helium abundance

[1]The wavelengths quoted are in air.

throughout the interstellar medium is less dramatic than that of the heavier elements (e.g. Rayo, Peimbert & Torres-Peimbert 1982).

In this paper, we present observations of the He I 2.058 μm/Br γ ratio in a sample of UC H II regions in order to examine radiative-transfer and density effects on the theoretical models. Section 2 describes the observational details; Sections 3 and 4 examine the corrections for the effects of telluric absorption on the He I line flux and dust extinction towards each source, respectively. In Section 5, the theoretical models are described, and the effects of collisional excitation and internal dust on the He I 2.058 μm/Br γ ratio are discussed. In Section 6, the results of the observations of UC H II regions are compared with these models.

2 OBSERVATIONS AND DATA REDUCTION

The UC H II regions observed and their equatorial coordinates are given in Table 1. They were selected from an extensive VLA survey at 5 and 15 GHz by Wood & Churchwell (1989) so as to sample the range of spectral types of the ionizing stars for UC H II regions, namely O4 to B1. Infrared spectra of the UC H II regions were obtained on the 3.8-m United Kingdom Infrared Telescope (UKIRT) on the nights of 1990 September 2 and 3. Observations were made with the cooled grating spectrometer CGS2, using a circular aperture of 5 arcsec. The 633 line mm^{-1} grating provided an instrumental resolution at 2.2 μm of ~730, or 400 km s^{-1}. The observations were sky-subtracted by nodding the telescope 30–40 arcsec off the source, to a position determined from previous infrared imaging so as to be free of emission from surrounding sources. The on-chip exposure time was 1.5 s for each of the 21 grating positions covering the range 2.0 to 2.2 μm, and the spectra were sampled three times per resolution element.

Subsequent observations were obtained on the night of 1991 June 23 with the newly commissioned cooled grating spectrometer CGS4 (Mountain et al. 1990), which has a 58×62 InSb pixel detector array. At 2.2 μm, the resolving power of CGS4 with the 75 line mm^{-1} grating and 150-mm focal length camera is ~340, or 900 km s^{-1}. To ensure that the spectra were fully sampled, the detector was stepped four times over two pixels for the wavelength range 2.0–2.4 μm. The offset positions for sky-subtraction were 30 arcsec west. The spectra were flat-fielded by observation of a blackbody at 1073 K, taken with the same instrumental configuration as the astronomical targets. Wavelength calibration accurate to 0.002 μm was carried out, using observations of atmospheric OH emission lines. The final spectra were obtained by summing the central five detector rows along the slit to give a 3.1×15.5 arcsec^2 synthesized aperture.

The conventional method for correction of the instrumental response and atmospheric absorption is to divide the object spectrum by that of a standard star, and then to multiply by a blackbody with effective temperature appropriate to that of the spectral standard, so as to remove the coarse spectral shape of the star. To this end, the spectroscopic standards listed in Table 2 were observed at regular intervals between source observations, so that airmass variations were minimal. A-type stars were chosen because, apart from their Br γ absorption lines at 2.165 μm, they have featureless spectra in the K window. These Br γ absorption lines were removed from the stellar spectrum by interpolation. If not already known, the magnitude of the spectroscopic standard was determined by comparison of its spectrum with that of a flux standard, observed on the same night and close in airmass.

However, the He I line lies amidst strong CO_2 telluric absorption around 2.06 μm. Division by the spectroscopic standard will correct the continuum around the He I 2.058 μm line, but not the line itself which is intrinsically extremely narrow (1/10–1/45 of the resolution of the spectrometer for CGS2 and CGS4, respectively). The correction applied for this effect is discussed in more detail in Section 3.

The He I and Br γ recombination lines were fitted with Gaussian profiles in the case of the CGS2 data, and triangular profiles for the CGS4 data (the convolution of the slit on square pixels), which are good approximations to the instrumental profiles. Both lines were fitted simultaneously with the same best-fitting FWHM, since the change in dispersion will be negligible ($\leq$0.001 μm) between the two lines. The spectra are shown in Figs 1(a)–(j).

3 CORRECTION FOR ATMOSPHERIC ABSORPTION

The molecules CO_2, H_2O and O_2 in the Earth's atmosphere are responsible for the presence of several strong absorption bands at infrared wavelengths. In the K window there is a

Table 1. Object list.

Object	Equatorial Coordinates		Distance
	α(1950)	δ(1950)	kpc
G5.48	17 55 58.65	-24 20 43.24	14.3
G5.97	18 00 36.44	-24 22 53.74	1.9
G15.04	18 17 31.68	-16 12 57.94	2.1
G29.96	18 43 27.07	-02 42 36.46	9.0
G35.20	18 59 14.05	01 09 03.12	3.2
G43.89	19 12 02.82	09 17 19.10	10.3
G45.07	19 11 00.42	10 45 42.87	9.7
G45.12	19 11 06.24	10 48 25.82	9.5

Table 2. Standard star list.

Name	Equatorial Coordinates		K mag	Spectral Type
	α(1950)	δ(1950)		
BS 6746	18 02 34.5	-30 25 46.5	0.66	KOIII
BS 6798	18 08 16.8	-19 51 16.3		A4V
BS 7314	19 14 38.2	38 02 41.6	1.66	KOIII
SAO 104272	18 53 53.7	18 02 29.0		K2I
SAO 104728	19 17 32.0	11 26 28.6		A2

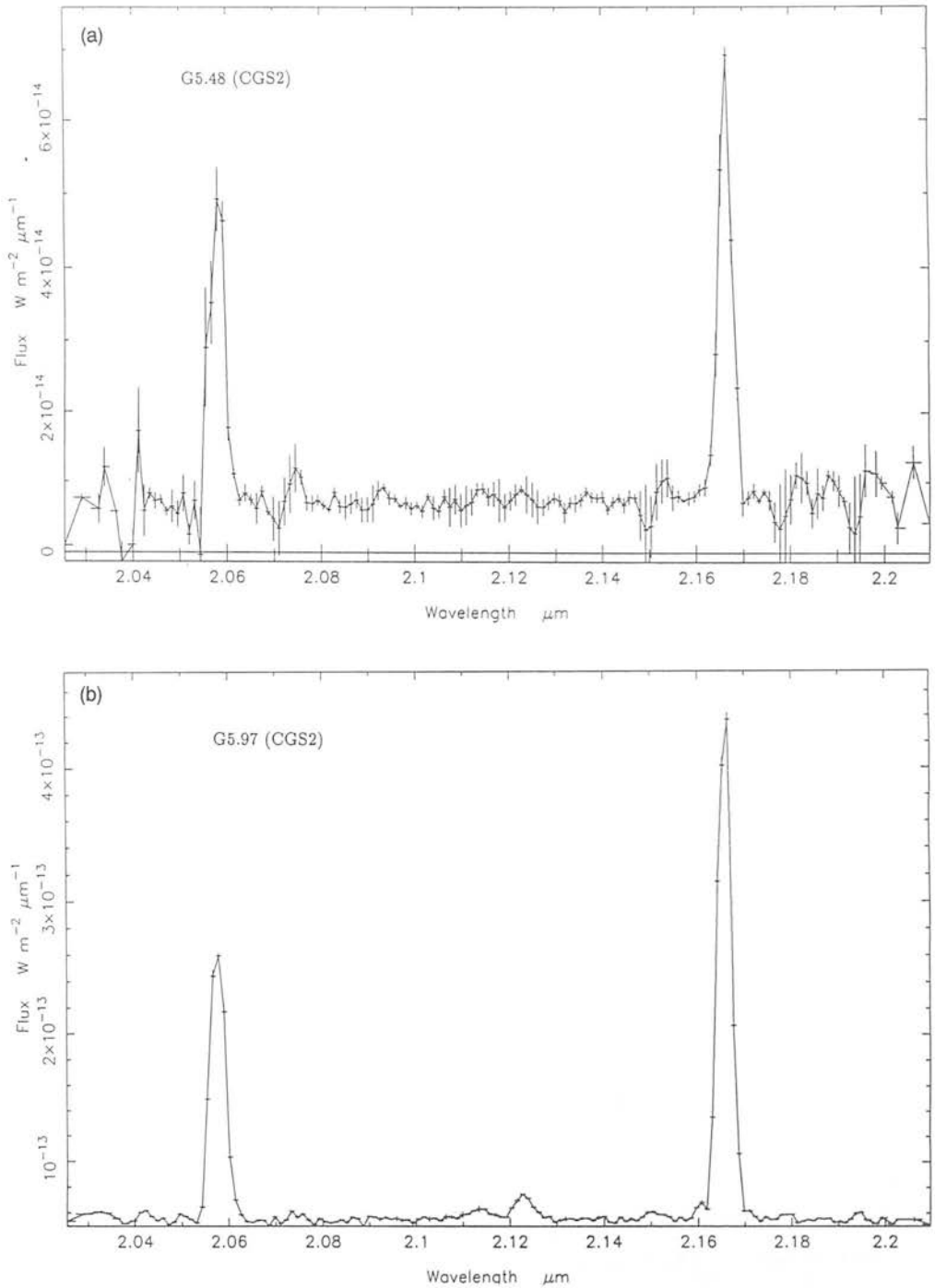

Figure 1. *K*-band spectra of ultracompact H II regions. (a)–(f) are observations taken with CGS2, and (g)–(j) are subsequent observations taken with CGS4.

CO_2 absorption feature at 2.06 μm. At high resolution, this absorption feature consists of a host of sharp, individual lines, corresponding to rotational transitions within the CO_2 molecule. From radio recombination line (RRL) measurements of the UC H II regions at H76α, H90α and H110α (Downes et al. 1980; Wink, Altenhoff & Mezger 1982; Wood & Churchwell 1989), assuming that RRL broadening is dominated by processes other than thermal motions (see Section 6), we infer that the intrinsic width of the He I 2.058-μm emission line is ~ 20–40 km s^{-1}, which is only 2–4 times greater than the width, and only 3.5–4.5 times less than the separation of the individual telluric lines which comprise the CO_2 absorption feature at 2.06 μm. The instrumental resolution, 400 km s^{-1} for CGS2 and 900 km s^{-1} for CGS4, is such that the individual CO_2 lines are heavily smoothed when convolved with the instrumental profile. However, since the atmospheric transmission affecting the line is a rapidly varying function of wavelength, the amount of He I line absorption will depend critically on the relative radial velocity of the Earth and H II region (cf. the analysis of

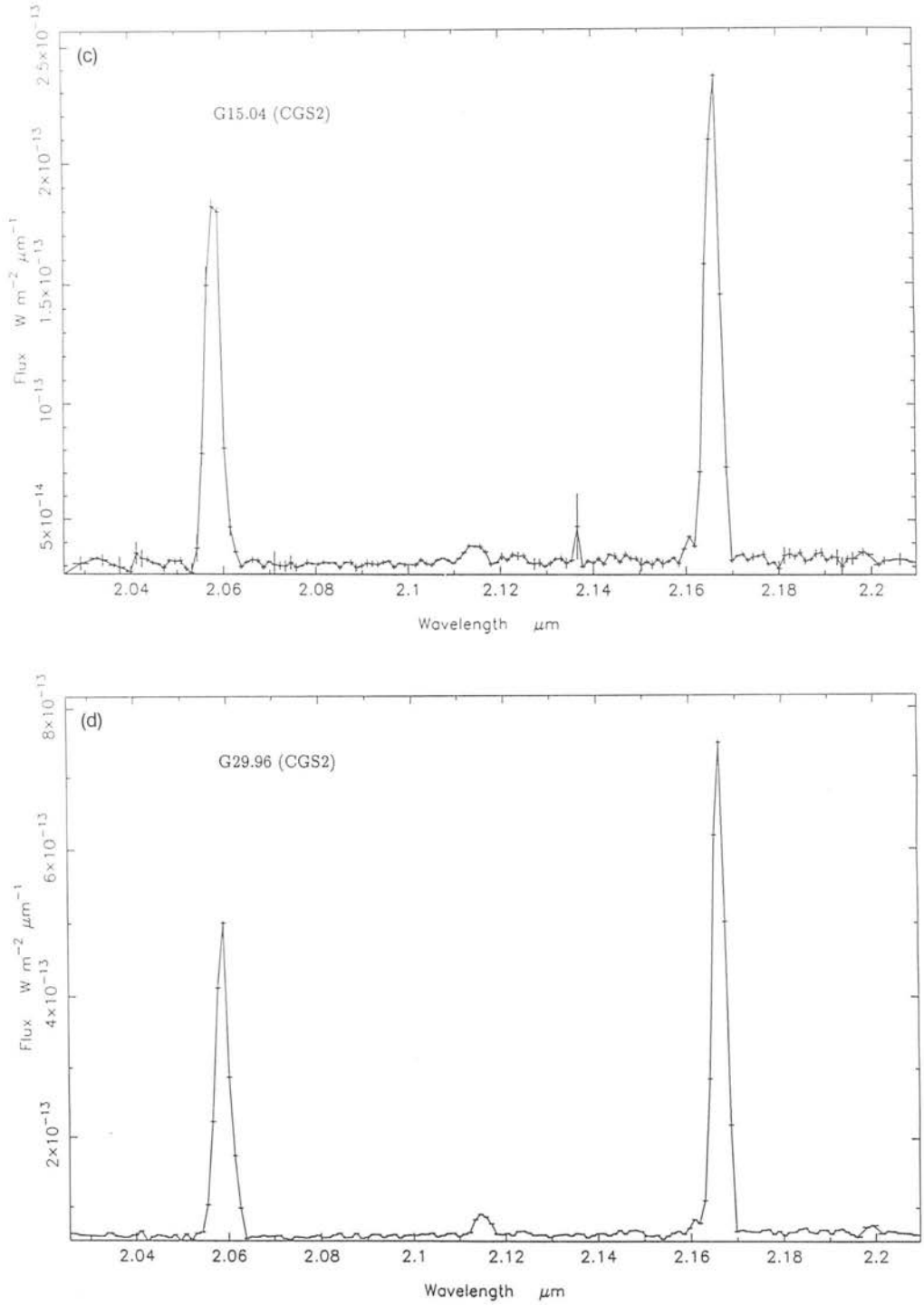

Figure 1 – *continued*

the He I 1.083-μm line by Kingdom & Ferland 1991). For example, if the He I emission line coincides with that of a telluric line, then a substantial amount of the He I line flux will be absorbed before reaching the telescope, whereas, if the He I line falls between absorption lines (spacing interval 90 km s^{-1}), an insignificant amount of the line flux will be absorbed before reaching the telescope. At the resolution employed, the smoothed transmission would have the same value in both cases, thus making it impossible to differentiate between these two extreme cases; in the first instance the flux replaced on division by the standard will be underestimated, and in the latter overestimated. Therefore, to calculate accurately the amount of flux lost on transmission through the atmosphere, it is necessary to know the He I linewidth and the radial velocity of the source. The date of the observation must also be known, because a given He I emission line will shift by up to 30 km s^{-1}, with respect to the telluric lines, as a result of the Earth's orbital motion.

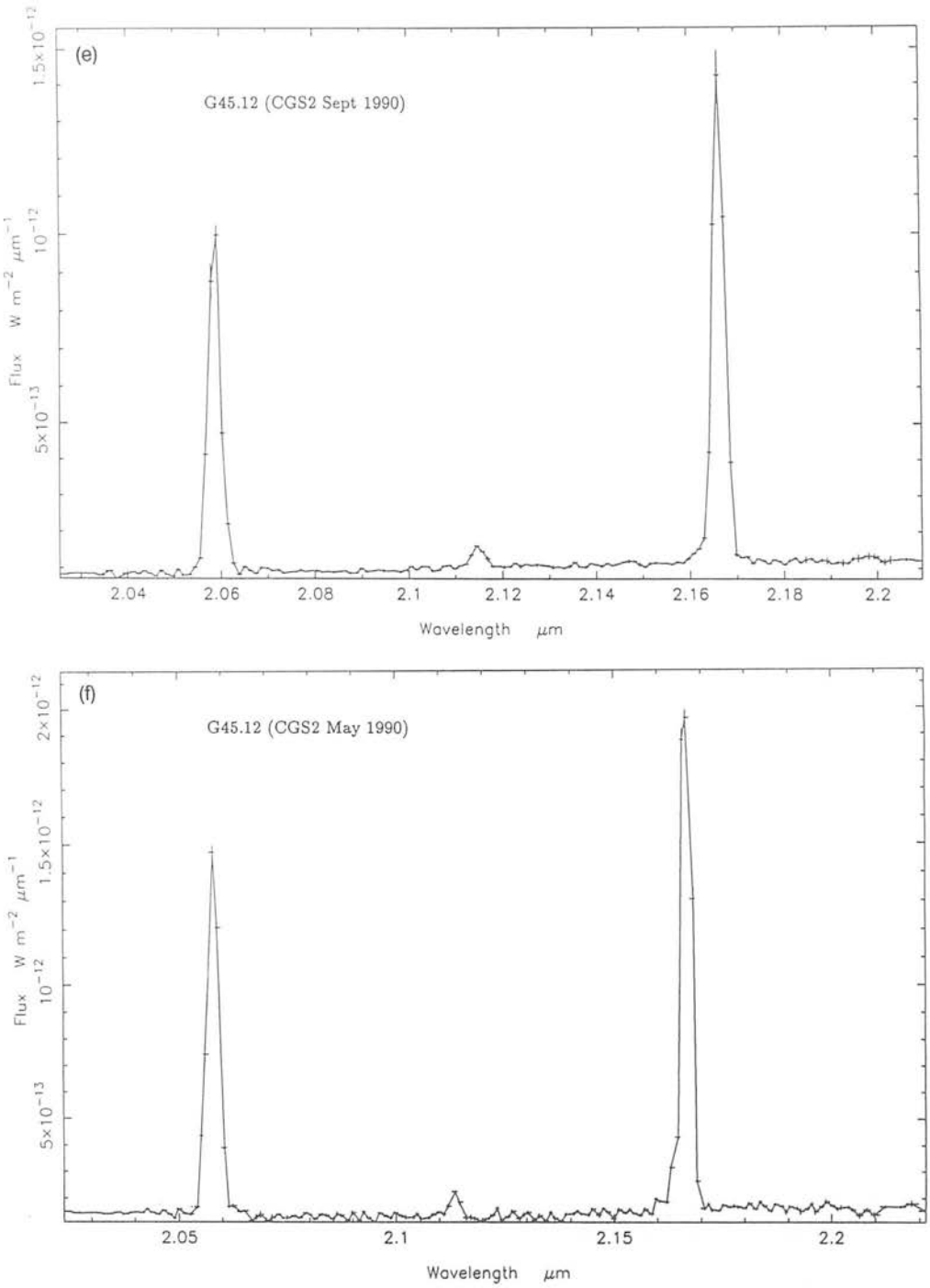

Figure 1 – *continued*

The method employed to estimate the percentage of He I flux absorbed for each UD H II region was as follows.

(i) A synthetic He I emission line was generated with a FWHM derived from radio recombination line (RRL) observations for each UC H II region; H110α (Downes et al. 1980), H76α (Wood & Churchwell 1989), and H76α and H90α (Wink et al. 1982). Comparison of RRL linewidths of H40α, H50β and He40α by Gordon & Walmsley (1990) for a sample of H II regions shows the He I recombination linewidths to be similar to the H I linewidths.

(ii) The radio recombination line local standard of rest (LSR) velocities were transformed into geocentric velocities for the date of the observations, so as to discern the Doppler-shifted position of the He I line (see Table 3). This transformation involved the resolution of two separate velocity components in the direction of the object, that of the Sun with respect to the LSR (with standard solar motion), and that of the Earth around the Sun.

(iii) The atmospheric transmission spectrum around the wavelength of the He I line was generated from a radiative-transfer model using the program HITRAN, originally

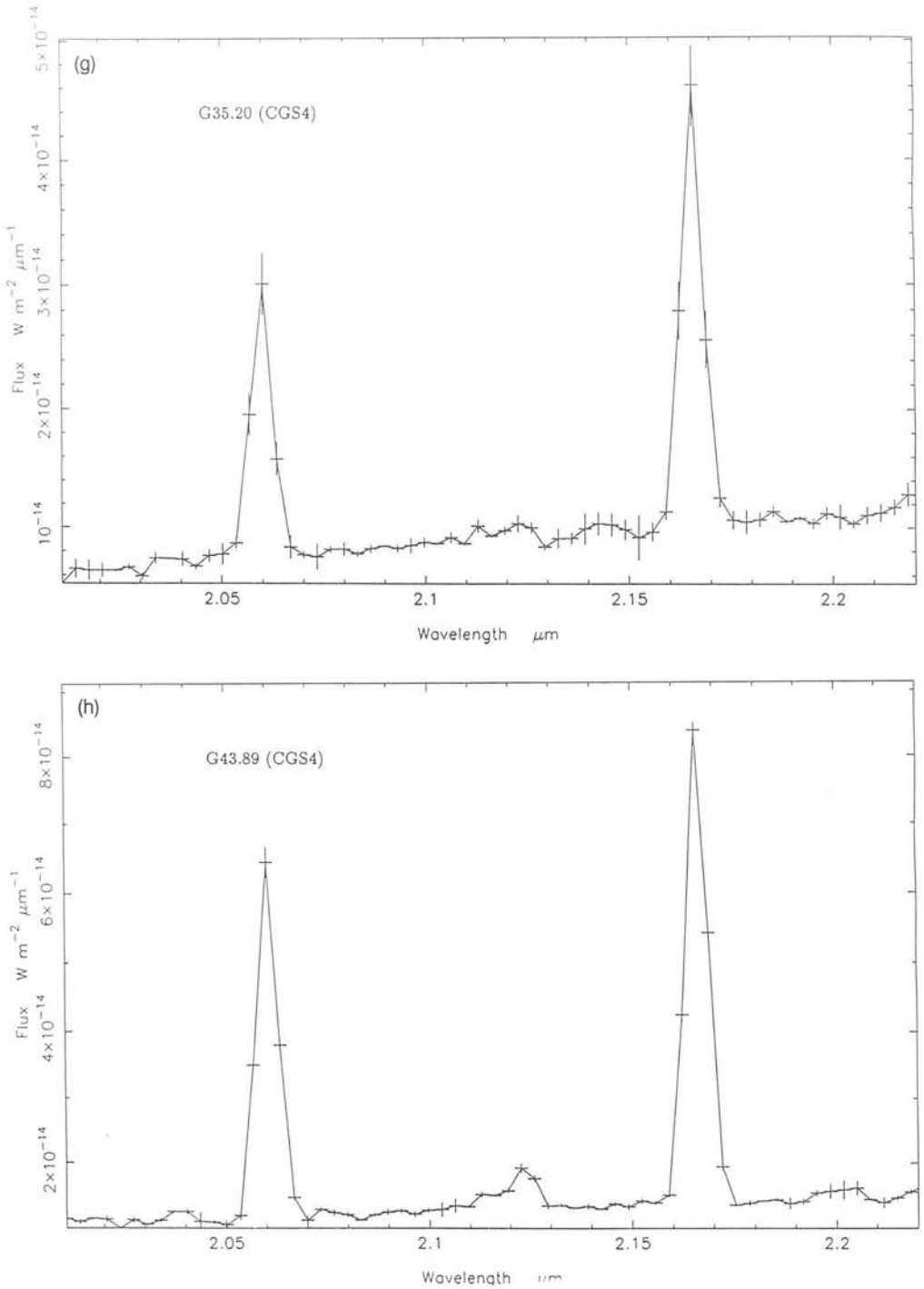

Figure 1 – *continued*

developed by the US Air Force Geophysical Laboratory, giving the transmission profile appropriate for Mauna Kea. The telluric line shape, characterized by a Voigt profile, is a convolution of collisional broadening by air molecules and thermal broadening, and is a function of column density. The latter varies with the airmass, which was recorded for each UC H II observation.

(iv) The synthetic He I line was multiplied by the transmission spectrum over the same wavelength range and, from integration under the incident and transmitted profiles, the percentage of He I flux lost by telluric absorption was calculated for each UC H II region.

For the UC H II regions on the dates observed, the He I line flux lost ranged from 5 to 36 per cent (Table 3). The errors on the RRL values for the LSR velocity, hence on the wavelength of the line centre, and the FWHM, were incorporated into the modelling to calculate the errors on the percentage flux lost (Table 3).

If we let F_λ be the helium line profile and T_λ the

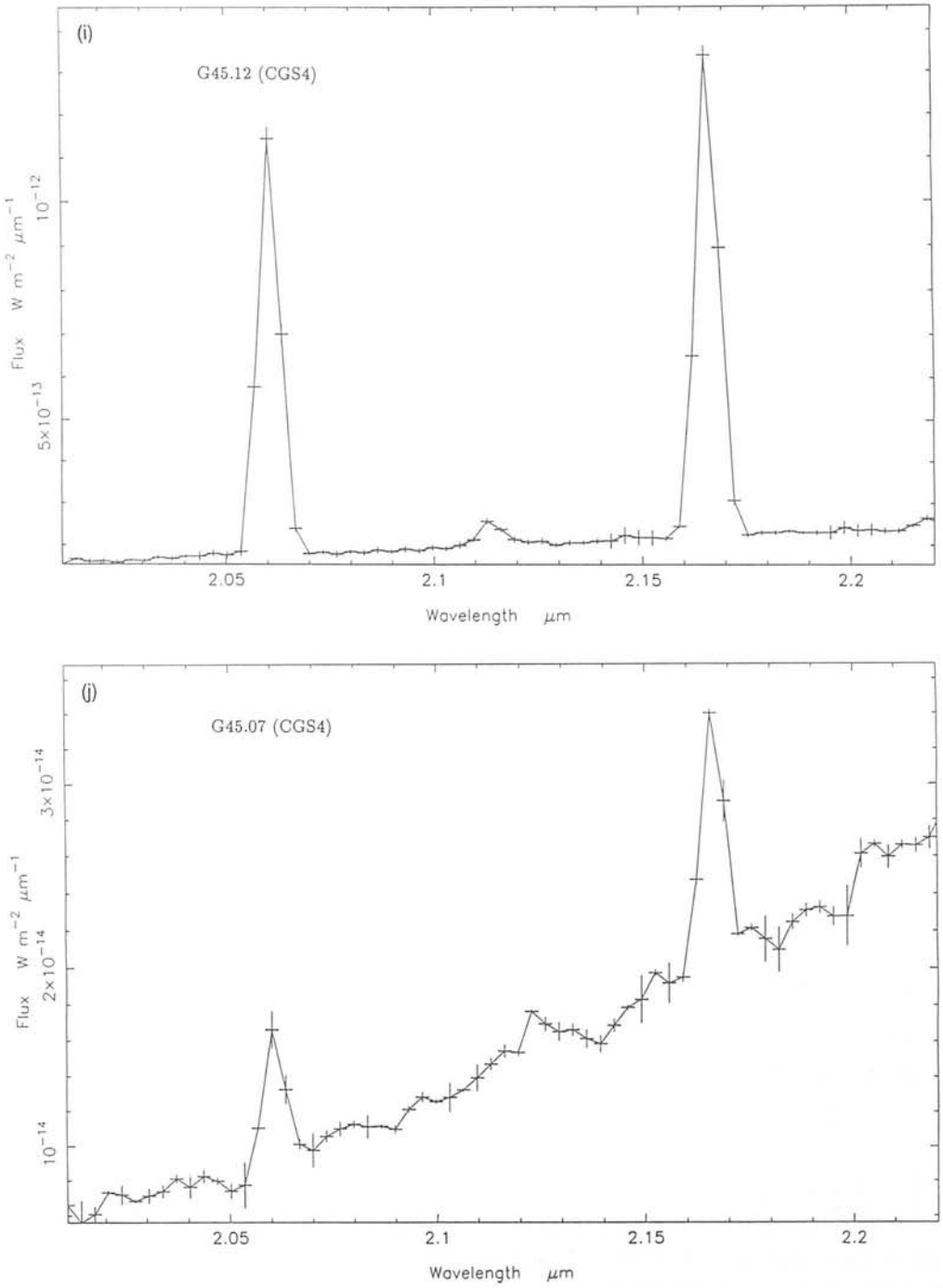

Figure 1 – *continued*

atmospheric transmission, then the atmospheric correction factor applied to each UC H II region is

$$\overline{T} \times \frac{\int F_\lambda \, d\lambda}{\int F_\lambda T_\lambda \, d\lambda},$$

where the integration is performed over a wavelength range corresponding to about six times the RRL width. The factor $\overline{T}$ arises because the object spectrum has been divided by the spectral standard which corrects for the continuum flux lost due to telluric absorption, and for the instrumental response. Consequently, the He I line in the H II region spectrum has already been divided by the smoothed atmospheric transmission in the standard around 2.058 μm. Therefore a further correction factor, $\overline{T}$ (found to be in the range 0.82–0.86), representing this average percentage atmospheric transmission in the standard at 2.058 μm, must be applied.

4 CORRECTION FOR DUST EXTINCTION

The dust extinction to an H II region can be calculated by comparing the observed Br γ line flux with the value inferred from the free–free radio flux density using hydrogen

Table 3. Atmospheric corrections.

Object	Velocities (kms^{-1}) LSR	Geocentric	HeI flux absorbed %
G5.48	22.9	39.3	5±1
G5.97	3.5	19.8	23±2
G15.04	11.5	24.7	13±3
G29.96	95.3	102.6	26±4
G35.20[1]	47.9	23.8	13±6
G43.89[1]	52.5	26.1	10±7
G45.07[1]	47.7	21.3	18±3
G45.12	58.7	59.6	10±2
G45.12[2]	58.7	22.6	17±2
G45.12[1]	58.7	32.3	11±3

[1]Taken with CGS4, 1991 June.
[2]Repeat observation, taken with CGS2, 1990 May.

Table 4. The He I 2.058 μm/Br γ ratio in UC H II regions.

Object	τ_{15GHz}	C_k	Brγ flux $\times10^{-16}Wm^{-2}$	HeIλ2.058/Brγ ratio Observed	Corrected
G5.48	0.13	1.21	2.15±0.09	0.761	0.823±0.072
G5.97	0.30	1.17	14.9±0.1	0.564	0.688±0.032
G15.04	0.77	1.11	8.19±0.08	0.790	0.858±0.044
G29.96	0.20	1.26	24.9±0.1	0.681	0.997±0.048
G35.20[1]	0.10	1.55	2.30±0.19	0.610	0.891±0.122
G43.89[1]	0.10	1.25	4.79±0.06	0.697	0.788±0.052
G45.07[1]	0.63	1.52	0.84±0.05	0.545	0.820±0.108
G45.12	0.40	1.24	44.6±0.10	0.698	0.799±0.041
G45.12[2]	0.40	1.20	65.1±0.5	0.695	0.838±0.029
G45.12[1]	0.40	1.19	75.0±1.4	0.857	0.929±0.038

[1]Taken with CGS4, 1991 June.
[2]Repeat observation, taken with CGS2, 1990 May.

recombination theory. Wood & Churchwell (1989) measured the free–free flux densities integrated over the source, for their large sample of UC H II regions at both 5 and 15 GHz. Relation of the number of Lyman continuum photons to the free–free integrated flux density S_ν, for an electron temperature and density of $T_e = 10^4$ K and $n_e = 10^4$ cm^{-3} respectively, and a ratio of recombinations to Br γ photons $N_{Lyc}/N_{Br\gamma} \sim 70$ (Hummer & Storey 1987), gives a theoretical Br γ flux (Rubin 1968) of

$$I^{theo}_{Br\gamma} = 8.25\times10^{-15}\left(\frac{\nu}{GHz}\right)^{0.1}\left(\frac{S_\nu}{Jy}\right), \quad (1)$$

if the free–free continuum is optically thin. This is not the case for UC H II regions, which are optically thick at 5 GHz and marginally so at 15 GHz (see Table 4). In the case of finite optical depth, equation (1) becomes

$$I^{theo}_{Br\gamma} = 1.08\times10^{-14}\left(\frac{S_{15\,GHz}}{Jy}\right)\left(\frac{\tau_{15\,GHz}}{1-e^{-\tau_{15\,GHz}}}\right). \quad (2)$$

The free–free optical depth was calculated from the flux densities given by Wood & Churchwell (1989) for each UC H II region. At high spatial resolution, these VLA observations may resolve out extended emission, resulting in an underestimate of the total flux density and an optical depth weighted towards the compact regions of the source. Such extended emission might be detected in our lower resolution infrared observations, resulting in an underestimate of the extinction. However, we do not expect this effect to be a significant problem for most of the regions in our sample, which are dominated by a central source, with the possible exceptions of G5.48 and G5.97 which have a core–halo morphology. Assuming purely foreground extinction, the dust optical depth may thus be calculated from the observed and predicted Br γ emission:

$$I^{obs}_{Br\gamma} = I^{theo}_{Br\gamma}\, e^{-\tau_{Br\gamma}}. \quad (3)$$

The dust optical depths at Br γ of the UC H II regions ranged from $\tau_{Br\gamma} = 1.1$ to 4.9. From the Br γ extinction values, by application of the interstellar extinction curve of Draine (1989) which assumes a power law with spectral index −1.75 in the range 0.7–5 μm, C_k, the differential interstellar extinction correction factor between He I (2.058 μm) and Br γ (2.165 μm) was calculated. For $T_e = 10^4$ K, C_k proved to be in the range 1.11–1.55 (Table 4); for an electron temperature of 5×10^3 K, C_k would be reduced by a factor of 0.96.

The resultant He I 2.058 μm/Br γ ratios and their errors, corrected for extinction and atmospheric absorption, are given in Table 4.

5 MODEL He I/Br γ LINE FLUX RATIOS

5.1 The basic models

The theoretical He I 2.058 μm/Br γ ratio for stellar effective temperatures ranging from 25 000 to 50 000 K, equivalent to spectral types of B1–O4, has been modelled by DPJ. For stars with these spectral types, they determined fluxes for the helium and hydrogen ionizing photons, using the Kurucz (1979) stellar atmosphere models. The Lyman continuum flux is roughly described by a steep power-law function of the mass ($N_{Lyc} \propto m^\alpha$). For stars with masses in the range 10–40 $M_\odot$, corresponding to effective temperatures in the range 22 500–41 000 K, the index α is ~7 and ~11 for H and He, respectively (Puxley 1988). The relative helium to hydrogen ionizing fluxes, and hence the He I 2.058 μm/Br γ ratio, are therefore a strong function of the stellar mass. The equations derived by DPJ for the line flux as a function of ionizing photon flux are

$$\frac{I_{He\,I\,\lambda2.058}}{I_{Br\gamma}} = \frac{N^{He}_{Lyc}}{N^{H}_{Lyc}}\,\frac{\alpha_B(H^+)}{\alpha_B(He^+)}\,\frac{\alpha_{He\,I\,\lambda2.058}}{\alpha_{Br\gamma}}\,\frac{\lambda_{Br\gamma}}{\lambda_{He\,I\,\lambda2.058}}, \quad (4)$$

$$R_{He^+} < R_{H^+},$$

$$\frac{I_{\mathrm{He\,I}\,\lambda 2.058}}{I_{\mathrm{Br}\gamma}} = \frac{N_{\mathrm{He}}}{N_{\mathrm{H}}} \frac{\alpha_{\mathrm{He\,I}\,\lambda 2.058}}{\alpha_{\mathrm{Br}\gamma}} \frac{\lambda_{\mathrm{Br}\gamma}}{\lambda_{\mathrm{He\,I}\,\lambda 2.058}}, \quad (5)$$

$$R_{\mathrm{He}^+} = R_{\mathrm{H}^+},$$

where R_{He^+} and R_{H^+} are the radii of the helium and hydrogen ionized zones, respectively. $N^{\mathrm{He}}_{\mathrm{Lyc}}/N^{\mathrm{H}}_{\mathrm{Lyc}}$ is the relative number of helium and hydrogen ionizing photons and $N_{\mathrm{He}}/N_{\mathrm{H}}$ is the helium abundance. $\alpha_{\mathrm{B}}(\mathrm{H}^+)$ and $\alpha_{\mathrm{B}}(\mathrm{He}^+)$ are the total recombination coefficients for hydrogen and helium (case B), respectively. $\alpha_{\mathrm{He\,I}\,\lambda 2.058}$ and $\alpha_{\mathrm{Br}\gamma}$ are the effective recombination coefficients of the He I 2.058-μm and Br γ transitions.

The radii of the two ionized zones R_{He^+} and R_{H^+} coincide at a critical stellar effective temperature when the photons emitted from the recombination of helium dominate the ionization of hydrogen, and hence the He I 2.058 μm/Br γ ratio saturates. As can be seen from equation (5), above this saturation temperature the ratio is solely dependent on the helium abundance.

Values for the hydrogen and helium recombination coefficients are given in Table 5 for electron temperatures of $T_e = 10^4$ K and 5×10^3 K and densities of $n_e = 10^2$, 10^4 and 10^6 cm^{-3}. Inferred values of T_e for the sample UC H II regions are given by Wood & Churchwell (1989) and Downes et al. (1980), and lie in the range 6000–10 830 K, with uncertainties of up to 2500 K. Similarly, electron densities inferred by Wood & Churchwell (1989) from peak radio flux density measurements lie in the range $n_e = 10^4$–10^5 cm^{-3}.

Values for the $\alpha_{\mathrm{He\,I}\,\lambda 2.058}$ effective recombination coefficient are derived from recent He I recombination line spectrum models by Smits (1991), who tabulates the line strength of He I 2.058 μm relative to He I 4472 Å. The $\alpha_{\mathrm{He\,I}\,\lambda 2.058}$ effective recombination coefficient is the recombination coefficient from all levels to the 2^1P singlet level, multiplied by the fraction of those atoms that radiatively decay to the 2^1S level, emitting a 2.058-μm photon.

For electron densities applicable to UC H II regions given above, the 2^1P singlet level population is substantially enhanced by collisions from the metastable 2^3S triplet level. This mechanism has been included in the Smits models, and is discussed in detail in Section 5.2. As a consequence, the effective He I 2.058-μm recombination coefficient, unlike that of Br γ, is highly density-dependent (Table 5).

Atoms in the 2^1P state decay with a probability of 0.999 to the ground state (1^1S) with emission of a line photon at 0.0584 μm. The resonance line photon will either be promptly reabsorbed by a neighbouring helium atom and return to the 2^1P excited level or ionize a neutral hydrogen atom. In the absence of dust, approximately one-third of the 0.0584-μm photons are absorbed by hydrogen, whilst two-thirds are scattered by helium atoms, ultimately to populate the 2^1S level, via emission of a 2.058-μm photon. To account for this process, the He I 2.058-μm recombination coefficients, derived from Smits and given in Table 5, have been multiplied by a factor of 2/3. Comparison with the hydrogen ionization rate derived from the Kurucz (1979) model atmospheres implies that the total number of hydrogen-ionizing photons is increased by a negligible amount, and thus the Br γ flux is unaffected.

Figs 2 and 3 show the theoretical He I 2.058 μm/Br γ ratio versus stellar effective temperature for two electron temperatures, $T_e = 10^4$ and 5×10^3 K respectively, calculated from equations (4) and (5). The three solid model curves represent the low-density case, $n_e = 10^2$ cm^{-3}, the high-density case, $n_e = 10^6$ cm^{-3}, and an intermediate density case, $n_e = 10^4$ cm^{-3}. The last value is most representative of the densities of the UC H II regions (Wood & Churchwell 1989). For an assumed Galactic abundance of $N_{\mathrm{He}}/N_{\mathrm{H}} = 0.1$, the He and H ionizing zones coincide near the effective stellar temperature of 38 000 K (O7 star). In Fig. 2, for an electron temperature of $T_e = 10^4$ K, the He I 2.058 μm/Br γ ratio saturates at ratios of 0.80 ($n_e = 10^2$ cm^{-3}), 1.28 ($n_e = 10^4$ cm^{-3}) and 1.55 ($n_e = 10^6$ cm^{-3}) in the three cases. Corresponding saturation ratios for $T_e = 5 \times 10^3$ K (Fig. 3) are 0.68, 0.82 and 0.96, respectively.

We note that, if hydrogen were relatively more ionized than helium in the He^+ zone, then helium atoms would reprocess almost all of the 0.0584-μm photons, and the fraction of atoms that are de-excited to the 2^1S state would be much closer to unity. In this case, the curves labelled $n_e = 10^2$ cm^{-3} and $n_e = 10^4$ cm^{-3} would saturate at values of 1.2 and 1.92 (1.02 and 1.23), respectively, for $T_e = 10^4$ K ($T_e = 5 \times 10^3$ K).

5.2 Effects of collisional excitation

Above a critical density of 4–6×10^3 cm^{-3}, the triplet 2^3S (metastable) He I level is preferentially collisionally excited to the 2^1P and 2^1S levels (Osterbrock 1989), rather than undergoing single-photon decay at 19.8 eV to the ground state. This will enhance the population of the He I 2^1P level, and

Table 5. Recombination coefficients for H I and He I.

Recomb. coeff	$T_e = 10^4$K			$T_e = 5 \times 10^3$K		
cm^{-3}s^{-1}	$n_e = 10^2$cm^{-3}	$n_e = 10^4$cm^{-3}	$n_e = 10^6$cm^{-3}	$n_e = 10^2$cm^{-3}	$n_e = 10^4$cm^{-3}	$n_e = 10^6$cm^{-3}
$\alpha_B(H^+)$[1]	2.59×10^{-13}	2.59×10^{-13}	2.59×10^{-13}	4.54×10^{-13}	4.54×10^{-13}	4.54×10^{-13}
$\alpha_B(He^+)$[1]	2.73×10^{-13}	2.73×10^{-13}	2.73×10^{-13}	4.34×10^{-13}	4.34×10^{-13}	4.34×10^{-13}
$\alpha_{Br\gamma}$[2]	3.74×10^{-15}	3.71×10^{-15}	3.63×10^{-15}	7.90×10^{-15}	7.85×10^{-15}	7.68×10^{-15}
$\alpha_{HeI\lambda 2.058}$[3]	4.25×10^{-14}	6.78×10^{-14}	8.03×10^{-14}	7.68×10^{-14}	9.16×10^{-14}	1.05×10^{-13}

[1] Values from Osterbrock (1989).
[2] Values from Hummer & Storey (1987).
[3] Values from Smits (1991).

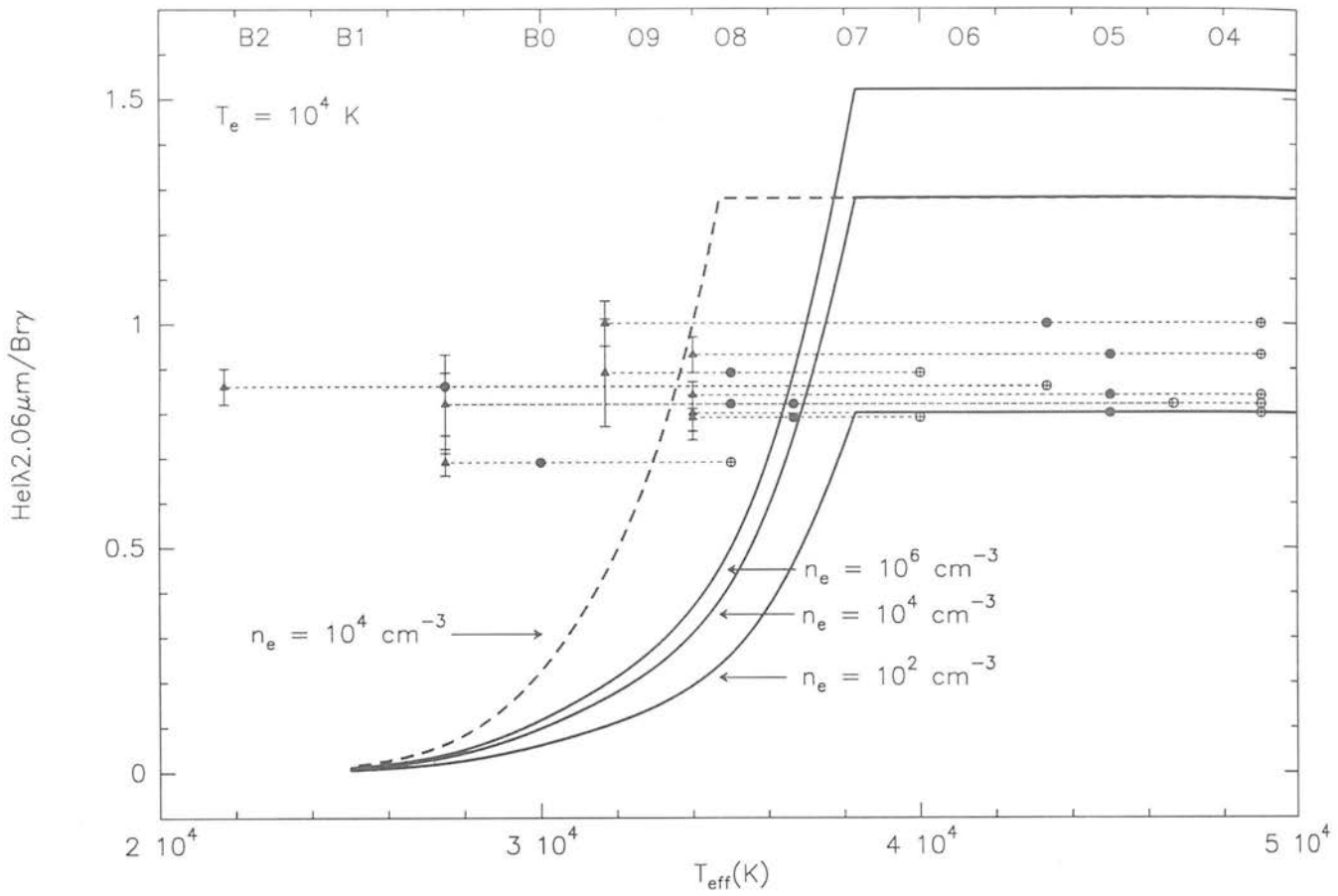

Figure 2. The He I 2.058 μm/Br γ ratio versus stellar effective temperature for an electron temperature of $T_e = 10^4$ K and densities of $n_e = 10^2$, $n_e = 10^4$ and $n_e = 10^6$ cm^{-3}. The dashed curve represents the line ratio for dusty H II regions for $n_e = 10^4$ cm^{-3}. All curves are calculated for a Galactic helium abundance of 0.1. T_{eff} is estimated from N_{Lyc} (filled circles) and L_{IR} (open circles) appropriate to single stars, and N_{Lyc}/L_{IR} (filled triangles), appropriate to a cluster of stars. Error bars (1σ) show the uncertainty in the He I 2.058 μm/Br γ ratio after correction for extinction and telluric absorption.

thus increase the He I 2.058 μm/Br γ ratio. To examine the importance of this mechanism, treated in detail by Smits (1991), consider an H II region with an electron temperature and density of $T_e = 10^4$ K and $n_e = 10^4$ cm^{-3}. Osterbrock estimates that of all 2^3S to singlet collisions, 72 per cent of the 2^3S depopulation, 17 per cent lead to population of 2^1P. The fraction of all helium recombinations to singlet and triplet states are in the ratio 1:3, and approximately two-thirds of all singlet captures lead to 2^1P. The enhancement of the He I 2.058 μm/Br γ ratio is therefore given by

$$\frac{\text{recombination to } 2^1\text{P} + \text{collisions from } 2^3\text{S}}{\text{recombinations to } 2^1\text{P}}$$

$$\simeq \frac{\frac{1}{4}\times\frac{2}{3}+\frac{3}{4}\times 0.17\times 0.72}{\frac{1}{4}\times\frac{2}{3}} \simeq 1.55. \qquad (6)$$

In a more detailed calculation, Smits (1991), using recent collision cross-sections, finds an enhancement of 1.58 for this temperature and density. For an electron temperature of $T_e = 5\times10^3$ K, this factor decreases due to the dependence of the collision cross-sections on T_e.

The vertical displacement of the curves labelled $n_e = 10^4$ cm^{-3} and $n_e = 10^6$ cm^{-3} from the curve labelled $n_e = 10^2$ cm^{-3} in Figs 2 and 3 represents the effect of collisional excitation on the He I 2.058 μm/Br γ ratio.

5.2.1 *Photoionization*

Photoionization from the 2^3S level may be an important process, since it can decrease the 2^3S population. Clegg & Harrington (1989) have investigated this mechanism in various planetary nebulae, and show photoionization by Ly α to be the most dominant photoionization process. Their equation (12) gives the ratio of 2^3S depopulation by photoionization by Ly α compared with collisions to singlets. The line intensity of Ly α is governed by the rate of destruction of these photons by dust. Using the dust parameters from DPJ, corresponding to a dust-to-gas mass ratio of 10^{-2}, a ratio for the depopulation of 2^3S of ~0.13 was obtained. For a dust-to-gas mass ratio lower by a factor of 10, Clegg & Harrington obtained a ratio of 0.18. Since the fraction of collisions from 2^3S to 2^1P is only 17 per cent of total collisions at $T_e = 10^4$ K, photoionization from 2^3S reduces the 2^1P population by $0.17\times0.13 \sim 2$ per cent, and thus the effect on the He I 2.058 μm/Br γ ratio is also negligible. The extra ionizations will increase the number of atoms recombining to the 2^1P level. However, since the population $N(2^3\text{S})/N(\text{He}^+) \sim 10^{-6}$ at

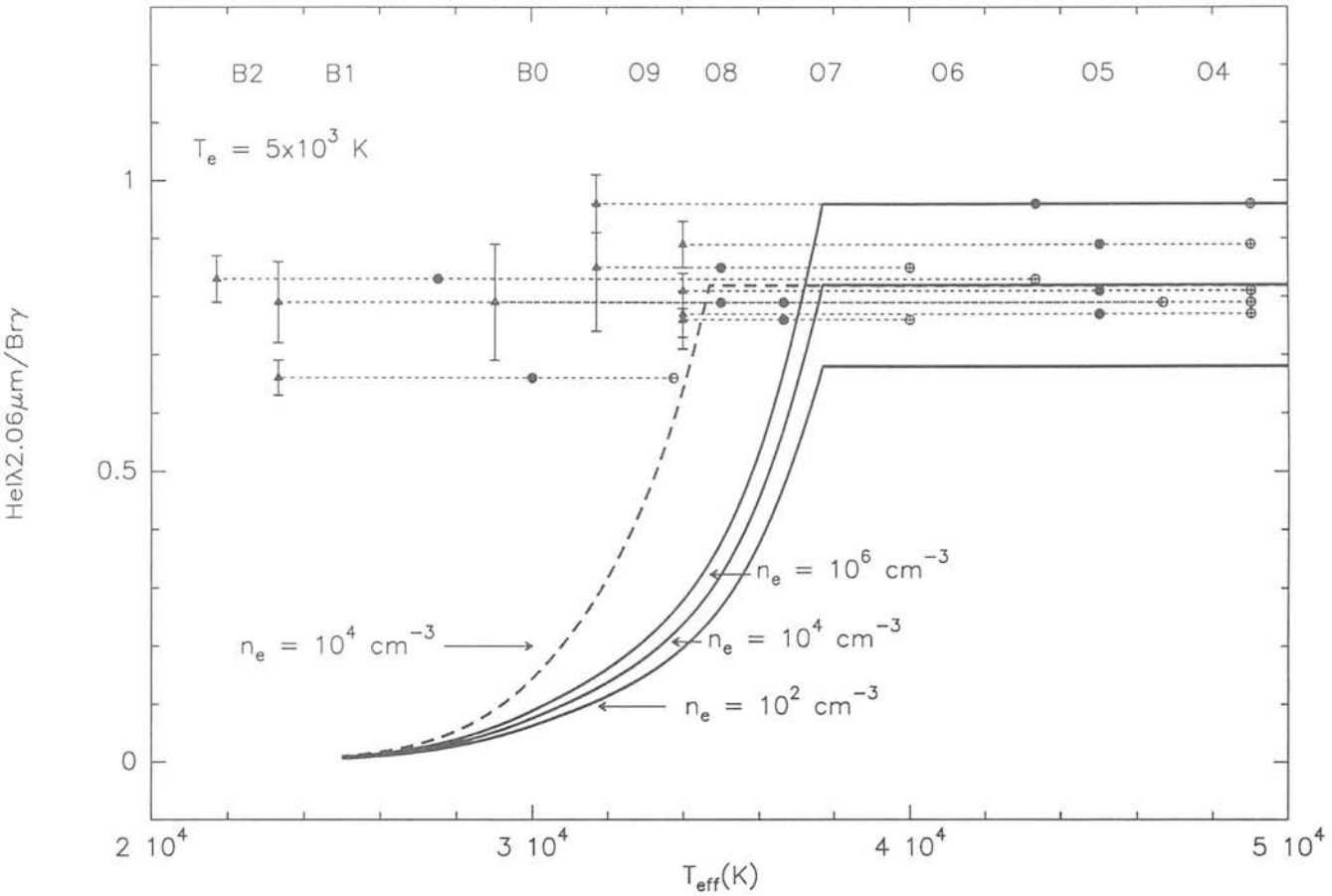

Figure 3. The He I 2.058 μm/Br γ ratio versus stellar effective temperature for an electron temperature of $T_e = 5 \times 10^3$ K (symbols as Fig. 2).

$n_e = 10^4$ cm^{-3} (Clegg 1987), this overall increase is negligible. Photoionization of the 2^3S level will be studied in a following paper, in which we examine the strength of the He I 4^3S–3^3P and 4^1S–3^1P transitions with respect to He I 2^1P–2^1S.

5.3 Effects of internal dust

Wood & Churchwell (1989) discuss evidence for the presence of internal dust in UC H II regions. The effects of this dust are potentially two-fold. First, dust absorbs some fraction of the helium and hydrogen ionizing photons. The dust photo-absorption cross-section peaks around 800 Å (15.5 eV), much closer to the Lyman limit for hydrogen than for helium, and thus dust competes predominantly with hydrogen in absorbing ionizing photons. As a result, the radius of the Strömgren sphere for hydrogen will be smaller than if no dust were present, whereas the corresponding radius for helium will be relatively unaffected. Consequently, these radii will coincide, and hence the He I 2.058 μm/Br γ ratio will saturate, at lower stellar effective temperatures in a dusty H II region.

The dashed curves labelled $n_e = 10^4$ cm^{-3} in Figs 2 and 3 represent the He I 2.058 μm/Br γ ratios recalculated for dusty H II regions, based on the models of DPJ, for such an electron density. The effect of dust within an H II region is shown by the horizontal displacement of the dashed curves from the solid curves. At a density of $n_e = 10^4$ cm^{-3}, dust has a considerable effect on the line flux ratio, causing the He I 2.058 μm/Br γ ratio to saturate at a temperature of about 35 000 K (O8 star). However, as pointed out by DPJ, the dusty model is highly sensitive to the dust-to-gas mass ratio. DPJ use a ratio of 10^{-2}, which is the value for the diffuse interstellar medium; models of dusty H II regions by Chini, Krügel & Kreysa (1986) and Hoare, Roche & Glencross (1991) suggest that the dust-to-gas mass ratio is lower by a factor of about 10. In this case, dust will have a considerably reduced effect on the He I 2.058 μm/Br γ ratio (DPJ).

The second possible effect of internal dust, which was not incorporated into the simple dusty H II region models of DPJ, is to alter the value of the effective He I 2.058-μm recombination coefficient from its value in a dust-free environment. As discussed in Section 5.1, in the absence of dust, approximately one-third of the 0.0584-μm photons are absorbed by hydrogen, whilst two-thirds are reprocessed by helium atoms. Using the dusty H II region models of DPJ, the absorption of 0.0584 μm photons by dust has been investigated further. These models assume the uniform grain size distribution of Mathis, Rumpl & Nordsieck (1977) including both silicate and graphite particles, for grains of radii 0.005 μm up to 0.25 μm, and a constant dust-to-gas mass ratio of 10^{-2}. The mean free path of a 0.0584-μm photon before (a) absorption by a helium atom, at $T_e = 10^4$ K, ultimately resulting in population of the 2^1S level, (b) photoionization of a hydrogen atom, and (c) absorption by dust were calculated. The mean free path lengths are approximately in the ratio

1:2:6000; hence dust absorbs a negligible fraction of 0.0584-μm photons, and therefore has virtually no effect on the effective He I 2.058-μm recombination coefficient.

6 COMPARISON WITH OBSERVATIONS

To compare our observed He I 2.058 μm/Br γ recombination line ratios with the theoretical curves in Figs 2 and 3, the spectral type of the exciting stars in the UC H II regions must be determined. Both the radio and *IRAS* fluxes from these UC H II regions can be used to estimate the spectral types by comparison with models from Puxley (1989), obtained by integrating Kurucz (1979) model atmospheres and using the conversion between effective temperature, mass, radius and spectral type from Landolt–Börnstein (1982). The radio flux density yields a lower limit to the number of Lyman continuum photons $N_{\rm Lyc}$ (Wood & Churchwell 1989), since dust inside the H II region can absorb a significant number of ionizing photons. Integration of the *IRAS* fluxes for each UC H II region gives the infrared luminosity, $L_{\rm IR}$. For computational simplicity we have assumed the flux at λ 1 mm to be the same as that at 12 μm in order to correct for the luminosity outside the *IRAS* bands. These values of $L_{\rm IR}$ are in excellent agreement with those given for several of the UC H II regions by Chini, Krügel & Wargau (1987). The spectral type derived from the *IRAS* fluxes will be an upper limit, as the size of the *IRAS* beam (5×3 arcmin^2 at 100 μm) is much greater than that of a typical UC H II region (~ 5 arcsec). The spectral types derived from $N_{\rm Lyc}$ and $L_{\rm IR}$ are given in Table 6, assuming that a single star is responsible for the emission.

Studies of compact H II regions by Lacy, Beck & Geballe (1982) and Hoare et al. (1991) conclude that such regions may be excited by a cluster of stars. Therefore a third estimate of the spectral type, i.e. the effective stellar temperature $T_{\rm eff}$, was evaluated for an H II region excited by a stellar cluster. The ratio of $N_{\rm Lyc}/L_{\rm IR}$, dependent only on the effective temperature of the radiation from the cluster, yields a lower limit to the characteristic spectral type, because of dust and the *IRAS* beamsize. This limit is in agreement to within one subclass with the cluster temperature derived by Lacy et al. (1982) for G29.9, and 0.5 of a subclass for $T_{\rm eff}$ derived by Hoare et al. (1991) for G45.12 from analysis of the mid-infrared, fine-structure lines. These values, which are lower limits for $T_{\rm eff}$, are several subclasses lower than those found by assuming the emission to be from a single source. The three estimates of the effective temperature for each UC H II region are shown in Figs 2 and 3. The dotted lines joining the estimates of $T_{\rm eff}$ represent the uncertainty in the spectral types of the exciting stars in the UC H II regions.

Table 6. Spectral-type estimates derived from observed properties.

Object	IRAS (L_{IR}) (single star)	Radio (N_{Lyc}) (single star)	N_{Lyc}/L_{IR} (cluster)
G5.48	O4.5	O8	B0.5
G5.97	O8	B0	B0.5
G15.04	O5.5	B0.5	B2
G29.96	O4	O5.5	O9.5
G35.20	O6	O8	O9.5
G43.89	O6	O7.5	O8.5
G45.07	O4	O7.5	B0.5
G45.12	O4	O5	O8.5

The corrected observed He I 2.058 μm/Br γ ratios from Table 4 are plotted in Figs 2 and 3 against the model curves (the data for Fig. 3 are scaled by the dust extinction factor appropriate to $T_{\rm e} = 5 \times 10^3$ K). For the UC H II region G45.12, data were obtained with both CGS2 and CGS4. The CGS2 data points are entirely consistent after atmospheric corrections are applied, and also consistent with the CGS4 fluxes for He I and Br γ (difference of 1.66σ).

For an electron temperature of $T_{\rm e} = 5 \times 10^3$ K (Fig. 3), the observed line ratios, with a mean value 0.81, are generally in good agreement with the predicted model for a density of $n_{\rm e} = 10^4$ cm^{-3}. For a gas temperature of $T_{\rm e} = 10^4$ K, as inferred for several UC H II regions by Wood & Churchwell (1989) and Downes et al. (1980), the observed line ratios lie closer to the curve labelled $n_{\rm e} = 10^2$ cm^{-3} than to the curve labelled $n_{\rm e} = 10^4$ cm^{-3} (Fig. 2). This is surprising, because the densities of these UC H II regions, discussed in Section 5.1, lie in the range 10^4–10^5 cm^{-3}. One possible explanation is that there are large density variations throughout the UC H II regions, so that the integrated He I 2.058 μm/Br γ ratio is much less than the He I 2.058 μm/Br γ ratio in the denser areas of the UC H II regions. However, Wood & Churchwell (1989) have measured the electron densities for two of these objects, using their integrated radio flux measurements, and found that these electron densities are of the same order of magnitude as the peak flux density values. From the mean observed He I 2.058 μm/Br γ ratios the predicted beam-averaged electron densities of these objects would have to be $\sim 1 \times 10^3$ cm^{-3} for $T_{\rm e} = 10^4$ K. Analysis of the long-slit CGS4 data for G43.89 suggests that the He I 2.058 μm/Br γ ratio varies across the source, being greatest at the central position and decreasing outwards, consistent with a gradient in electron density. However, when these observations were made, there was a small misalignment between the dispersion axis and the detector rows, which results in the He I and Br γ lines being sampled at slightly different spatial positions; thus this result, whilst suggestive, must be regarded as only preliminary. In Fig. 2, the observed He I 2.058 μm/Br γ ratio for G5.97 is seen to be lower even than the predicted model for $n_{\rm e} = 10^2$ cm^{-3}. We now consider other mechanisms which may alter the He I 2.058 μm/Br γ ratio and account for the discrepancy between the observed values and the model predictions for UC H II regions with $T_{\rm e} = 10^4$ K (Fig. 2).

Inspection of the H II region models, as described by equations (4) and (5), reveals that the only parameters subject to significant uncertainty are $N_{\rm Lyc}^{\rm He}/N_{\rm Lyc}^{\rm H}$, $N_{\rm He}/N_{\rm H}$ and $\alpha_{\rm He\,I\,\lambda 2.058}$; we consider these in turn. $N_{\rm Lyc}^{\rm He}/N_{\rm Lyc}^{\rm H}$, the relative ionization rate of helium to hydrogen, depends on the reliability of the stellar atmosphere models. Comparison of different stellar atmosphere models by Skillman (1989) shows that the Kurucz models are in fairly good agreement with observed ionization distributions. However, it must be noted that the presence of stellar winds may dramatically affect the emerging spectrum. Although the helium abundance $N_{\rm He}/N_{\rm H}$ is less varied across the interstellar medium than that of the heavier metals, there is still an abundance gradient through-

out the Galaxy. For our observations at $T_e = 10^4$ K to be consistent with the curve labelled $n_e = 10^4$ cm^{-3}, the helium abundance would have to be ~0.07, a value that is less than the primordial value; this possibility may therefore be discounted.

The He I 2.058 μm/Brγ effective recombination coefficient, $\alpha_{\mathrm{He\,I}\lambda 2.058}$, has been discussed in Section 5.2, and the mean free paths of a 0.0584-μm photon before absorption by helium and ionization by hydrogen were compared. The mean free path is inversely proportional to the absorption cross-section for a given electron density. The absorption cross-section at the line centre for a helium resonance line, a_0, can be written as

$$a_0 = \frac{3\lambda^3 A}{8\pi}\left(\frac{1}{\Delta V_D}\right). \quad (7)$$

A is the Einstein coefficient, and ΔV_D is the thermal Doppler width, which is ~6 km s^{-1} for helium atoms at $T_e = 10^4$ K. Assuming this width and electron temperature, comparison of mean-free-path lengths implies that two-thirds of the photons from the He I 2^1P level are reprocessed by helium atoms, and one-third ionize hydrogen. However, the RRL width measurements of the UC H II regions, at about 20–45 km s^{-1} in a 2.6-arcmin beam, are considerably broader than the thermal width, and thus a further broadening process(es) is occurring. Possible mechanisms are: (i) pressure broadening due to electron impacts, (ii) bulk motions of the ionized gas, and (iii) turbulence. In their study of G29.96, Wood & Churchwell (1991) see no evidence of (i), and Garay (1989) concludes that pressure broadening of the H76α RRL is negligible in their observations of compact H II regions. To be rigorous, a full set of radiative-transfer equations should be solved, incorporating the effects of processes (ii) and (iii); however, we can examine the importance of these mechanisms in a simple model.

Consider the scenario whereby further broadening of the helium 1^1S–2^1P resonance line is solely due to turbulent motions and thus a Gaussian distribution remains appropriate. The effective Doppler width becomes

$$V_D^2 = \frac{2kT}{m_{He}} + V_{turb}^2. \quad (8)$$

If this process increases the linewidth to ~17 km s^{-1}, then only ~44 per cent of the resonance line photons from the He I 2^1P level are reprocessed by helium. The value of the He I 2.058-μm effective recombination coefficient would therefore decrease by a factor of ~1.52, and the theoretical He I 2.058 μm/Brγ ratio, for $T_e = 10^4$ K and a Galactic abundance of 0.1, would saturate at a value of 0.84. This saturation value is in good agreement with our observed He I 2.058 μm/Brγ ratios (see Table 4).

To summarize, the observations of UC H II regions are consistent with two possible models: (a) an H II region model for an electron temperature of $T_e = 5 \times 10^3$ K and an electron density of $n_e = 10^4$ cm^{-3}, assuming purely Doppler broadening, or (b) an electron temperature of $T_e = 10^4$ K and an electron density of $n_e = 10^4$ cm^{-3}, where line broadening, e.g. due to turbulence, is important on scales comparable with the 0.0584-μm He I photon mean free path (10^{12} cm; cf. H II region radius of ~10^{16} cm).

7 CONCLUSIONS

K-band measurements of He I 2.058-μm and Brγ recombination lines were carried out for a sample of UC H II regions with spectral types B1–O4, and the results compared to theoretical predictions. We have investigated modifications to the models due to collisional excitation and radiative-transfer effects. The following conclusions were drawn.

(i) Our observed ratios are in good agreement with the theoretical H II region model for an electron temperature of $T_e = 5 \times 10^3$ K, an electron density of $n_e = 10^4$ cm^{-3}, and a Galactic helium abundance assuming purely thermal broadening of the He I line. Alternatively, if the intrinsic He I linewidth is broadened, e.g. by turbulent motions of the ionized gas, to ~17 km s^{-1}, then, for an electron temperature of $T_e = 10^4$ K, an electron density of $n_e = 10^4$ cm^{-3} and a Galactic helium abundance, the effective He I 2.058-μm recombination coefficient and consequently the theoretical He I 2.058 μm/Brγ ratio would decrease sufficiently to be consistent with our UC H II region observations. The RRL measurements of our observed UC H II regions are broadly consistent with the latter model, but small-beam measurements of the He I 2.058-μm and Brγ linewidths are needed as a definitive test. Without further observations, it is not possible to distinguish between these models.

(ii) The He I 2.058 μm/Brγ ratio is not a good indicator of effective temperature in UC H II regions, as the presence of dust can limit the sensitivity to spectral types earlier than about O8. Observations of less dense H II regions, in which the complications due to collisional excitation may be neglected, and which are of later spectral type, are required. Nevertheless, we note that the galaxies observed by DPJ have He I 2.058 μm/Brγ ratios in the range 0.4–0.6, significantly less than for UC H II regions; this suggests that a population of such objects does not dominate the emission.

(iii) For observations of the narrow He I line at 2.058 μm, the effect of telluric CO_2 absorption must be calculated. For our observations, this absorption removed 5–36 per cent of the He I line flux for different UC H II regions. As the intrinsic width of the He I line is comparable with that of the individual CO_2 atmospheric lines, these amounts will vary throughout the year.

ACKNOWLEDGMENTS

RMD acknowledges the support of the UK Science and Engineering Research Council (SERC) studentships. RD is financially supported via a post-doctoral fellowship from the Natural Science and Engineering Research Council of Canada. The UK Infrared Telescope is operated by the Royal Observatory, Edinburgh on behalf of the UK SERC. We thank Dolores Walther for her assistance in making these observations, Alistair Glasse for use of the HITRAN code, Stuart Lumsden for fruitful discussions, and the referee for constructive comments which improved the presentation of this work.

REFERENCES

Aitken D. K., Roche P. F., Allen M. C., Phillips M. M., 1982, MNRAS, 199, 31P

Campbell A., Terlevich R., Melnick J., 1986, MNRAS, 223, 811
Chini R., Krügel E., Kreysa E., 1986, A&A, 167, 315
Chini R., Krügel E., Wargau W., 1987, A&A, 181, 378
Clegg R. E. S., 1987, MNRAS, 229, 31P
Clegg R. E. S., Harrington J. P., 1989, MNRAS, 239, 869
Downes D., Wilson T. L., Bieging J., Wink J. E., 1980, A&AS, 40, 379
Doyon R., Puxley P. J., Joseph R. D., 1992, ApJ, 397, 117 (DPJ)
Draine B. T., 1989, in Kaldeich B. H., ed., Proc. 22nd Eslab Symposium, Infrared Spectroscopy in Astronomy. ESA Publications, p. 93
Garay G., 1989, in Gordon M. A., Sorochenko R. L., eds, Radio Recombination Lines: 25 Years of Investigation. Kluwer, Dordrecht, p. 73
Gordon M. A., Walmsley C. M., 1990, ApJ, 365, 606
Hoare M. G., Roche P. F., Glencross W. M., 1991, MNRAS, 251, 584
Hummer D. G., Storey P. J., 1987, MNRAS, 224, 801
Kingdom J., Ferland G. J., 1991, PASP, 103, 752
Kurucz R. L., 1979, ApJS, 40, 1
Lacy J. H., Beck S. C., Geballe T. R., 1982, ApJ, 255, 510
Landolt-Börnstein, 1982, in Schiaffers K., Voigt H. H., eds, Astronomy & Astrophysics, 2b, Stars and Star Clusters, p. 31
Mathis J. S., Rumpl W., Nordsieck K. H., 1977, ApJ, 244, 483
Mountain C. M., Robertson D. J., Lee T. J., Wade R., 1990, in Crawford D. L., ed., Proc. SPIE, Instrumentation in Astronomy VII, 1235, p. 25
Osterbrock D. E., 1989, Astrophysics of Gaseous Nebulae. University Science Books, p. 29
Puxley P. J., 1988, PhD thesis, Univ. Edinburgh
Rayo J. F., Peimbert M., Torres-Peimbert S., 1982, ApJ, 255, 1
Rubin R. H., 1968, ApJ, 154, 391
Scalo J., 1989, in Renzini A., Fabbiano G., Gallagher J. S., eds, Windows on Galaxies. Kluwer, Dordrecht, p. 125
Skillman E. D., 1989, ApJ, 347, 883
Smits D. P., 1991, MNRAS, 248, 193
Wink J. E., Altenhoff W. J., Mezger P. G., 1982, A&A, 108, 227
Wood D. O. S., Churchwell E., 1989, ApJS, 69, 831
Wood D. O. S., Churchwell E., 1991, ApJ, 372, 199